



Université catholique de Louvain
Faculté des Sciences
Département de Physique
Center for Particle Physics and Phenomenology

Photoproduction of Top and Higgs Particles at the LHC

Doctoral dissertation presented by
Ovyn Séverine
for the degree of Doctor in Sciences

Pr Vincent Lemaître (Advisor)	(CP3) UCL
Pr Bernard Piraux (Chairman)	UCL
Pr Michele Arneodo	Università del Piemonte Orientale
Pr David d'Enterria	Universitat de Barcelona
Pr Laurent Favart	Université Libre de Bruxelles
Pr Fabio Maltoni	(CP3) UCL
Pr Krzysztof Piotrkowski	(CP3) UCL

Avril 2010

De tout mon coeur, je voudrais vous remercier pour votre soutien!

Ces quelques mots résumant le fond de ma pensée. . . Néanmoins, peu d'entre vous se contenteront d'une si courte phrase de remerciement. Je vais donc tenter de remercier personnellement les personnes qui ont permis l'accomplissement de ce travail. Même si la rédaction de cette partie du manuscrit est habituellement considérée comme étant la plus agréable à écrire, je me heurte ici à une tâche bien ardue. Effectivement, si l'avantage d'une thèse par rapport à un article est qu'il n'y a qu'une seule personne signataire, un grand nombre d'intervenants ont contribué de près ou de loin à la concrétisation de ce travail. Toute la difficulté réside par conséquent en l'énumération complète de toutes ces personnes. C'est pourquoi, je remercie par avance ceux dont le nom n'apparaît pas dans cette page et qui m'ont aidée d'une manière ou d'une autre.

La thèse constitue une expérience intense et passionnante que je n'aurais pas eu l'opportunité de vivre sans mon promoteur. C'est pourquoi mes premiers remerciements s'adressent au Professeur Vincent Lemaître d'avoir accepté de m'accueillir au sein de son laboratoire. Je salue sa souplesse, son dynamisme et son infatigable énergie ainsi que la large marge de liberté qu'il m'a accordée et grâce à laquelle j'ai su mener à bien ce travail de recherche. Nos oppositions, contradictions et confrontations ont certainement été la clé de notre travail commun.

Je voudrais aussi remercier messieurs les membres de mon jury pour leur collaboration durant la préparation de ce manuscrit et pour leur participation à la soutenance. J'adresse particulièrement ma reconnaissance au Professeur David d'Enterrin qui a toujours été présent pour me rassurer lors des moments de doute. Il a su me faire profiter de ses nombreuses connaissances au travers des conférences que nous avons pu réaliser ensemble. Une pensée sincère me vient aussi pour Monika Grothe sans qui l'aventure au CERN n'aurait pas été identique. Grâce à ses conseils, l'immense travail effectué au sein du groupe Forward n'aurait probablement jamais pu être réalisé.

En regardant ces 6 dernières années, je me rends compte que ce travail n'aurait pas été possible sans le soutien des nombreuses personnes qui ont croisé ma route en CP3. Ils ont tous contribué de près ou de loin à la réussite de cette thèse. Je tiens ainsi à remercier Guillaume Leibenguth et Muriel Vander Donckt pour leurs encouragements et pour les discussions que nous avons eues en tout début de thèse, à un moment critique où je manquais de repères. Merci à Simon de Visscher de m'avoir

supportée depuis près de 10 ans. Nos pauses à la Kfet se sont malheureusement faites trop rares. Merci à Christophe Delaere pour avoir patiemment répondu à mes “Dis Chris, j’aurais une bête question...”. J’en profite pour remercier dans la volée Nicolas Schul, Loïc Quertenmont, Jérôme de Favereau, Michel Herquet et Vincent Boucher pour avoir contribué discrètement mais indiscutablement à l’ambiance agréable dans laquelle j’ai baigné à CP3. Merci également à tout le personnel administratif et notamment à Ginette Tabordon, notre secrétaire, qui malgré son énorme travail au sein du laboratoire m’a toujours accordé du temps pour résoudre mes “soucis”. Merci aussi à Thomas Keutgen, Pavel Denim et Fabrice Charlier, pour leur support technique.

Est-ce dû à un concours de circonstances ou dois-je comprendre que personne ne pouvait partager son lieu de travail avec moi plus d’une année? Cela restera un mystère... Néanmoins je tiens à remercier chaleureusement les 6 personnes que j’ai eu l’occasion de côtoyer dans mon bureau durant cette thèse. Je remercie personnellement Bruno Bertrand pour avoir survécu à mes incessantes discussions. Il me reste à adresser un remerciement très spécial à Xavier Rouby. Plus qu’un collègue, je crois avoir trouvé en lui un ami qui m’a aidé aussi bien dans le travail que dans la vie lorsque mon moral n’était pas au plus haut. Grâce à lui et à notre étonnante complémentarité, nous avons réussi à relever des défis qui semblaient insurmontables. Ceci n’étant que le début d’une aventure encore plus palpitante, il ne reste qu’à espérer que notre avenir sera couronné d’autant de succès. Promis, il ne te faudra plus relire ma thèse maintenant!

Je tiens également à remercier toute ma famille pour son soutien constant tout au long de mes études et de mon doctorat. J’aimerais continuer ces lignes en évoquant mon compagnon Jean-Marc. Présent depuis le début de cette aventure, je voulais te remercier d’avoir accepté tant de sacrifices durant ces dernières années. Merci de m’avoir tenu la main jusqu’aux dernières lignes de cette thèse et de m’avoir entouré de ta tendresse. En plus de me supporter dans des conditions “normales”, ce qui n’est déjà pas une mince affaire je le conçois, tu as subi mes humeurs de “femme enceinte en fin de thèse”. Pour tout cela et pour ces années passionnantes, du fond du coeur : merci d’être auprès de moi tous les jours. Ces remerciements ne sauraient être complets sans parler de ma plus belle réussite, ma fille, Leane. Par son calme et sa joie de vivre, elle illumine mon quotidien et a contribué, à sa manière, à rendre cette fin de thèse exceptionnelle.

*Il n'y a qu'une chose qui puisse rendre un rêve impossible,
c'est la peur d'échouer.*

Paulo Coelho (l'Alchimiste)

CONTENTS

Introduction	1
1 The Standard Model	5
1.1 The gauge sector of the Standard Model	6
1.2 The Spontaneous Symmetry Breaking	8
1.3 The Top quark	12
1.3.1 Cross section and $ V_{tb} $ measurement	13
1.3.2 Experimental measurements of $ V_{tb} $	14
1.4 The Higgs boson	16
1.4.1 Higgs boson properties	16
1.4.2 Experimental restrictions on the Higgs mass	17
2 Photon interactions at hadron colliders	21
2.1 The equivalent photon flux	21
2.1.1 Elastic photon flux of protons	23
2.1.2 Hadronic cross sections	24
2.2 Physics potential of γ interactions at the LHC	27
2.2.1 Two-photon interactions	27
2.2.2 Photoproduction	29
2.3 Difficulties related to γp interactions	31
2.3.1 Rescattering effects	31
2.3.2 Inelastic interactions	32
2.3.3 Diffractive background at the LHC	33
2.3.4 Pile-up events	34
3 The DELPHES fast simulation	37
3.1 The Large Hadron Collider	37
3.2 Simulation of the detector response	40
3.3 High-level object reconstruction	46
3.3.1 Photon and charged lepton reconstruction	46
3.3.2 Jet reconstruction	47

3.3.3	<i>b</i> -tagging	49
3.3.4	τ identification	49
3.3.5	Missing transverse energy	50
3.4	Trigger emulation	51
3.5	Very forward detector simulation at the LHC	52
3.6	Validation	56
3.7	Visualisation	61
3.8	Conclusion and perspectives	62
4	<i>W</i> associated single top photoproduction	65
4.1	Top quark production at the LHC	65
4.1.1	Top-antitop production	65
4.1.2	Single-top production	66
4.2	Top quark photoproduction at the LHC	68
4.2.1	Top-antitop photoproduction	68
4.2.2	Single-top photoproduction	69
4.3	Search for <i>Wt</i> associated photoproduction	70
4.3.1	Signal and background generation	71
4.3.2	Signal discrimination of semi-leptonic events	73
4.3.3	Signal discrimination of di-leptonic events	85
4.3.4	Event selection for higher luminosities	89
4.4	Cross section and $ V_{tb} $ measurements	96
4.4.1	Systematic uncertainties	97
4.4.2	Expected $ V_{tb} $ measurement	99
4.5	Conclusion and perspectives	103
5	<i>Wt</i> photoproduction in CMS	105
5.1	The Compact Muon Solenoid experiment	105
5.2	The CMSSW framework	112
5.2.1	Reconstruction of basic quantities	112
5.2.2	PAT layers	116
5.3	Signal selection at $L < 10^{32} \text{cm}^{-2} \text{s}^{-1}$	121
5.3.1	Online selection	121
5.3.2	Offline analysis	122
5.3.3	Results after 10fb^{-1}	129
5.4	Signal selection at $L = 2 \times 10^{33} \text{cm}^{-2} \text{s}^{-1}$	130
5.4.1	Online selection	130
5.4.2	γp cuts	132
5.4.3	Results after 10fb^{-1}	132
5.5	Conclusion	133

6 Associated WH production	135
6.1 Higgs production at the LHC	135
6.1.1 Higgs boson production processes	135
6.1.2 Searches for a SM-like scalar Higgs boson	136
6.2 Higgs photoproduction at the LHC	138
6.3 Search for WH associated photoproduction	140
6.3.1 Signal event signatures	140
6.3.2 Signal and background generation	141
6.3.3 Topological and γp cuts	142
6.3.4 Final discrimination of $WHq' \rightarrow \ell b \bar{b} q'$	144
6.3.5 Final discrimination of $WHq' \rightarrow jj\tau\tau q'$	145
6.3.6 Final discrimination of $WHq' \rightarrow WWWq'$	150
6.4 Results	153
6.4.1 Confidence levels	153
6.4.2 Discriminant distributions	155
6.4.3 Expected observability	158
Conclusion	161
References	i
Figures	xi

INTRODUCTION

Developed in the early 1970s, the Standard Model represents nowadays the best theoretical description of the fundamental constituents of matter and their interactions. Interestingly, even the origin of the mass of elementary particles is the result of interactions. The so-called Brout-Englert-Higgs (BEH) mechanism predicts that masses of all elementary particles are directly related to their interaction with a yet undiscovered massive particle, the Higgs Boson.

In the next few months, the start-up of the Large Hadron Collider (LHC) constructed in the former LEP tunnel in the Geneva region will open a new fascinating chapter of particle physics. It will yield head-on collisions of two proton beams at the unprecedented centre of mass energy of 14 TeV and will operate with luminosities ranging from $\mathcal{L} = 10^{31} \text{ cm}^{-2} \text{ s}^{-1}$ to $\mathcal{L} = 10^{34} \text{ cm}^{-2} \text{ s}^{-1}$. The analysis of data that will be collected by the two general purpose detectors, ATLAS and CMS, located around the beam crossing points should allow the discovery of this Higgs boson.

If the discovery of the Higgs boson, although quite challenging, is basically guaranteed provided enough luminosity is delivered by the LHC, extracting its Standard Model nature is a far more difficult task. This is particularly true for a light Higgs boson ($m_H < 130 \text{ GeV}/c^2$) which decays predominantly to a $b\bar{b}$ quark-antiquark pair. Indeed, due to large QCD backgrounds, its discovery will have to be made from topologies resulting from production modes and decay products predicted by quantum loops and not by the dominant Hbb tree level coupling.

Apart from elucidating the Higgs mechanism, another goal of the LHC collider is to provide evidence of physics beyond the Standard Model. In this context, the study of the heaviest elementary particle observed to date, the top quark, is particularly interesting since it is the only fermion with a natural Yukawa coupling to the Higgs boson of the order of unity. Moreover its charged weak coupling might be particularly sensitive to the existence of an

additional heavy fermion. These couplings can be probed by measuring specific top quark production cross section and branching ratios.

These measurements will be challenging due to the composite internal structure of the colliding particles. As already emphasised, many particle final states can simply be invisible by the large QCD (or even electroweak) backgrounds. In addition, the exact centre-of-mass energy of the collisions occurring between the partons of protons is not precisely known. Moreover, the interesting produced particles could be difficult to separate from the large amount of particles present in the central detector arising from underlying events. High energy interactions involving quasi-real incoming photons may provide a solution to some of these problems.

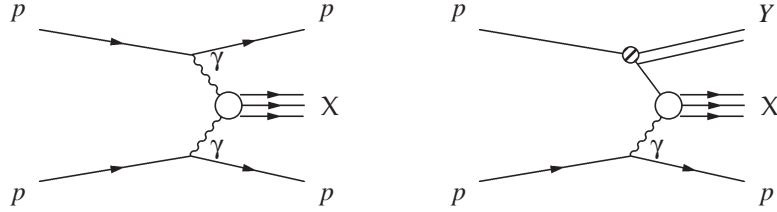


Figure 1: Generic Feynman diagrams for the photon-induced processes at the LHC. Left, emission of a photon by both protons. The photons collide yielding the creation of a central system X and two protons scattered at low angles $pp(\gamma\gamma \rightarrow X)pp$. Right, only one of the incoming proton emits a photon that interact with a parton of the second proton. A system Y is also created $pp(\gamma q/g \rightarrow X)Yp$.

Even if photon interactions are favourably produced by high energy electron or positron beams, the LHC can also be used as a high energy photon-proton or photon-photon collider since two different types of interactions involving photons can occur. Firstly, a process where photons radiated off by both protons collide (Figure 1) producing a central system X , referred as a *photon-photon interaction*. This process is usually characterised by very clean experimental conditions as only the system X will be detected by the central detector. The two protons remaining intact escape from the central detection and continue their path close to the beam line. Alternatively, in *photoproduction*, a photon from a proton induces a deep inelastic scattering with the incoming proton producing a proton remnant Y in addition to the centrally produced X system. Throughout this thesis, these two interactions will be noted as $pp(\gamma\gamma \rightarrow X)pp$ and $pp(\gamma q/g \rightarrow X)pY$ respectively, where Y is the proton remnant.

For the first time, the LHC will allow to study photon-induced interactions occurring at energies beyond the electroweak energy scale allowing to use these interactions as a complementary tool to the parton-parton collisions at

the LHC. Despite a lower available luminosity than in the nominal partonic collisions, photoproduction is attractive thanks to the large luminosity of the LHC, better known initial conditions and usually final states containing fewer particles.

The studies presented in this dissertation focus on the photoproduction of a single top quark or the Higgs boson in association with a W boson at the LHC. Chapter 1 recalls some important aspects of the Standard Model with a particular emphasis put on the current experimental knowledge of the top properties. A review of the BEH mechanism and the experimental constraints on the Higgs mass is also given. Chapter 2 develops photon-induced physics at the LHC. It includes theoretical and experimental aspects that must be considered when a photon-induced analysis is performed. In order to easily obtain an evaluation of the physics potential of such processes, a framework allowing to perform a fast simulation of a typical LHC detector has been developed. This simulation software, called DELPHES, is presented in Chapter 3 and gives the simulation details needed for the subsequent chapters. DELPHES allows to quickly obtain a realistic estimation of the reconstructed quantities such as leptons, jets, tagging of heavy flavour jets and missing transverse energy necessary to study topologies involving hard jets in the final state. The photoproduction at the LHC of a Wt is discussed in Chapter 4. Strategies to extract the signal out of the background events are debated, leading to estimates of the observability of such signal. The techniques used to separate photon-induced events from the conventional proton-proton interactions like rapidity gaps and exclusivity conditions are discussed. A more realistic analysis of the Wt photoproduction in the di-leptonic channel using the official software of the CMS detector is developed in Chapter 5 for a more realistic estimation of the expected signal and backgrounds in the very low and low luminosity phases. Finally, in Chapter 6 a quick evaluation of the potential of the $pp(\gamma p \rightarrow WHq')$ reaction in five different final states is done using DELPHES.

The work presented in this Thesis is based on the following publications

- S. Oryn, X. Rouby, V. Lemaître, *Delphes, a framework for fast simulation of a generic collider experiment* CP3-09-01 (2009), [arXiv:0903.2225v2 \[hep-ph\]](#),
- J. de Favereau de Jeneret, V. Lemaitre, Y. Liu, S. Oryn, T. Pierzchala, K. Piotrkowski, X. Rouby, N. Schul, M. Vander Donckt, *High energy photon interactions at the LHC*, [arXiv:0908.2020v1 \[hep-ph\]](#),
- J.J. Hollar, S. Oryn, X. Rouby, *Exclusive $\gamma\gamma \rightarrow \ell^+\ell^-$ and $\gamma p \rightarrow Yp \rightarrow \ell^+\ell^-p$ production*, (CP3-07-28), [CMS PAS-DIF-07-001](#),
- S. Oryn, X. Rouby, J.J. Hollar, *Forward Physics Triggers*, (CP3-08-07), [CMS IN-2008/028](#)

and has also been presented in the following international conferences:

- Photon-LHC-2008, CERN presented by S. Oryn, *Associated W and Higgs boson photoproduction and other electroweak photon induced processes at the LHC*, (CP3-08-14), Nucl. Phys. B, Proc. Suppl. 179-180 (2008) 269-276, [arXiv0806.1157 \[hep-ph\]](#),
- TOP 2008, Isola d'Elba presented by S. Oryn, J. de Favereau de Jeneret, *High energy single top photoproduction at the LHC*, (CP3-08-28), Nuovo Cim.123B (2008) 1126-1133, [arXiv:0806.4841v1 \[hep-ph\]](#),
- DIS08, London presented by S. Oryn on behalf of the CMS Collaboration, *Exclusive dilepton and Upsilon production with CMS: a feasibility study*, CMS CR-2008-036,
- HLPW08, Liège presented by S. Oryn, *High energy photoproduction at the LHC*, (CP3-08-15), [AIP Conference Proceedings No 1038](#),
- PHOTON 2007, Paris presented by S. Oryn, *High energy photoproduction at the LHC*, (CP3-07-27), Nucl. Phys. B (Proc. Suppl.) 184 (2008) 166-168.

THE STANDARD MODEL

Over the past century, one of the important goals in physics was the understanding of the fundamental structure of the matter. Several decades were necessary to bring physicists to the current model that explains the fundamental behaviour of *elementary particles* as well as the strong, electromagnetic and weak interactions acting on them: the *Standard Model* (SM). The two latter interactions are combined in a theory known as the *electroweak theory* of Glashow, Weinberg and Salam [1]. Elementary particles are classified according to their spin quantum number: spin- $\frac{1}{2}$ particles called *fermions* and *gauge bosons* having an integral spin equal to 1 (W^\pm and Z^0 bosons, photon and gluons). The twelve fermions known nowadays are arranged into *leptons* (e^- , μ^- , τ^- , ν_e , ν_μ and ν_τ) and *quarks* (u, d, s, c, b, t). Finally, for every fermion, there exists an antiparticle partner with identical mass but differing from its counterpart by opposite signs of its quantum numbers.

The major keys that lead to the success of the Standard Model are the introduction of local gauge invariance that generates the so-called *gauge bosons* and the implementation of the *Spontaneous Symmetry Breaking* mechanism (SSB) that gives their masses to weak bosons and fermions. Until now, the Standard Model has been outliving plenty of precise experimental verifications. Among them, one can emphasise the discovery of Neutral Currents [2], the violation of parity observed in beta decays and the discovery of gauge bosons at the SPS collider at CERN in 1983 [3] which definitely confirmed the validity of the Standard Model (SM). Still, an essential ingredient eludes to be found by experiments: the anticipated Higgs boson.

1.1 The gauge sector of the Standard Model

In the Standard Model, interactions result from the local invariance of the Lagrangian under specific groups. In order to incorporate into the SM electromagnetism and the weak interaction, the invariance under the $SU(2)_L \otimes U(1)_Y$ local gauge symmetry is applied on the Lagrangian, that is connected to the conservation of the *weak hypercharge* Y and the *weak isospin* T respectively ¹. The gauge group associated to the strong interactions is $SU(3)_C$, where C refers to colour.

Gauge transformations introduce real vector boson fields, that mediate the interactions between elementary particles. Since the number of these fields is equal to the number of generators of the group, the electroweak gauge sector of the SM is composed of four vectorial fields: B_ν and $W_\nu^{1,2,3}$ associated respectively to the generators of $U(1)_Y$ and $SU(2)_L$. These bosons have been experimentally observed as the W^\pm and Z bosons, carriers of the weak interaction, and the photon that mediates the electromagnetic interaction. The $SU(3)$ group possesses eight generators leading to the physically identifiable gluons as mediators of the strong interaction.

Table 1.1: The leptons of the Standard Model arranged in $SU(2)_L \otimes U(1)_Y$ multiplets and their quantum numbers Q (electric charge), T (weak isospin), T_3 and Y (weak hypercharge). The index $j = 1, 2, 3$ on each field refers to the generation while the L and R indexes refer to chirality [4]. Antileptons are similarly arranged, with identical corresponding masses and opposite quantum numbers.

Fields	Generation			Quantum number			
	1 st	2 nd	3 rd	Q	T	T_3	Y
L_L^j	$\begin{pmatrix} \nu_e \\ e \end{pmatrix}_L$	$\begin{pmatrix} \nu_\mu \\ \mu \end{pmatrix}_L$	$\begin{pmatrix} \nu_\tau \\ \tau \end{pmatrix}_L$	0	1/2	+1/2	-1
L_R^j	e_R	μ_R	τ_R	-1	0	0	-2

Leptons are particles that carry an integral *electric charge* $Q = 0, \pm 1$ and which are only influenced by the electromagnetic and the weak forces ². They are grouped together to form three sets called *generations* or *families* with similar properties except for the mass. The electron (e) and the electron-neutrino (ν_e) compose the first generation, while the muon (μ) and the tau (τ) are similarly arranged with their corresponding neutrinos (ν_μ and ν_τ) to form the second and third generations. The lepton fields that make up the Standard

¹The weak hypercharge is defined using the the Gell-Mann-Nishijima relation $Q = T_3 + \frac{Y}{2}$, with Q the electric charge and T_3 is the third axis projection of the weak isospin.

²Because the Standard Model does not include the effects of gravitational interactions, we will not talk about it throughout this theoretical introduction.

Model are summarised in Table 1.1 along with their quantum numbers. The left-handed and right-handed fields that transform respectively as doublets and singlets of $SU(2)_L$ are defined by means of the chirality operator.

Table 1.2: The quarks of the Standard Model arranged in $SU(2)_L \otimes U(1)_Y$ multiplets and their electroweak quantum numbers, Q (electric charge), T (weak isospin), T_3 and Y (weak hypercharge). The L and R indexes refer to chirality [4]. Antiquarks are similarly arranged, with identical corresponding masses and opposite quantum numbers.

Fields	Generation			Quantum number			
	1 st	2 nd	3 rd	Q	T	T_3	Y
\mathcal{Q}_L^j	$\begin{pmatrix} u \\ d \end{pmatrix}_L$	$\begin{pmatrix} c \\ s \end{pmatrix}_L$	$\begin{pmatrix} t \\ b \end{pmatrix}_L$	+2/3 -1/3	1/2 1/2	+1/2 -1/2	+1/3 +1/3
u_R^j	u_R	c_R	t_R	+2/3	0	0	+4/3
d_R^j	d_R	s_R	b_R	-1/3	0	0	-2/3

Quarks have fractional electric charges of $+\frac{2}{3}|e|$ or $-\frac{1}{3}|e|$. Since they are the only fermions which feel the strong interaction, their most significant property is that they possess an additional quantum number, the *colour*. Quarks are likewise leptons organised into pairs that differ by one unit of electric charge: *up* and *down* quarks are forming the lower generation and the two other generations contain corresponding heavier quarks, namely *charmed*, *strange* and *top*, *bottom* pairs. The particle content of the quarks families, the associated fields as well as their quantum numbers are summarised in Table 1.2. Thanks to their colour charge, quarks also interact via the strong force.

The particles of the SM are described by combining the kinematic term of the fermion fields and their interactions with the gauge boson fields $\mathcal{L}_{fermions}$:

$$\mathcal{L} = \mathcal{L}_{fermion} - \frac{1}{4}B_{\mu\nu}B^{\mu\nu} - \frac{1}{4}W_{\mu\nu}^iW^{i\mu\nu} - \frac{1}{4}G_{\mu\nu}^aG^{a\mu\nu}, \quad (1.1)$$

whit the strength tensors $W_{\mu\nu}^i$, $B_{\mu\nu}$ and $G_{\mu\nu}^a$ defined as

$$B_{\mu\nu} = \partial_\mu B_\nu - \partial_\nu B_\mu, \quad (1.2)$$

$$W_{\mu\nu}^i = \partial_\mu W_\nu^i - \partial_\nu W_\mu^i - g\epsilon^{ijk}W_\mu^jW_\nu^k \quad (1.3)$$

$$G_{\mu\nu}^a = \partial_\mu G_\nu^a - \partial_\nu G_\mu^a - g_s f^{abc}G_\mu^bG_\nu^c, \quad a, b, c = 1, \dots, 8, \quad (1.4)$$

where G_ν^a are the eight vectorial fields associated to the generators of $SU(3)_C$, and finally g and g_s are respectively the weak and the strong interaction couplings. As an example, the purely electroweak term of the $\mathcal{L}_{fermions}$ Lagrangian

is given by

$$\mathcal{L}_{fermion}^{EW} = \sum_{j=1}^3 i \left[\bar{L}_L^j \gamma^\mu (\partial_\mu + igW_\mu^i \frac{\sigma^i}{2} + ig'B_\mu \frac{-1}{2}) L_L^j + \bar{L}_R^j \gamma^\mu (\partial_\mu + ig'B_\mu \frac{-2}{2}) L_R^j \right], \quad (1.5)$$

where L_L^j and L_R^j fields are respectively the left and right components of the fields associated to the leptons and σ^i are the Pauli matrices. The terms including g and g' are respectively proportional to the weak isospin T and the hypercharge Y .

It should be noticed that the fermion fields in the above Lagrangian cannot be massive because the fermion mass terms mix left-handed and right-handed fields, so the resulting mass terms break the gauge symmetry. Identically, even if the very accurate experimental measurements of W^\pm and Z^0 boson masses clearly indicate values different from zero, leaving the photon as the only massless boson, the addition of mass terms $m_W W_\mu W^\mu$ and $\frac{1}{2} m_Z Z_\mu Z^\mu$ for the gauge bosons would violate the gauge invariance of the SM. These two mass problems are solved by using an alternative scenario called the Spontaneous Symmetry Breaking which will be introduced in the next section.

1.2 The Spontaneous Symmetry Breaking

Spontaneous Symmetry Breaking (SSB) is an elegant way to generate the masses of the W^\pm and Z^0 gauge bosons without spoiling the gauge invariance of the Lagrangian. In the SM, it is applied on the electroweak $SU(2)_L \otimes U(1)_Y$ sector and reduces it to a $U(1)_{em}$ symmetry. An additional term needed to break the electroweak theory must be added into Equation 1.1. This \mathcal{L}_{Higgs} term which is invariant under the gauge transformations takes the following form

$$\mathcal{L}_{Higgs} = |\mathcal{D}_\mu \Phi|^2 - V(\Phi), \quad (1.6)$$

where Φ is a fundamental complex $SU(2)_L$ doublet with hypercharge $Y = 1$ called *the Higgs field*

$$\Phi = \begin{pmatrix} \phi^+ \\ \phi^0 \end{pmatrix} = \begin{pmatrix} \phi_1 + i\phi_2 \\ \phi_3 + i\phi_3 \end{pmatrix} \quad (1.7)$$

and $V(\Phi)$ is the potential term for which the most general form is given by

$$V(\Phi) = \mu^2 |\Phi|^2 + \lambda |\Phi|^4; \quad \lambda > 0, \quad (1.8)$$

where the sign of λ has been chosen to bound the potential from below. Although two possibilities exist for the the sign of the μ^2 parameter, only one allows to break the symmetry. For a positive value of μ^2 , the potential possesses a unique minimum at $|\Phi| = 0$; on the contrary, if $\mu^2 < 0$ there exists

infinite degenerate minima situated at

$$|\Phi| = \sqrt{\frac{-\mu^2}{2\lambda}} \equiv \frac{v}{\sqrt{2}}, \quad (1.9)$$

where v the *vacuum expectation value* (vev) of the Higgs field Φ . The potential chosen for the SSB in the SM is shown in Figure 1.1 as a function of a neutral complex scalar field, where the circle of minima appears.

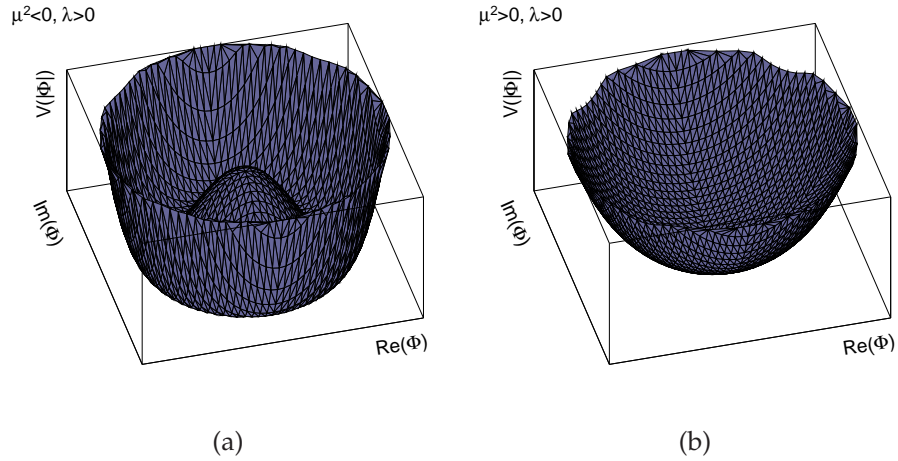


Figure 1.1: Scalar Higgs potential as a function of the components of a complex scalar field. The four sign combinations are shown. (a) corresponds to the Standard-Model choice. The circle of infinite minima at $|\Phi| = \frac{v}{\sqrt{2}}$ is clearly visible. Plot (b) shows that the $\mu^2 > 0$ and $\lambda > 0$ choice does not break the symmetry as the minimum is at the origin.

A breakdown in the form $SU(2)_L \otimes U(1)_Y \rightarrow U(1)_{em}$ occurs by choosing a particular vev that respects the electromagnetic $U(1)_{em}$ such as

$$\langle \Phi \rangle_0 = \frac{1}{\sqrt{2}} \begin{pmatrix} 0 \\ v \end{pmatrix}, \quad (1.10)$$

where the vacuum expectation value for the charged Higgs field ϕ^+ has been set to 0 leading to a resulting state invariant under $U(1)_{em}$.

In the unitary gauge, the expansion of the Higgs field ϕ around the ground state gives

$$\Phi = \begin{pmatrix} \phi^+ \\ \phi^0 \end{pmatrix} = \frac{1}{\sqrt{2}} \begin{pmatrix} 0 \\ v + H \end{pmatrix}, \quad (1.11)$$

where H is a real scalar field. The gauge boson mass spectrum is obtained by inserting the hereabove field into the covariant derivative part of Equation 1.6. More specifically, after the symmetry breaking, the covariant derivative of the Higgs fields leads to

$$\mathcal{D}_\mu\Phi = \frac{1}{\sqrt{2}} \left\{ \partial_\mu \begin{pmatrix} 0 \\ H \end{pmatrix} + \frac{i}{2} \begin{pmatrix} g\sqrt{2}W_\mu^+(v+H) \\ (-gW_\mu^3 + g'B_\mu)(v+H) \end{pmatrix} \right\}, \quad (1.12)$$

where the W^+ and W^- fields are obtained by combinations of the original vector gauge fields W_μ^1 and W_μ^2 .

$$W_\mu^\pm = \frac{W_\mu^1 \mp iW_\mu^2}{\sqrt{2}}, \quad (1.13)$$

Furthermore, the mass eigenstates which define the physical neutral Z^0 and γ gauge bosons are obtained by rotating the weak eigenstates using the Weinberg mixing angle defined by the relation of the couplings $g = g' \tan \theta_W$:

$$\begin{pmatrix} A_\mu \\ Z_\mu \end{pmatrix} = \begin{pmatrix} \cos \theta_W & \sin \theta_W \\ -\sin \theta_W & \cos \theta_W \end{pmatrix} \begin{pmatrix} B_\mu \\ W_\mu^3 \end{pmatrix}, \quad (1.14)$$

where the first field A_μ represents the photon field while the second one is associated to the Z boson. The kinematic term may therefore be written as

$$|\mathcal{D}_\mu\Phi|^2 = \frac{1}{2}(\partial_\mu H)(\partial^\mu H) + \frac{g^2 v^2}{4} W_\mu^+ W^{-\mu} + \frac{(g^2 + g'^2)v^2}{8} Z_\mu Z^\mu + \dots \quad (1.15)$$

where the appearance of the masses has become explicit through terms involving v . Specifically, the mediators of the weak interaction, the W^\pm and Z^0 bosons, acquire masses characterised by

$$m_W = \frac{gv}{2}, \quad m_Z = \frac{v}{2} \sqrt{g^2 + g'^2} = \frac{gv}{2 \cos \theta_W}, \quad m_A = 0. \quad (1.16)$$

Fermion masses and the CKM matrix

In order to finalise the Lagrangian of the Standard Model, the fermions also need to acquire mass. While an explicit mass term is forbidden, interaction terms between the fermion fields and the Higgs doublet Φ can freely be introduced in the Lagrangian. Such a gauge invariant term is called the *Yukawa* Lagrangian and is written

$$\mathcal{L}_{Yukawa} = -\lambda_\ell^{ij} \bar{L}_L^i \Phi L_R^j - \lambda_d^{ij} \bar{Q}_L^i \Phi d_R^j - \lambda_u^{ij} \bar{Q}_L^i (i\sigma_2 \Phi^*) u_R^j + h.c. \quad (1.17)$$

where $\lambda_{(\ell,u,d)}$ are 3×3 complex matrices and the isodoublet $i\sigma_2 \Phi^*$ is required in order to generate the masses of up-quarks. After the electroweak symmetry breaking, the mass terms appear by inserting Equation 1.10 into Equation 1.17.

Since by definition the mass basis corresponds to diagonal mass matrices, the fermion mass terms are expressed as:

$$m_f = \frac{\lambda_f v}{\sqrt{2}}, \quad (1.18)$$

where the Yukawa couplings of fermions λ_f result from the diagonalisation of the $\lambda_{(\ell, u, d)}$ matrices. Due to the absence of neutrino masses, such a diagonalisation does not affect the leptons.

The diagonalisation of the $\lambda_{(u, d)}$ matrices appearing in Equation 1.17 is always possible using two unitary matrices V_{qL} and V_{qR} such that

$$V_{qL} \lambda_q V_{qR}^\dagger = \lambda_q^{diag}, \quad (q = u, d), \quad (1.19)$$

with λ_q^{diag} is diagonal and real. In the mass basis, the charged current interaction term for quarks appearing in Equation 1.5 can be rewritten as

$$\mathcal{L}_{W^\pm} = \frac{g}{\sqrt{2}} \bar{u}_L^i \gamma^\mu V_{CKM}^{ij} d_L^j W_\mu^\pm + h.c., \quad (1.20)$$

where u_L^i and d_L^j are the quark mass eigenstates and V_{CKM} is a unitary 3×3 matrix defined as

$$V_{CKM} = V_{uL} V_{dL}^\dagger. \quad (1.21)$$

and called the *Cabibbo-Kobayashi-Maskawa* mixing matrix V_{CKM} [5]. The left-chiral eigenstates of the down d , strange s and bottom b quarks are therefore given by combinations of the mass eigenstates (d', s', b') through the following unitary transformation

$$\begin{pmatrix} d \\ s \\ b \end{pmatrix} = \begin{pmatrix} V_{ud} & V_{us} & V_{ub} \\ V_{cd} & V_{cs} & V_{cb} \\ V_{td} & V_{ts} & V_{tb} \end{pmatrix} \begin{pmatrix} d' \\ s' \\ b' \end{pmatrix} = V_{CKM} \begin{pmatrix} d' \\ s' \\ b' \end{pmatrix}, \quad (1.22)$$

implying that the weak interaction eigenstates are misaligned with respect to the fermion mass eigenstates.

Whereas the CKM unitary matrix introduces nine new degrees of freedom in the SM, five of them can be reabsorbed into the phases of the quark fields leaving only four remaining parameters: three rotation angles and one phase. Among the various existing parametrisations of the CKM matrix, the complete form of the matrix can be expressed using the three angles θ_{12} , θ_{23} , θ_{13} and the phase δ as

$$V_{CKM} = \begin{pmatrix} c_{12}c_{13} & s_{12}c_{13} & s_{13}e^{-i\delta} \\ -s_{12}c_{23} - c_{12}s_{23}s_{13}e^{i\delta} & c_{12}c_{23} - s_{12}s_{23}s_{13}e^{i\delta} & s_{23}c_{13} \\ s_{12}s_{23} - c_{12}c_{23}s_{13}e^{i\delta} & -c_{12}s_{23} - s_{12}c_{23}s_{13}e^{i\delta} & c_{23}c_{13} \end{pmatrix} \quad (1.23)$$

with $c_{ij} = \cos \theta_{ij}$ and $s_{ij} = \sin \theta_{ij}$. Because the theory does not predict the magnitude of any of the four parameters, one of the actual goals of the running experiments is to precisely determine their values, with special attention put on the $|V_{tb}|$ matrix element. Indeed, while its value is often assumed to be roughly equal to one, the value of this element has never been determined without the assumption of the unitarity of the CKM matrix. Nevertheless, a direct measurement of $|V_{tb}|$ smaller than one would be a hint of the existence of either a family of quarks beyond the three known ones either an additional heavy quark [6] which has not been ruled out by experimental measurements.

In absence of any direct measurement, the most precise expectation value of the $|V_{tb}|$ matrix element is obtained by inferring its value from other measured matrix elements. Hence, using theoretical considerations based on the unitarity requirement of the matrix and the assumption of exactly three generations of quarks, the absolute value of the third element of the third row is constrained within the following range [7]

$$0.9990 < |V_{tb}| < 0.9992 \quad (1.24)$$

at 95% C.L. Relaxing the assumption of three generations but maintaining the unitarity yields to the following bounds: $0 < |V_{tb}| < 0.9992$. The parameter range allowed for this matrix element can be constrained using the electroweak production cross section of single top events since it is directly proportional to the square of the CKM matrix element $|V_{tb}|$.

1.3 The Top quark

The top quark is currently a source of a wealth of physical results. Since the b quark discovery in 1977, the existence of its weak isospin partner, the t quark, has been anticipated. Nevertheless, several decades were necessary before its first direct observation [8] in 1995 during RUN I of the TEVATRON [9] by the CDF [10] and DØ [11] experiments. Indeed, since the LEP measurements, the t quark was expected to be by much heavier than all known elementary particles. Due to its relatively recent discovery, a number of the top properties have still to be precisely measured providing stringent tests of the SM. Last but not least, due to the large number of top quarks that will be produced at the Large Hadron Collider [12] (LHC), top events constitute an important source of background in searches for new physics. Until the start-up of the LHC, the TEVATRON is the only collider where the top quark can be produced. This section focuses on the current knowledge of the top properties obtained at the TEVATRON.

1.3.1 Cross section and $|V_{tb}|$ measurement

Because the SM assumes the CKM matrix to be unitary, and with the small experimentally measured V_{ub} and V_{cb} matrix elements [4], it turns out that the dominant electroweak decay mode of the top quark is $t \rightarrow Wb$. The dominant partial decay width of the top into a W boson and a b quark is given by

$$\Gamma(t \rightarrow Wb) \propto \frac{G_F m_t^3}{8\pi\sqrt{2}} |V_{tb}|^2, \quad (1.25)$$

where G_F is the *Fermi constant* with value given by

$$\frac{G_F}{\sqrt{2}} = \frac{g^2}{8m_W^2}. \quad (1.26)$$

This allows to obtain an important feature of the top quark since the high top mass implies a relatively large decay width which is immediately convertible into a lifetime value of approximately $\tau_{top} = \hbar/\Gamma_{top} \simeq 5 \times 10^{-25}$ s if $|V_{tb}| \approx 1$. Because this value is almost one order on magnitude smaller than the characteristic formation time of hadrons $\tau_{form} \approx 2 \times 10^{-24}$ s the top quark decays before hadronisation and does not form hadronic bound states [13]. Even if it is commonly assumed that the top quark decays before hadronisation, a precise determination of the $|V_{tb}|$ matrix element is necessary to confirm this assumption. Indeed, in addition to the not so widely different formation and decay time scales, the dependence of the decay width to the squared of the $|V_{tb}|$ matrix element implies that for a value of $|V_{tb}| \ll 1$ the lifetime may become longer than the typical strong interaction time scale allowing the formation of open-flavour hadrons.

Production Cross Section

At hadron colliders, such as the TEVATRON, top quarks are primarily produced in pairs of $t\bar{t}$. Because the TEVATRON accelerates and collides proton-antiproton at a centre-of-mass energy of $\sqrt{s} \sim 2$ TeV, $t\bar{t}$ pair production is dominated by the $q\bar{q}$ annihilation of valence quarks since they carry more momentum than gluons. Hence, at the TEVATRON, roughly 85% of the top pairs are due to the $q\bar{q} \rightarrow t\bar{t}$ process. The leading order Feynman diagram of such process is shown in the left part of Figure 1.2. Next to leading order calculations have been performed [14] that predict a combined production cross section of $6.9_{-0.64}^{+0.46}$ pb at $\sqrt{s} = 1.96$ TeV for a top quark mass of 175 GeV/ c^2 . It should be noticed that an increase of \sqrt{s} will lead to an inversion of the main production mechanism as at the LHC ($\sqrt{s} = 14$ TeV) gluon fusion becomes a copious source of $t\bar{t}$ pairs.

In addition to the production of top quarks through QCD interactions, top quark production is also possible using electroweak charged current interactions. In the so-called *s-channel single top* production process, a W boson

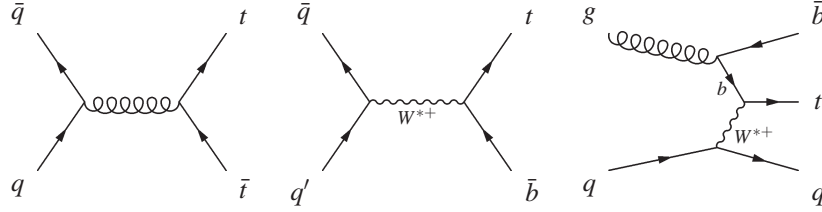


Figure 1.2: Feynman diagrams for top quark production at the TEVATRON. From left to right, $t\bar{t}$ pair production through quark-antiquark annihilation, single top s-channel and the one single top t-channel processes.

formed from a $q'\bar{q}$ annihilation decays to a top and a bottom quarks. In the t-channel, a virtual W boson strikes a b quark producing a light quark and a top quark. These two electroweak processes are represented respectively in the central and right part of Figure 1.2. The theoretically predicted production cross sections at next-to-leading order in α_s are equal to $1.98^{+0.28}_{-0.22}$ pb [15] and 1.02 ± 0.08 pb [16] for the t-channel and s-channel respectively. Finally, it should be mentioned that there exists a third production mode where the top quark is created in association with a W boson. Nevertheless, due to the small cross section of this process at the TEVATRON 0.25 ± 0.03 pb [16], this production channel is unexploitable.

1.3.2 Experimental measurements of $|V_{tb}|$

A precise determination of the top quark pair production cross section $\sigma_{t\bar{t}}$ is crucial since new phenomena could alter this value and give insight of new physics beyond the Standard Model (see e.g. [17]). Because in the SM the preferred decay of the top quark is $t \rightarrow Wb$ with a branching ratio close to 100%, only three possible final states of $t\bar{t}$ events exist in relation with the decay products of the W bosons. When both W bosons decay leptonically, the final state is named the *di-leptonic channel* ($\ell^+ \nu \ell^- \bar{\nu} \bar{b}$). Events with only one or both W bosons decaying hadronically are called respectively *semi-leptonic* ($\ell \nu q q' \bar{b} \bar{b}$) and *fully-hadronic* ($qq' b q q' \bar{b}$) channels. Using the different decay channels, the CDF and DØ experiments have measured the respective production cross section:

$$\text{CDF: } 7.0 \pm 0.3(\text{stat.}) \pm 0.4(\text{syst.}) \pm 0.4(\text{lumi}) \text{ pb [18]}, \quad (1.27)$$

$$\text{DØ: } 7.8 \pm 0.5(\text{stat.}) \pm 0.6(\text{syst.}) \pm 0.5(\text{lumi}) \text{ pb [19]} \quad (1.28)$$

It is obvious that these results are consistent with each other and with the theoretically predicted SM cross section assuming a top quark mass of $175 \text{ GeV}/c^2$.

Although the measurement of the single top quark production cross section is challenging at the TEVATRON, the first clear evidence of the presence of the electroweak production of single top quarks in $p\bar{p}$ collisions has recently

been established. The discovery of the top quark constitutes together with the first evidence of single top events, one of the major experimental successes of the TEVATRON collider. Combining three multivariate techniques such as matrix element methods, likelihood function or neural networks, a cross section of $2.2_{-0.6}^{+0.7}$ pb [20] is obtained at CDF using 2.3 fb^{-1} of data at $\sqrt{s} = 1.96 \text{ TeV}$ while the DØ collaboration evaluates it to $3.94 \pm 0.88 \text{ pb}$ [21]. The two values are consistent with the SM prediction of $2.9 \pm 0.4 \text{ pb}$ ($tb + tqb$ channels).

$|V_{tb}|$ matrix element

This section describes the results obtained at TEVATRON from a direct measurement of $|V_{tb}|$ using top quark decay in $t\bar{t}$ event and the less constraining measurement using single top production. To extract a value of $|V_{tb}|$, the ratio of branching fractions of the top decaying into Wb to top decaying to down type quark is defined

$$R_b \equiv \frac{\text{BR}(t \rightarrow Wb)}{\text{BR}(t \rightarrow Wq)} = \frac{|V_{tb}|^2}{|V_{td}|^2 + |V_{ts}|^2 + |V_{tb}|^2}, \quad (1.29)$$

where q stands for d , s and b quarks. Experimentally, the measurement of R_b is based on the relative number of $t\bar{t}$ -like events containing zero, one and two tagged b -jets. Because of the definition of R_b , the measurement is independent of the uncertainties on the production cross section of $t\bar{t}$ events, while it is obvious that it depends critically on the knowledge of the efficiency of labelling a jet as coming from a b quark. Because at both DØ and CDF the measured ratio is close to 1, this implies that $|V_{tb}| \gg |V_{td}|, |V_{ts}|$. In order to measure $|V_{tb}|$ using the $t\bar{t}$ produced events at TEVATRON, the unitarity of the matrix should be assumed so the denominator of R_b is unity. Using respectively 162 pb^{-1} and 0.9 fb^{-1} of $p\bar{p}$ collisions at $\sqrt{s} = 1.96 \text{ TeV}$, the CDF and DØ collaborations obtained the following lower limits at 95% C.L.: $|V_{tb}| > 0.78$ [22] (using leptons+jets and dileptons) and 0.89 [23] (investigating only lepton+jets events).

Compared to the previous technique using $t\bar{t}$ events, the determination of V_{tb} by measuring the single top production cross section does not assume the unitarity of the CKM matrix. Based on the measurements of the single top production cross sections by CDF and DØ, a value of $|V_{tb}|$ of $0.91 \pm 0.11(\text{stat} + \text{syst}) \pm 0.07(\text{theory})$ and $|V_{tb}| > 0.71$ at the 95% C.L. [20] has been extracted at while DØ finds $|V_{tb}| = 1.07 \pm 0.12$ and $|V_{tb}| > 0.78$ at the 95% C.L. [21]. We can therefore conclude that both results are consistent with the SM expectations.

1.4 The Higgs boson

1.4.1 Higgs boson properties

The Brout-Englert-Higgs mechanism introduced in the previous section is the simplest way to allow elementary particles to be massive since mass terms appear through the interactions of particles with the Higgs particle. After the application of the Electroweak Symmetry Breaking, Lagrangian 1.6 can be rewritten in terms of physical fields:

$$\begin{aligned} \mathcal{L}_{Higgs} = & \frac{1}{2}(\partial_\mu H)(\partial^\mu H) - \frac{1}{2}m_H^2 H^2 \\ & + m_W^2 W_\mu^+ W^{-\mu} \left(1 + \frac{2}{v}H + \frac{1}{v^2}H^2\right) + \frac{1}{2}m_Z^2 Z_\mu Z^\mu \left(1 + \frac{2}{v}H + \frac{1}{v^2}H^2\right) \\ & - \frac{m_H^2}{2v}H^3 - \frac{m_H^2}{8v^2}H^4 + \frac{m_H^2}{8}v^2, \end{aligned} \quad (1.30)$$

where the mass of the Higgs boson $m_H = -2\mu^2$ has been introduced. In addition to the coupling of the Higgs boson to fermions introduced in Section 1.2, the couplings of the Higgs boson to gauge bosons clearly emerge in Equation 1.30 by looking terms linear in H as

$$g_{HVV} = \delta_V \frac{m_V^2}{v} \quad (1.31)$$

where V represents either the W or Z bosons and the δ_V related parameters are respectively equal to 2 and 1.

Beside the rich program related to the top physics, the Higgs boson discovery is vital in order to validate this mechanism. Nevertheless, even if actual running experiments are competing against each other for its discovery, the Higgs boson eludes experimental verification. The search is greatly complicated by the fact that the Higgs mass is not predicted by the SM. Fortunately, since the mass of the Higgs boson is the only free parameter of the Higgs sector, all variables including the branching ratios, could be determined unambiguously for a given mass. Using the above expressions of the Higgs coupling to fermions and gauge bosons, the partial decay widths can be calculated allowing to obtain the decay modes that could be promising for the detection of the Higgs boson. The branching ratios, calculated using the HDECAY [24] program, are reported in Figure 1.3 as a function of the unknown Higgs boson mass.

It is worth remarking that as long as the Higgs boson mass is higher than $2m_V$, the dominant decay modes are the decays of a Higgs boson into gauge bosons. Below this threshold, the Higgs boson would decay into fermions. Since, the $H \rightarrow f\bar{f}$ decay implies a coupling vertex which is proportional to

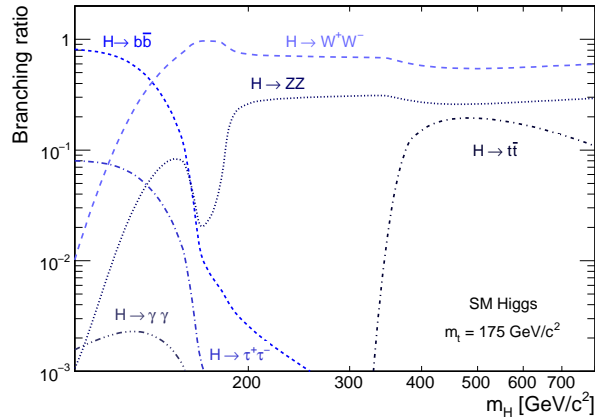


Figure 1.3: Branching ratios of the Standard Model Higgs boson as a function of its unknown mass.

the fermion mass, the decay into lighter fermions is disfavoured. The small branching ratio into a photon pair is also represented as it provide nowadays the most promising way to detect the Higgs boson having a small mass.

1.4.2 Experimental restrictions on the Higgs mass

Depending on the collider (e^+e^- at LEP and $p\bar{p}$ at TEVATRON) and the available centre-of-mass energy, the direct Higgs boson search is performed by exploiting different production mechanisms.

Searches at LEP

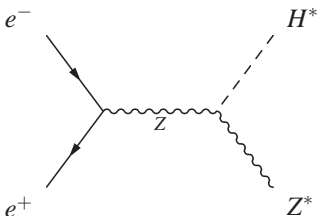


Figure 1.4: Higgsstrahlung at LEP.

The Large Electron-Positron (LEP) collider started its operation in 1989 with a centre-of-mass energy of ~ 91 GeV (LEP I phase). The energy was adjusted to the Z mass in order to explore the Higgs boson through the *Higgsstrahlung* mechanism $e^+e^- \rightarrow Z \rightarrow Z^*H$, where H is radiated from a Z boson (Figure 1.4) and the final state Z is virtual. Since a light Higgs boson decays predominantly in leptons (see Figure 1.3), the dominant decay mode is $H \rightarrow b\bar{b}$. Using the $Z^* \rightarrow \ell^+\ell^-, \nu\bar{\nu}, q\bar{q}$ decay channels, the LEP collaboration has excluded Higgs boson with mass less than $66 \text{ GeV}/c^2$ at 95% C.L.

Before its dismantling in 2000, the centre-of-mass energy of collisions was upgraded up to $\sqrt{s} \sim 209$ GeV (LEP II phase). The favoured production mechanism is therefore the Higgsstrahlung with the real or virtual Z boson being reversed $e^+e^- \rightarrow Z^* \rightarrow ZH$. Because of the higher centre-of-mass energy available, even if the production cross section is small compared to the dominant Higgsstrahlung process, the contribution of the vector boson fusion $e^+e^-(W^+W^- \rightarrow H)\nu_e\bar{\nu}_e$ and $e^+e^-(ZZ \rightarrow H)e^+e^-$ is becoming non-negligible. Taking into account all the possible final states inherent from the Z boson decay and the dominant $H \rightarrow b\bar{b}$, as well as the final state $HZ \rightarrow q\bar{q}\tau^+\tau^-$, the available data from the four LEP experiments have been combined. The absence of experimental signature of the Higgs boson in the entire kinematical range available at LEP implies that the existence of a Higgs boson with mass less than $114.4 \text{ GeV}/c^2$ is excluded at 95% C.L. [25].

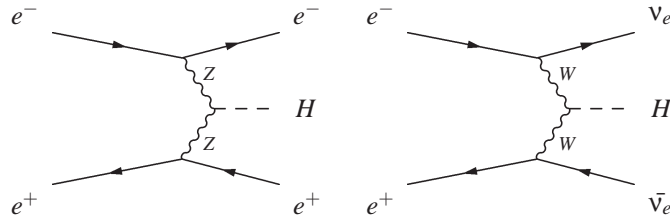


Figure 1.5: Production of the Higgs boson through vector boson fusion at LEP.

Searches at TEVATRON

The TEVATRON experiment now underway at Fermilab has collided, during RUN II, protons and antiprotons at $\sqrt{s} = 1.96$ TeV. The search for the SM Higgs boson is at the forefront of its physics program. The most relevant production mechanisms are the gluon fusion through top quark loop ($gg \rightarrow H$), the vector boson fusion ($q\bar{q}(WW \rightarrow H)q\bar{q}$ and $q\bar{q}(ZZ \rightarrow H)q\bar{q}$) and the Higgsstrahlung of W, Z ($q\bar{q} \rightarrow VH$, where $V = W, Z$). The Feynman diagrams of such processes are depicted in Figure 1.6.

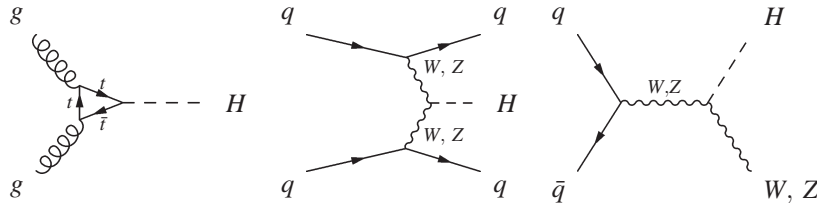


Figure 1.6: Major Higgs production processes at the TEVATRON. From left to right: gluon-gluon fusion through a top loop, vector boson fusion and Higgsstrahlung of a W^\pm or Z boson.

Due to the large gluon relative luminosity, gluon fusion is by far the dominant production channel at TEVATRON: the cross section ranges from about 200 to ~ 2000 fb depending on the Higgs boson mass. Nevertheless, the copious source of Higgs $gg \rightarrow H$ followed by the preferable $H \rightarrow b\bar{b}$ disintegration is not experimentally exploitable due to the huge number of QCD events produced in hadron-hadron collisions. Hence, thanks to a clean signature and more manageable backgrounds, the most studied production channel at TEVATRON is the Higgsstrahlung [26, 27] where the Higgs subsequently decays into $b\bar{b}$ and the associated boson decays leptonically.

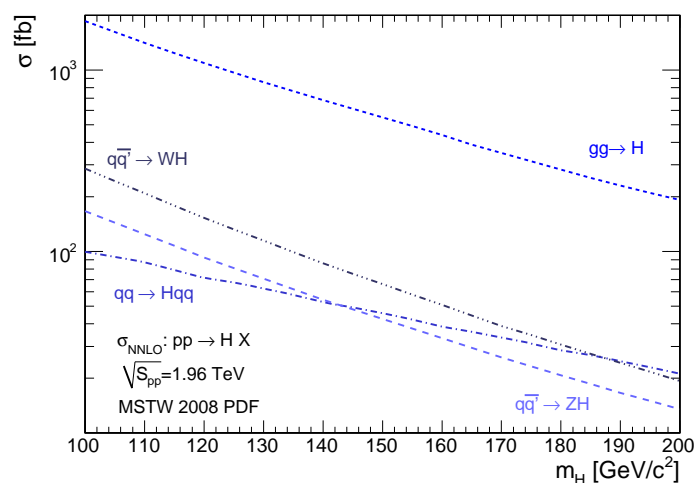


Figure 1.7: Cross sections of the four major production processes of a Standard Model Higgs boson as a function of its hypothetical mass at the TEVATRON in fb for $\sqrt{s} = 1.96$ TeV.

The production cross section of these two primary processes are shown in Figure 1.7 as a function of the Higgs boson mass when the dominance of the gluon fusion is clear. Looking more attentively at the Higgsstrahlung processes, we can see that the cross section for $pp \rightarrow W^{\pm*} \rightarrow W^{\pm}H$ ranges between 290 fb and 20 fb for $m_H = 100$ to 200 GeV/c^2 and the one for $pp \rightarrow ZH$ is roughly a factor two lower for the same Higgs mass range. It should also be emphasised that when the $m_H \gtrsim 135$ GeV/c^2 , the decay into W bosons becomes dominant. Depending on the production mechanism, the Higgs search can also be carried out by exploiting the W^+W^- [28], $W^{\pm}W^+W^-$ and ZW^+W^- final states [29], due to the presence of multiple high energy leptons coming from the disintegration of the W bosons. Finally, the vector boson fusion can also be used because this process becomes increasingly important with rising Higgs mass. Nevertheless, due to the small production cross

section the sensitivity is rather limited [30].

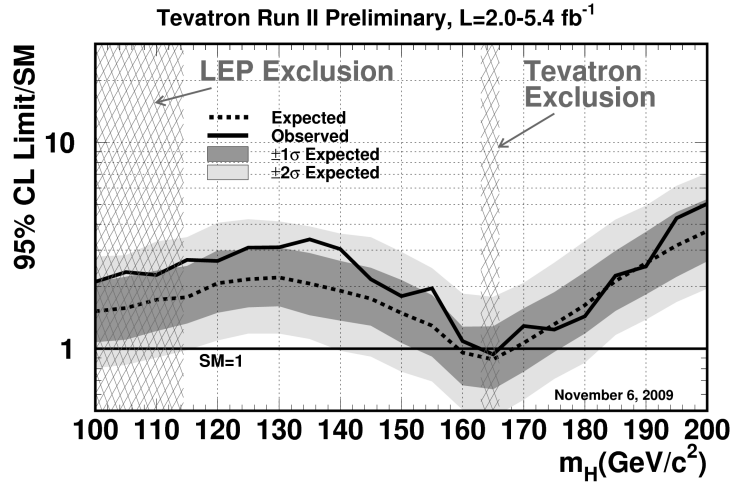


Figure 1.8: Preliminary observed and expected 95% C.L. upper limits on the SM Higgs boson production cross section expressed in multiple of the Standard Model cross section. The limits have been obtained by combining the results of both the CDF and DØ. The straight and dotted lines represents respectively the observed and expected limits while the two grey bands indicate the 68% and 95% probability regions where the limits can fluctuate, in the absence of signal [31].

In 2009, preliminary results [31] based on RUN II ($\sqrt{s} = 1.96$ TeV) data have been published by the TEVATRON community that combine both results of the DØ and CDF collaborations with up to 5.4 fb^{-1} . Based on Bayesian [32] combination method, expected and observed 95% C.L. upper limits on SM Higgs boson production cross section are extracted using the contributions of the different production and decay channels presented hereabove. These limits, plotted in Figure 1.8, are expressed as a multiple of the Standard Model cross section and as a function of the hypothetical Higgs mass. Since a value lower than one indicates the exclusion of the existence of a Higgs boson, the TEVATRON collaboration excludes at 95% C.L. the existence of a Higgs boson with a mass ranging from 163 to 166 GeV/c^2 . Since only a fractional part of the available data have been used, and because the total delivered luminosity will continue to increase, these preliminary results will certainly be improved in the near future...

PHOTON INTERACTIONS AT HADRON COLLIDERS

Photon interactions have been extensively studied at HERA and LEP colliders, in processes involving exchange of quasi-real photons collinear to the incoming electron. In most of these studies the hadronic sector of photon physics has been investigated at rather limited energies. In a similar manner, a significant fraction of proton-proton collisions at the LHC will involve (quasi-real) photon interactions, however this time occurring at energies beyond the electroweak energy scale. The much smaller available effective luminosity is compensated by better known initial conditions and usually simpler final states. Hence, the LHC can to some extent be considered as a high-energy photon-photon or photon-proton collider, offering a unique possibility for novel and complementary researches to standard pp interactions.

2.1 The equivalent photon flux

The electromagnetic field surrounding high energy protons can be interpreted as a flux of quasi-real photons distributed with some density $dN(x_\gamma, Q^2)$, where x_γ is the fraction of the incident proton energy carried out by the photon and Q^2 is its virtuality¹. Photon-induced interactions can in good approximation be viewed as proceeding in two steps: first, the photons are emitted by one or both incoming protons and second, the photons collide producing a central system X (see Figure 2.1).

This separation is theoretically permitted using the *Equivalent Photon Approximation* (EPA) [33] as photoproduction is characterised by very small

¹The photon virtuality is defined as $(p_2 - p_1)^2 = q^2 = -Q^2$ with p_1 and p_2 the four-momenta of the proton before and after the emission of the photon.

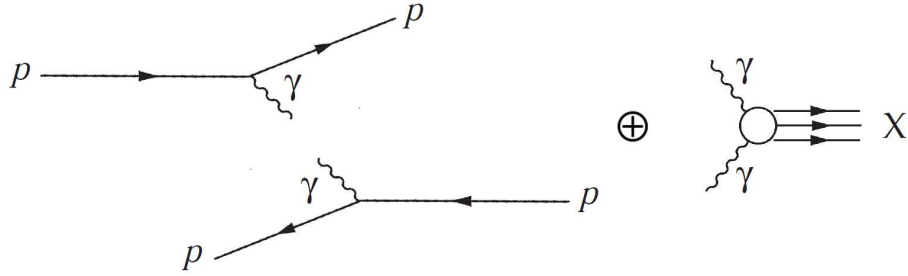


Figure 2.1: Schematic view of the photon-induced processes. Interactions can be divided into two steps. First (left) one or both incoming proton emit a photon and secondly (right) the hard interaction yielding the central system X .

momentum transfers (i.e. small photon virtualities). With this approximation, the cross section can be written as the convolution of the probability that the proton radiates off a photon with the cross section of the real photon-induced subprocess ($\sigma_{\gamma\gamma}$ or $\sigma_{\gamma p}$). Nevertheless, it is important to emphasize that this approximation considers the photon as real and interacting without polarization. Therefore, EPA is only applicable when the production cross section is roughly insensitive to the photon virtuality. Most processes possess a cut-off Λ_γ such that for virtualities smaller than this value, the EPA is valid. In other terms, the existence of such a Λ_γ means that the photon-photon or photon-proton cross section differs only slightly from the real photon cross section and decreases quickly for a higher value of the photon virtuality. The exclusive production of lepton pairs ($pp(\gamma\gamma \rightarrow \ell^+\ell^-)pp$) is an example of inapplicability of the approximation because the cross section is not decreasing with the virtuality of the photon.

Considering that the hypotheses required to apply the equivalent approximation are satisfied, the generalised equation of the photon density from an incoming particle with energy E , as derived by Budnev et al. [33], is given by

$$dN(x_\gamma, Q^2) = \frac{\alpha}{\pi} \frac{dQ^2}{Q^2} \frac{dx_\gamma}{x_\gamma} \left\{ (1-x_\gamma) \left(1 - \frac{Q_{min}^2}{Q^2} \right) F_E(Q^2) + \frac{x_\gamma^2}{2} F_M(Q^2) \right\}, \quad (2.1)$$

where $\alpha = e^2/4\pi$ is the fine structure constant, $F_E(Q^2)$ and $F_M(Q^2)$ functions are the electric and magnetic *form factors* of the incident particle. This density function is directly related to the photon flux $f_\gamma(x_\gamma)$ defined as the integral over Q^2 of the photon density:

$$f_\gamma(x_\gamma) = \int_{Q_{min}^2}^{Q_{max}^2} dN(x_\gamma, Q^2), \quad (2.2)$$

where Q_{min}^2 is the minimum photon virtuality fixed from the kinematics. Finally, the photon fluxes emitted from electrons and protons can be obtained by inserting the appropriate functions $F_E(Q^2)$ and $F_M(Q^2)$ in Equation 2.1. The following sections give an overview of the calculation methods to compute the corresponding proton-proton (σ_{pp}) cross sections which we refer in this thesis as the *cross sections*.

2.1.1 Elastic photon flux of protons

A convenient way to describe the composite structure of protons is to parametrise them in terms of *form factors*. Thereby, the functions $F_E(Q^2)$ and $F_M(Q^2)$ required in Equation 2.1 to obtain the elastic photon flux can be expressed by

$$F_E(Q^2) = \frac{4m_N^2 G_E^2 + Q^2 G_M^2}{4m_N^2 + Q^2}, \quad (2.3)$$

$$F_M(Q^2) = G_M^2, \quad (2.4)$$

where in spite of using the electromagnetic form factors ($F_k(Q^2)$, $k = 1, 2$), the more commonly used electromagnetic and magnetic *Sachs form factors* that measure the charge and the magnetisation respectively, $G_E(Q^2)$ and $G_M(Q^2)$, have been introduced. They are defined as a linear combination of F_1 and F_2 by

$$G_E(Q^2) = F_1(Q^2) - \frac{Q^2}{4m_p^2} F_2(Q^2), \quad (2.5)$$

$$G_M(Q^2) = F_1(Q^2) + F_2(Q^2), \quad (2.6)$$

and their normalisations for a real photon are given by the proton charge and magnetic moment, $G_E(0) = 1$ and $G_M(0) = \mu_p = 2.79$. Experimentally, for modest virtualities ($Q^2 \ll 1$), the Sachs form factors seem consistent with the following approximation :

$$G_E(Q^2) \approx \frac{G_M(Q^2)}{\mu_p} = \left(1 + \frac{Q^2}{\Lambda^2}\right)^{-2}, \quad (2.7)$$

where $\Lambda = 0.71 \text{ GeV}^2$ is called the *dipole form factor* [34, 35].

The typical form factor evolutions for elastic photon emission by a proton are shown in Figure 2.2. Because of the sharp drop off with the increasing photon virtuality, the form factors limit the momentum transfer q^2 to small values. This guarantees the existence of the cut-off Λ_γ that allows the applicability of the equivalent photon approximation. The elastic photon flux can finally be obtained by integrating Equation 2.2 over Q^2 with a Q_{min}^2 value obtained from

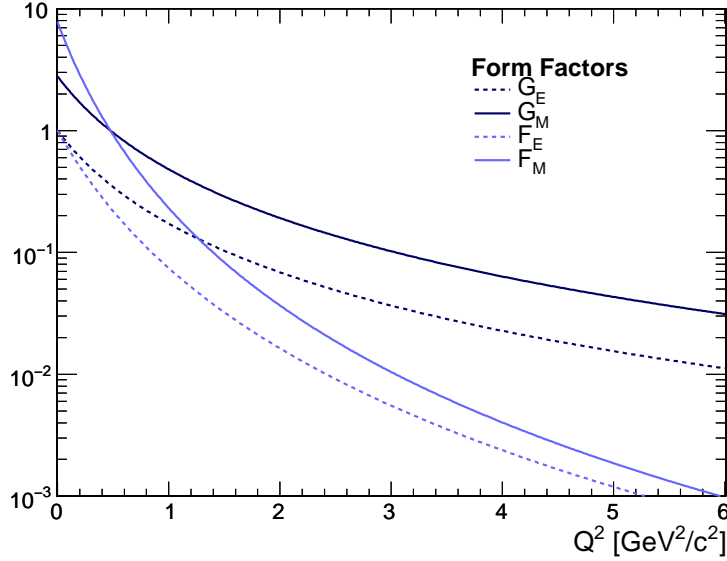


Figure 2.2: Behaviour of the Sachs form factors (blue) and the $F_E(Q^2)$ and $F_M(Q^2)$ functions as a function of the photon virtuality Q^2 .

the kinematics to

$$Q_{min}^2 \approx m_p^2 c^2 \frac{x_\gamma^2}{1 - x_\gamma}. \quad (2.8)$$

2.1.2 Hadronic cross sections

In the following, cross sections for photon-proton and photon-photon interactions are considered. Using the equivalent photon approximation (EPA) their respective hadronic cross sections are computable by convoluting the photon-photon and photon-proton cross sections, $\sigma_{\gamma\gamma}$ and $\sigma_{\gamma p}$, with the photon spectra $dN(x_\gamma, Q^2)$:

$$d\sigma_{pp} = \sigma_{\gamma p}(W_{\gamma p}) dN(x_\gamma, Q^2), \quad (2.9)$$

$$d\sigma_{pp} = \sigma_{\gamma\gamma}(W_{\gamma\gamma}) dN(x_{\gamma_1}, Q_1^2) dN(x_{\gamma_2}, Q_2^2), \quad (2.10)$$

where $x_\gamma = E_\gamma/E$, E_γ is the photon energy, E is the beam energy, $W_{\gamma\gamma}$ is the invariant mass of the produced system in the $\gamma\gamma \rightarrow X$ process

$$W_{\gamma\gamma} = 2\sqrt{x_{\gamma_1} x_{\gamma_2}} E, \quad (2.11)$$

$W_{\gamma p}$ is the photon-proton centre-of-mass system energy and the indices 1 and 2 are used to distinguish the variables characterising the two photons.

Photon-photon interactions

As mentioned hereabove, the LHC can be considered as a high energy $\gamma\gamma$ collider when both protons emit a photon elastically. It is convenient to define the *elastic photon luminosity spectrum* $\frac{dL_{\gamma\gamma}}{dW_{\gamma\gamma}}$, obtained by integrating the product of the photon densities from both protons over the photon virtualities and energy fractions:

$$\frac{dL_{\gamma\gamma}}{dW_{\gamma\gamma}} = \int_{\frac{W_{\gamma\gamma}^2}{s}}^1 2 W_{\gamma\gamma} f_{\gamma}(x_{\gamma}) f_{\gamma}\left(\frac{W_{\gamma\gamma}^2}{x_{\gamma}s}\right) \frac{dx_{\gamma}}{x_{\gamma}s}, \quad (2.12)$$

with $s = 4E^2$ is the squared centre-of-mass energy (c.m.s) of the hadronic interaction. Using the elastic luminosity spectrum, the hadronic cross section of the photon-photon process can therefore be rewritten

$$\sigma_{pp(\gamma\gamma \rightarrow X)pp} = \int dW_{\gamma\gamma} \frac{dL_{\gamma\gamma}}{dW_{\gamma\gamma}} \sigma_{\gamma\gamma}(W_{\gamma\gamma}), \quad (2.13)$$

with $\sigma_{\gamma\gamma}$, the cross section of the $\gamma\gamma \rightarrow X$ subprocess. The elastic luminosity spectrum is shown in Figure 2.3 assuming the upper virtuality of $2 \text{ GeV}^2/c^2$. As expected from the behaviour of the form factors that fall rapidly as a function of the increasing virtuality, the luminosity spectrum peaks at low $W_{\gamma\gamma}$.

Even if small invariant masses of the central produced system X are favoured, the elastic luminosity spectrum is still at the level of a few per mil of the nominal proton-proton interactions. Moreover, if the partonic cross section is roughly independent on the energy at which the interaction occurs, the *relative luminosity spectrum* $L_{\gamma\gamma}$ obtained by integrating the photon luminosity spectrum above a minimum c.m.s energy (W_0) reaches almost 1% of the total available luminosity of the LHC collider for a minimal value $W_0 = 23 \text{ GeV}$. The smallness of the partonic cross sections is therefore counterbalanced by the high expected nominal luminosity of the LHC.

Photon-proton interactions

Similarly, the elastic luminosity spectrum of the photon-proton collisions is defined by

$$\frac{dL_{\gamma q/g}}{dW_{\gamma q/g}} = \int_{\frac{W_{\gamma q/g}^2}{s}}^1 2 W_{\gamma q/g} f_{\gamma}(x_{\gamma}) q_{q/g}\left(\frac{W_{\gamma q/g}^2}{x_{\gamma}s}\right) \frac{dx_{\gamma}}{x_{\gamma}s}, \quad (2.14)$$

where f_{γ} is the Q^2 integrated luminosity spectrum, $q_{q/g}$ is the parton-density-function of parton q/g in the proton. This leads to the following cross section expression for the photon-hadron interaction

$$\sigma_{pp(\gamma q/g \rightarrow X)pY} = \int dW_{\gamma q/g} \frac{dL_{\gamma q/g}}{dW_{\gamma q/g}} \sigma_{\gamma q/g \rightarrow X}(W_{\gamma q/g}). \quad (2.15)$$

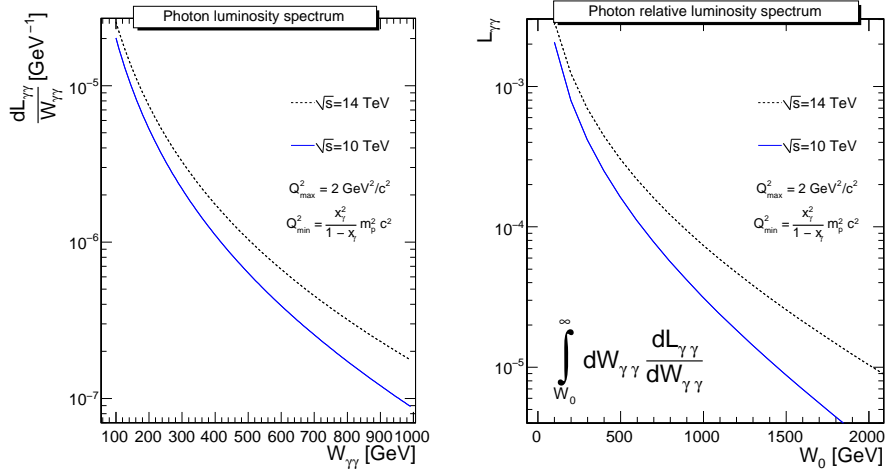


Figure 2.3: Photon luminosity spectrum $\frac{dL_{\gamma\gamma}}{dW_{\gamma\gamma}}$ (left) as a function of the centre-of-mass energy of the $\gamma\gamma$ system $W_{\gamma\gamma}$ and relative elastic luminosity spectrum $L_{\gamma\gamma}$ (right) of photon-photon collisions obtained by integrating the photon luminosity spectrum above a minimum c.m.s. (W_0) at the LHC for the integration range $Q_{\min}^2 < Q^2 < 2 \text{ GeV}^2/c^2$.

Even if drawbacks of photoproduction are the less clean final topologies and a lower potential to constrain the kinematics, the higher luminosity and c.m.s. energy of photoproduction processes compared to $\gamma\gamma$ events offers interesting possibilities for the study of electroweak interaction and for searches beyond the Standard Model (BSM) up to the TeV scale.

Heavy ion fluxes

Finally, the same way protons interact through the emission of photons, at the LHC photon induced processes can also be observed in heavy ions collisions. If the expected luminosity of ion-ion collision is smaller than for pp ones, this is by far compensated by the intensity of the electromagnetic field coming with fast ions. Indeed, the high photon fluxes scale with the square of the charge number of the nucleus. In general, lower c.m.s. energies are available for photon collisions in this case, but the diffractive backgrounds are usually significantly suppressed with respect to the pp case [36].

2.2 Physics potential of photon interactions at the LHC

Although photon-induced interactions have been investigated at LEP and HERA, the performed studies suffer from the very low statistics available. The use of the LHC as a photon-photon and a photon-proton collider dramatically extends the energy reach for the measurement of $\gamma\gamma$ and γp interactions providing the possibility to test the electroweak sector of the Standard Model as well as physics beyond the SM. A brief overview of possible photon-induced physics at the LHC is given in this section.

2.2.1 Two-photon interactions

Even if two photon interactions are not considered in the following of the thesis, a brief introduction of interesting $\gamma\gamma$ -induced processes is now given. In elastic $\gamma\gamma$ collisions, the final state multiplicity is, in general, much lower than in parton-parton ones yielding very clean final state topologies: a central system X separated on both sides by a large rapidity gap from the escaping protons. Even if the available luminosity is smaller than the nominal one, efficient selection could compensate for the small production number. The physics potential of photon-photon interactions is illustrated in Figure 2.4 where the most promising hadronic cross sections have been computed using MadGraph/MadEvent (MG/ME) [37]² that allows to produce processes with photons in the initial state based on the Equivalent Photon Approximation. The di-muon cross section has been computed using LPAIR [38] with a minimal cut on the transverse momentum of the muons of 2 GeV/ c and $|\eta^\mu| < 3.1$. Since the cross sections for pair production depend only on charge, spin and mass of the produced particles, the results are shown for charged and colourless fermions and scalars of two different masses.

Since the production cross section can be calculated very precisely (this is a nearly pure QED process), the exclusive dilepton pair production can be used for a precise determination of the luminosity at hadron colliders. This idea was considered already in the 70's by Budnev, Ginzburg, Meledin and Serbo [39]. This application of $pp(\gamma\gamma \rightarrow \ell^+\ell^-)pp$ events has recently been investigated by the CMS collaboration [40] showing that the muon topology looks favourable. In addition, if very forward detectors are located close to the beam pipe in order to detect the leading protons, the precise reconstruction of the leptons by the central detector allows their calibration [41, 42].

Photon-photon interactions are also relevant to test the Standard Model predictions using the possibility to directly measure the self couplings of the gauge bosons (e.g. triple $WW\gamma$ and quartic $WW\gamma\gamma$) [43, 44] through exclusive

²Using version 4.1.31 of MadGraph/MadEvent.

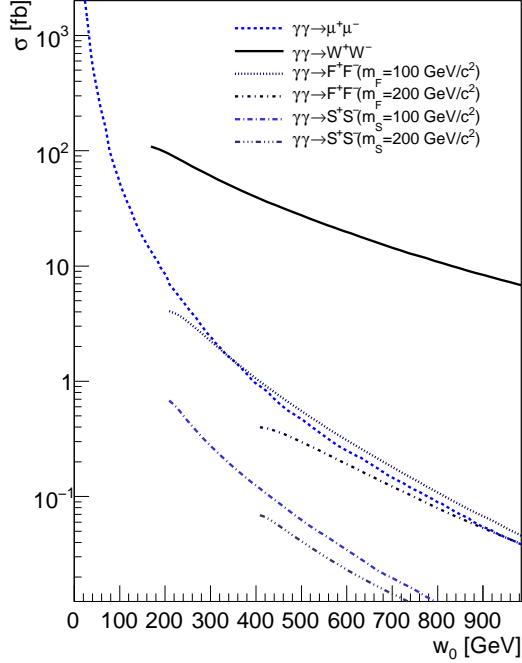


Figure 2.4: Cross-section for several $pp(\gamma\gamma \rightarrow X)pp$ processes (F for fermion, S for scalar). The $pp(\gamma\gamma \rightarrow \mu^+\mu^-)pp$ cross section has been computed for $p_T^\mu > 2 \text{ GeV}/c$ and $|\eta^\mu| < 3.1$.

W pair production. An experimental observation leading to differences with the precise expectations of the $\gamma\gamma \rightarrow WW$ cross section would be a signal due to beyond Standard Model effects. As an example, already after 10 fb^{-1} of integrated luminosity, the previously established LEP2 limits on the triple gauge coupling can be improved by a factor of 10,000 [43].

The large two-photon centre-of-mass energy of up to several hundred GeV available at the LHC allow one to search for new massive charged particles [45]. Interestingly, the measurement of the two escaping protons allows one to make the distinction between various contributions to the supersymmetric particle spectrum by looking at the distribution of the photon-photon centre-of-mass energy $W_{\gamma\gamma}$. Moreover, provided enough statistics is available ($\sim 100 \text{ fb}^{-1}$), a direct constraint of the masses of the supersymmetric particles irrespectively of the decay mode of the centrally produced particle [46] can be obtained.

2.2.2 Photoproduction

In γp interactions, when light quarks are assumed to be massless, a singularity arises in t-channel diagrams, when the outgoing quarks are collinear to the incoming photon. This computational problem is avoided when the *resolved* photon contribution³ is used for some choice of factorisation scale, in addition to the *direct* contribution. Another possibility is to include direct processes only and to apply very loose cuts on specific quantities (i.e. on the transverse momentum of the outgoing quark) acting as a regulator of this singularity.

The second approach gives therefore an approximation of the total cross section. A process for which possible high singularities (and therefore also a significant contribution from resolved photon processes) might be expected is for example the photoproduction of single W obtained by scattering a photon on an incoming u quark $\gamma u \rightarrow W^+ d$. A cross section of 13.7(2) pb for 7 TeV incoming protons was computed at Leading Order (LO) using the resolved photon contributions. It compares very well with the cross section of 14 pb obtained using the direct process only, calculated with CalcHEP [47], and for a minimal transverse momentum $p_T > 1$ GeV/ c for the outgoing massless quark. This result has been shown to be fairly stable with respect to the p_T cut and indicates that the resolved contribution is small. Another indication of the smallness of resolved contribution was obtained by comparing the CalcHEP computed cross section without p_T cut but using different values of d -quark mass as regulator. The cross section was ranging from 18 pb for $m_d = 0.001$ GeV/ c^2 to 12.8 pb for $m_d = 5$ GeV/ c^2 (the value of 14 pb being obtained for $m_d = 0.8$ GeV/ c^2). In the following, only the direct contributions at LO have been calculated and a cut at 1 GeV/ c on p_T for the outgoing quark (labeled q') has been applied for all processes with a possible singularity in the t-channel diagrams. This is for instance the case for the cross section $\gamma q \rightarrow WHq'$, even if a p_T cut as low as 0.3 GeV/ c already gives a very stable result.

The cross sections at leading order (LO) of the direct contribution for various electroweak reactions have been calculated with MG/ME. Figure 2.5 shows cross sections for $pp(\gamma g/q \rightarrow X)pY$ processes as a function of the minimal photon-parton c.m.s. energy \hat{W}_0 . A large variety of processes have sizeable cross section up to the electroweak scale and could therefore be studied during the running of the LHC. Assuming that all processes non-mediated by photons can be omitted, it is very interesting to observe that potentially dangerous Standard Model background processes with hard leptons, missing energy and jets coming from the production of gauge bosons, have cross sections only one or two orders of magnitude higher than those involving Higgs boson or top quarks (calculated for $m_t = 174.3$ GeV/ c^2 and

³In the resolved process, the photon fluctuates into a $q\bar{q}$ state which interacts hadronically.

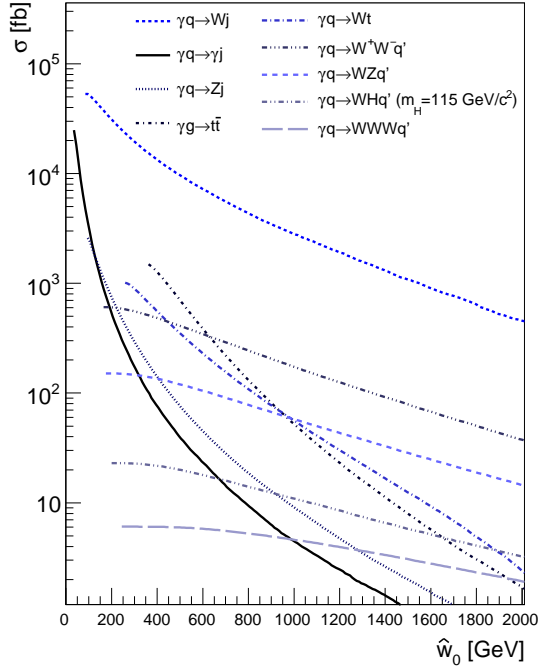


Figure 2.5: Cross sections for $pp(\gamma q/g \rightarrow X)pY$ processes as a function of the minimal photon-parton c.m.s. energy \hat{W}_0 . For all jets, $p_T^{jet} > 10$ GeV/c, $|\eta^{jet}| < 5$ and $\Delta R(j, j) > 0.3$. No other cut than the regularization cut $p_T > 1$ GeV/c is applied on q' .

$$m_b = 4.7 \text{ GeV}/c^2).$$

In Chapter 6, the potential of photoproduction at LHC to observe the Standard Model Higgs boson produced in association with a W will be presented. Indeed, the WH photoproduction cross section is non-negligible as it reaches more than 20 fb for a 115 GeV/ c^2 Higgs boson, representing more than 2% of the total inclusive WH production at the LHC. Then, photoproduction may contribute to the search of the SM Higgs boson or, at least, to the measurement of some of its properties.

Also interesting, the SM top quark photoproduction cross section reaches about 2.5 pb. Due to the high number of photo-produced top quarks and the large ratio of single top production cross section to the SM background

production-cross section ⁴, photoproduction offers an interesting framework for studying e.g. the electric charge of the top quark and the $|V_{tb}|$ CKM matrix element.

Probing the anomalous photoproduction of single top via flavour-changing neutral currents (FCNC) is also possible at the LHC because of the high expected cross section compared to the one at HERA. For $k_{tW\gamma} = 0.15$ and $k_{tc\gamma} = 0$ values of the anomalous couplings, the cross section is expected to be two orders of magnitude higher. Furthermore, while at HERA only the up quark content of the proton contributes, the energy of the LHC allows to probe the proton at lower momentum fractions, opening the opportunity to study the effect of the c quark via the $k_{tc\gamma}$ coupling [48].

2.3 Difficulties related to γp interactions

Because photon-induced interactions occur through the exchange of a colour-singlet object, a clear experimental signature of such processes is the presence of a large region devoid of produced hadrons between the escaping proton and the central system X . Depending if one or both protons interact by the exchange of a photon, a so-called *rapidity gap* can be observed in one or both sides of the central detector. Even if this characteristic seems at first sight very attractive to select photon-photon or photon-proton interactions, several aspects should be kept in mind that can dramatically decrease the interest of using such rapidity gaps as a clear evidence of photon-induced interactions.

2.3.1 Rescattering effects

The composite structure of the incoming beam particles may alter significantly the visible rapidity gap in the detector. Indeed, the gaps can be filled by additional particles originating from secondary strong interactions between spectator partons. The generic diagrams for such production are shown in Figure 2.6 without (left) and with (right) such *rescattering* effects. As noted by Bjorken [49], the difference between the theoretically computed rate (F_{theo}) and the actual measured rate (F_{exp}) can be understood by introducing a correction factor (\hat{S}^2) referred as the *survival factor* $F_{exp} = \hat{S}^2 \times F_{theo}$. Generally, calculation of the survival factor is done in the impact parameter space, assuming the factorisation as in the EPA. In the elastic case, this survival factor basically corresponds to the probability of the scattered proton not to dissociate due to the secondary interactions.

⁴In contrast to proton-proton interactions where the ratio of Wt associated production cross section to the sum of all top production cross sections is only about 5%, it is about 10 times higher in photoproduction.

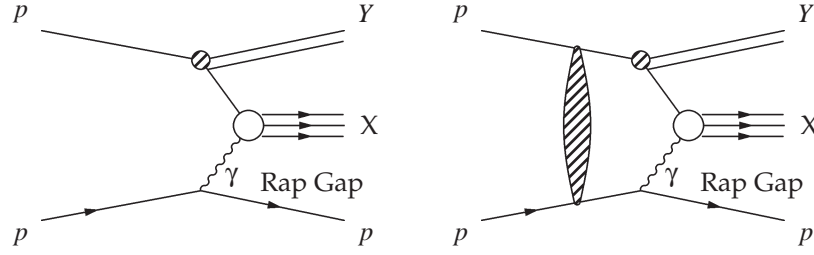


Figure 2.6: Generic Feynman diagrams for the photoproduction at the LHC without (left) and with (right) rescattering corrections. The region devoid of produced particles between the escaping proton and the central system X is labelled RapGap.

The most impressive consequence of these additional particles populating the gaps has been seen at the TEVATRON through the apparent low yield of events containing rapidity gap [50]. Since photon-induced processes are dominated by emission of photons with very small virtualities ($Q^2 \approx 0.01 \text{ GeV}^2/c^2$) which corresponds to interactions occurring at large impact parameters⁵, the value of the survival factor \hat{S}^2 would generally be larger than for diffractive events, close to 1. As an example, the central exclusive diffractive Higgs production at the LHC is roughly 0.03 [51] while the same process mediated by photon exchange possess a survival factor of 0.86 [52]. Finally, even if the survival factor would be higher for the two-photon interactions, the photon-proton processes would not undergo too strongly the rescattering effects. As an example, the survival factor is expected to be of about 0.7 for single W boson photoproduction [53].

Even if a large number of studies have been published about the calculation of survival probabilities, a large uncertainty remains about the real suppression factor that will be effective at the LHC. In order to tackle this problem, comparison of the experimental rate of few photon-induced processes with well-known predicted cross section would be mandatory. Hence, exclusive production of lepton pairs as well as single W boson photoproduction [54] may be used to constrain the survival factor of photon-photon and photon-proton interactions respectively.

2.3.2 Inelastic interactions

Due to the fact that protons are not point-like particles, it is necessary to distinguish between the *elastic* and the *inelastic* emissions of a photon by a proton. In the former case, which has been presented above, the proton does not break up and therefore continues its path with a trajectory which is

⁵The proton impact parameter is approximately inversely proportional to $\sqrt{Q^2}$.

only slightly affected by the photon emission. In the latter case, the proton does not survive from the emission and the proton therefore dissociates into a resonant system R with mass M_R . The generic Feynman diagrams for the elastic and inelastic production of a system X via photon-proton collisions at the LHC are shown in Figure 2.7.

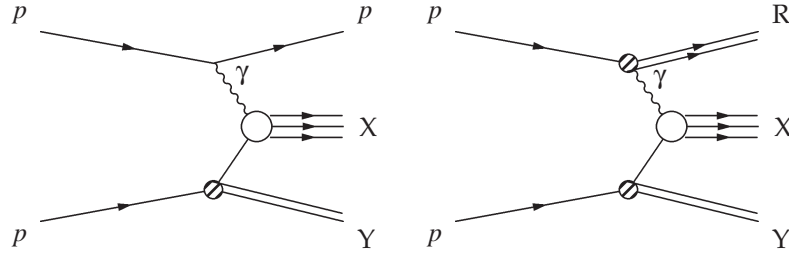


Figure 2.7: Generic diagrams of elastic ($pp(\gamma \rightarrow X)Yp$) and inelastic events ($pp(\gamma \rightarrow X)YR$). The proton emitting the photon dissociates into a heavier system R .

The production cross sections of inelastic processes is nowadays still not known with a high accuracy. The contributions of the two processes (elastic and inelastic ones) have to be disentangled by applying dedicated experimental cuts. The detection of the leading protons would as an example remove all inelastic interactions. On the opposite side, using the rapidity rap as tagging technique of elastic photon emission will select a mixture of elastic and inelastic events when the produced hadronic systems escape from the detection of the central detector. The spread of the final hadronic system being proportional to its mass, a value of $M_R \sim 20 \text{ GeV}/c^2$ is a realistic assumption that prevents the hadronic system R from being observable in central detectors [55]. Nevertheless, the *inelastic* relative γp luminosity spectrum obtained using this maximum allowed value for M_R are significant, even larger than the elastic one. Fortunately, the average photon virtuality is generally higher implying a typical impact parameter much smaller.

2.3.3 Diffractive background at the LHC

Although rapidity gaps are produced in $\gamma\gamma$ and γp collisions, the lack of produced particles in an extended pseudorapidity region may also be caused in purely strong interactions, due to the exchange of objects with vacuum quantum numbers such as the so-called *pomeron* (\mathbb{P}).

Identically to photon emission, in diffractive events the proton can emerge from the interaction either intact or dissociated into a low mass state, leading to different types of diffractive processes occurring in proton-proton

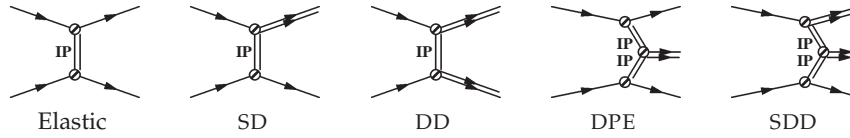


Figure 2.8: Event topologies for elastic and diffractive proton-proton interactions. From left to right: elastic scattering, Single-diffractive (SD), Double-Diffractive (DD), Double-Pomeron-Exchange (DPE) and Single+Double-Diffractive (SDD) events.

collisions. They are represented in Figure 2.8. In the elastic scattering, both protons emerge intact in the final state. Single-diffractive (SD) and Double-Pomeron-Exchange (DPE) events are characterised by the presence of respectively one or two rapidity gaps in the final state. Finally, interactions mediated by pomerons may also produce Double-Diffractive (DD) and Single+Double-Diffractive (SDD) events. Because diffractive and photon-induced interactions possess similar final states, the selection of $\gamma\gamma$ and γp through the detection of the escaping protons or the presence of rapidity gaps will yield to a mixture of photon-induced and diffractive events.

To estimate the order of magnitude of the diffractive contribution, the results obtained at TEVATRON can be combined with the calculations of the corresponding survival probabilities at the LHC [56]. As an example, about 1% of the observed singly produced W bosons at TEVATRON were containing LRGs [57]. Because the survival probability decreases with the momentum transfer, this fraction is expected to be about 0.5% at the LHC [41]. Similarly, the diffractive top quark pair production at the LHC is expected to be below 0.5% of the total inclusive production: the diffractive production will therefore have similar rate as for photoproduction. Figure 2.9 compares the differential cross sections for single-diffractive processes and photoproduction. Finally, one should note that the photoproduction drops slower with energy, which favours studies of final states with large invariant mass.

2.3.4 Pile-up events

The major drawback of the high luminosity expected at a hadron collider such as the LHC is the non-negligible probability that several protons can interact during one single bunch crossing. The hard scattering of interest will be overlaid with a luminosity-dependent average number of events ranging from 1 to 25 simultaneous collisions. For example, the mean number of pile-up events expected during the “medium luminosity” ($\mathcal{L} = 10^{33} \text{ cm}^{-2} \text{ s}^{-1}$) reaches 7 inelastic events per crossing while for the nominal luminosity of

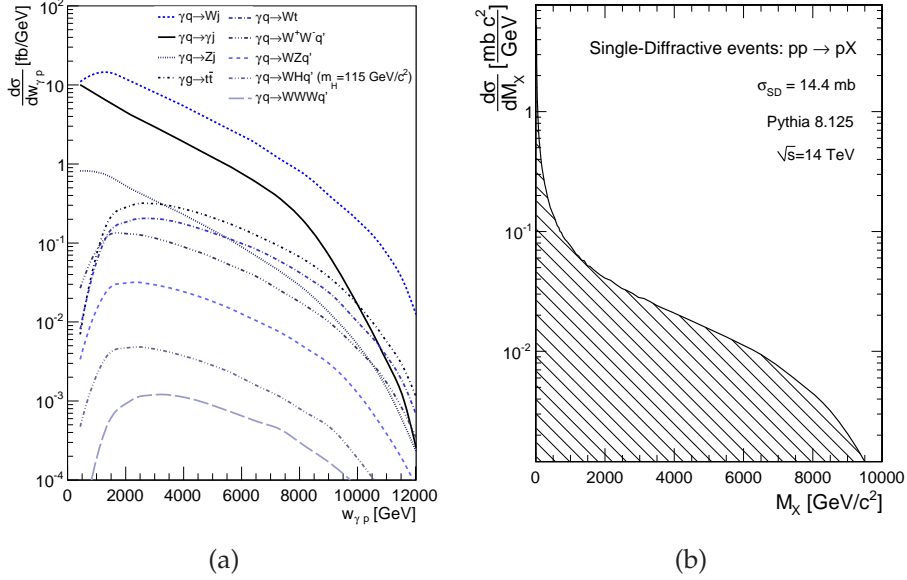


Figure 2.9: Left: Differential cross section $\frac{d\sigma}{dM_X}$ for single-diffractive production $pp \rightarrow pX$ as a function of the proton remnant mass M_X . Right: Differential cross section $\frac{d\sigma}{dW_{\gamma p}}$ for $pp(\gamma q/g \rightarrow X)pXY$ as a function of the photon-proton c.m.s. energy $W_{\gamma p}$. Different cuts detailed in Figure 2.5 have been applied.

$\mathcal{L} = 10^{34} \text{ cm}^{-2} \text{ s}^{-1}$ the average number of events for each bunch crossing is roughly 25.

Photon-induced processes can be selected either using a calorimeter (through the rapidity gap signature) or by detecting the escaping protons using *very forward detectors* (VFDDs). Nevertheless, even in absence of pile-up, the rapidity gaps occurring in photon-induced interactions may be populated by particles created in a secondary proton-proton collision. A schematic representation of the effect of pile-up events on the rapidity gap is shown in Figure 2.10. The upper part represents a photon-proton collision with the presence of the characteristic lack of hadronic activity in a large pseudorapidity region. The lower part shows that the rapidity gap is filled by additional simultaneous hadronic interactions.

The extraction of photon-induced interactions relying on the presence of survival protons is also complicated by pile-up events since the inclusive SD and DPE cross sections amount respectively to approximately 10% and 1% of the total proton-proton cross section ($\sigma_{pp}^{tot} \approx 100 \text{ mb}$). Therefore, diffractive

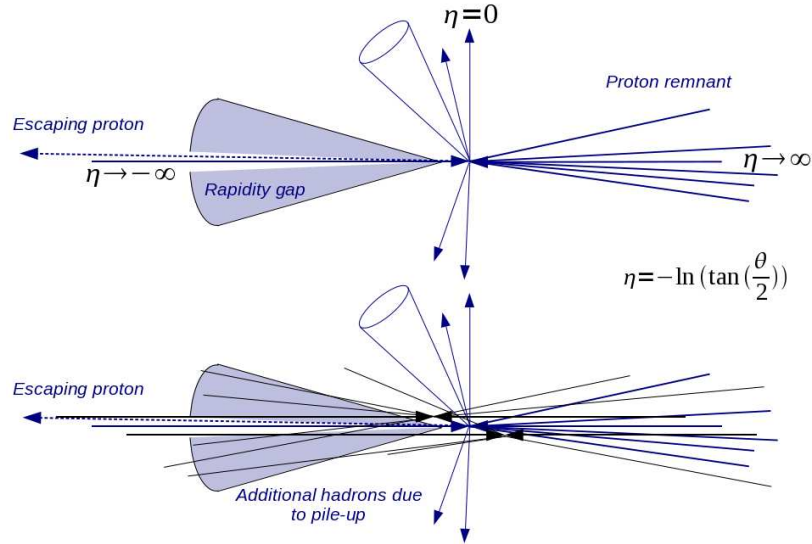


Figure 2.10: Schematic representation of the effect of pile-up events on the rapidity gap. The upper part of the figure represents photoproduction with the presence of the characteristic lack of hadronic activity in a large pseudorapidity region, while in the lower part additional collisions destroy the gap signature.

processes may represent a non negligible background source to photon-induced processes when they occur in coincidence with photoproduction. Separation of simultaneous interaction may only be possible by using a detector measuring very precisely the arrival time ($\delta t \sim 10 - 20$ ps) of forward protons [58]. Such a precise measurement will allow the determination of the z -coordinate of the event vertex yielding a clear separation of pile-up events.

DELPHES, A FAST SIMULATION OF A LHC-DETECTOR

It is sometimes difficult to know whether theoretical predictions can be observed in a high energy collider experiment, especially when expected experimental signature involve jets and missing transverse energy. For this purpose, a new C++-based framework, DELPHES, has been designed performing a fast multipurpose detector response simulation. The simulation includes a tracking system, embedded into a magnetic field, calorimeters and a muon system, and possible very forward detectors arranged along the beamline. The framework outputs observables such as isolated leptons, missing transverse energy and collection of jets which can be used for dedicated analyses. The simulation of the detector response takes into account the effect of magnetic field, the granularity of the calorimeters and subdetector resolutions. A simplified preselection can also be applied on processed events for trigger emulation. Detection of very forward scattered particles relies on the transport in beamlines with the HECTOR software. Finally, the FROG 2D/3D event display is used for visualisation of the collision final states.

3.1 The Large Hadron Collider

The goal for the Large Hadron collider [59] (LHC) is to conceive a collider to be installed in the existing underground circular LEP tunnel at CERN in Geneva (Switzerland) and able to explore the validity and the limitations of the Standard Model by investigating processes with tiny cross sections. It was therefore mandatory to build a machine capable of reaching centre-of-mass energies much higher than the previous LEP ones. Since the synchrotron radiation losses intrinsically limits the energy of electron in circular beams, these particles are inappropriate to reach the mandatory energy of the beams:

the choice of a hadron collider was therefore obvious.

At the LHC, the hadrons are circulating inside the 27 km circumference ring inside two vacuum pipes. The use of a large variety of magnets is mandatory to guide and steer the beams around the ring and to optimise the probability for head-on collisions of the particles. Hence, along the ring, 1232 dipole magnets (“bending magnets”) are used to keep the beams on their circular path, and 392 quadrupole magnets are devoted to focus the beams inside the vacuum chambers (“focusing magnets”). Since the circumference of the machine as well as the bending power of the magnetic system limit the achievable beam energy, another key parameter of the collider to raise the event rate is the luminosity \mathcal{L} . Indeed, the event collider rate R is calculated as

$$R = \mathcal{L} \sigma, \quad (3.1)$$

where σ is the cross section of the studied event reaction and \mathcal{L} is the machine luminosity. It is therefore clear that rare events would benefit from a high luminosity, as it provides the only chance to obtain a sufficient number of events having low cross section. This has driven the choice of a proton-proton collider instead of a proton-antiproton one since it is unfeasible to produce the number of antiprotons needed to reach the desired luminosity. The design operation of the LHC is therefore the acceleration of two counter-rotating proton beams which are brought to head-on collisions at a centre-of-mass energy of 14 TeV, roughly an order of magnitude higher than the previous generation of colliders, and a luminosity exceeding $10^{33} \text{ cm}^{-2} \text{ s}^{-1}$.

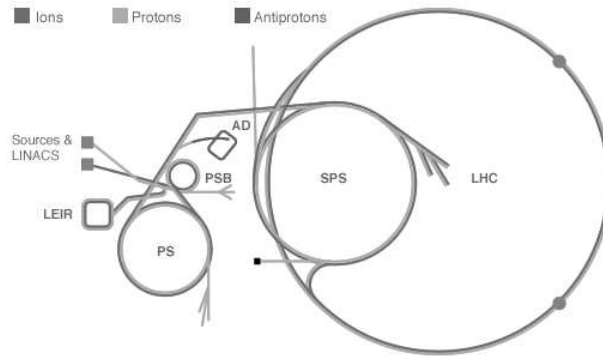


Figure 3.1: Schematic view of the “CERN accelerator complex” allowing to produce a proton beam with an energy of 7 TeV, starting from the beam production component (LINAC2) to the final LHC ring.

To achieve the design center-of-mass energy, 7 TeV per beam need to be

reached: before being injected into the LHC ring, the protons are initially prepared by the “CERN accelerator complex” composed of existing accelerating facilities. The whole accelerator complex is shown in Figure 3.1. The production of the LHC beams starts using the LINAC2 linear accelerator, where protons are produced with an energy of 50 MeV. The energy of the protons will then be raised gradually to 7 TeV by using four ring accelerators. Hence, once the beam has been ejected from the LINAC2, the Proton Synchrotron Booster (PSB) is fed with the protons in order to reach an energy of 1.4 GeV. The following injection in the Proton Synchrotron (PS) allows to increase their energy to 25 GeV and to provide the final 25 ns bunch spacing. Finally, before their insertion into the LHC ring, an ultimate pre-acceleration is performed by the Super Proton Synchrotron (SPS) that allows the protons to reach an energy of 450 GeV. Finally when the protons are injected into the LHC, the two rotating beams are boosted from 450 GeV to the final energy of 7 TeV.

With a collision centre-of-mass energy of 14 TeV the LHC will be the first collider able to fully explore the TeV energy scale beyond the Tevatron. Moreover, the LHC will also operate with heavy ions beams, providing in addition a very rich physics program. As an example, the LHC will be used to collide lead (Pb) ions with a design luminosity $\mathcal{L} = 10^{27} \text{cm}^{-2} \text{s}^{-1}$ and an energy of 2.75 TeV per nucleon. Unfortunately, the first proton beam injection in September 2008 ended without any performed collisions due to a technical problem [60]. The first collisions at 7 TeV in March 2010 were therefore highly awaited. The two beams will collide in four interaction points where experiments are built in order to analyse the collisions allowing to verify the consistency of the the Standard Model and maybe to reveal new physics beyond it with an unprecedented precision. The first two, named the ATLAS [61] and the CMS [62] experiments are large “multi-purpose” detectors designed to cover the widest possible range of physics at the LHC. The two others are smaller and are more specialised detectors: ALICE [63] will study properties of the quark-gluon plasma in heavy ion collisions while LHC-b [64], is dedicated to the CP violation phenomena in the interactions of B-particles.

Motivation for a fast detector simulation

Multipurpose detectors at high energy colliders are very complex systems. Their simulation is in general performed by means of the GEANT [65] package and final observables used for analyses usually require sophisticated reconstruction algorithms. This complexity is handled by large collaborations, and data and the expertise on reconstruction and simulation software are only available to their members. Precise data analyses require a full detector simulation, including transport of the primary and secondary particles through the detector material accounting for the various detector inefficiencies, the dead material, the imperfections and the geometrical details. Such simulation is very complicated, technical and requires a large CPU power. On the other

hand, phenomenological studies, looking for the observability of given signals, may require only fast but realistic estimates of the expected signal signatures and their associated backgrounds.

A new framework, called DELPHES [66], is introduced for the fast simulation of a general-purpose collider experiment. Starting from the output of event generators, the simulation of the detector response takes into account the subdetector resolutions, by smearing the kinematic properties of the final-state particles¹. In the current DELPHES version, particles other than electrons (e^\pm), photons (γ), muons (μ^\pm), neutrinos (ν_e, ν_μ and ν_τ) and neutralinos are simulated as hadrons for their interactions with the calorimeters. The simulation of stable particles beyond the Standard Model should therefore be handled with care. Tracks of charged particles and deposits of energy in calorimetric cells (or *calotowers*) are then created. These two types of quantities are used for the reconstruction of jets and the isolation of leptons. DELPHES includes the most crucial experimental features, such as: the geometry of both central and forward detectors, magnetic field for tracks and energy flow, reconstruction of photons, leptons, jets, b -jets, τ -jets and missing transverse energy, lepton isolation, trigger emulation and an event display. Although this kind of approach yields much more realistic results than a simple “parton-level” analysis, a fast simulation comes with some limitations. Detector geometry is idealised, being uniform, symmetric around the beam axis, and having no cracks nor dead material. Secondary interactions, multiple scatterings, photon conversion and bremsstrahlung are also neglected.

3.2 Simulation of the detector response

The overall layout of the multipurpose detector simulated by DELPHES is shown in Figure 3.2. It consists in a central tracking system (TRACKER) surrounded by an electromagnetic and a hadron calorimeters (ECAL and HCAL, each with a central region and two endcaps). Two forward calorimeters (FCAL) ensure a larger geometric coverage for the measurement of the missing transverse energy. Finally, a muon system (MUON) encloses the central detector volume. A detector card allows a large spectrum of running conditions by modifying basic detector parameters, including calorimeter and tracking coverage and resolution, thresholds or jet algorithm parameters. Even if DELPHES has been developed for the simulation of general-purpose detectors at the LHC (namely CMS and ATLAS), this input parameter file interfaces a flexible parametrisation for other cases, e.g. at future linear colliders. If no detector card is provided, predefined values based on “typical” CMS acceptances and resolutions are used. The geometrical coverage of the various subsystems used in the default configuration are summarised in Table 3.1.

¹Those considered as stable by the event generator

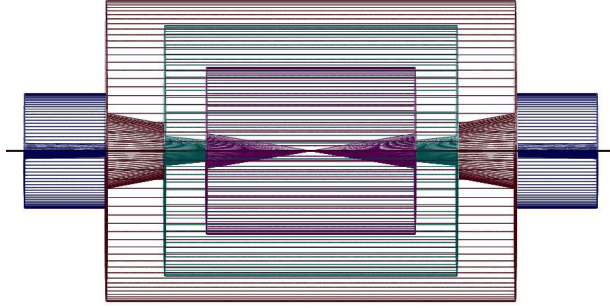


Figure 3.2: Profile of layout of the generic detector geometry assumed in DELPHES. The innermost layer, close to the interaction point, is a central tracking system (pink). It is surrounded by a central calorimeter volume (green) with both electromagnetic and hadronic sections. The outer layer of the central system (red) consist of a muon system. In addition, two end-cap calorimeters (blue) extend the pseudorapidity coverage of the central detector. The detector parameters are defined in the user-configuration card. The extension of the various subdetectors, as defined in Table 3.1, are clearly visible. The detector is assumed to be strictly symmetric around the beam axis (black line). Additional forward detectors are not depicted.

Table 3.1: Default extension in pseudorapidity η of the different subdetectors. Full azimuthal (ϕ) acceptance is assumed.

	η	ϕ
TRACKER	$[-2.5; 2.5]$	$[-\pi; \pi]$
ECAL, HCAL	$[-1.7; 1.7]$	$[-\pi; \pi]$
ECAL, HCAL endcaps	$[-3; -1.7] \& [1.7; 3]$	$[-\pi; \pi]$
FCAL	$[-5; -3] \& [3; 5]$	$[-\pi; \pi]$
MUON	$[-2.4; 2.4]$	$[-\pi; \pi]$

Magnetic field

In addition to the subdetectors, the effects of a solenoidal magnetic field are simulated for the charged particles. This affects the position at which charged particles enter the calorimeters and their corresponding tracks. In case of a dipolar magnetic field, an exact integral of the transport of a charged particle is performed. All the following development is based on equations:

$$\frac{d\vec{p}}{dt} = q\vec{v} \times \vec{B} \quad , \quad \frac{d\vec{x}}{dt} = \vec{v} \quad \text{and} \quad \vec{p} = \gamma m \vec{v} = \gamma m \frac{d\vec{x}}{dt} \quad , \quad (3.2)$$

where \vec{p} is the momentum of the charged particle, \vec{x} is its vector position and γ is the Lorentz factor. The magnetic field is supposed to be aligned with the

z axis ($B_x = 0$, $B_y = 0$, $B_z = B$), homogeneous and constant in a cylinder of length $2 \times z_{max}$ and of radius R_{max} corresponding to the tracker volume. The entire following development is dedicated to express the position and momentum of the charged particle at any time t , using the initial charged particle position (x_0, y_0, z_0) and its initial momentum (p_{x0}, p_{y0}, p_{z0}) . The propagation of a charged particle in the magnetic field is depicted in Figure 3.3. The variables defining the extension of the tracker are also shown.

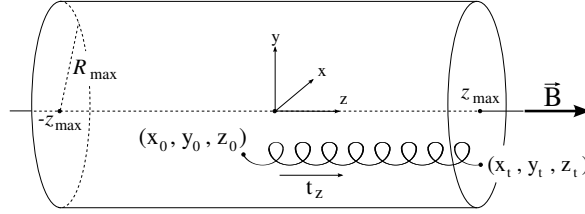


Figure 3.3: Propagation of a charged particle in the dipolar magnetic field. The variables defining the extension of the tracker are also shown: the maximum radius R_{max} and its longitudinal extension, $2 \times z_{max}$.

In order to describe the motion of a charged particle in the magnetic field, the definition of some variables is mandatory. Hence, since in such a magnetic field, the particle trajectory is a circle in the transverse plane (x, y) , with a radius r and a center at coordinates (x_c, y_c) or (R_c, Φ_c) , the coordinates of the charged particle, with respect to the laboratory frame are simply the parametric equations of a helix of constant radius

$$\begin{cases} x(t) = x_c + r \sin(\omega t - \phi_0) \\ y(t) = y_c + r \cos(\omega t - \phi_0) \\ z(t) = z_0 + \frac{p_{z0}}{\gamma m} t \end{cases} \quad (3.3)$$

where r is the helix radius given by $p_{T0}/\omega\gamma mc$, ω is the giration frequency $(q B_z)/\gamma m$ and ϕ_0 is the initial transverse momentum direction. The position of the charged particle can equivalently be expressed in terms of the spherical (R, θ, ϕ) coordinates:

$$\begin{cases} R(t) = \sqrt{x(t)^2 + y(t)^2} = \sqrt{R_c^2 + r^2 + 2rR_c \cos(\Phi_c - (\phi_0 + \omega t))} \\ \Phi(t) = \text{atan}\left(\frac{y(t)}{x(t)}\right) \\ \Theta(t) = \text{acos}\left(\frac{z(t)}{\sqrt{z(t)^2 + R(t)^2}}\right) = \text{atan}\left(\frac{R(t)}{z(t)}\right) \end{cases} \quad (3.4)$$

Since the particle will move in the magnetic field along its helix until it exits the tracker volume, the time at which to stop the propagation has to be

determined. If particles are already outside the magnetic field volume before the propagation, they are simply ignored, meaning that they are not taken into account even if they would come-back into the tracker volume. The time needed to reach the end of the magnetic field in the longitudinal direction, t_z can be calculated using $z(t_z) = z_{\max} \times \text{sign}(p_{z0})$ by

$$t_z = \frac{\gamma m}{p_{z0}} \left(-z_0 + z_{\max} \times \text{sign}(p_{z0}) \right), \quad (3.5)$$

while the time needed to reach the end of the tracker by the transverse direction, t_T , is obtained by noticing that a particle exits the volume by the side once $R(t) = R_{\max}$. The solution therefore appears from the geometrical intersection of two circles in the transverse plane, i.e. the magnetic field limits and the particle trajectory:

$$t_T^{1,2} = \frac{1}{\omega} \left[\delta_\phi \pm \text{asin} \left(\frac{R_{\max}^2 - (R_c^2 + r^2)}{2rR_c} \right) \right], \quad (3.6)$$

where δ_ϕ is the difference between Φ_c and ϕ_0 , re-assigned in the $[-\pi; \pi]$ interval. Moreover, since the transverse momentum might be too small and the initial position too central, it could be possible that the particle never reaches the transverse side of the cylinder. The t_T time becomes therefore infinite and the $|R_c - r| < R_{\max} < (R_c + r)$ criteria has to be checked in order to avoid this infinity. In such a case, the time to exit from the tracker is obviously provided by t_z . Furthermore, as the $q \times B_z$, or equivalently, the ω variable defines the direction of rotation, the corresponding times t_z^1 and t_z^2 are consecutive and obviously positive. The value $\min(t_z^1, t_z^2)$ gives the *time of exit* from the B-field volume, while $\max(t_z^1, t_z^2)$ gives the time at which the particle would have re-entered this volume.

Finally, the time at which to stop the propagation, t_{\max} , is given by $t_{\max} = \min(t_T, t_z)$. The modified ϕ and pseudorapidity values of the charged particle at which it enters the calorimeters can therefore be calculated by using Equations 3.2 and 3.4 and remembering that

$$\Phi(t_{\max}) = \text{atan} \frac{y(t_{\max})}{x(t_{\max})}, \quad (3.7)$$

$$\eta(t_{\max}) = -\ln \tan \frac{\Theta(t_{\max})}{2}. \quad (3.8)$$

Track reconstruction

Every stable charged particle with a transverse momentum above some threshold and lying inside the detector volume covered by the tracker provides a track. By default, a track is assumed to be reconstructed with 90%

probability if its transverse momentum p_T is higher than $0.9 \text{ GeV}/c$ and if its pseudorapidity $|\eta| \leq 2.5$. No smearing is currently applied on tracks.

Calorimetric cells

The response of the calorimeters to energy deposits of incoming particles depends on their segmentation and resolution. In the CMS and ATLAS detectors, for instance, the calorimeter characteristics are not identical in every direction, with typically finer resolution and granularity in the central regions [67, 68]. It is thus very important to compute the exact coordinates of the entry point of the particles into the calorimeters, via the magnetic field calculations. The response of each sub-calorimeter is parametrised through a Gaussian smearing of the particle energy with a variance σ :

$$\frac{\sigma}{E} = \frac{S}{\sqrt{E}} \oplus \frac{N}{E} \oplus C, \quad (3.9)$$

where S , N and C are the *stochastic*, *noise* and *constant* terms, respectively, and \oplus stands for quadratic additions.

In the default parametrisation, the calorimeter is assumed to cover the pseudorapidity range $|\eta| < 3$ and consists in an electromagnetic and hadronic parts. Coverage between pseudorapidities of 3.0 and 5.0 is provided by forward calorimeters, with different response to electromagnetic objects (e^\pm, γ) or hadrons. Muons and neutrinos are assumed not to interact with the calorimeters. The default values of the stochastic, noise and constant terms are given in Table 3.2.

Table 3.2: Default values for the resolution of the central and forward calorimeters (for both electromagnetic and hadronic parts). Resolution is parametrised by the *stochastic* (S), *noise* (N) and *constant* (C) terms (Eq. 3.9).

	S ($\text{GeV}^{1/2}$)	N (GeV)	C
ECAL	0.05	0.25	0.0055
ECAL, end caps	0.05	0.25	0.0055
FCAL, e.m. part	2.084	0	0.107
HCAL	1.5	0	0.05
HCAL, end caps	1.5	0	0.05
FCAL, had. part	2.7	0	0.13

The energy of electrons and photons found in the particle list are smeared using only the ECAL resolution terms, while charged and neutral final-state hadrons interact with all calorimeters. Some long-living particles, such as the

K_s^0 and Λ 's, with lifetime $c\tau$ smaller than 10 mm are considered as stable particles by the generators although they decay before the calorimeters. The energy smearing of such particles is performed using the expected fraction of the energy, determined according to their decay products, that would be deposited into the ECAL (E_{ECAL}) and into the HCAL (E_{HCAL}). Defining F as the fraction of the energy leading to a HCAL deposit, the two energy values are given by

$$\begin{cases} E_{\text{HCAL}} = E \times F \\ E_{\text{ECAL}} = E \times (1 - F) \end{cases} \quad (3.10)$$

where $0 \leq F \leq 1$. The electromagnetic part is handled the same way for the electrons and photons. The resulting calorimetry energy measurement given after the application of the smearing is then $E = E_{\text{HCAL}} + E_{\text{ECAL}}$. For K_s^0 and Λ hadrons, the energy fraction is F is assumed to be 0.7.

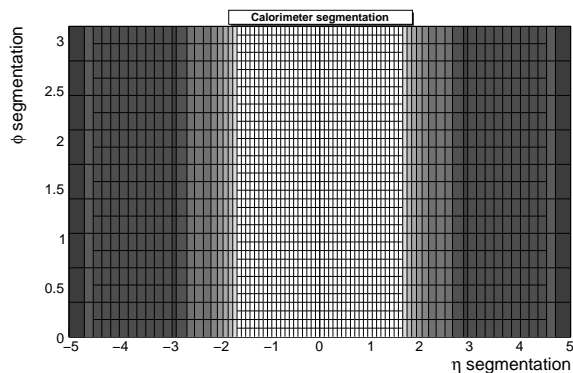


Figure 3.4: Default segmentation of the calorimeters in the (η, ϕ) plane. Only the central detectors (ECAL, HCAL) and FCAL are considered. ϕ angles are expressed in radians.

The smallest unit for geometrical sampling of the calorimeters is a *cell*; it segments the (η, ϕ) plane for the energy measurement. No longitudinal segmentation is available in the simulated calorimeters. DELPHES assumes that ECAL and HCAL have the same segmentations and that the detector is symmetric in ϕ and with respect to the $\eta = 0$ plane. Figure 3.4 illustrates the default calorimeter segmentation. No sharing between neighbouring cells is implemented when particles enter a cell very close to its geometrical edge. Due to the finite segmentation, the smearing, as defined in Eq. 3.9, is applied directly on the accumulated electromagnetic and hadronic energies of each calorimetric cell. The calorimetric cells directly enter in the calculation of the missing transverse energy (MET), and as input for the jet reconstruction algorithms.

3.3 High-level object reconstruction

Analysis object data contain the final collections of particles (e^\pm, μ^\pm, γ) or objects (light jets, b -jets, τ -jets, E_T^{miss}) and are stored in the output file created by DELPHES. While electrons, muons and photons are easily identified, some other objects are more difficult to measure, like jets or missing energy due to invisible particles. For most of these objects, their four-momentum and related quantities are directly accessible in DELPHES output (E, \vec{p}, p_T, η and ϕ). Additional properties are available for specific objects (like the charge and the isolation status for e^\pm and μ^\pm , the result of application of b -tag for jets and time-of-flight for some detector hits).

3.3.1 Photon and charged lepton reconstruction

From here onwards, *electrons* refer to both positrons (e^+) and electrons (e^-), and *charged leptons* refer to electrons and muons (μ^\pm), leaving out the τ^\pm leptons as they decay before being detected. The collections of electrons, photons and muons are filled in with candidates observing some fiducial and reconstruction cuts, and are based on the true particle ID provided by the generator. Consequently, no fake candidates enter these collections. However, when needed, fake candidates can be added into the collections at the analysis level, when processing DELPHES output data. As effects like bremsstrahlung are not taken into account along the lepton propagation in the tracker, no clustering is needed for the electron reconstruction in DELPHES.

Electrons and photons

Real electron (e^\pm) and photon candidates are identified if they fall into the acceptance of the tracking system and have a transverse momentum above a threshold (default $p_T > 10 \text{ GeV}/c$). A calorimetric cell will be activated in the detector and electrons will leave in addition a track. Subsequently, electrons and photons create a candidate in the jet collection. Assuming a good measurement of the track parameters in the real experiment, the electron energy can be reasonably recovered. In DELPHES, electron energy is smeared according to the resolution of the calorimetric cell where it points to, but independently of any other deposited energy in this cell. This approach is still conservative as the calorimeter resolution is worse than the tracker one.

Muons

Generator-level muons entering the detector acceptance are considered as candidates for the analysis level. The acceptance is defined in terms of a transverse momentum threshold to be exceeded that should be computed using the chosen geometry of the detector and the magnetic field considered (default:

$p_T > 10 \text{ GeV}/c$) and of the pseudorapidity coverage of the muon system (default: $-2.4 \leq \eta \leq 2.4$). The application of the detector resolution on the muon momentum depends on a Gaussian smearing of the p_T variable. Neither η nor ϕ variables are modified beyond the calorimeters: no additional magnetic field is applied. Multiple scattering is neglected. This implies that low energy muons have in DELPHES a better resolution than in a real detector. Furthermore, muons leave no deposit in calorimeters. At last, the particles which might leak out of the calorimeters into the muon systems (*punch-through*) will not be seen as muon candidates in DELPHES.

Charged lepton isolation

To improve the quality of the contents of the charged lepton collections, additional criteria can be applied such as isolation. This requires that electron or muon candidates are isolated in the detector from any other particle, within a small cone. In DELPHES, the default charged lepton isolation demands that there is no other charged particle with $p_T > 2 \text{ GeV}/c$ within a cone of $\Delta R = \sqrt{\Delta\eta^2 + \Delta\phi^2} < 0.5$ around the lepton. The result (i.e. *isolated* or *not*) is added to the charged lepton measured properties. In addition, the sum p_T of the transverse momenta of all tracks but the lepton one within the isolation cone is provided:

$$p_T = \sum_{i \neq \mu}^{\text{tracks}} p_T(i).$$

No calorimetric isolation is applied, but the muon collection contains also the ratio ρ_μ between (1) the sum of the transverse energies in all calorimetric cells in a $N \times N$ grid around the muon, and (2) the muon transverse momentum:

$$\rho_\mu = \frac{\sum_i E_T(i)}{p_T(\mu)}, \quad i \text{ in } N \times N \text{ grid centred on } \mu.$$

3.3.2 Jet reconstruction

Because of QCD confinement, quarks or gluons involved in physics processes cannot be observed directly but instead undergo a fragmentation and a hadronisation phases. The experimentally observed objects detected by the tracking and calorimeter systems and associated with the quarks and gluon are called *jets*. A realistic analysis requires a correct treatment of particles which have hadronised. Therefore, the most widely currently used jet algorithms have been integrated into the DELPHES framework using the FASTJET tools [69]. Six different jet reconstruction schemes are available, with three cone algorithms and three recombination algorithms. The first three belong to the cone algorithm class while the last three are using a sequential recombination scheme. For all of them, the calorimetric cells are used as inputs for the jet clustering. Jet algorithms differ in their sensitivity to soft particles or collinear splittings,

and in their computing speed performances. By default, reconstruction uses a cone algorithm with $\Delta R = 0.7$. Jets are stored if their transverse energy is higher than 20 GeV.

Cone algorithms

1. *CDF Jet Clusters* [70]: Basic cone reconstruction algorithm used by the CDF experiment in Run II. All cells lying in a circular cone around the jet axis with a transverse energy E_T higher than a given threshold are used to seed the jet candidates. This algorithm is fast but sensitive to both soft particles and collinear splittings.
2. *CDF MidPoint* [71]: Cone reconstruction algorithm developed for the CDF Run II to reduce infrared and collinear sensitivities compared to purely seed-based cone by adding ‘midpoints’ (energy barycentres) in the list of cone seeds.
3. *Seedless Infrared-Safe Cone* [72]: The SISCONe algorithm is simultaneously insensitive to additional soft particles and collinear splittings, and fast enough to be used in experimental analysis.

Recombination algorithms

The three sequential recombination jet algorithms are safe with respect to soft radiations (i.e. *infrared safe*) and collinear splittings. They rely on recombination schemes where calorimeter cell pairs are successively merged. The definitions of the jet algorithms are similar except for the definition of the *distances* d used during the merging procedure. Two such variables are defined: the distance d_{ij} between each pair of cells (i, j) , and a variable d_{iB} (*beam distance*) depending on the transverse momentum of the cell i . The jet reconstruction algorithm browses the calorimetric cell list. It starts by finding the minimum value d_{\min} of all the distances d_{ij} and d_{iB} . If d_{\min} is a d_{ij} , the cells i and j are merged into a single cell with a four-momentum $p^\mu = p^\mu(i) + p^\mu(j)$ (*E-scheme recombination*). If d_{\min} is a d_{iB} , the cell is declared as a final jet and is removed from the input list. This procedure is repeated until no cells are left in the input list. Further information on these jet algorithms is given here below, using k_{ti} , y_i and ϕ_i as the transverse momentum, rapidity and azimuth of calorimetric cell i and $\Delta R_{ij} = \sqrt{(y_i - y_j)^2 + (\phi_i - \phi_j)^2}$ as the jet-radius parameter:

4. *Longitudinally invariant k_t jet* [73], with $d_{ij} = \min(k_{ti}^2, k_{tj}^2) \times \frac{\Delta R_{ij}^2}{R^2}$ and $d_{iB} = k_{ti}^2$,
5. *Cambridge/Aachen jet* [74], with $d_{ij} = \frac{\Delta R_{ij}^2}{R^2}$ and $d_{iB} = 1$,
6. *Anti k_t jet* [75], where hard jets are exactly circular in the (y, ϕ) plane: $d_{ij} = \min(1/k_{ti}^2, 1/k_{tj}^2) \times \frac{\Delta R_{ij}^2}{R^2}$ and $d_{iB} = \frac{1}{k_{ti}^2}$.

Energy flow

In jets, several particles can leave their energy into a given calorimetric cell, which broadens the jet energy resolution. However, the energy of charged particles associated to jets can be deduced from their reconstructed track, thus providing a way to identify some of the components of cells with multiple hits. When the *energy flow* is switched on in DELPHES, the energy of tracks pointing to calorimetric cells is extracted and smeared separately, before running the chosen jet reconstruction algorithm. This option allows a better jet E reconstruction.

3.3.3 b -tagging

A jet is tagged as b -jets if its direction lies in the acceptance of the tracker and if it is associated to a parent b -quark. By default, a b -tagging efficiency of 40% is assumed if the jet has a parent b quark. For c -jets and light jets (i.e. originating in u , d , s quarks or in gluons), a fake b -tagging efficiency of 10% and 1% respectively is assumed. The (mis)tagging relies on the true particle identity (PID) of the most energetic particle within a cone around the observed (η, ϕ) region, with a radius equal to the one used to reconstruct the jet (default: ΔR of 0.7). In current version of DELPHES, the displacement of secondary vertices is not simulated.

3.3.4 τ identification

Jets originating from τ -decays are identified using a procedure consistent with the one applied in a full detector simulation [67]. The tagging relies on two properties of the τ lepton. First, 77% of the τ hadronic decays contain only one charged hadron associated to a few neutrals (Table 3.3). Tracks are useful for this criterion. Secondly, the particles arising from the τ lepton produce narrow jets in the calorimeter (this is defined as the jet *collimation*).

Table 3.3: Branching ratios for τ^- lepton [4]. h^\pm and h^0 refer to charged and neutral hadrons, respectively. $n \geq 0$ and $m \geq 0$ are integers.

Leptonic decays		Hadronic decays	
$\tau^- \rightarrow e^- \bar{\nu}_e \nu_\tau$	17.9%	$\tau^- \rightarrow h^- (n \times h^\pm) (m \times h^0) \nu_\tau$	64.7%
$\tau^- \rightarrow \mu^- \bar{\nu}_\mu \nu_\tau$	17.4%	$\tau^- \rightarrow h^- (m \times h^0) \nu_\tau$	50.1%
		$\tau^- \rightarrow h^- h^+ h^- (m \times h^0) \nu_\tau$	14.6%

Table 3.4: Default values for parameters used in τ -jet reconstruction algorithm. Electromagnetic collimation requirements involve the inner *small* cone radius R^{em} , the minimum transverse energy for calorimetric cells E_T^{tower} and the collimation factor C_τ . Tracking isolation constrains the number of tracks with a significant transverse momentum p_T^{tracks} in a cone of radius R^{tracks} . Finally, the τ -jet collection is purified by the application of a cut on the p_T of τ -jet candidates.

Electromagnetic collimation		Tracking isolation	
R^{em}	0.15	R^{tracks}	0.4
min E_T^{tower}	1.0 GeV	min p_T^{tracks}	2 GeV/c
C_τ	0.95		

Electromagnetic collimation

To use the narrowness of the τ -jet, the *electromagnetic collimation* C_τ is defined as the sum of the energy of cells in a small cone of radius R^{em} around the jet axis, divided by the energy of the reconstructed jet. To be taken into account, a calorimeter cell should have a transverse energy E_T^{tower} above a given threshold. A large fraction of the jet energy is expected in this small cone. This fraction, or *collimation factor*, is represented in Figure 3.5 for the default values (see Table 3.4).

Tracking isolation

The tracking isolation for the τ identification requires that the number of tracks associated to particles with significant transverse momenta is one and only one in a cone of radius R^{tracks} (3-prong τ -jets are dropped). This cone should be entirely incorporated into the tracker to be taken into account. Default values of these parameters are given in Table 3.4.

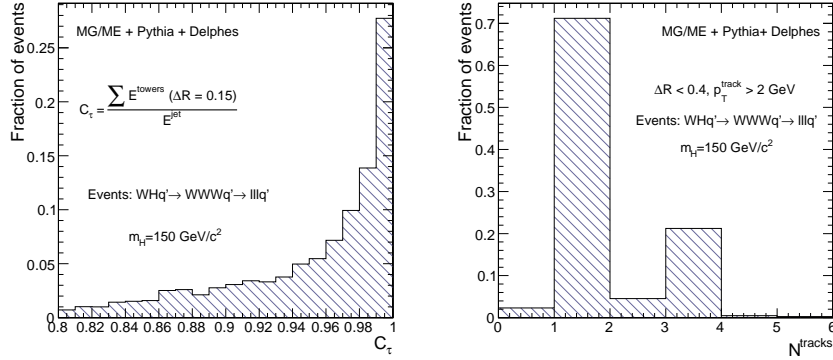
3.3.5 Missing transverse energy

In an ideal detector, momentum conservation imposes the transverse momentum of the observed final state \vec{p}_T^{obs} to be equal to the \vec{p}_T vector sum of the invisible particles, written \vec{p}_T^{miss} .

$$\vec{p}_T = \begin{pmatrix} p_x \\ p_y \end{pmatrix} \text{ and } \begin{cases} p_x^{\text{miss}} = -p_x^{\text{obs}} \\ p_y^{\text{miss}} = -p_y^{\text{obs}} \end{cases} \quad (3.11)$$

The *true* missing transverse energy, i.e. at generator-level, is calculated as the opposite of the vector sum of the transverse momenta of all visible particles – or equivalently, to the vector sum of invisible particle transverse mo-

Figure 3.5: Left: Distribution of the electromagnetic collimation C_τ variable for true τ -jets, normalised to unity. This distribution is shown for associated WH photoproduction, where the Higgs boson decays into a W^+W^- pair. Each W boson decays into a $\ell\nu_\ell$ pair, where $\ell = e, \mu, \tau$. Events generated with MadGraph/MadEvent. Final state hadronisation is performed by PYTHIA [76]. Histogram entries correspond to true τ -jets, matched with generator-level data. Right: Distribution of the number of tracks N^{tracks} within a small jet cone for true τ -jets, normalised to unity. Photoproduced WH events, where W bosons decay leptonically (e, μ, τ), as in Figure 3.5. Histogram entries correspond to true τ -jets, matched with generator-level data.



menta. In a real experiment, calorimeters measure energy and not momentum. Any problem affecting the detector (dead channels, misalignment, noisy cells, cracks) worsens directly the measured missing transverse energy \vec{E}_T^{miss} . In this document, MET is based on the calorimetric cells and only muons and neutrinos are not taken into account for its evaluation:

$$\vec{E}_T^{\text{miss}} = - \sum_i^{\text{towers}} \vec{E}_T(i) \quad (3.12)$$

However, as muon candidates, tracks and calorimetric cells are available in the output file, the missing transverse energy can always be reprocessed a posteriori with more specialised algorithms.

3.4 Trigger emulation

New physics signals in collider experiments are often characterised by low cross section values, compared to the Standard Model (SM) processes. As only a tiny fraction of the observed events can be stored for subsequent *offline* analyses, a very large data rejection factor should be applied directly as the events are produced. This data selection is supposed to reject only

well-known SM events². Dedicated algorithms of this *online* selection, or *trigger*, should be fast and very efficient for data rejection, in order to preserve the experiment output bandwidth. They must also be as inclusive as possible to avoid losing interesting events.

Most of the usual trigger algorithms select events containing objects (i.e. jets, particles, MET) with an energy scale above some threshold. This is often expressed in terms of a cut on the transverse momentum of one or several objects of the measured event. Logical combinations of several conditions are also possible. For instance, a trigger path could select events containing at least one jet and one electron such as $p_T^{\text{jet}} > 100 \text{ GeV}/c$ and $p_T^e > 50 \text{ GeV}/c$. A trigger emulation is included in DELPHES, using a fully parametrisable *trigger table*. When enabled, this trigger is applied on analysis-object data.

3.5 Very forward detector simulation at the LHC

Most of the recent experiments in beam colliders have additional instrumentation along the beamline that extends the η coverage to higher values. At HERA, both the ZEUS and H1 detectors have been complemented by VFD in order to detect protons and electrons that have lost energy. Similarly, at the TEVATRON, $D\phi$ and CDF have also very forward detectors aiming to study soft and hard diffraction and to monitor beam losses. It is therefore natural that, since the potential of forward physics has been revealed, the LHC experiments have a forward physics program based on very small-angle detectors. In this section the additional instrumentation located in forward regions around the CMS interaction point is listed.

CASTOR calorimeters

CASTOR [77] is a sampling calorimeter located downstream at 14 m from the interaction point containing both an electromagnetic and a hadronic calorimeter part. It extends the calorimetric coverage of the CMS central detector, with $-5.2 \leq \eta \leq -6.6$ ³. Its initial physics program is to study the hadronic activity in the forward region, looking for forward jets for a better understanding of forward hadronic activity.

Zero Degree Calorimeters

Zero Degree Calorimeters (ZDC) are sampling calorimeters located at zero angle, i.e. are aligned with the beamline axis at the interaction point, and placed beyond the point where the paths of incoming and outgoing beams separate.

²In real experiments, some bandwidth is allocated to minimum-bias and/or zero-bias (“random”) triggers that store a small fraction of random events without any selection criteria.

³The second side will be equipped in future years, if funded.

Stable neutral particles coming from the interaction point, mainly n and γ , can thus be detected by these Cerenkov devices [67] as they are not deflected. They are located at 140 m from the interaction point, on both side of CMS and allow to detect neutral particles with large pseudorapidities: $|\eta| > 8.1$. Similarly to CASTOR, they are made of separate electromagnetic and hadronic sections, allowing to measure and reconstruct photons above 20 GeV and neutrons above 50 GeV.

TOTEM

The TOTEM experiment [78] is based on a series of detectors placed inside and outside of the CMS volume. Its initial purpose was to measure the total proton-proton cross section with a high precision, but also offers many opportunities for diffraction and photon physics studies. While the LHC is operated below $5 \times 10^{33} \text{ cm}^{-2} \text{ s}^{-1}$, a large physics programme is foreseen in common with the CMS experiment [79] although an increase of the luminosity will lead to a forecast removal of the TOTEM detectors since the radiation damage will become dramatical.

The TOTEM experiment consists of four main subparts: two telescopes and two roman pot stations. The first tracking device (T1) placed at 7.5 m from the IP in front of the forward hadronic calorimeter and covers the $3.1 \leq |\eta| \leq 5.2$ pseudorapidity range. The second telescope (T2) is fixed to the beam pipe at 14 m in front of the CASTOR calorimeter ($5.3 \leq |\eta| \leq 6.6$). One of the roman pot station is placed at ~ 150 m from the IP just after the beam separation and after the ZDC while the second is located at 220 m from the interaction point. These roman pots consist of moveable silicon detectors that can approach the beam to nearly 1 mm, efficiently detecting protons in the beam with non-nominal energy. The distance of approach of the detector directly determines its acceptance. For instance, roman pots at 220 m and 2 mm from the beam axis see the protons with an energy loss between 120 GeV and 1 TeV.

Forward proton taggers

FP420 is a common *R&D* project for both ATLAS and CMS that evaluates the addition of forward proton detectors located between ± 420 and 428 m, from the corresponding IP [80, 41]. These forward proton taggers will be able to measure protons that underwent a very low energy loss (less than 2%) during the interaction. In addition, they are able to measure the proton position, direction and time-of-flight. This latter measurement can help for the pile-up signal rejection in case of simultaneous double-tag, since it allows to estimate the z component of the interaction vertex.

Implementation of VFD s in DELPHES

Among the previously mentioned detectors, only the Zero Degree Calorimeters and the forward taggers called here RP220, for “roman pots at 220 m” and FP420 “for forward proton taggers at 420 m” are implemented in DELPHES. The default location of the implemented very forward detectors in DELPHES are summarised in Figure 3.6.

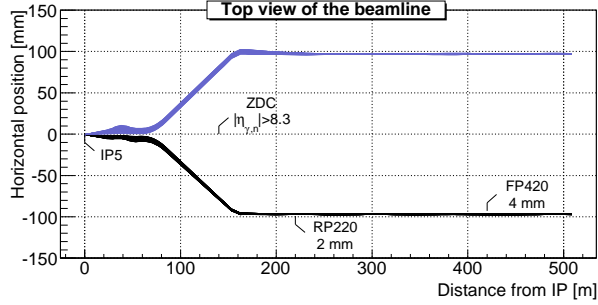


Figure 3.6: Default location of the very forward detectors, including ZDC, RP220 and FP420 in the LHC beamline. Incoming (red) and outgoing (black) beams on one side of the CMS interaction point ($s = 0$ m). The Zero Degree Calorimeter is located in perfect alignment with the beamline axis at the interaction point, at 140 m, the beam paths are separated. The forward taggers are near-beam detectors located at 220 m and 420 m. Beamline simulation with HECTOR [42]. All very forward detectors are located symmetrically around the interaction point.

Zero Degree Calorimeters

The fact that additional charged particles may enter the ZDC acceptance is neglected in DELPHES. The energy of the observed neutral particle is smeared according to Equation 3.9 and the corresponding section resolutions given in Table 3.5). The ZDC hits do not enter in the calorimeter tower list used for reconstruction of jets and missing transverse energy.

Moreover, the ZDCs have the ability to measure the time-of-flight of the particle. This corresponds to the delay after which the particle is observed in the detector, with respect to the bunch crossing reference time at the interaction point (t_0). The measured time-of-flight t is simply given by:

$$t = t_0 + \frac{1}{v} \times \left(\frac{s - z}{\cos \theta} \right), \quad (3.13)$$

where t_0 is thus the true time coordinate of the vertex from which the particle originates, v the particle velocity, s is the ZDC distance to the interaction point,

Table 3.5: Default values for the resolution of the zero degree calorimeters. Resolution on energy measurement is parametrised by the *stochastic* (S), *noise* (N) and *constant* (C) terms (Equation 3.9). The time-of-flight is smeared according to a Gaussian function.

ZDC, electromagnetic part	hadronic part	
S (GeV ^{1/2})	0.7	1.38
N (GeV)	0	0
C	0.08	0.13
ZDC, timing resolution		
σ_t (s)	0	

z is the longitudinal coordinate of the vertex, θ is the particle emission angle. It is then assumed that the neutral particle observed in the ZDC is highly relativistic, i.e. travelling at the speed of light c . We also assume that $\cos\theta = 1$, i.e. $\theta \approx 0$ or equivalently η is large. As an example, $\eta = 5$ leads to $\theta = 0.013$ and $1 - \cos\theta < 10^{-4}$. The formula therefore reduces to

$$t = \frac{1}{c} \times (s - z). \quad (3.14)$$

For example, a photon takes $0.47 \mu\text{s}$ to reach a ZDC located at $s = 140$ m, neglecting z and θ . For the time-of-flight measurement, a Gaussian smearing can be applied according to the detector resolution (Table 3.5). In the current version of DELPHES, only neutrons, antineutrons and photons are assumed to be able to reach the ZDCs, all other particles being neglected.

Forward taggers

To be able to reach the forward taggers, particles must have a charge identical to the beam particles, and a momentum very close to the nominal value of the beam. In practice, at the LHC, only positively charged muons (μ^+) and protons can reach the forward taggers as other particles with a single positive charge coming from the interaction points will decay before their possible tagging. In DELPHES, extra hits coming from the beam-gas events or secondary particles hitting the beampipe in front of the detectors are not taken into account.

While neutral particles propagate along a straight line to the ZDC, a dedicated simulation of the transport of charged particles is needed for RP220 and FP420. This fast simulation uses the HECTOR software [42], which includes the chromaticity effects and the geometrical aperture of the beamline elements of any arbitrary collider. Forward taggers are able to measure the hit positions (x, y) and angles (θ_x, θ_y) in the transverse plane at the location of the detector

(s meters away from the IP), as well as the time-of-flight⁴ (t). Out of these the particle energy (E) and the momentum transfer it underwent during the interaction (q^2) can be reconstructed⁵. The time of flight measurement is estimated with Equation 3.14, which gives a lower bound to the real value. A smearing can be applied with a Gaussian distribution (default value $\sigma_t = 0$ s).

3.6 Validation

The quality and validity of the output of DELPHES are assessed by comparing the resolutions on the reconstructed data to the expectations for both the CMS [67] and the ATLAS [68] detectors. Electrons and muons are by construction equal to the experiment designs, as the Gaussian smearing of their kinematics properties is defined according to the detector specifications. Similarly, the b -tagging efficiency (for real b -jets) and misidentification rates (for fake b -jets) are taken directly from the expected values of the experiment. Unlike these simple objects, jets and missing transverse energy should be carefully cross checked.

Jet resolution

The majority of interesting processes at the LHC contain jets in the final state. The jet resolution obtained using DELPHES is therefore a crucial point for its validation, both for CMS- and ATLAS-like detectors. This validation is based on $pp \rightarrow gg$ events produced with MadGraph/MadEvent and hadronised using PYTHIA.

For a CMS-like detector, a similar procedure as the one explained in published results is applied here. The events were arranged in 14 bins of gluon transverse momentum \hat{p}_T . In each \hat{p}_T bin, every jet in DELPHES is matched to the closest jet of generator-level particles, using the spatial separation between the two jet axes

$$\Delta R = \sqrt{(\eta^{\text{rec}} - \eta^{\text{MC}})^2 + (\phi^{\text{rec}} - \phi^{\text{MC}})^2} < 0.25. \quad (3.15)$$

The jets made of generator-level particles, here referred as *MC jets*, are obtained by applying the algorithm to all particles considered as stable after hadronisation (i.e. including muons). Jets produced by DELPHES and satisfying the matching criterion are called hereafter *reconstructed jets*. All jets are computed with the clustering algorithm (JetCLU) with a cone radius R of 0.7.

⁴It should be noted that for both CMS and ATLAS experiments, the taggers located at 220 m are not able to measure the time-of-flight, contrary to FP420 detectors.

⁵The reconstruction of E and q^2 are not implemented in DELPHES but can be performed at the analysis level.

The ratio of the transverse energies of every reconstructed jet E_T^{rec} to its corresponding MC jet E_T^{MC} is calculated in each \hat{p}_T bin. The $E_T^{\text{rec}}/E_T^{\text{MC}}$ histogram is fitted with a Gaussian distribution in the interval ± 2 RMS centred around the mean value. The resolution in each \hat{p}_T bin is obtained by the fit mean $\langle x \rangle$ and variance $\sigma^2(x)$:

$$\frac{\sigma\left(\frac{E_T^{\text{rec}}}{E_T^{\text{MC}}}\right)_{\text{fit}}}{\left\langle\frac{E_T^{\text{rec}}}{E_T^{\text{MC}}}\right\rangle_{\text{fit}}}\left(\hat{p}_T(i)\right), \text{ for all } i. \quad (3.16)$$

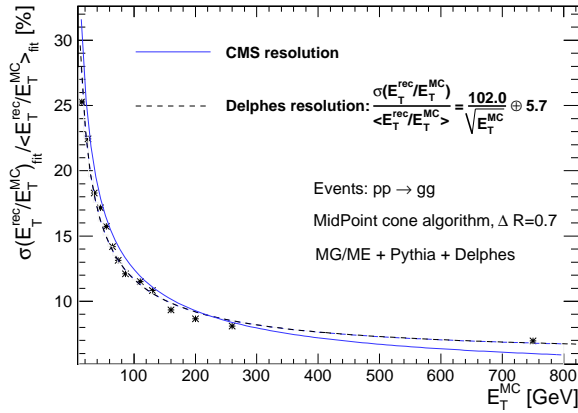


Figure 3.7: Resolution of the transverse energy of reconstructed jets E_T^{rec} as a function of the transverse energy of the closest jet of generator-level particles E_T^{MC} , in a CMS-like detector. The jets events are reconstructed with the JetCLU clustering algorithm with a cone radius of 0.7 in the $|\eta| < 5$ region. The maximum separation between the reconstructed and MC-jets is $\Delta R = 0.25$. Dotted line is the fit result for comparison to the CMS resolution [67], in blue. The $pp \rightarrow gg$ dijet events have been generated with MadGraph/MadEvent and hadronised with PYTHIA.

The resulting jet resolution as a function of E_T^{MC} is shown in Figure 3.7. This distribution is fitted with a function of the following form:

$$\frac{a}{E_T^{\text{MC}}} \oplus \frac{b}{\sqrt{E_T^{\text{MC}}}} \oplus c, \quad (3.17)$$

where a , b and c are the fit parameters. It is then compared using the same jet algorithm to the resolution published by the CMS collaboration [67]. The resolution curves from DELPHES and CMS are in good agreement.

Similarly, the jet resolution is evaluated for an ATLAS-like detector. The $pp \rightarrow gg$ events are here arranged in 8 adjacent bins in p_T . A k_T reconstruction algorithm with $R = 0.6$ is chosen and the maximal matching distance between the MC-jets and the reconstructed jets is set to $\Delta R = 0.2$. The relative energy resolution is evaluated in each bin by:

$$\frac{\sigma(E)}{E} = \sqrt{\left\langle \left(\frac{E^{\text{rec}} - E^{\text{MC}}}{E^{\text{rec}}} \right)^2 \right\rangle - \left\langle \frac{E^{\text{rec}} - E^{\text{MC}}}{E^{\text{rec}}} \right\rangle^2}. \quad (3.18)$$

Figure 3.6 shows a good agreement between the resolution obtained with DELPHES, the result of the fit with Equation 3.17 and the corresponding curve provided by the ATLAS collaboration [68].

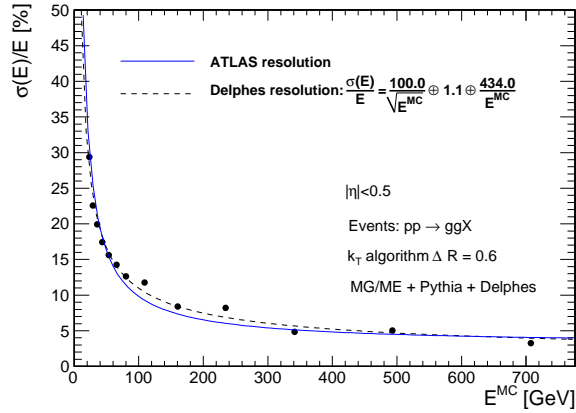


Figure 3.8: Relative energy resolution of reconstructed jets as a function of the energy of the closest jet of generator-level particles E^{MC} , in an ATLAS-like detector. The jets are reconstructed with the k_T algorithm with a radius $R = 0.6$ in the $|\eta| < 5$ region. The maximal matching distance between MC- and reconstructed jets is $\Delta R = 0.2$. Only central jets are considered ($|\eta| < 0.5$). Dotted line is the fit result for comparison to the ATLAS resolution [68], in blue. The $pp \rightarrow gg$ di-jet events have been generated with MadGraph/MadEvent and hadronised with PYTHIA.

MET resolution

All major detectors at hadron colliders have been designed to be as much hermetic as possible in order to detect the presence of one or more neutrinos and/or new weakly interacting particles through apparent missing transverse energy. The resolution of the E_T^{miss} variable, as obtained with DELPHES, is

then crucial.

The samples used to study the MET performance are identical to those used for the jet validation. It is worth noting that the contribution to E_T^{miss} from muons is negligible in the studied sample. The input samples are divided in five bins of scalar E_T sums (ΣE_T). This sum, called *total visible transverse energy*, is defined as the scalar sum of transverse energy in all cells. The quality of the MET reconstruction is checked via the resolution on its horizontal component E_x^{miss} .

The E_x^{miss} resolution is evaluated in the following way. The distribution of the difference between E_x^{miss} in DELPHES and at generator-level is fitted with a Gaussian function in each (ΣE_T) bin. The fit RMS gives the MET resolution in each bin. The resulting value is plotted in Figure 3.9 as a function of the total visible transverse energy, for CMS- and ATLAS-like detectors.

The resolution σ_x of the horizontal component of MET is observed to behave like

$$\sigma_x = \alpha \sqrt{E_T} \quad (\text{GeV}^{1/2}), \quad (3.19)$$

where the α parameter depends on the resolution of the calorimeters. The MET resolution expected for the CMS detector for similar events is $\sigma_x = (0.6 - 0.7) \sqrt{E_T} \text{ GeV}^{1/2}$ with no pile-up (i.e. extra simultaneous pp collision occurring at high-luminosity in the same bunch crossing) [67], which compares very well with the $\alpha = 0.63$ obtained with DELPHES. Similarly, for an ATLAS-like detector, a value of 0.53 is obtained by DELPHES for the α parameter, while the experiment expects it in the range [0.53 ; 0.57] [68].

τ -jet efficiency

Due to the complexity of their reconstruction algorithm, τ -jets have also to be checked. Table 3.6 lists the reconstruction efficiencies in DELPHES for the hadronic τ -jets from $H, Z \rightarrow \tau^+ \tau^-$. The mass of the Higgs boson is set successively to 140 and 300 GeV/c^2 . The inclusive gauge boson productions ($pp \rightarrow HX$ and $pp \rightarrow ZX$) are performed with MadGraph/MadEvent and the τ lepton decay and further hadronisation are handled by PYTHIA/TAUOLA. All reconstructed τ -jets are 1-prong, and follow the definition described in section 3.3.3, which is very close to an algorithm of the CMS experiment [81]. At last, corresponding efficiencies published by the CMS and ATLAS experiments are quoted for comparison. The agreement is good enough at this level to validate the τ -reconstruction.

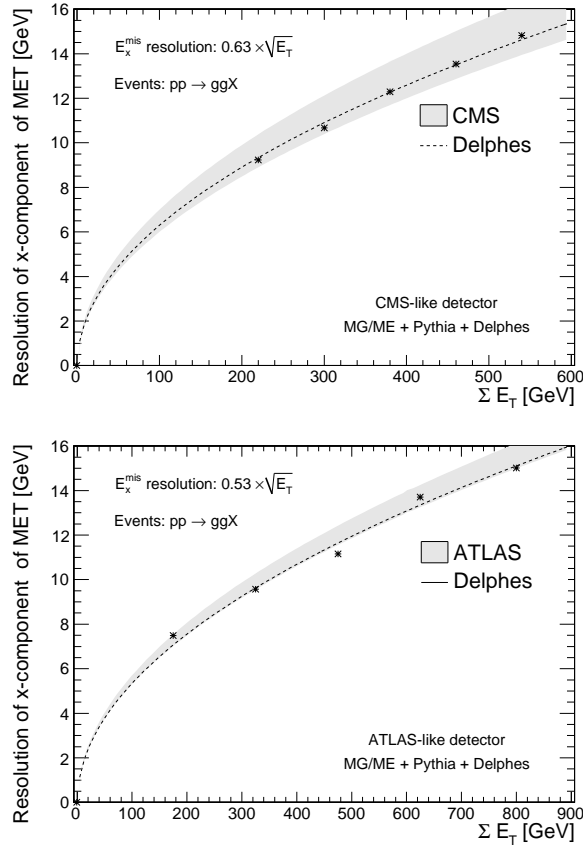


Figure 3.9: $\sigma(E_x^{\text{mis}})$ as a function on the scalar sum of all cells (ΣE_T) for $pp \rightarrow gg$ events, for a CMS-like detector (top) and an ATLAS-like detector (bottom), for di-jet events produced with MadGraph/MadEvent and hadronised with PYTHIA.

Validation of the magnetic field

As an illustration, Figure 3.10 shows the effect of magnetic fields of 3.8 T and 7.6 T on reconstructed tracks in DELPHES. There is a clear cut in the p_T of the reconstructed tracks corresponding to particles that cannot exit the tracker volume from the transverse direction. Below a given value (0.7 GeV/ c for $B_z = 3.8$ T and 1.4 GeV/ c for 7.6 T) the particle helix has a too small radius to exit from the sides of the tracker, and consequently these particles drift to one of the ends of the tracker. If particles are produced from a vertex away from $(0, 0, z)$, they still might reach the tracker sides even below the theoretical p_T threshold.

Table 3.6: Reconstruction efficiencies of τ -jets in $\tau^+\tau^-$ decays from Z or H bosons, in DELPHES, CMS and ATLAS experiments [81, 68]. Two scenarios for the mass of the Higgs boson are investigated. Events generated with MadGraph/MadEvent and hadronised with PYTHIA. The decays of τ leptons is handled by the *Tauola* version embedded in PYTHIA.

	CMS	DELPHES	ATLAS	DELPHES
$Z \rightarrow \tau^+\tau^-$	38.2%	$32.4 \pm 1.8\%$	33%	$28.6 \pm 1.9\%$
$H(140) \rightarrow \tau^+\tau^-$	36.3%	$39.9 \pm 1.6\%$		$32.8 \pm 1.8\%$
$H(300) \rightarrow \tau^+\tau^-$	47.3%	$49.7 \pm 1.5\%$		$43.8 \pm 1.6\%$

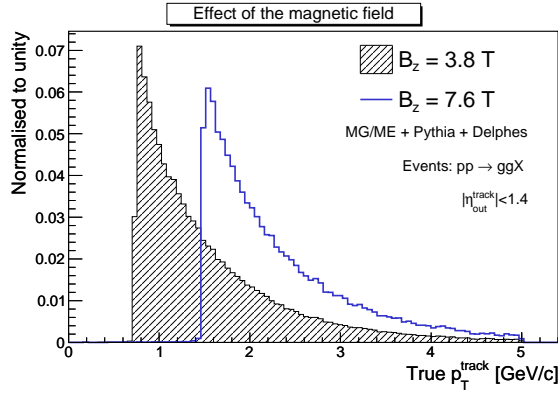


Figure 3.10: Transverse momentum distribution for reconstructed tracks in DELPHES for two values of a homogeneous B_z field.

3.7 Visualisation

When performing an event analysis, a visualisation tool is useful to convey information about the detector layout and the event topology in a simple way. The *Fast and Realistic OpenGL Displayer* FROG [82] has been interfaced in DELPHES, allowing an easy display of the defined detector configuration.

Two and three-dimensional representations of the detector configuration can be used for communication purposes, as they clearly illustrate the geometric coverage of the different detector subsystems. As an example, the generic detector geometry assumed in this thesis is shown in Figure 3.2 and 3.11. The extensions of the central tracking system, the central calorimeters and both forward calorimeters are visible. Note that only the geometrical coverage is depicted and that the calorimeter segmentation is not taken into account in

the drawing of the detector. Moreover, both the radius and the length of each sub-detectors are just display parameters and are not relevant for the physics simulation.

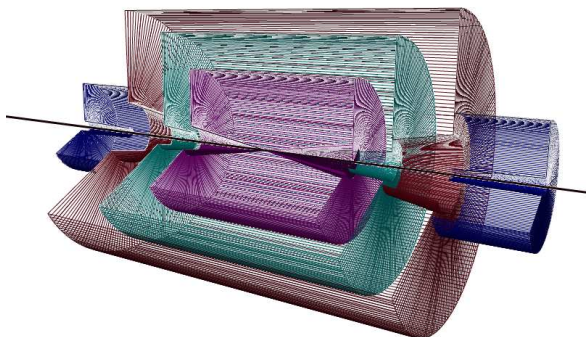


Figure 3.11: Layout of the generic detector geometry assumed in DELPHES. Open 3D-view of the detector with solid volumes. Same colour codes as for Figure 3.2 are applied. Additional forward detectors are not depicted.

Deeper understanding of interesting physics processes is possible by displaying the events themselves. The visibility of each set of objects (e^\pm , μ^\pm , τ^\pm , jets, missing transverse energy) is enhanced by a colour coding. Moreover, kinematic information of each object is visible by a simple mouse action. As an illustration, an associated photoproduction of a W boson and a t quark is shown in Figure 3.12. This corresponds to a $pp(\gamma p \rightarrow Wt)pX$ process, where the Wt pair is induced by an incoming photon emitted by one of the colliding protons [48, 83]. This leading proton survives after photon emission and is present in the final state. As the energy and virtuality of the emitted photon are low, the surviving proton does not leave the beam and escapes from the central detector without being detected. The experimental signature is a lack of hadronic activity in the forward hemisphere where the surviving proton escapes. The t quark decays into a W boson and a b quark. Both W bosons decay into leptons ($W \rightarrow \mu\nu_\mu$ and $W \rightarrow e\nu_e$). The balance between the missing transverse energy and the charged lepton pair is clear, as well as the presence of an empty forward region. It is interesting to notice that the reconstruction algorithms build a fake τ -jet around the electron.

3.8 Conclusion and perspectives

The major features of the DELPHES framework have been described here, introduced for the fast simulation of a collider experiment. This framework is a tool meant for feasibility studies in phenomenology, gauging the observability

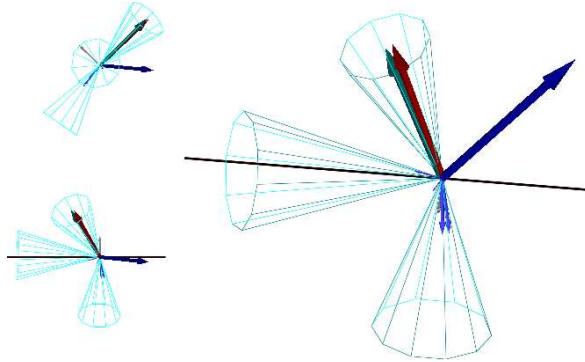


Figure 3.12: Example of $pp(\gamma p \rightarrow Wt)pY$ event display in different orientations, with $t \rightarrow Wb$. One W boson decays into a $\mu\nu_\mu$ pair and the second one into a $e\nu_e$ pair. The surviving proton leaves a forward hemisphere with no hadronic activity. The isolated muon is shown as the dark blue vector. Around the electron, in red, is reconstructed a fake τ -jet (green vector surrounded by a blue cone), while the reconstructed missing energy (in grey) is very small. One jet is visible in one forward region, along the beamline axis, opposite to the direction of the escaping proton.

of model predictions in collider experiments. The simulation includes central and forward detectors to produce realistic observables using standard reconstruction algorithms. Moreover, the framework allows trigger emulation and 3D event visualisation. DELPHES has been developed using the parameters of the CMS experiment but can be easily configured to match ATLAS and other non-LHC experiments, as at TEVATRON or at the ILC. Further developments include a more flexible design for the subdetector assembly and possibly the implementation of an event mixing module for pile-up event simulation. This framework has already been used for several analyses, in particular in photon-induced interactions at the LHC [83, 84, 85].

W ASSOCIATED SINGLE TOP PHOTOPRODUCTION

4.1 Top quark production at the LHC

As presented in Chapter 1, since the top quark discovery at Fermilab in 1995, several properties (like its mass and charge) have already been examined. However, all these measurements are limited by the small collected statistics at the TEVATRON. At the LHC several millions of top quarks will be produced leading to a significant improvement of the knowledge of top quark properties already after the first months of running of the LHC at low luminosity (10 fb^{-1} of integrated luminosity). In this section, the single top quark observation potential at the LHC is therefore briefly summarised with a particular emphasis given on measurements devoted to directly constrain the value of the CKM matrix element $|V_{tb}|$.

4.1.1 Top-antitop production

In hadron-hadron collisions, the predominant source of top quarks is the top-antitop ($t\bar{t}$) production. Contrary to the production at the TEVATRON, at the LHC the relative importance of the gluon fusion and the quark-quark annihilation is reversed since the gluon scattering is expected to produce $\sim 90\%$ of $t\bar{t}$ events while the remaining fraction comes from quark-antiquark annihilation. The corresponding Feynman diagrams for these processes are depicted in Figure 4.1. The production cross section is therefore greatly enhanced (833 pb [86] at NLO) being roughly ~ 100 times larger than at the TEVATRON.

Since the top quark decays exclusively through the single mode $t \rightarrow Wb$, with the W boson decaying almost immediately either hadronically ($\text{BR}(W \rightarrow$

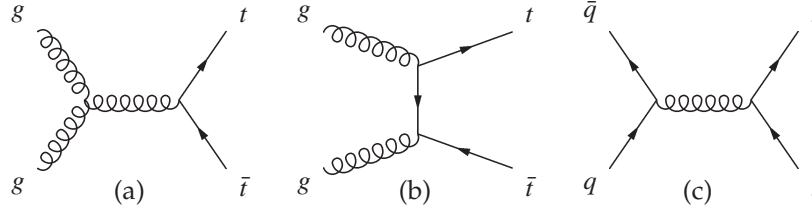


Figure 4.1: Feynman diagrams of the LO processes for $t\bar{t}$ production: gluon-gluon scattering diagrams (a) and (b) and quark-antiquark annihilation (c).

$q\bar{q}$) $\sim 2/3$) or leptonically ($\text{BR}(W \rightarrow \ell\bar{\nu}_\ell) \sim 1/3$, where ℓ stands for the three lepton flavours), the top pairs can be distinguished according to the decay products of the two W bosons as *di-leptonic*, *semi-leptonic* and *fully hadronic*. The same naming convention will be kept throughout this thesis.

Measurement of the $t\bar{t}$ cross section

The determination of the top pair production cross section is one of the measurements that will be carried out just after the turn-on of the LHC. An accurate experimental determination of the production cross section provides a stringent test of the Standard Model. Indeed, non Standard Model top quark production can significantly increase the cross section and moreover, new physics may also modify the cross section times branching ratio differently in various decay channels [87]. After an integrated luminosity of 10 fb^{-1} , the total error in the di-leptonic topology is expected to be $\Delta\sigma_{t\bar{t}}/\sigma_{t\bar{t}} = 11\%(\text{syst}) \pm 0.9\%(\text{stat}) \pm 3\%(\text{luminosity})$ [88] in CMS. As predictable by the large available amount of data, the statistical uncertainty will be negligible: an improvement of the accuracy on $\sigma_{t\bar{t}}$ would therefore be very challenging as it requires to reduce the experimental and theoretical systematics.

4.1.2 Single-top production

Even if the most copious source of top quarks at the LHC is their production in $t\bar{t}$ pairs through strong interaction, a significant number of top quarks is also produced singly via the weak interaction. In the Standard Model, single-top quark production at the LHC occurs through three separate production processes which may be distinguished by the virtuality of the W boson: t-channel ($-Q^2 < 0$), s-channel ($-Q^2 > 0$), and the associated Wt production ($-Q^2 = m_W^2$). The corresponding diagrams are shown in Figure 4.2. Because two Chapters of this thesis focus on the study of the Wt associated single top photoproduction, we will briefly describe the three single-top production mechanisms with emphasis on the current experimental expectations at the LHC.

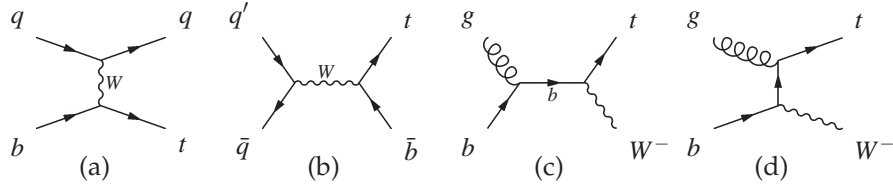


Figure 4.2: Leading order Feynman diagrams for single-top quark production at the LHC: t-channel (a), s-channel (b) and two diagrams for W -associated productions (c) and (d).

t-channel single-top production

The t-channel process involves a space-like W boson that strikes a b quark in the proton sea. Since this b quark originates from a gluon splitting into $b\bar{b}$, this production mode is also referred to as *Wg-fusion*. Among the three existing channels, the t-channel process provides the dominant contribution to single-top with a production cross section that accounts for about 240 pb [89]. This value reaches roughly one third of the production cross section of top quark pairs.

s-channel single-top production

The s-channel single-top production is the second process that produces single top quarks. It is obtained when a time-like W boson with $-Q^2 \geq (m_t + m_b)^2$ is produced by the annihilation of a quark and an anti-quark. The single-top quark appears by the subsequent decay of the W boson into $t\bar{b}$. This process is therefore also named $t\bar{b}$ production. The production cross section is the smallest one of the three single-top processes: 10 pb [90]. Nevertheless, because the two quark distribution functions are well known, the global theoretical uncertainty of this process is much smaller than for the t-channel cross section.

W associated production

Finally single-top quarks may also be produced in association with a real W boson having $-Q^2 = m_W^2$. The expected production cross section at the LHC is sizeable as it reaches 66 pb [91]. Similarly to the t-channel process, the initial b quark is a sea quark inside the proton. Because such a b quark arises from the splitting of a virtual gluon into collinear $b\bar{b}$ quarks, there exists implicitly a \bar{b} quark in the final state. Nevertheless, due to the small p_T of this \bar{b} quark, this accompanying quark is usually unobservable.

Expected cross section measurement at CMS

The total cross sections for these three single-top production processes, as well as the top quark pair production are summarised in Table 4.1. When

no references are given, the cross sections values have been obtained at LO using MG/ME. The cross sections are given for pp collisions at the LHC ($\sqrt{s} = 14.0$ TeV) and $p\bar{p}$ collisions at the TEVATRON ($\sqrt{s} = 1.96$ TeV) allowing a direct comparison between the rates expected at these two facilities. Comparing the cross sections, it is obvious that if the Wt production rate is negligible at the TEVATRON, the cross section at the LHC is important and even exceeds the s-channel one. The CMS collaboration argues that all three processes will be observable at the LHC.

Table 4.1: Total cross section in pb for the three single-top quark production and the top pair production. The cross sections are given for pp collisions at the LHC ($\sqrt{s} = 14.0$ TeV) and $p\bar{p}$ collisions at the TEVATRON ($\sqrt{s} = 1.96$ TeV). All cross sections are evaluated at $m_t = 175$ GeV/ c^2 .

	\sqrt{s}	t-channel	s-channel	Wt	$t\bar{t}$
σ_{LHC} (pb)	14.0 TeV	240	10	66	833
σ_{TEVATRON} (pb)	1.96 TeV	1.02	1.98	0.25	6.9

Hence, thanks to the high cross section of the t-channel, this channel is most likely the best candidate to first observe with $\geq 5\sigma$ significance single top production at the LHC. After 10 fb^{-1} , the expected uncertainty on the cross section is $\Delta\sigma_t/\sigma_t = 2.7\%(\text{stat.}) \oplus 8.0\%(\text{sys.}) \oplus 8.7\%(\text{lumi.}) \simeq 12\%$ [92]. Even if the Wt process is more challenging, a clear evidence may also be obtained after the same integrated luminosity. Considering events where one of the W -bosons (either the one produced together with the top quark or the one appearing in the top quark decay) decays leptonically and the other one hadronically, the expected accuracy on the cross section is $\Delta\sigma_{Wt}/\sigma_{Wt} = 7.5\%(\text{stat.}) \oplus 15.6\%(\text{sys.}) \oplus 7.8\%(\text{lumi.}) \simeq 19\%$ [92] while for the di-leptonic topology the result is $\Delta\sigma_{Wt}/\sigma_{Wt} = 8.8\%(\text{stat.}) \oplus 22.8\%(\text{sys.}) \oplus 5.4\%(\text{lumi.}) \simeq 25\%$ [92]. Moreover, because this channel is invisible at the TEVATRON, this evidence would be the first direct evidence of the existence of the Wt process. Finally, because the cross section of the s-channel is almost a factor 100 smaller than the most dangerous background coming from the $t\bar{t}$ process, it will be difficult to observe this process with data corresponding to about 10 fb^{-1} of integrated luminosity. For an integrated luminosity of 10 fb^{-1} , the error is large: $\Delta\sigma_s/\sigma_s = 18\%(\text{stat.}) \oplus 31\%(\text{sys.}) \oplus 19\%(\text{lumi.}) \simeq 41\%$ [92].

4.2 Top quark photoproduction at the LHC

4.2.1 Top-antitop photoproduction

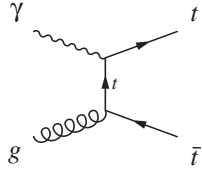


Figure 4.3: Representative leading order Feynman diagrams of the top quark pair photoproduction.

The high luminosity and the high c.m.s. energy of photoproduction processes at the LHC offer interesting possibilities for the study of electroweak interaction up to the TeV scale. Indeed, if the LHC will be a top quark factory, producing millions of top pairs through the $pp \rightarrow t\bar{t}$ process, the high energy of the incoming proton beams combined with the very high expected luminosity allows to

study top quark pair production through a purely electromagnetic process, $pp(\gamma\gamma \rightarrow t\bar{t})pp$, and via photon-gluon fusion $pp(\gamma g \rightarrow t\bar{t})pY$. Nevertheless, the pure electromagnetic production mechanism is negligible at the LHC compared to the gluon-fusion one since the strength of the electromagnetic coupling is much smaller, cut-offs are introduced by the form factors and the expected luminosity is much smaller. The top quark pair photoproduction has a cross section of 1.54 pb and could therefore be studied during the very low ($\mathcal{L} < 10^{32} \text{ cm}^{-2} \text{ s}^{-1}$) and low luminosity ($\mathcal{L} = 10^{33} \text{ cm}^{-2} \text{ s}^{-1}$) phases of the LHC. The leading order Feynman diagram of this process is depicted in Figure 4.3. Hence, the top quark photoproduction process may allow to measure top quark related Standard Model parameters, such as the top quark mass, its electric charge and the value of the $|V_{tb}|$ element of the CKM matrix. This offers a unique possibility for studying the top quark particle in a complementary way to the usual parton-parton processes because the smaller production cross sections is effectively compensated by better known initial conditions and usually simpler final states.

4.2.2 Single-top photoproduction

Other very interesting photon-induced processes that can be considered are the production of single-top quarks. In the following, the same categorisation in three production mechanisms will be used: t-channel (Figure 4.4-a), s-channel (Figure 4.4-b) and W -associated production (Figure 4.4-c). If in parton-parton production, the initial partons are issued from the proton, in photoproduction the source of one of the quarks in the t-channel is the photon. In addition to the presence of an additional quark in the final state, this leads to a subsequent decrease of the production cross section. This effect is strongly illustrated by looking at the production cross sections of the t-channel process, 28.5 fb, obtained using MG/ME, as well as the cut on the transverse momentum of the outgoing quarks introduced in Section 2.2.2. The s-channel has a negligible cross section of 64 ab, and is therefore unusable. Although in parton-parton interaction, the dominant production mode is the t-channel process, at the LHC, the most copious source of photoproduced single-top quarks is the W -associated process: the cross section obtained using the five-flavour scheme reaches 1.01 pb, and is

therefore responsible for a few percent of the total proton-proton cross section.

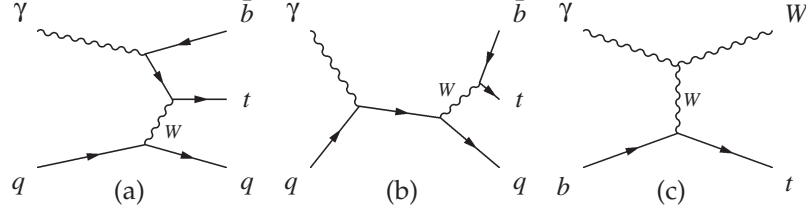


Figure 4.4: Representative leading order Feynman diagrams of the three single-top photon-induced production modes. From left to right : t-channel, s-channel and a diagram for the W -associated production.

Table 4.2 compares the production cross sections of single-top events as well as the value of the most dangerous background, the $t\bar{t}$ events, produced in parton-parton and in photon-proton events. Consequently, the interest of studying this process is obvious: compared to the “nominal” production modes of particles at the LHC where the $\sigma_{Wt}/\sigma_{t\bar{t}}$ fraction reduces down to $\sim 6\%$, in parton-parton interactions, the contribution from the W -associated photoproduction accounts for about 40% of all the top quark photoproduction modes.

Table 4.2: Total cross sections in pb for the three single-top quark modes and the top pair production process. The values for the $pp \rightarrow X$ events contain NLO corrections and the $pp(\gamma q/g \rightarrow X)pY$ value has been evaluated at tree-level using MG/ME at $m_t = 175 \text{ GeV}/c^2$. The cross sections are given for pp collisions at the LHC with $\sqrt{s} = 14.0 \text{ TeV}$.

Process	t-channel	s-channel	Wt	$t\bar{t}$
$\sigma_{pp \rightarrow X}$ (pb)	240	10	66	833
$\sigma_{pp(\gamma q/g \rightarrow X)pY}$ (pb)	0.029	64×10^{-6}	1.01	1.54

4.3 Search for Wt associated photoproduction

As within the SM the top quark is expected to decay almost exclusively through the $t \rightarrow Wb$ mode, the $pp(\gamma b \rightarrow Wt)pY$ process results in a b -quark and two W bosons where one emerges from the hard process and the other originates from the top quark decay. Like in the parton-parton Wt -channel, the initial parton is a b quark arising from the splitting of a virtual gluon and has therefore usually a small transverse momentum. For that reason we shall not require more than one b -jet to be detected. In the following Chapter, we

will consider both final states: the di-leptonic topology ($Wt \rightarrow \ell^- \bar{\nu} \ell^+ \nu b$) when the two W bosons undergo a leptonic decay and the semi-leptonic topology ($Wt \rightarrow \ell \nu j j b$) where only one of the W bosons decays leptonically. Throughout this Chapter, for all the relevant simulated processes, a *leptonically decaying W boson* means that it was allowed to decay into all three leptons: electron, muon and tau.

4.3.1 Signal and background generation

Apart for the $pp \rightarrow W$ +jets backgrounds for which ALPGEN¹ was used, the signal events and background events have been automatically generated using the MG/ME package with the $m_t = 174.3 \text{ GeV}/c^2$ value. Using the PYTHIA Monte Carlo generator², the obtained partonic processes are decayed to the desired topologies. Moreover, PYTHIA was employed to simulate the parton showering, the hadronisation of the partons produced in both the hard interaction and the proton remnants, and the decays of unstable particles. Finally, to properly consider the effect of jet algorithms and the efficiency of event selection under realistic experimental conditions, the fast detector simulation was performed using DELPHES version 1.8 with the default parametrisation for the CMS detector. Samples that have been used in the analysis are described hereafter.

In the $t\bar{t}$ events, apart from the presence of a second b -quark, the final state is similar to the W -associated events. Hence, the high cross section of this process makes it the dominant source of irreducible background³ when this additional jet escapes from detection (either the jet is not reconstructed or the jet misses the acceptance of the detector). For the di-leptonic topology, another source of events is the production of WWq' , when the two bosons decay leptonically and the quark has enough transverse momentum. Having relatively twice the cross section of the di-leptonic topology, the production of a Z boson in association with a parton has also to be considered as background. Nevertheless, due to the absence of missing transverse energy and of real b -jet, its contribution will be limited. Finally, when one or two charged leptons escape the geometrical detector acceptance, the production of ZZj events can also provide a source of background. Nevertheless, due to the tiny cross section (1.73 fb) of this process compared to the signal production rate, in the following analysis, we completely neglect these latter events. Some representative Feynman diagrams of all these backgrounds can be seen in Figure 4.5.

¹ALPGEN is an event generator dedicated for simulating hard multi-parton processes

²Version 6.412 was used because this public release allows to correctly treat the scattered proton after the photon exchange.

³Processes with final state similar to the one of the signal.

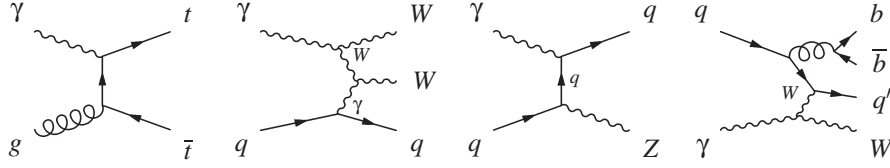


Figure 4.5: Examples of representative leading order diagrams of $pp(\gamma q/g \rightarrow X)pY$ processes being background of the di-leptonic and/or semi-leptonic signal topologies. From left to right: $t\bar{t}$, WWq' , Zj and $Wb\bar{b}q'$ events.

Following the $t\bar{t}$ photoproduction, the second most important source of background in the semi-leptonic topology stems from W +jets production. However, due to the existence of a b -quark in the signal topology, the associated production should easily be separated from the W +jets events since a light or a c -jet must be mistagged as a b -jet in order to fake the signal event signature. A W boson which is produced with two b -quarks ($pp(\gamma q \rightarrow Wb\bar{b}q')pY$) has also to be considered as background. Finally, the parton-parton t-channel single-top production possesses a large cross section and may therefore be an important source of signal-like final state. The production cross sections times the branching ratio into the desired topology, as well as the sample size of the considered backgrounds, are given in Table 4.3.

Table 4.3: Background processes used in the semi-leptonic and di-leptonic channels. Cross-sections include generation cuts of $p_T > 1$ GeV/ c for q' and $p_T > 10$ GeV/ c , $|\eta| < 5$ for jets. The W +jets modes (labelled Wjj , $Wjjj$ and $Wjjjj$) have been generated using ALPGEN with a minimal p_T^{cut} on the jets of 20 GeV/ c . Branching ratio of the W boson into leptons (e , μ or τ) is taken into account. The two labels in the first row refers respectively to the photon-induced and parton-induced processes.

Process	$\gamma p \rightarrow X$		$pp \rightarrow X$	
	σ [fb]	sample size	$\sigma \times Br$ [fb]	sample size
$t\bar{t}(2\ell)$	159.1	200 k	77.7×10^3	130 k
$t\bar{t}(1\ell)$	671.8	179 k	328×10^3	390 k
$WWq' - WWj(2\ell)$	62.5	70 k	5.2×10^3	100 k
$Zj(2\ell)$	287.3	50 k	-	-
Wjj	-	-	2.4×10^6	830 k
$Wjjj$	2793	264 k	6.9×10^5	264 k
$Wjjjj$	-	-	1.7×10^5	105 k
$Wb\bar{b}q' - Wb\bar{b}j$	55.2	10 k	2.7×10^5	120 k
tj	-	-	6.7×10^3	100 k

Even if photon-induced processes can efficiently be separated from parton-parton processes, due to their cross sections higher by several order of magnitude, the same topologies produced using $pp \rightarrow X$ processes are also taken as backgrounds. Nevertheless, the $pp \rightarrow Wt$ process that possesses exactly the same final state is not considered in the following analyses, because its cross section of 66 pb reduces to a negligible value once the photon-related tags are applied.

4.3.2 Signal discrimination of semi-leptonic events

In this section, the selection strategy applied to obtain a signal-enriched final sample is presented. The final state of semi-leptonic Wt events is characterised by exactly one isolated lepton (electron or muon) with high missing transverse energy, as well as the presence of a b -jet and two light flavour jets. Despite the very distinct signal signatures, the backgrounds associated to the semi-leptonic topology are considerable ($t\bar{t}$, $Wb\bar{b}q'$, W +jets and t +jet) involving the necessity to apply challenging selection cuts in order to obtain the separation between signal and background events.

The background reduction is performed in three steps that are categorised as following: first, purely *topological cuts* are applied that rely solely on the final state of the signal events. Secondly, because partonic backgrounds have typical cross sections of three order of magnitude larger than photoproduction, a rejection based on both the maximum allowed energy and on the track multiplicity in the “empty” hemisphere is applied. In the following, these two cuts will be mentioned as *γp cuts*. Finally, in order to further reduce the backgrounds that conserved a non-negligible cross section, the events will need to fulfil more specific criteria, the *final cuts*. No trigger selection is applied in the following analysis. Nevertheless, the reduction factor consequent to such a preselection would be negligible since the threshold values applied on the transverse momentum of the isolated leptons are larger than those used by the trigger.

Topological cuts

The selection procedure starts by requiring the presence of exactly one isolated lepton⁴. To be taken into account, the lepton pseudorapidity must satisfy $|\eta| < 2.5$ and its transverse momentum must be greater than 20 GeV/ c . Even if in this analysis only background events containing a leptonically decaying W boson are considered, the presence of a high p_T lepton allows to considerably suppress QCD background as well as to allow an efficient trigger selection.

⁴The used isolation criterion is the default one implemented in DELPHES.

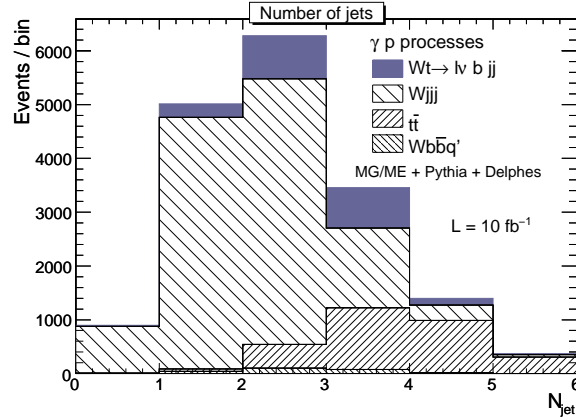


Figure 4.6: Cumulative distribution of the number of reconstructed central ($|\eta| < 3$) jets with $p_T > 20$ GeV/ c after the cut on the lepton. Jets are reconstructed using the Midpoint cone algorithm with a cone size of 0.7 and the normalisation corresponds to 10 fb^{-1} .

In order to suppress jets reconstructed around the isolated lepton, any jet closer than $\Delta R = 0.1$ to the identified lepton candidate is removed from the jet collection. Having this in mind, an event candidate is conserved only if it contains exactly three jets with $p_T > 30$ GeV/ c and pseudorapidity $|\eta| < 3$. Moreover, the jet counting is an efficient discriminator against the $t\bar{t}$ background as can be seen in Figure 4.6 where the cumulative distribution of the number of jets reconstructed with the $p_T > 20$ GeV/ c and $|\eta| < 3$ conditions is shown. While the Wt distribution peaks at two jets, $t\bar{t}$ background mainly contains at least 3 jets. An event is therefore rejected if an additional jet with $p_T > 20$ GeV/ c is reconstructed in the same detector coverage. When the analysis is performed on real data, it will therefore rely on the ability of the detector to reconstruct jets with transverse momentum as low as 20 GeV/ c .

Photon-induced selection (γp cuts)

Photon-induced interactions are characterised by the presence of a very forward scattered proton and a large pseudorapidity region devoid of any hadronic activity, usually called *large rapidity gap* (LRG). During the LHC operation at very low luminosity, the number of pile-up events is negligible and the observed activity in the detector will subsequently come from a single collision. Thanks to the colour flow in pp interactions between the proton remnant and the centrally produced particles, a simple way to suppress generic pp interactions is to use the presence of the LRG by looking at the

energy E_{min}^{FCAL} measured in the forward calorimeter ($3 < |\eta| < 5$) containing the minimal activity. The *empty hemisphere* is defined as the one where the forward activity is minimum. The minimum of energies E_{min}^{FCAL} measured in the two forward calorimeters is displayed in Figure 4.7-a for two photon-induced events ($pp(\gamma b \rightarrow Wt)pY$ and $pp(\gamma g \rightarrow t\bar{t})pY$) and the $pp \rightarrow t\bar{t}$ process. As expected, the energy measured in proton-proton events is larger due to the presence of the proton remnant.

For a E_{CUT}^{FCAL} value of 50 GeV, a typical reduction factor of ~ 140 for parton-parton is expected (Figure 4.7-b) while 73% of the $t\bar{t}$ and Wt photon-induced events survive the cut. Decreasing the E_{CUT}^{FCAL} value down to 30 GeV, the respective values become 400 and 70%. The percentage of events that will be selected by the rapidity gap condition as a function of the maximum allowed measured energy in the forward hemisphere $3 < |\eta| < 5$ is given in Table 4.4. Values are given after the application of the topological cuts. If the photon-induced processes are only slightly affected by the decrease from $E_{CUT}^{FCAL} = 50$ GeV to $E_{CUT}^{FCAL} = 30$ GeV, parton-parton events are reduced by a factor comprised between 2 and 3. For the rest of this thesis, the 30 GeV value has been chosen and is therefore applied in the photon-proton tagging procedure.

Table 4.4: Percentage of events that will be selected by the rapidity gap condition as a function of the maximum allowed measured energy in the forward hemisphere $3 < |\eta| < 5$. Values are given for after the requirement of the presence of one isolated lepton with $p_T > 20$ GeV/ c and three jets with $p_T > 30$ GeV/ c within $|\eta| < 3$.

Process	γp events		pp events	
	$t\bar{t} \rightarrow \ell\nu jjb$	$Wjjj$	$t\bar{t} \rightarrow \ell\nu jjb$	$Wjjj$
$E_{CUT}^{FCAL} = 50$ GeV	91.8%	95.2%	1.0%	2.0%
$E_{CUT}^{FCAL} = 30$ GeV	90.2%	93.7%	0.4%	0.8%

Potentially dangerous backgrounds arise when topologies similar to signal events are produced from the small fraction of parton-parton collisions containing rapidity gaps, but not due to diffractive scattering. The typical reduction factors obtained using the rapidity gap condition might not be sufficient for the considered parton-induced events given their very large production cross section. An additional reduction is obtained by applying a selection cut that exploits the region devoid of additional tracks in photon-induced events although there is a presence of tracks beyond the ones expected from the lepton and jet candidates in proton-proton collisions. Due to the heavy particle produced in the single-top processes, the photoproduction multiplicity is further reduced since the majority of the photon energy

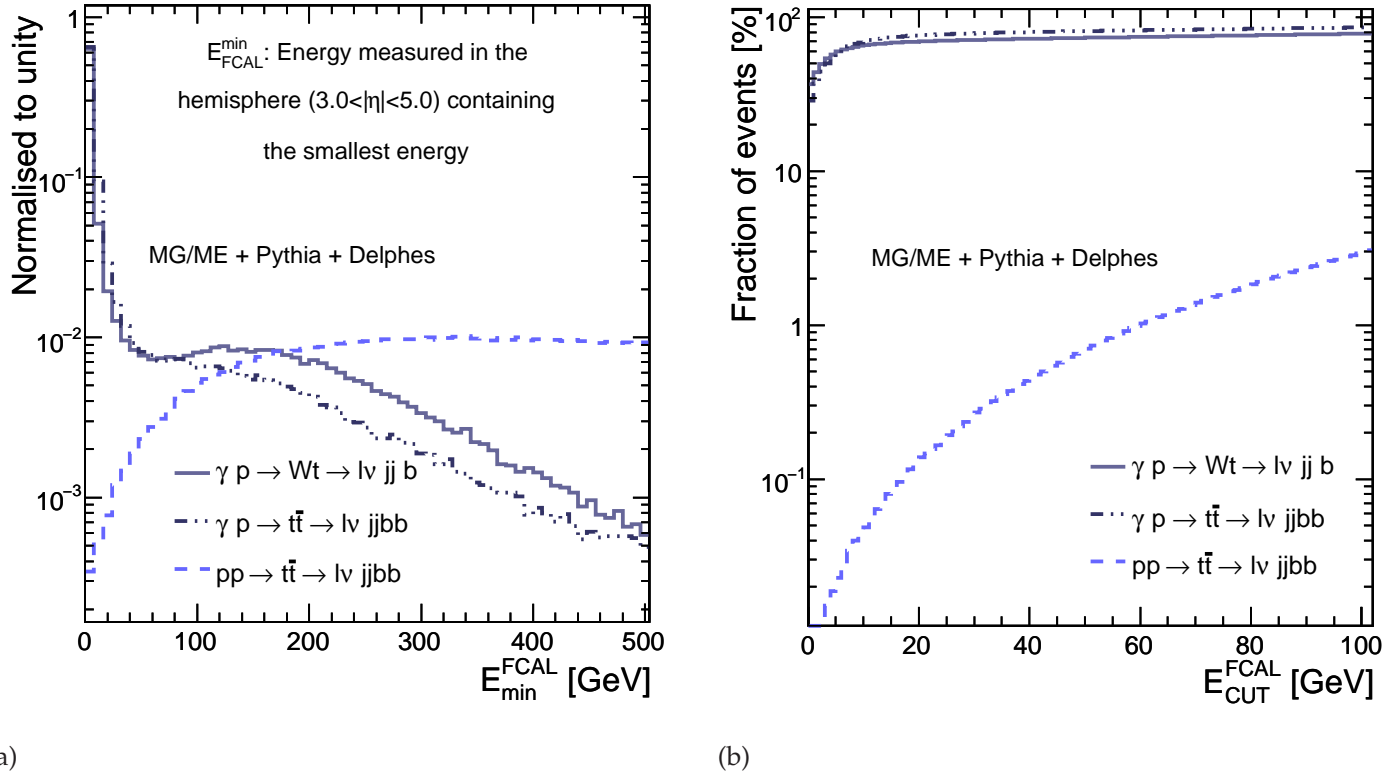


Figure 4.7: Left: minimum of energies E_{min}^{FCAL} measured in the two forward calorimeters assumed to be located at $3 < |\eta| < 5$ for two photon-induced events ($pp(\gamma b \rightarrow Wt)pY$ and $pp(\gamma g \rightarrow t\bar{t})pY$) and the $pp \rightarrow t\bar{t}$ process. Right: fraction of selected events as a function of the maximum allowed measured energy in the empty hemisphere (E_{CUT}^{FCAL}). No other acceptance cut is applied.

is needed to produce the Wt pair, leaving less energy to produce additional particles.

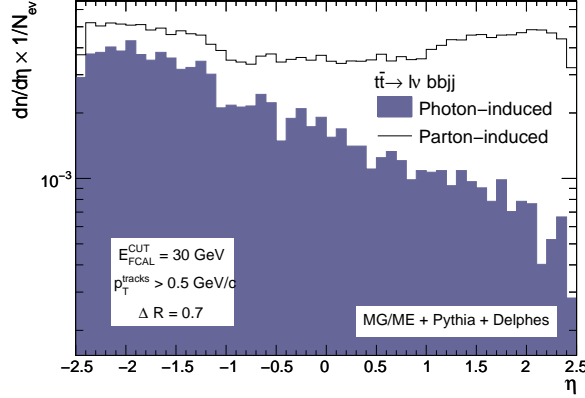


Figure 4.8: Pseudorapidity distribution of tracks with $p_T > 0.5$ GeV/ c in the tracker ($|\eta| < 2.5$) for photon-induced and proton-induced $Wjjj$ events after the requirements of the presence of one lepton and three jets. The tracks associated to the expected final states have been excluded. The positive pseudorapidity have been allocated to the hemisphere that contains a scattered protons in photon-induced events.

As depicted in Figure 4.8 photon-induced events have, on average, less additional tracks in the hemisphere that contains the scattered proton (associated to the positive pseudorapidity) than the parton-parton events. The track multiplicity distribution in the tracker coverage ($|\eta| < 2.5$) has been obtained after the application of topological cuts, and the tracks associated to an expected lepton or lying inside the cones of the selected jets have been excluded. Moreover, the *gap side* is selected as the one containing the lower measured energy in the forward detector even if this definition is only relevant for photon-induced events.

A straightforward use of such a distribution is the possibility to apply an *exclusivity* condition that would reflect the average lower number of tracks present in the empty hemisphere although the distribution of the parton-induced process exhibit a roughly flat track distribution. In the following, the exclusivity condition requires that no additional tracks are present in the central $1 < \eta < 2.5$ region of the tracker on the gap side. Because the rapidity gap condition acts on the forward calorimeter ($3 < |\eta| < 5$), while the tracker provides coverage in the central region, these two γp cuts are complementary since they cover different regions of pseudorapidity. The rapidity gap and the exclusivity conditions are therefore highly correlated and should always be

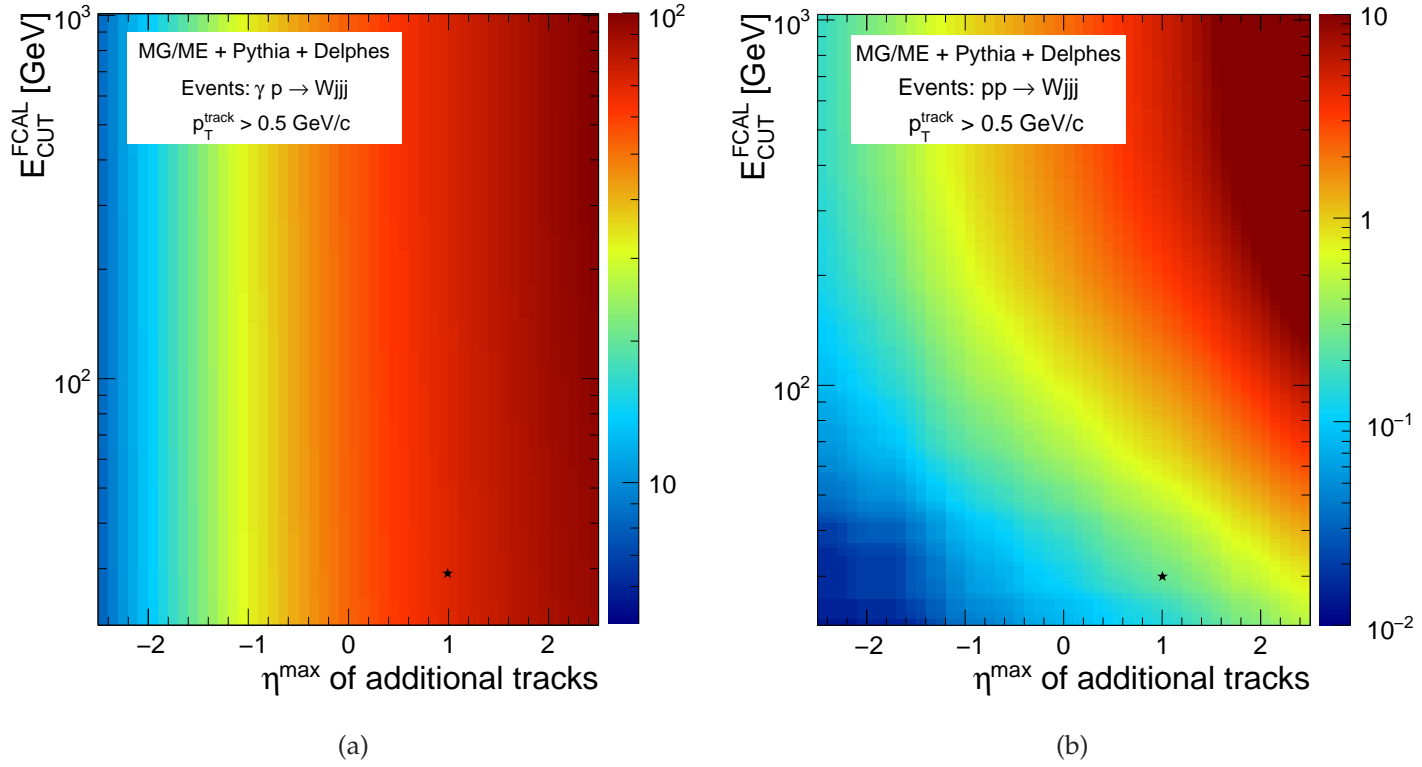


Figure 4.9: Two-dimensional plots of the percentage of events that are accepted by the γp cuts as a function of the value of the E_{CUT}^{FCAL} and the maximum allowed pseudorapidity of the additional tracks for $\gamma p \rightarrow Wjjj$ (left) and $pp \rightarrow Wjjj$ (right) events. The plots shown were obtained with a minimal cut on the transverse momentum of the tracks of 0.5 GeV/c. The star corresponds to the chosen values considered in the selection procedure for the E_{CUT}^{FCAL} cut and the maximum allowed value of the additional tracks.

applied together. Figure 4.9 shows the two-dimensional plot of the percentage of events that will be accepted by the γp cuts as a function of the value of the E_{CUT}^{FCAL} and the maximum allowed pseudorapidity of the additional tracks for $pp(\gamma p \rightarrow Wjjj)pY$ (left) and $pp \rightarrow Wjjj$ (right) events. While the two requirements are slightly correlated for photon-induced processes, parton-parton events clearly exhibit a dependence between the two requirements. Hence, when the E_{CUT}^{FCAL} is decreased from 50 to 30 GeV, the rejection factor of the exclusivity condition on the $pp \rightarrow Wjjj$ event changes from 4.4 to 4.1.

Table 4.5: Percentage of events that will be selected by the exclusivity condition as a function of the maximum allowed measured energy in the forward hemisphere. Values are given for after the application of the rapidity gap condition with a value of $E_{CUT}^{FCAL} = 30$ GeV. The effect of the minimum transverse momentum of the track is shown using two different p_T values: 0.5 GeV/ c and 1.0 GeV/ c .

Process	γp events		pp events	
	$t\bar{t} \rightarrow \ell\nu jjb$	$Wjjj$	$t\bar{t} \rightarrow \ell\nu jjb$	$Wjjj$
$p_T^{track} = 0.5$ GeV/ c	58.8%	74.8%	24.3%	31.2%
$p_T^{track} = 1.0$ GeV/ c	64.9%	79.9%	38.1%	48.4%

Although the γp cuts are quite effective to reduce parton-parton background, the rejection power would benefit from an efficient low p_T track reconstruction. Indeed a clear gain is already visible in Table 4.5 when the minimum transverse momentum of tracks is decreased from 1.0 GeV/ c to 0.5 GeV/ c : for a E_{CUT}^{FCAL} of 30 GeV, while 38% of the $pp \rightarrow Wjjj$ events remains after the application of the exclusivity cut, only 24% survived the cuts when a track as low as 0.5 GeV/ c can be reconstructed. The exclusivity cut used in this analysis therefore uses a minimal p_T^{track} of 0.5 GeV/ c and a reconstruction efficiency of 90% which is realistic for a general purpose detector such as CMS [93].

With the defined rapidity gap and exclusivity conditions, the selection efficiency for photon-induced processes drops roughly by a factor of two while the reduction factors for parton-induced interactions are better than 10^{-3} . The large parton-parton cross sections combined with this tiny efficiency implies that a huge Monte Carlo statistics should be needed so that a significant number of pp events pass the whole selection procedure, allowing to realistically estimate the impact of the *final cuts*.

In order to avoid the generation of millions of events, we assumed that the γp and *final cuts* are almost uncorrelated since the selection cuts belonging to the *final cuts* category are roughly independent of the forced geometrical

constraint inherent from the γp cuts. Efficiencies for signal and background for each of the two cut groups are therefore determined individually and the estimation of the visible cross sections at each stage of the selection procedure is obtained using a “combined efficiency” calculated as the product of the efficiencies $\epsilon_{\gamma p \text{ cuts}} \times \epsilon_{\text{final cuts}}$.

Final cuts

At this stage of the selection the sample is still dominated by the $Wjjj$ processes that do not contain any b -quark. The identification of b -jet is therefore an important tool to suppress these backgrounds since single-top events feature one energetic b -quark jet, while the heavy flavour content in $Wjjj$ events is relatively low. Requiring that exactly one of the three jet candidates is b -labeled suppresses $Wjjj$ events very effectively since the contribution of processes containing one b -jet in the final state only represents 11% of the entire W +jets samples: only 6.6% of these samples are passing this selection cut.

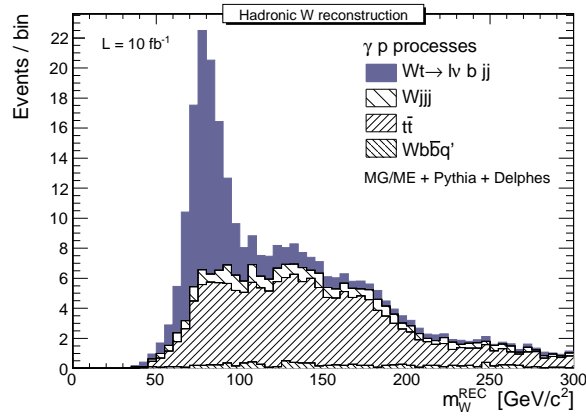


Figure 4.10: Cumulative distribution of the invariant mass of the two reconstructed central ($|\eta| < 3$) jets that are not b -tagged after the cuts on the lepton, the jets, rapidity gap selection and the exclusivity condition. The normalisation corresponds to 10 fb^{-1} .

In order to fulfill the next selection criterion, the presence of two jets compatible with the presence of a W boson that decayed hadronically is mandatory. To be selected, the invariant mass value of the two non- b -like jets must therefore lie within a window of $20 \text{ GeV}/c^2$ around the W mass. The two-jet invariant mass distribution is shown in Figure 4.10. It clearly demonstrates the presence of a sharp peak in the Wt events while the distribution of backgrounds is roughly flat: this cut therefore serves to eliminate events that

do not contain a second W boson. In addition, this cut provides an additional discriminating power against $t\bar{t}$ events since the presence of an untagged b -jet implies an incorrect allocation of the jets arisen from the W decay.

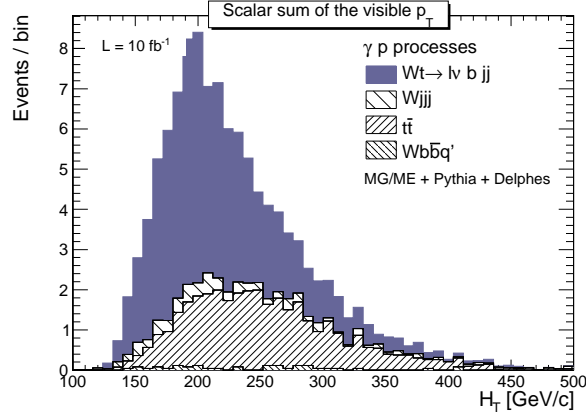


Figure 4.11: Cumulative distribution of the scalar sum of the transverse momentum of the visible selected objects (one lepton and three jets) after the cuts on the lepton, the jets, rapidity gap selection, the exclusivity condition and the cut on the W boson mass. The normalisation corresponds to 10 fb^{-1} .

The dominant background that survived the selection cuts up to this point are the $t\bar{t}$ processes. Hence, the final separation between signal and background events makes use of a dedicated kinematic variable whose distribution is different for $t\bar{t}$ background: the scalar sum (H_T) of the transverse momenta of the three observed jets and the lepton. In Figure 4.11, the H_T distribution for the Wt signal events is compared with the ones for photon-induced background events. If we require that the scalar sum must not exceed $230 \text{ GeV}/c$, this cut rejects 60% of the $\gamma p \rightarrow t\bar{t}$ background while preserving 67% of the Wt signal events.

Top quark reconstruction

After the selection chain presented hereabove, the surviving sample is supposed to be signal-enriched. The most obvious way to check that the sample exhibits a single-top feature is to look after the presence of a reconstructed mass peak located around the top quark mass. This reconstruction can be performed in two steps each requiring some decision to be taken.

First, due to the presence of the neutrino, the leptonically decaying W boson should carefully be reconstructed. Because of the presence of only

one energetic neutrino in the final state, we can assume that it represent the only source of missing transverse energy for signal events⁵: the x and y -components of the neutrino are therefore uniquely determined. In order to reconstruct the leptonic W boson from its decay products, the longitudinal component of the neutrino (v_z) should also be computed. This can be performed by using the four-momentum conservation of the $W \rightarrow \ell\nu$ decay which leads to the following quartic equation

$$(\ell_z^2 - \ell_0^2)v_z^2 + 2\rho\ell_z v_z + \rho^2 - \ell_0^2 E_T^{miss^2} = 0, \quad (4.1)$$

where the $\rho = m_W^2/2 + \ell_x v_x + \ell_y v_y$ parameter has been introduced and ℓ_μ and v_μ are respectively the four vectors of the lepton and the neutrino. When the missing transverse energy is so badly reconstructed such that the neutrino-lepton invariant mass is above the W boson mass, the longitudinal neutrino component is imaginary. Several schemes exist to deal with this situation; here the real part is taken as the answer. In most of the cases, the value of v_z is not unambiguously determined because two solutions exists to the above equation. The longitudinal momentum of the neutrino is therefore determined up to a twofold ambiguity among which the most central one is chosen, which is found to be correct in $\sim 60\%$ of the cases.

Secondly, because the hadronically decaying W -boson can be either the one produced together with the top quark either the one appearing in the top quark decay, the reconstruction of the top quark mass will require to find which of the two W bosons should be arranged with the b -jet to build a top. Even if several methods exist, in this analysis, we choose to assign to the top quark the W boson the closest to the b -jet.

Figure 4.12 shows the mass of the reconstructed top quark for events passing the full selection procedure. When real data is available, the observation of a such a peak at approximately m_{top} in the selected sample will be a clear evidence of the presence of top quarks. For t +jet, W +jets and $Wb\bar{b}j$ events, the distribution tends to be broad and soft. In $t\bar{t}$ events, a peak is present but it is broadened with respect to the Wt signal. Because of bad achieved resolution, this simple reconstruction method can not be used to directly perform a top quark mass measurement. Nevertheless, because it is very characteristic of top events, this distribution will have a central role in the signal extraction in real data.

Summary of selection cuts and results after 10 fb^{-1}

The outcome of the presented selection is summarised in Table 4.17 where the effective cross sections at each stage of the analysis for the semi-leptonic

⁵This is only an approximation as other, softer, neutrinos can be present in the event such as those coming from leptonic b -decay.

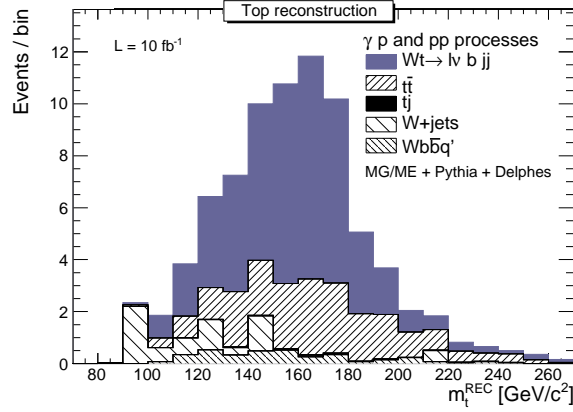


Figure 4.12: Cumulative distribution of the reconstructed top mass after the application of the entire selection chain: lepton and jet cuts, rapidity gap selection, the exclusivity condition, the b -tagging requirement, the hadronic W boson mass reconstruction and the H_T selection. In addition to the photon-induced processes, parton-parton processes are also depicted. The normalisation corresponds to 10 fb^{-1} .

$pp(\gamma p \rightarrow Wt)pY$ events and their relevant photon-induced and proton-induced backgrounds are shown. The expected yields corresponding to an integrated luminosity of 10 fb^{-1} are also given.

The clear strong suppression of processes that do not contain a real b -quark in the final state is visible. Furthermore, the requirement on the hadronic W mass reconstruction is responsible of a clear enhancement of the signal to background ratio. The dominating remaining background that stem from $t\bar{t}$ processes is effectively suppressed by the final step of the selection, the H_T cut. In spite of this very efficient selection procedure, many background processes occurring in proton-proton collisions conserved a non-negligible cross section. Hence, even using the dedicated γp cuts, the proton-proton events still contribute to $\sim 54\%$ of the total remaining backgrounds. Based on the estimations for 10 fb^{-1} , the signal to background ratio is found to be $48.7/47.2 = 1.03$ for the semi-leptonic Wt channel. For comparison, the ratio obtained in parton-induced interactions is estimated to be 0.18 [94], mostly due to the huge contamination by the $t\bar{t}$ process.

Finally, it is found that the *final cuts* are not totally uncorrelated to the photon-related selection criteria, most probably due to the H_T selection. As an example, the final visible cross section obtained by multiplying the $\epsilon_{\gamma p \text{ cuts}}$ and $\epsilon_{\text{final cuts}}$ efficiencies is 0.89 fb for $pp \rightarrow Wjjj$ events while an effective cross section of 0.75 fb is obtained by applying cuts in series. These values have been

σ [fb]	signal	$t\bar{t}$		$Wjjj$		$Wb\bar{b}q'$		t +jet	
		γp	pp	γp	pp	γp	pp	pp	
Production		440.6	830.8	405×10^3	2.8×10^3	326×10^4	55.2	267×10^3	67×10^3
Topo. cuts	$p_T^{lept} > 20 \text{ GeV}/c$	195.9	376.7	171×10^3	1.2×10^3	129×10^4	24.8	94.7×10^3	30.0×10^3
	$p_T^{jet} > 30 \text{ GeV}/c$	35.9	91.4	31.5×10^3	64.7	72×10^3	4.3	4.6×10^3	1.3×10^3
γp cuts		25.8	46.9	33.0	46.6	190.8	3.1	5.8	2.0
Final cuts	$N_{bjet} = 1$	10.3	20.6	14.7	3.1	8.8	1.4	2.4	0.8
	$ m_{jj} - m_W < 20 \text{ GeV}/c^2$	7.3	4.3	2.7	0.7	1.5	0.2	0.4	0.1
	$H_T < 230 \text{ GeV}/c$	4.9	1.7	1.1	0.4	1.1	< 0.1	0.2	< 0.1
Yields for 10 fb^{-1}		48.7	17.3	11.5	3.7	11.1	0.7	2.2	0.7

Table 4.6: Summary of effective cross sections at each stage of the analysis for the semi-leptonic $pp(\gamma p \rightarrow Wt)pY$ events and their relevant photon-induced and proton-induced backgrounds. All values are in femptobarn except that of the last row which gives the expected number of events for 10 fb^{-1} . The selection procedure to separate γp events from the huge pp ones is usable during the phase of instantaneous very low luminosity $\mathcal{L} < 10^{32} \text{ cm}^{-2} \text{ s}^{-1}$.

calculated by applying all cuts except the b -tagging criteria in order to conserve enough statistics, the reduction by the b -tagging criterion being applied through a reduction factor of 21.7. Nevertheless, because the obtained effective cross sections for the backgrounds are over-estimated compared to the ones established without applying any selection cut factorisation, the results presented in Table 4.17 obtained by making use of the factorisation procedure are conservative.

4.3.3 Signal discrimination of di-leptonic events

In addition to the semi-leptonic topology presented hereabove, a second study designed to isolate Wt signal events in which the two W bosons decay into leptons has been performed. Because the final state results in a very clean signature composed of two charged leptons with high transverse momentum, one b -jet and the presence of large missing transverse energy (E_T^{miss}), this topology is not expected to suffer from large irreducible backgrounds. In particular, the rejection of the irreducible $t\bar{t}$ background will rely on a robust jet counting. The selection procedure scheme used to increase the ratio of Wt signal to background events proceeds in a similar way as in Section 4.3.2.

Topological cuts

The selection procedure for di-leptonic single-top events starts by requiring the presence of exactly two isolated leptons (muons or/and electrons) with a transverse momentum higher than 20 GeV/ c . The lepton requirement is further constrained by exploiting the information that the two initial W bosons that decay leptonically have opposite charges. Even if the present analysis only focuses on backgrounds that contain two real leptons, samples possessing only one lepton can eventually constitute non-negligible sources of signal-like signature when an extra lepton is faked. Nevertheless, because fake leptons are not simulated in DELPHES and since the isolation of the leptons prevent this effect to be dramatic, the impact of such probable source of backgrounds will not be discussed further.

Figure 4.13 shows that the lepton pair of the Zj background finds its origin in the Z boson decay as a sharp Z mass peak is visible for these events in the invariant mass distribution of the two lepton candidates. Eventually, if future analyses establish a non-negligible contribution of the Zj events, we can use this information to suppress this backgrounds by applying a cut window around the Z mass value.

Figure 4.14 shows the number of reconstructed jets in an event for the signal and each of its main photon-induced backgrounds. As expected from the final states, the $t\bar{t}$ events usually contain more jets with $p_T > 30$ GeV/ c : at leading order the signal would be expected to have one final state parton,

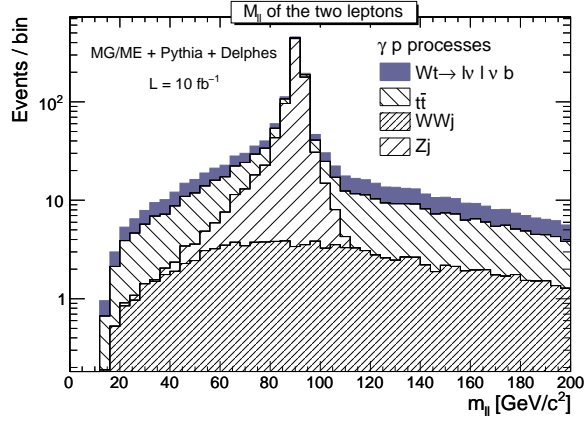


Figure 4.13: Cumulative distribution of the invariant mass of the two lepton candidates indicating that the cut window may remove Zj events. The normalisation corresponds to 10 fb^{-1} .

while $t\bar{t}$ events would have two. Therefore, we can substantially reduce the $t\bar{t}$ background by vetoing events with more than one jet with $p_T > 30 \text{ GeV}/c$ and $|\eta| < 2.5$. This cut preserves 69% of the signal events and rejects $\sim 70\%$ of the $\gamma p \rightarrow t\bar{t}$ processes. For parton-induced top pair production, the fraction of events satisfying this condition decreases down to 25%.

Final cuts

An event is selected if the jet candidate is found to be tagged as a b -jet, justifying the requirement that the jet must be within the tracker coverage. If the dominant $t\bar{t}$ background cannot be suppressed with the b -tagging requirement due to the presence of two true b -quarks, the WWq' and Zj processes only contain light flavoured jets in the final states and are therefore drastically decreased. Indeed, although the contribution of the WWq' background is very important for single jet events with no b -tagging, it is otherwise almost completely negligible since only 6.3% of the events are fulfilling the b -tagging requirement via a b -mistag of the light jet. This procedure would therefore benefit from a robust ability of the experiment to efficiently label true b -quark while keeping a reasonable mistagging rate.

Finally, a cut exploiting the energy unbalance in the transverse plane is applied. The rejection power of a $E_T^{\text{miss}} > 20 \text{ GeV}/c$ cut is illustrated in Figure 4.15 where the distribution of the missing transverse energy (E_T^{miss}) is shown for the signal and the photon-induced backgrounds. The DELPHES

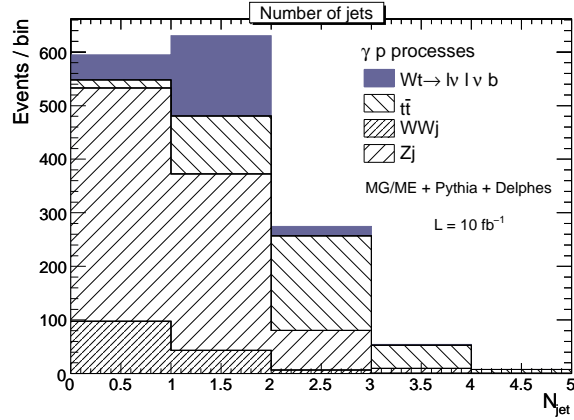


Figure 4.14: Cumulative distribution of the number of reconstructed central ($|\eta| < 2.5$) jets with $p_T > 30$ GeV/c after the cut on the lepton. Jets are reconstructed using the Midpoint cone algorithm with a cone size of 0.7. The normalisation corresponds to 10 fb^{-1} .

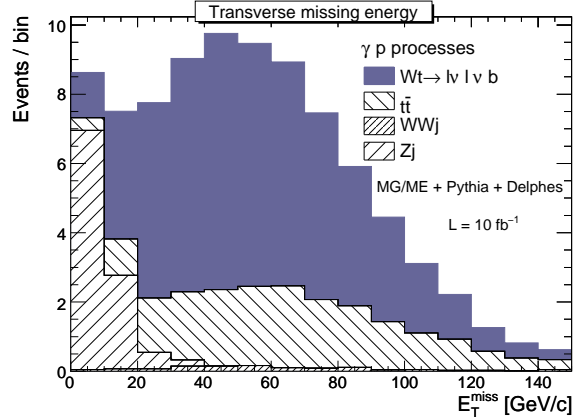


Figure 4.15: Cumulative distribution of the missing transverse energy, after the cut on the lepton, the jet, the rapidity gap selection, the exclusivity condition and the b -tagging requirement. The normalization corresponds to 10 fb^{-1} .

E_T^{miss} , defined by projecting the energy contributions of all calorimeters into the transverse plane, is corrected by the transverse momentum of the muons present in the event. In addition to the rejection factor of 94% against Zj events due to the unexpected presence of missing transverse energy, this extra cut should also significantly reduce $WZq' \rightarrow jj\ell^+\ell^-q'$ events which can fake

the di-leptonic single-top topology when one jet escapes from the detection.

Summary of selection cuts

The visible cross sections at each stage of the selection procedure are summarised in Table 4.7 for the signal and all considered backgrounds. The values are obtained, using the special treatment presented at the beginning of the section, by multiplying the respective efficiencies by the production cross sections. The expected final event yields, scaled to an integrated luminosity of 10 fb^{-1} are provided in the last row.

Table 4.7: Effect of various cuts on the cross section of the di-leptonic topology for photon-induced and parton-induced backgrounds for very low luminosity $\mathcal{L} < 10^{32} \text{ cm}^{-2} \text{ s}^{-1}$.

σ [fb]		signal	$t\bar{t}$		WWq'		Zj
			γp	pp	γp	pp	γp
Production		104.3	159.1	77×10^3	62.5	5×10^3	287.3
Topo. cuts	$N_{lept} = 2$	21.6	35.1	14.2×10^3	14.8	970.9	84.9
	$N_{jet} = 1$	15.0	10.8	3.6×10^3	4.3	463.0	34.1
γp cuts		13.7	5.2	3.0	4.1	0.7	21.7
Final cuts	$N_{bjet} = 1$	5.6	2.1	1.2	0.1	0.2	1.0
	E_T^{miss}	5.1	1.9	1.1	0.1	0.2	< 0.1
Yields for 10 fb^{-1}		51.1	19.4	10.9	1.2	1.5	0.6

After the application of the leptonic and the jet requirements, the selected sample is largely dominated by the parton-parton processes, motivating therefore the use of the γp cuts. After their applications, the $pp \rightarrow X$ yields are drastically reduced becoming even smaller than the corresponding photon-induced events. Except the dominating $t\bar{t}$ backgrounds, the $\gamma p \rightarrow Zj$ and $\gamma p \rightarrow WWq'$ are significantly reduced by the use of b -tagging. The E_T^{miss} cut rejects mostly Zj events; if this cut is not used this background contamination would represent 23% of the total background. Finally it can be seen that, as expected by the similar final state, the residual dominant background is $t\bar{t}$. Although the identical relative efficiencies compared to the signal ones for most of the selection cuts, thanks to the jet veto and the exclusivity condition, the $\sigma_{Wt}/\sigma_{t\bar{t}}$ ratio is enhanced: starting from 0.65 at production it increases slowly up to 2.6. Finally, after 10 fb^{-1} of data taking, the estimated amount of signal events that pass the whole selection is $51 \pm 7(\text{stat})$ events. While the backgrounds are efficiently suppressed, as their total estimated yield is only 33.6 events, the

final signal over background ratio is 1.5, mainly due to the remaining contamination of top quark pairs

4.3.4 Event selection for higher luminosities

At collider machines such as the LHC, the luminosity is fully characterised by the following equation:

$$\mathcal{L} = \frac{f_{LHC} \gamma k_b N_p^2 F}{4\pi \varepsilon_b \beta^*}, \quad (4.2)$$

where $f_{LHC} = 11245$ Hz is the revolution frequency, γ is the relativistic Lorentz factor, k_b is the number of bunches per beam, N_p is the number of protons per bunch, F is the geometric luminosity reduction factor due to the crossing angle at the interaction point, ε_b is the normalised transverse beam emittance and β^* is the lateral extension of the beam at the IP, named the *betatron function*.

Since the luminosity only depends on the beam parameters, the bunch structure of the beam plays a decisive role in the obtained value of the luminosity. At the LHC, the minimal time between successive bunch injection is limited to 25 ns that translates into a filling scheme containing 3564 bunches per ring. Nevertheless, due to practical considerations the most dense set-up foreseen at the LHC will consist of a pattern of 2808 particle bunches per ring. During the first months, the LHC luminosity will increase from its initial operation value of $\mathcal{L} < 10^{27} \text{ cm}^{-2} \text{ s}^{-1}$ until it reaches the nominal luminosity of $\mathcal{L} = 2 \times 10^{34} \text{ cm}^{-2} \text{ s}^{-1}$, referred in the following as the *high luminosity*. During this increase the 1×1 , 43×43 , 156×156 , 936×936 crossing patterns are also planned. Finally, keeping the bunch pattern fixed, the luminosity can be modified by adapting the particle density and the betatron function allowing to significantly reduce the pile-up events in some configuration. The number of average interactions per bunch crossing ($\langle N_c \rangle$) estimated using the following equation

$$\langle N_c \rangle = \frac{\mathcal{L} \sigma}{f_{LHC} k_b}. \quad (4.3)$$

is shown for some luminosity conditions in Table 4.8, $\sigma = 80$ mb.

Results presented in Section 4.3.2 and 4.3.3 require a very clean environment where on average only one interaction happens during the same bunch crossing. As can be seen by looking at Table 4.8, these analyses may only be performed during the very low luminosity phase of the LHC ($\mathcal{L} \ll 10^{32} \text{ cm}^{-2} \text{ s}^{-1}$). Nevertheless, the data collected at this very low luminosity phase will represent a small fraction of the large number of collisions that will be stored by the experiments. The total integrated LHC luminosity for such no-pileup conditions cannot be precisely estimated but 1 fb^{-1} seems to be a realistic assumption. The previous analyses must be updated to the cases where the pile-up is becoming non-negligible since

Table 4.8: Average number of interactions per bunch crossing for various luminosity scenarios [95]. Each scenario is detailed in terms of the number of colliding bunches k_b , the number of protons per bunch N_p and the value of the betatron oscillation at the IP β^* .

$k_b \times k_b$	β^* [m]	N_p	\mathcal{L} [$\text{cm}^{-2}\text{s}^{-1}$]	$\langle N_c \rangle$
43×43	9	3×10^{10}	5.5×10^{29}	0.09
43×43	4	3×10^{10}	1.2×10^{30}	0.2
156×156	4	9×10^{10}	5.6×10^{31}	2.6
156×156	2	9×10^{10}	1.1×10^{32}	5.0
2808×2808	2	4×10^{10}	3.4×10^{32}	0.86
2808×2808	2	6×10^{10}	7.6×10^{32}	1.9
2808×2808	0.55	6×10^{10}	2.8×10^{33}	7.1
2808×2808	0.55	1.15×10^{11}	1.0×10^{34}	25.3

approximately 10 fb^{-1} of integrated luminosity are expected to be collected each year at the LHC when the crossings of proton will be accomplished at the $\mathcal{L} = 2 \times 10^{33} \text{ cm}^{-2} \text{ s}^{-1}$ luminosity.

As already emphasised in Section 2.3.4, at such low luminosity, the LRG technique cannot be used anymore. The major challenge is therefore to obtain a procedure to properly extract the photon-induced processes from the proton-proton interactions. Indeed, the exclusivity condition alone cannot reduce partonic backgrounds to a level that allows proper signal extraction: 71% of $\gamma p \rightarrow Wjjj$ are accepted by this condition while the reduction factor of $pp \rightarrow Wjjj$ events is only 20. In that case, in addition to the exclusivity condition, the use of very forward detectors to detect the escaping proton is mandatory.

A forecast of the rejection factor of VFDS can be obtained by estimating the efficiency for a single diffractive event event to be tagged by VFDS and the average number of SD events occurring at each bunch crossing. Finally, by combining these two predictions, one can obtain the rejection power of VFDS due to such accidental coincidence. The tagging efficiency has been computed using HECTOR_1.5.2 [42] within DELPHES for three different scenarios: the presence of two proton detector stations located on both sides of the IP at 220 m or 420 m of the central detector, and the tagging capability of the combination of the four stations. The obtained results are summarised in Table 4.9.

Similarly to the number of collisions occurring at each bunch crossing, an estimate of the average number of total SD events per bunch crossing can be obtained using Equation 4.3 with a cross section of 14.4 mb, predicted by

Table 4.9: Single diffractive event tagging efficiencies for different detector scenarios. The presence of two proton detectors located at 220 m or 420 m of the central detector on both sides, and the tagging capability of the combination of the four tagging stations. The results have been obtained using HECTOR in DELPHES.

Running scenario	220 m only		420 m only		220 m + 420 m
	Left	Right	Left	Right	
SD events	8.8%	8.9%	6.0%	4.7%	28.4%

PYTHIA 8.125 [76]. The obtained values are summarised in Table 4.10 for three benchmark luminosity scenarios.

Table 4.10: Average number of single diffractive events per bunch crossing for various luminosity scenarios [95]. Each scenario is detailed in terms of the number colliding bunches k_b , the number of protons per bunch N_p and the value of the betatron oscillation at the IP β^* .

$k_b \times k_b$	β^* [m]	N_p	\mathcal{L} [$\text{cm}^{-2}\text{s}^{-1}$]	$\langle N_{sd} \rangle$
156×156	2	9×10^{10}	1.1×10^{32}	0.90
2808×2808	0.55	6×10^{10}	2.8×10^{33}	1.28
2808×2808	0.55	1.15×10^{11}	1.0×10^{34}	4.56

The Poisson distribution can be taken to estimate the probability of having exactly n considered diffractive events (SD and/or DPE) per beam bunch crossing. It is therefore straightforward to obtain the number of protons that will be simultaneously tagged by the VFD (Y) since the probability of having at least one tagged proton is given by:

$$P(Y \geq 1) = 1 - P(Y = 0) \quad (4.4)$$

where the probability of having no forward proton detected is given by

$$P(Y = 0) = e^{-\langle N_{sd} \rangle p} \sum_{n=0}^{\infty} \frac{(\langle N_{sd} \rangle (1-p))^n e^{\langle N_{sd} \rangle (1-p)}}{n!}, \quad (4.5)$$

where p is the probability for the considered diffractive event to yield a hit in the VFD. Using the definition of the Poisson distribution, the last Equation can be rewritten as

$$P(Y = 0) = e^{-\langle N_d \rangle p} \sum_{n=0}^{\infty} P_{\langle N_d \rangle (1-p)}(n) = e^{-\langle N_d \rangle p}. \quad (4.6)$$

A similar calculation leads to the probability that exactly one diffractive event per bunch crossing is tagged in the very forward detectors:

$$P(Y = 1) = \langle N_d \rangle p e^{-\langle N_d \rangle p}. \quad (4.7)$$

The entire above development is valid for the tagging efficiency in a very forward detector located at one side of the central detector. Nevertheless, since the tagging stations are located on both side of CMS, and that several processes can cause a hit in the VFD, the probability to get at least one or exactly one proton tag in the very forward detectors might be determined. Using simple probability rules, this leads respectively to the following equations:

$$\begin{aligned} P_{2 \text{ sides}}(Y \geq 1) &= 1 - \prod_{i,j} e^{-\langle N_d \rangle_j p_i^j} = 1 - \left[e^{-\sum_{i,j} \langle N_d \rangle_j p_i^j} \right], \\ P_{2 \text{ sides}}(Y = 1) &= \left[\sum_{i,j} \langle N_d \rangle_j p_i^j \right] \left[e^{-\sum_{i,j} \langle N_d \rangle_j p_i^j} \right], \end{aligned} \quad (4.8)$$

where the sum over i is related to the number of detectors to be taken into account in the various tagging scenarios, and the index j corresponds to the number of considered diffractive processes. Nevertheless, since the DPE process has a production cross section of 1 mb, the contribution from this process is neglected in the rest of this Chapter. The related rejection factors, simply given by $R = 1/P_{2 \text{ sides}}$, for different tagging configurations and considered diffractive processes are summarised in Table 4.11. The values have been obtained for a luminosity of $\mathcal{L} = 2 \times 10^{33} \text{ cm}^{-2} \text{ s}^{-1}$ and a 2808×2808 crossing pattern.

Table 4.11: Rejection factors due to single diffractive events, given by $R = 1/P_{2 \text{ sides}}$, for different tagging configurations. The values have been obtained for a luminosity of $\mathcal{L} = 2 \times 10^{33} \text{ cm}^{-2} \text{ s}^{-1}$ and a 2808×2808 crossing pattern. The very forward detectors are placed at 220 m and 420 m from the IP. The different tagging efficiencies for beam 1 and beam 2 have been taken into account.

Running scenario	220 m only		420 m only		220 m + 420 m	
	$Y \geq 1$	$Y = 1$	$Y \geq 1$	$Y = 1$	$Y \geq 1$	$Y = 1$
$\mathcal{L} = 1 \times 10^{33} \text{ cm}^{-2} \text{ s}^{-1}$	12.9	13.4	20.3	21.6	8.2	8.8
$\mathcal{L} = 2 \times 10^{33} \text{ cm}^{-2} \text{ s}^{-1}$	6.7	7.3	10.8	11.3	4.4	5.0

Requiring exactly one proton tag in the very forward detector possesses a major drawback. Indeed, if it allows to reject more parton-parton backgrounds, the global gain is not significant. For low luminosities, the difference between the $Y \geq 1$ and $Y = 1$ is even negligible. As an example, for a luminosity of $2 \times 10^{33} \text{ cm}^{-2} \text{ s}^{-1}$, the rejection factor increases from 6.7 to 7.3 when only the forward detectors at 220 m are present. Moreover, beside the small improvement of the rejection factor, the number of photon-induced events are

also dramatically affected, especially at high luminosity since the it is mandatory that diffractive events cannot leave a tag in the VFD. The evolution of all these reduction factors is depicted in Figure 4.16 for two scenarios of bunch fillings: 936×936 and 2808×2808 . The dramatic rising of the rejection factor as a function of the luminosity increase is clearly visible.

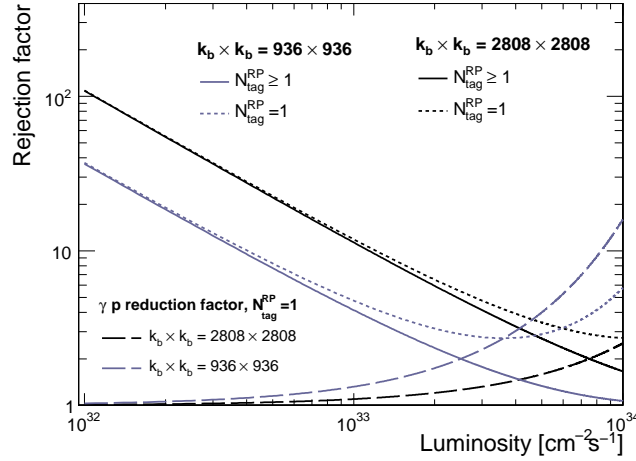


Figure 4.16: Rejection power of parton-parton backgrounds as a function of the instantaneous luminosity for two different bunch-crossing rates scenarios. This factor can directly be applied to the cross section in order to get its contribution after the requirement of at least one VFD hit. The graphs have been obtained by considering a configuration where only the detectors at 220 m from the IP are present taking into account the coincidence induced by both the single diffractive events.

Summary of selection cuts and results after 10 fb^{-1}

Keeping the application of the γp cuts aside, the two other steps of the selection procedure (*topological cuts* and *final cuts*) are similar to those applied during the very low luminosity phase since all the aforementioned detailed justification of the cuts remains valid. Concerning the γp cuts, the rapidity gap selection has been replaced by the probability of tagging a forward proton in the event while the exclusivity remains unchanged. Since very forward detectors located at 420 m from the IP are not expected to be present for early LHC runs and that moreover $\sim 56\%$ of the $pp(\gamma p \rightarrow Wt \rightarrow \ell v j j b)pY$ signal events are leaving a hit in the VFD located at 220 m although only 7% are tagged by the 420 m, the detector scenario that has been chosen only contains the VFD at 220 m on both sides of the central detector. Moreover, since no

kinematic constraint on the central detector measurement that would use the proton energy measurement will be performed the selection procedure only requires at least one hit in the very forward detectors. The visible cross section at each step of the selection procedure as well as the expected yields for 10 fb^{-1} of integrated luminosity are given on Tables 4.12 and 4.13 for the di-leptonic and semi-leptonic topologies respectively. The rejection factor has been computed to be 6.7 for $\mathcal{L} = 2 \times 10^{33} \text{ cm}^{-2} \text{ s}^{-1}$ and $k_b \times k_b = 2808 \times 2808$.

Table 4.12: Effect of various cuts on the cross section of the di-leptonic topology for photon-induced and parton-induced backgrounds for low luminosity $\mathcal{L} = 2 \times 10^{33} \text{ cm}^{-2} \text{ s}^{-1}$.

σ [fb]	signal	$t\bar{t}$		WWq'		Zj	
		γp	pp	γp	pp	γp	
Production	104.3	159.1	77×10^3	62.5	5×10^3	264.9	
Topo. cuts	$N_{lept} = 2$	21.6	35.1	14.2×10^3	14.8	970.9	84.9
	$N_{jet} = 1$	15.0	10.8	3.6×10^3	4.3	463.0	34.1
γp cuts		10.2	3.8	30.4	2.9	5.5	10.0
Final cuts	$N_{bjet} = 1$	4.2	1.5	12.0	0.1	1.3	0.5
	E_T^{miss}	3.8	1.4	11.1	< 0.1	1.3	< 0.1
Yields for 30 fb^{-1}		114.2	42.7	332.9	2.7	37.7	0.8

The final signal on background ratios are both 0.27 for both the di-leptonic and the semi-leptonic topologies, mainly due to the proton-proton backgrounds. Indeed, after the entire selection procedure, the sample is still dominated by parton-induced backgrounds despite the use of VFD tagging and exclusivity condition. Indeed, in comparison to the very low luminosity phase, the contribution of proton-proton backgrounds to the total remaining background rises from 54% to 88% in the semi-leptonic topology while the increase is dramatic for di-leptonic topology: from 37% up to 89%. This may motivate the application of additional photon-related selection cuts by exploiting the *asymmetry* of the energy in the two forward detectors:

$$Asym = \frac{|E_+^{FCAL} - E_-^{FCAL}|}{E_+^{FCAL} + E_-^{FCAL}}, \quad (4.9)$$

where $E_{+,-}^{FCAL}$ represent respectively the energy measured in the positive and negative forward central detector hemisphere. Nevertheless, a proper simulation of the pile-up as well as a more precise modelling of the forward detector response would be mandatory.

σ [fb]		signal	$t\bar{t}$		$Wjjj$		$Wb\bar{b}q'$		t +jet
			γp	pp	γp	pp	γp	pp	pp
Production		440.6	830.8	405×10^3	2.8×10^3	326×10^4	55.2	267×10^3	67×10^3
Topo. cuts	$p_T^{lept} > 20 \text{ GeV}/c$	195.9	376.8	171×10^3	1.2×10^3	129×10^4	24.8	94.7×10^3	30.0×10^3
	$p_T^{jet} > 30 \text{ GeV}/c$	35.9	91.4	31.5×10^3	64.7	96×10^3	4.3	4.6×10^3	1.3×10^3
γp cuts		27.3	50.4	298.0	47.4	586.4	3.3	53.8	19.3
Final cuts	$N_{bjet} = 1$	10.9	22.1	132.6	3.1	27.0	1.5	22.5	7.8
	$ m_{jj} - m_W < 20 \text{ GeV}$	7.7	4.6	24.7	0.7	4.0	0.2	3.3	1.1
	$H_T < 230 \text{ GeV}/c$	5.2	1.9	10.3	0.4	3.7	< 0.1	2.1	0.7
Yields for 30 fb^{-1}		154.5	55.7	310.0	11.2	110.8	2.1	62.8	21.4

Table 4.13: Summary of effective cross sections at each stage of the analysis for the $\gamma p \rightarrow Wt \rightarrow \ell\nu jjb$ events and their relevant photon-induced and proton-induced backgrounds. All values are in fb except that of the last row which gives the expected number of events for 30 fb^{-1} . The selection procedure to separate γp events from the huge pp ones is usable during the phase of instantaneous low luminosity $\mathcal{L} = 2 \times 10^{33} \text{ cm}^{-2} \text{ s}^{-1}$.

Finally, while results presented in Tables 4.12 and 4.13 have been obtained using the following benchmark point, a 2808×2808 crossing pattern and a luminosity of $\mathcal{L} = 2 \times 10^{33} \text{ cm}^{-2}\text{s}^{-1}$, it is straightforward to predict the relative expected yields for $\mathcal{L} = 1 \times 10^{33} \text{ cm}^{-2}\text{s}^{-1}$: while the number of photon-induced events remains similar, the final number of parton-induced backgrounds is obtain by reweighing the above yields by 0.56. For such a luminosity the values of the signal on background ratios are 0.45 for both the semi-leptonic and the di-leptonic topologies.

4.4 Cross section and $|V_{tb}|$ measurements

In order to obtain an estimate of the V_{tb} matrix element, we first need to derive from the signal-enriched sample the expected accuracies on the production cross sections that can be reached in the two studied topologies. The high statistics expected to be obtained at the LHC for photon-induced single-top production allows to simply measure the production cross section using a counting experiment. During the early stages of the LHC, not relying on Monte Carlo distributions is a significant advantage since these simulations may not have been fully validated or corrected with data.

The Wt cross section can be estimated from the total number of events (N) that survived to all criteria for the selection of a single-top signature, with:

$$\sigma = \frac{S}{\varepsilon \times L} = \frac{N - B}{\varepsilon \times L}, \quad (4.10)$$

where S is the number of signal events, calculated by subtracting from N the expected number of background events B , L is the integrated luminosity and ε the estimated signal selection efficiency calculated as the product of the γp and the final cut efficiencies. The total number of background events is estimated from Monte Carlo simulations using

$$B = \sum_i B_i = \sum_i \varepsilon_i \sigma_i L. \quad (4.11)$$

The relative error on the measured cross section is therefore given by a straightforward derivation of the uncertainties that yields the following formula:

$$\frac{\Delta\sigma_{obs}}{\sigma} = \frac{\Delta\varepsilon}{\varepsilon} \oplus \frac{\Delta L}{L} \oplus \left[\frac{B}{S} \right] \frac{\Delta B}{B} \oplus \left[\frac{B}{S} + 1 \right] \frac{\Delta N}{N}, \quad (4.12)$$

where $\Delta\varepsilon$ and ΔB are the systematic error estimates on the signal selection efficiency and on the predicted number of background events respectively. The systematic uncertainty on the cross section due to the luminosity determination, is factorised and mentioned as the separate ΔL uncertainty. Additionally, the statistical error on the number of selected events ΔN should be accounted for: assuming that N is Poisson distributed, the uncertainty on this number becomes \sqrt{N} .

4.4.1 Systematic uncertainties

Significant sources of systematic uncertainties affect the measurement of the cross section. Neglecting the error inherent from the factorisation of the γp cuts, the following most relevant systematics of instrumental origin have been investigated: luminosity, Jet Energy Scale (JES), b -tagging efficiency, the impact of the track reconstruction efficiency on the exclusivity condition and the effect of an incorrect measurement of the energy in the forward calorimeters. Moreover, the errors due to the theoretical calculation of background cross sections are also taken into account. In the following subsections, a description of the procedure used to determine each of the contributions to the total systematic uncertainty is given.

Luminosity

Due to its direct contribution to the total uncertainty of the production cross section, the absolute luminosity determination is crucial for precision measurements. Since the expected signal and background yields have been given for an integrated luminosity of 10 fb^{-1} , an overall luminosity uncertainty of 5% [67] has been assumed, which corresponds to the luminosity accuracy that may be achieved after 1 fb^{-1} of collected data by CMS.

Theoretical uncertainty

Since photon-induced processes represent a significant fraction of the final background sample, their theoretical uncertainties may greatly affect the measurement of the single-top cross section. Because at the time of writing, no theoretical predictions of the photon-induced cross sections exist in the literature, the same uncertainty as for the corresponding partonic process are taken. Because the cross section of photon-induced processes is less sensitive to e.g. the choice of the parton density functions, using the existing errors for pp events therefore represent pessimistic estimations of these theoretical uncertainties. The theoretical errors to the background events are then assumed to be 5% for $t\bar{t}$ [96], 17% for $Wb\bar{b}j$ and $Wjjj$, and 6% for WWj [97].

After cuts, an uncertainty of 2% is supposed to be reachable for partonic cross sections. Indeed, when data are available, the normalisation of the parton-parton backgrounds will be extracted by applying all the selection procedure except the γp cuts. Obtaining correct normalisation for these backgrounds from the data is therefore essential, since during the phase of very low luminosity, $\sim 24\%$ of the remaining background arises from $pp \rightarrow W + \text{jets}$. Such uncertainties produce 3.0% and 2.1% systematic errors on the cross section for the di-leptonic and the semi-leptonic channels, respectively.

Jet Energy Scale

Because the event selection of single-top events includes cuts on the transverse momentum of the leading jets, the effect of a systematic shift on the Jet Energy Scale (JES) needs to be investigated. In order to estimate the sensitivity of the analyses to this uncertainty, the selection chain is repeated while artificially rescaling up and down the energies of the jets by a factor α :

$$p_T^{scaled\pm} = (1 \pm \alpha)p_T^{meas}. \quad (4.13)$$

The resulting variation in the final visible cross section for each sample gives a measure of the systematic uncertainty due to the JES. Using the CMS estimations for the accuracies on the absolute jet energy scale, the shift factor is expected to be 5% for jets with $p_T < 30$ GeV/ c , 3% for jets with $p_T > 50$ GeV/ c and a linear interpolation between these two boundaries [67]. In the dileptonic topology, the uncertainty due to a miscalibration of the jet energies scale accounts for $\Delta B/B = 3.6\%$, while the contribution is larger for the semi-leptonic topology: $\Delta B/B = 12.6\%$. This higher value in the semi-leptonic topology can be explained by the presence of more hadronic activity compared to the di-leptonic topology as well as due to the veto on the number of jets with $p_T > 20$ GeV/ c used to separate the $t\bar{t}$ background from the signal.

Rapidity gap

In an analogue way as the measurement of the jet energies can be affected by a miscalibration of the detector, the energy measured to apply the E_{CUT}^{FCAL} can also be shifted. Due to the sharp increase of the E_{min}^{FCAL} distribution for proton-proton events this cut may therefore become a source of large uncertainty. Nevertheless, considering that a relative error on the measurement can presumably be reduced to a value of 10%, this uncertainty is manageable. In order to quantify the influence on the total systematic error, the cut on the energy in the forward calorimeter of the gap side is moved to 27 GeV and 33 GeV. Hence, if the effect is negligible for photon-induced events (at worst of the order of 1%), the uncertainty due to the proton-proton contribution is by far dominating ($\sim 20 - 30\%$) the other sources of systematic uncertainties.

Exclusivity condition

The second γp cut named “exclusivity condition” makes use of the ability of reconstructing a track with a transverse momentum as low as 500 MeV/ c which is a relevant source of possible systematic uncertainty. Indeed, because on average parton-induced processes have higher additional track multiplicities, a very poor reconstruction efficiency of the tracks will result in pp -like events to be considered as photon-like events. Conversely, a very efficient reconstruction of the tracks would reduce more reliably parton-induced events. In the

presented analyses, the systematic uncertainty due to the exclusivity condition is estimated by moving the track reconstruction efficiency, fixed to 90 % by default, to 85 % and 95 %. As an example, loosening the reconstruction efficiency in the di-leptonic topology, leads to an increase of the visible cross section of $pp \rightarrow t\bar{t}$ events of 8.1%.

***b*-tagging efficiency**

In the signal extraction procedure, the probability of identifying a jet as coming from a *b*-quark was set to 40% while the corresponding mistagging probabilities were supposed to be 10% and 1% for *c*-quark and other flavoured jets respectively. Because the CMS collaboration estimates that the achievable precision to measure the three hereabove efficiencies will be limited, the resulting uncertainty on the cross section should be estimated. In the present analyses, a relative error of 5% has been considered on the visible cross sections of events holding a real *b*-quark while a conservative 10% error was expected for samples that only contain light-jets. It turns out to be conservative since an exact value of 8.2% was obtained by a direct modification of the tagging and mistagging values for the $pp(\gamma p \rightarrow Wjjj)pY$ events.

4.4.2 Expected $|V_{tb}|$ measurement

Since the production cross section is directly related to the $|V_{tb}|$ matrix element term, once the uncertainty on the production cross section is known, the relative error on the CKM matrix element can directly be derived from the following formula:

$$\frac{\Delta|V_{tb}|}{|V_{tb}|} = \frac{1}{2} \left[\frac{\Delta\sigma_{obs.}}{\sigma} \oplus \frac{\Delta\sigma_{theo.}}{\sigma} \right], \quad (4.14)$$

where $\sigma_{obs.}$ is the absolute uncertainty on the cross section obtained by the counting experiment and $\sigma_{theo.}$ is the predicted theoretical error. Three hypotheses of luminosity, $\mathcal{L} < 10^{32} \text{ cm}^{-2} \text{ s}^{-1}$, $\mathcal{L} = 1 \times 10^{33} \text{ cm}^{-2} \text{ s}^{-1}$ and $\mathcal{L} = 2 \times 10^{33} \text{ cm}^{-2} \text{ s}^{-1}$ are considered, both using the 2808×2808 crossing pattern. The related considered integrated luminosities are respectively 10 fb^{-1} for the very low luminosity case and 30 fb^{-1} for the two considered low luminosity phases.

For all considered systematic sources, samples have been generated with the deviations from the default running scheme introduced in the previous paragraphs. As a conservative approach, for all variables that have been varied upwards and downwards, the biggest deviation of the cross section is used as an estimate of the corresponding relative error. For each of the considered systematics except the theoretical uncertainty, resulting errors in background yields are added for all background samples, since they are by definition fully correlated. The summed errors are then added quadratically.

Getting rid of the uncertainty on the rapidity gap, the same associated sources of uncertainties are considered during the low luminosity phases. Nevertheless, even if the use of very forward detectors can be the source of new possible systematic uncertainties, in the current analyses the loss of tagging efficiency due to the misalignment of an optical element of the beam line is considered as negligible. Moreover, since the energy of the proton that hit the detector is not used in the reconstruction, such a source of error is not relevant in the present analyses. As an example, the uncertainties obtained after 10 fb^{-1} of very low luminosity are summarised in Tables 4.14 and 4.15 for the di-leptonic and the semi-leptonic topologies.

Table 4.14: Systematic errors in % for the various sources of background for the di-leptonic topology during the very low luminosity phase, $\mathcal{L} < 10^{32} \text{ cm}^{-2} \text{ s}^{-1}$.

Process	signal	$t\bar{t}$		WWq'		Zj
		γp	pp	γp	pp	γp
JES	1.1	3.8	2.8	4.4	2.3	12.7
Rapidity gap	0.0	0.3	11.9	0.1	24.2	0.2
Exclusivity	0.3	1.4	8.1	0.2	6.9	1.1
b -tagging	5.0	5.0	5.0	10.0	10.0	10.0
Theoretical	6.0	5.0	2.0	6.0	2.0	5.0

Table 4.15: Systematic errors in % for the various sources of background for the semi-leptonic topology during the very low luminosity phase, $\mathcal{L} < 10^{32} \text{ cm}^{-2} \text{ s}^{-1}$.

Process	Signal	$t\bar{t}$		$Wjjj$		$Wbbq'$		tj
		γp	pp	γp	pp	γp	pp	pp
JES	6.4	15.1	20.1	10.0	2.0	12.5	2.0	11.1
Rapidity gap	0.3	0.0	19.9	0.2	21.0	0.0	21.4	33.3
Exclusivity	0.9	1.5	4.2	0.8	6.0	0.8	3.6	0.0
b -tagging	5.0	5.0	5.0	10.0	10.0	5.0	5.0	5.0
Theoretical	6.0	5.0	2.0	17.0	2.0	17.0	2.0	2.0

During the very low luminosity phase, the resulting combined systematic $\Delta B/B$ uncertainties are 9.6% and 18.7% for the di-leptonic and the semi-leptonic topologies respectively, mostly dominated by the Rapidity gap and b -tagging uncertainties. The total error on σ_{obs} and $|V_{tb}|$ obtained during the three luminosity scenarios for both topologies are shown in Table 4.16: the expected error on the measurement of $|V_{tb}|$ is 14.7% for the semi-leptonic channel and 10.9% for the di-leptonic one after 10 fb^{-1} of very low integrated

luminosity. After 10 fb^{-1} of integrated luminosity, the uncertainties on the $pp \rightarrow Wt$ cross section are 22.6 % for the di-leptonic and 19.2 % for the semi-leptonic Wt topologies [94]. A direct comparison of these results with the ones obtained in Table 4.16 allows to conclude that photoproduction is at least competitive with respect to partonic-based studies during the very low luminosity for the di-leptonic topology. Moreover, in this configuration, thanks to the very small B/S , the terms contributing mainly to the final cross section uncertainty are inverted: while the systematic term is dominating in the pp analysis, in the photon-induced di-leptonic topology, the major contribution arises from the statistical term. This lead to the possibility to achieve a complementary measurement of the $|V_{tb}|$ matrix element since its obtained value is sensible to different contributions.

Table 4.16: Summary of uncertainties of cross section measurement for 10 fb^{-1} of integrated luminosity for the semi-leptonic and the di-leptonic topologies during various luminosity phases.

Topology	$\mathcal{L} [\text{cm}^{-2}\text{s}^{-1}]$	$\frac{\Delta\epsilon}{\epsilon}$	$\frac{\Delta L}{L}$	$\left[\frac{B}{S}\right] \frac{\Delta B}{B}$	$\left[\frac{B}{S} + 1\right] \frac{\Delta N}{N}$	$\frac{\Delta\sigma_{obs}}{\sigma}$	$\frac{\Delta V_{tb} }{ V_{tb} }$
$Wt \rightarrow \ell\ell b$	$< 10^{32}$	7.1	5.0	6.4	18.0	21.2	10.9
	1×10^{33}	5.1	5.0	24.1	16.4	30.0	15.3
	2×10^{33}	5.1	5.0	43.6	20.2	48.6	24.5
$Wt \rightarrow \ell jjb$	$< 10^{32}$	8.2	5.0	18.3	20.2	28.9	14.7
	1×10^{33}	8.2	5.0	40.2	14.5	43.8	22.1
	2×10^{33}	8.2	5.0	68.9	17.5	71.7	36.0

Due to the larger B/S fraction of the semi-leptonic analysis of about 1.0, both the statistical and the systematic terms have a similar contribution to the final cross section uncertainty. In order to improve the total error in this topology, a more efficient rejection of parton-induced background should be reached. Nevertheless, the immediate price to pay is a reduction of the number of final signal events which is immediately related to an increase of the statistical term. It is worth mentioning that the effect of the enlarged background on signal ratio is dramatical during the phase of low luminosity. Indeed, the multiplying factor in front of the error on the predicted number of background events is 2.2 for the di-leptonic topology and 2.3 for the semi-leptonic topology during the $1 \times 10^{33} \text{ cm}^{-2} \text{ s}^{-1}$ luminosity hypothesis. It is even worse for the higher luminosity condition, reaching 3.6 and 3.7. Similarly, the statistical error on the number of selected events is greatly enhanced. Moreover, as expected, no gain due to an increase of the instantaneous luminosity is visible. On the contrary, the longest possible run of the LHC using a small pile-up configuration is the most favourable scenario to perform the presented analyses. Unfortunately, using the expected uncertainties summarised in Table 4.16 ob-

taining a competitive error on the $|V_{tb}|$ matrix element with the current existing selection chain seems hopeless at high luminosity.

Comments on b -tagging efficiencies

The choice of the b -tagging working point (b -tag WP) may be considered as pessimistic since a b -tagging efficiency of 60% may realistically be achievable in a high energy physics detector such as CMS. Nevertheless, the impact of the modification of this tagging efficiency on the results should be studied with care since a better b -tagging efficiency may imply also larger mistagging rates for c - and light jets. Table 4.4.2 summarises the expected event yields for the semi-leptonic topology after 10 fb^{-1} at very low luminosity. The numbers are obtained after the application of the entire selection procedure presented in Section 4.3.2 for two different b -tagging working points. The values used in this analysis (40%/10%/1% for b -tagging, c -mistagging and light jets misidentification, respectively) are compared with a working point with a larger tagging rate: 60% for b -jets, 15% for c -jets and 3% for light-jets.

signal	$t\bar{t}$		$Wjjj$		$Wb\bar{b}q'$		$t+\text{jet}$	
	γp	pp	γp	pp	γp	pp	pp	
Low efficiency b -tag (40/10/1)								
	48.7	17.3	11.5	3.7	11.1	0.7	2.2	0.7
High efficiency b -tag (60/15/3)								
	67.3	21.5	14.2	8.1	27.4	1.0	3.2	0.9

Table 4.17: Summary of the expected number of events for 10 fb^{-1} of integrated luminosity during the phase of very low luminosity for two b -tagging working points: the default values used in the analysis (40%/10%/1% for b -tagging, c -mistagging and light jets misidentification, respectively) and a working point with a larger tagging rate: 60% for b -jets, 15% for c -jets and 3% for light-jets.

The outcome is a lower signal-to-background ratio in the high tagging scenario. More specifically, the $pp \rightarrow Wjjj$ background increases from 11.1 to 27.4 selected events. This can be understood by the fact that $\sim 90\%$ of these events contain only light flavoured jets while the remaining 10% involves one c -jet. Consequently, in the high- b -tagging hypothesis, the uncertainty on $|V_{tb}|$ increases by 5.4% to reach 15.5%. This exercise shows that the purity of b -tagging jet algorithms is at least as important as its efficiency.

4.5 Conclusion and perspectives

Very optimistic results have been obtained for the Wt di-leptonic topology during the very low luminosity phase. Nevertheless, because the analyses used the fast simulation of a CMS-like detector, several experimental aspects were not considered in this study. In order to prepare this analysis for data-taking, a complete simulation of the CMS detector that takes into account the propagation of the particles through the detector and that simulates their interplay with the detector matter should be performed.

Last but not least, more elaborated treatments dedicated to reject pp backgrounds due to accidental coincidence as well as an improvement of the tagging of photon-induced procedure should be investigated to counter the dramatic effect of the presence of pile-up. Indeed, the results obtained by the present analyses for higher luminosities are pessimistic. Nevertheless, again a precise simulation of the CMS detector is mandatory to correctly reproduce the capability of the forward detectors to reconstruct accurately very low energies. The impact of the γp cuts should also be precisely investigated since they can suffer from the presence of fake tracks with low transverse momentum that could spoil the exclusivity condition. The effect of “dead” or “hot” calorimetric towers may also have an impact on the rejection of partonic backgrounds.

Wt PHOTOPRODUCTION IN CMS

After the results obtained in Chapter 4 showing the evident potential of the $pp(\gamma b \rightarrow Wt \rightarrow \ell\ell b)pY$ reaction to measure the $|V_{tb}|$ matrix element, this Chapter gives a comparison between the expected yields obtained with the DELPHES fast simulation and a more realistic simulation of the Compact Muon Solenoid using the official software CMSSW. The first part of the Chapter focuses on the description of the Compact Muon Solenoid experiment conducted at the Large Hadron Collider (LHC) while in the second part, identical selection procedures as those used in the DELPHES analysis are applied.

5.1 The Compact Muon Solenoid experiment

CMS is a general purpose experiment that has been assembled around one of the interaction points of the LHC. As its name suggests, the detector is characterised by a very compact design compared to the other multi-purpose detector ATLAS, which has almost eight times the CMS volume. Such a compactness is possible thanks to the high field strength of 3.8 T chosen for CMS. This very intense field is generated by the biggest superconducting magnet ever built: a 12.5 m long solenoid, with an inner diameter of 5.9 m, weighting 250 tons.

The detector is 21 m long and has a 15 m diameter for a total weight of 12,500 tons. As other general purpose detectors at colliders, CMS is composed of a multi-layered cylindrical structure coaxial with the beam direction (the *barrel region*) while a good hermiticity of the detector is achieved by enclosing the barrel by two additional disks (the *end-cap regions*) and forward detectors. An overview of the CMS central detector with the reference frame ¹ is shown

¹The coordinate frame in CMS is right-handed. The x -axis points toward the LHC centre, the y -axis vertical and upward, and the z -axis is parallel to the beam axis. The azimuthal angle in the

in Figure 5.1.

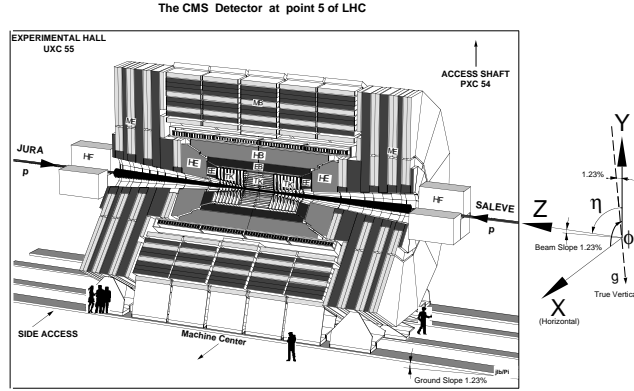


Figure 5.1: Overview of the CMS central detector, with subdetectors and reference frame [98].

The precise measurement of charged particle momentum, the track reconstruction and their association to primary and secondary vertices is ensured by a central tracker embedded into a strong magnetic field. Muon identification and measurement are performed using a muon system. Since the CMS detector was designed to elucidate the electroweak symmetry breaking mechanism, the detector contains an electromagnetic calorimeter with a very high segmentation and an excellent energy resolution in order to measure precisely a light Higgs boson ($m_H < 140 \text{ GeV}/c^2$) decaying into a photon pair. In addition, for heavier Higgs boson masses, CMS is optimised to measure very precisely muons in order to observe reactions such as $pp \rightarrow H \rightarrow ZZ \rightarrow \mu\mu\mu\mu$. Finally, the determination of the energy of neutral or charged particles interacting hadronically, and of the overall energy/momentum imbalance (missing transverse energy from weakly interacting particles escaping the detector) is performed by a hadronic calorimeter.

Tracking System

The tracking system is the closest layer of CMS to the interaction point, covering a pseudorapidity region from -2.5 to 2.5 . The role of the tracker is to provide a precise and efficient measurement of the trajectories of charged particles allowing to distinguish them from neutrals, to identify their charge and to measure their momentum from the track curvature. Moreover, the

plane transverse to the z axis is denoted ϕ , the polar angle θ is related to the z -axis and is used to calculate the pseudorapidity $\eta = -\ln \tan \frac{\theta}{2}$.

track reconstruction allows to find the position of the originating vertex of the particle, very useful for the identification of heavy flavour hadrons (jet flavour tagging) like b - and τ -jets.

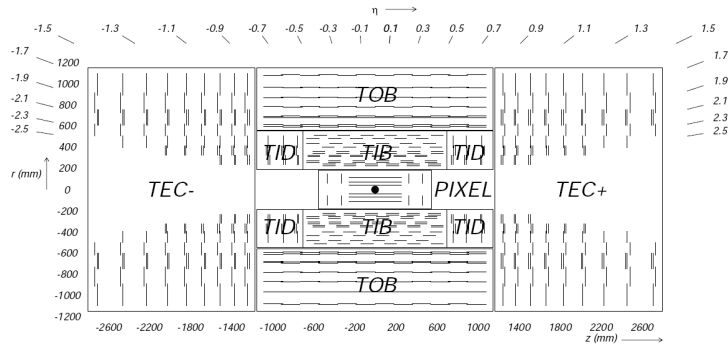


Figure 5.2: View of the tracker of the CMS experiment, in the $r - z$ plane [98].

The CMS tracker is fully based on silicon technology, with pixels and microstrip detectors totalising an active area of about 215 m^2 . In the inner part of the detector, three pixel layers are used for precise vertexing. The pixel tracker accounts for more than 60 millions of channels spread over about 1 m^2 . In order to fully reconstruct tracks, more than 15,000 microstrip sensors amounting for 9.6 million channels are surrounding the pixel detector. In the barrel, the silicon strip tracker is composed of the Tracker Inner Barrel (TIB) and the Tracker Outer Barrel (TOB) forming together ten cylindrical layers around the beam line at radii ranging from 25 to 108 cm. In the end-cap, the Tracker Inner Disk (TID) and the Tracker End Cap (TEC) consist respectively of three and nine concentric ring structures. A layout of the CMS tracker is shown in Figure 5.2: its outer radius extends up to 110 cm, for a length of 540 cm.

This tracker configuration allows to obtain a p_T resolution better than 1% for tracks with $p_T \leq 10 \text{ GeV}/c$ in the central region $|\eta| < 1$. The efficiency to reconstruct muons has been shown to be close to 100% in the full pseudorapidity range of the tracker while the efficiency for pions varies between 85% and 95%. Finally, using dedicated reconstruction algorithms, the p_T spectrum of charged particles can be reconstructed in the pixel detector only down to $0.5 \text{ GeV}/c$ with $\sim 85\%$ efficiency allowing to efficiently apply our exclusivity condition in the tracker.

Electromagnetic calorimeter

Surrounding the tracker, an hermetic electromagnetic calorimeter (ECAL) covers the pseudorapidity region between -3 and 3 . The calorimeter is compact enough to fit entirely inside the solenoid. The ECAL is made of lead tungstate (PbWO_4) scintillating crystals characterised by a high density (8.28 g/cm^3) or equivalently a short radiation length ($X_0 = 8.9 \text{ mm}$). Its small Molière radius (2.2 cm) ensures a good lateral confinement of the electromagnetic showers. Moreover, the decay time of the scintillation is short enough (10 ns) to collect most of the produced light within one bunch crossing time.

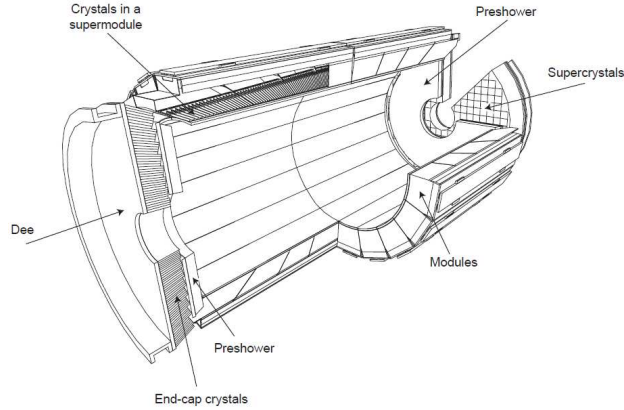


Figure 5.3: Layout of the electromagnetic calorimeter, including the barrel regions and the two end-caps. PbWO_4 crystals are arranged into supercrystals, modules and supermodules, with a quasi-projective alignment. Two lead-silicon preshowers are located in front of the end-caps, compensating for a broader granularity [98].

Similarly to the tracker, the ECAL is subdivided into a barrel ($|\eta| < 1.48$) and two endcaps ($1.48 < |\eta| < 3.0$), with a depth always larger than $24.7 X_0$. The segmentation is finer in the barrel ($\Delta\eta \times \Delta\phi = 0.0175 \times 0.0175$) than in the endcaps ($\Delta\eta \times \Delta\phi = 0.05 \times 0.05$), but this is compensated by the presence of a lead+silicon preshower in front of endcaps, allowing a better identification of neutral pions. Figure 5.3 shows how the 61,200 crystals are gathered into geometric sets, called *supercrystals*, *modules* and *supermodules* that assemble the complete ECAL. The final resolution of the ECAL is given by Equation 3.9 with the S , N and C values estimated as $0.05 \text{ GeV}^{1/2}$, 0.25 GeV and 0.0055 respectively.

Hadron Calorimeter

Surrounding the ECAL and the last layer enclosed within the magnet, the hadronic calorimeter (HCAL) completes the hermetic calorimetric coverage of the central CMS detector from -5 to 5 in pseudorapidity for the measurement of jets and missing transverse energy, in conjunction with the ECAL data. The hermiticity is provided by a depth of ~ 11 interaction lengths over the whole pseudorapidity range, and thanks to additional modules in the barrel region located behind the magnet coil (see Figure 5.4). The HCAL is subdivided into a barrel ($|\eta| < 1.3$) and two end-caps ($1.3 < |\eta| < 3.0$). It is complemented by two forward calorimeters ($3.0 < |\eta| < 5.0$), located outside the magnet at 11.2 m from the IP.

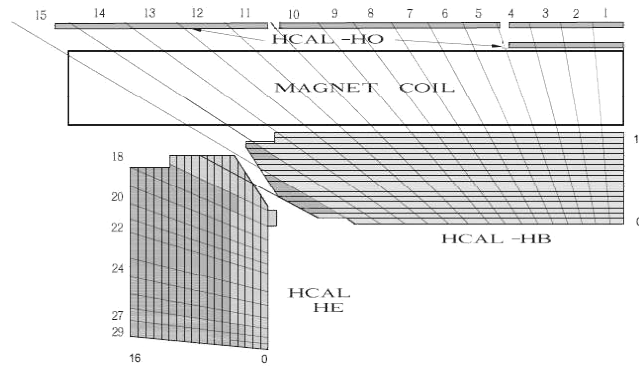


Figure 5.4: Longitudinal view of a quarter of the hadronic calorimeter [98].

The central hadron calorimeter ($|\eta| < 3$) is a sampling calorimeter using brass as absorber and plastic scintillators as active medium. This allows to reach 5 radiation lengths and up to 11 radiations lengths with the absorber layer placed just before the magnet. The layers of scintillator are organised into tiles providing a segmentation of 0.087×0.087 for $|\eta| < 1.6$ and $\sim 0.17 \times 0.17$ for $|\eta| \geq 1.6$. Moreover, the arrangement in tiles allows to avoid any detection crack nor projective dead areas.

Due to the strong radiation environment in the forward regions, the hadron forward calorimeters (HF) use plates of steel as absorber and bunches of quartz fibers as scintillator. One HF cap is a cylindrical structure composed of 18 wedges with a hole for the beam pipe. A wedge is made of 5 mm thick steel plates with grooves separated by 5 mm. These grooves, parallel to the beam line, are filled with $600 \mu\text{m}$ core-diameter quartz fibres. Two types of fibres alternate in grooves: *long fibres* referred in the text as HF (L) that run through the full length of the absorber and *short fibres* (HF (S)) that start 22 cm

deep from the front face of the calorimeter. The latter ones are therefore sensitive mostly to hadronic showers. The measured energy resolutions for electrons and pions are given respectively by [99]

$$\begin{aligned} \frac{\sigma}{E} &= \frac{1.98}{\sqrt{E}} \oplus 0.085 && \text{for electrons} \\ \frac{\sigma}{E} &= \frac{2.78}{\sqrt{E}} \oplus 0.120 && \text{for pions} \end{aligned} \quad (5.1)$$

Muon System

Muons are characterised by a relatively long lifetime and a large penetrating power inside material : if their p_T is greater than $0.9 \text{ GeV}/c$, they are able to cross the whole CMS detector, including the calorimeters, without being stopped. Consequently, the outermost layer of the CMS detector consists of a dedicated system for muon measurement (Figure 5.5). This composite system extends from -2.4 to 2.4 in pseudorapidity and is embedded within the magnet return yoke allowing in combination with data coming from the tracker to identify muons and to measure their charge and their kinematics.

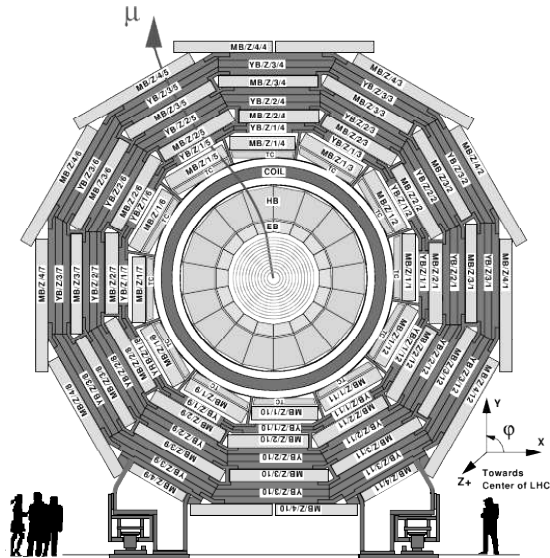


Figure 5.5: Transverse view of the CMS detector and layout of part of the muon system [98].

The muon chambers are based on three different technologies: Cathode Strip Chambers (CSC) in the barrel region ($|\eta| < 1.2$), where the magnetic

field is roughly uniform; Drift Tubes (DT) in the end-caps ($0.9 < |\eta| < 2.4$); and Resistive Plate Chambers (RPC) in both regions ($|\eta| < 1.6$). The 250 CSC's and 540 DT's provide an excellent spatial resolution, while a good timing measurement with a resolution of 1 ns is possible thanks to the 610 RPC's. These chambers altogether cover about 25,000 m². This muon system leads to a muon reconstruction efficiency above 90% for 100 GeV muons in the whole pseudorapidity range. The best resolution on the transverse momentum is obtained by combining information from both the tracker and the muon system: for 10 GeV/ c muons, the resolution ranges from 1% to 1.5%, depending on the pseudorapidity. At higher p_T the momentum resolution worsens since the curvature of the track is far more difficult to measure. It ranges from 6% to 17% [98].

The trigger system

Whereas the bunch crossing rate is 40 MHz, the CMS data acquisition system (DAQ) is designed to cope with an input rate of about 100 Hz, where each event accounts for about 1.5 MB of data. A very large reduction is consequently needed in the data flow. This selection is *online*, i.e. is performed along data taking, and is segmented into two stages, called the *Level One trigger* (L1) and the *High Level Trigger* (HLT).

The Level One trigger (L1) aims at reducing the data rate from 40 MHz to 100 kHz. During the first 3.2 μ s after a given bunch crossing, the coarse data from the calorimeters and the muon chambers is read-out, the decision to possibly store the event is taken and this decision is propagated back to the detector front-ends, where the raw data are stored and wait to be read-out or erased. This stage is evaluated by dedicated electronics, running fast algorithms on the output of the detectors. These algorithms are very constrained as it is not possible to do many operations, but only combinations of requirements typically on η and p_T of the four following quantities: e/γ , jets, muons, MET (i.e. energy sums). No difference is made between electrons, positrons and photons in L1 as the data from the tracker are missing. The Level One trigger is organised into calorimeter and muon triggers, subsequently combined into a global trigger that accepts or rejects the event.

Taking as an input the 100 kHz provided by the L1, the HLT has to reduce the data rate to 100 Hz. Contrary to L1, HLT decision is based on all the data from the detector, including the tracker. The algorithms for the HLT are processed on a farm of commercial CPUs, and thus are only constrained by the available resources (memory and processing time). The real-time selection is performed in about 1 s.

As the events which are not selected by the triggers are lost forever, a

great care has been put by the CMS experiment during the development of the different trigger menus. After selection by the triggers, the chosen events are presented to the storage unities where data will be prepared and processed in *offline* analyses.

5.2 The CMSSW framework

Although all the samples used in the di-leptonic $pp(\gamma b \rightarrow Wt)pY$ analysis are private production samples, all simulations rely on the official CMS software framework CMSSW². CMSSW is a C++/python framework composed of a collection of software with a modular architecture. Using the dedicated interface, the hadronisation of the MG/ME files used in Chapter 4 is realised within CMSSW using PYTHIA, followed by the simulation of the detector response. Firstly, the position of the event primary vertex located at the origin of the CMS coordinate system is smeared according to the expected distribution of the pp interaction positions bunch crossings. Secondly, the GEANT4 [65] toolkit is used to simulate the effects of energy loss, multiple scattering and showering of the generated particles in the detector materials. Finally, the so-called *digitization* step is performed that determines and digitises the hits in the various detection systems. It results in an output similar to the one expected from the real detector using real data.

While the chain described so far, referred to as the *full reconstruction chain* of the CMS detector, allows to obtain an accurate response of the detector, the analysis presented in this chapter is performed using the *fast simulation chain* of the CMS detector. In the fast simulation, the detector level quantities such as the hit positions in the tracker and the energy deposits in the calorimeters are described using parametrised functions aiming to reproduce the simulation of the detector effects using GEANT. Finally, the reconstructed quantities (RECO objects) such as vertices, tracks, electrons, muons or jets are created using exactly the same algorithms that will be used on real data.

5.2.1 Reconstruction of basic quantities

Electron candidates

Since an electron is characterised by an energy deposit in the electromagnetic calorimeter and a track pointing towards it, the electron reconstruction flow uses information from both the tracker and the electromagnetic calorimeter. Although the electromagnetic showers initiated by electrons deposit most

²Version 2.2.9

of their energy in a small number of crystals of the ECAL, due to the presence of the silicon layers of the tracker in front of the calorimeters and the strong magnetic field, the energy of the electron is significantly spread in the ϕ -direction because bremsstrahlung photons are radiated by the electron before reaching the ECAL. Since this effect can be large, when integrated along the entire electron trajectory, it is essential to collect them: the energy of the electron is recovered by using dedicated clustering algorithms [100] building a cluster of clusters, called *super-cluster*.

In order to differentiate electrons and photons, the obtained super-cluster may be compatible both in position and in the energy estimate with a reconstructed track. While the default reconstruction of tracks in CMS is based on the *Kalman-Filter* method [101], since electrons are affected by non-Gaussian fluctuations the dedicated *Gaussian Sum Filter* (GSF) approach is used instead. The GSF algorithm is a generalisation of the Kalman-Filter that requires that all the probability density functions of the energy loss of an electron involved in the track reconstruction are described by Gaussian mixtures. The track algorithm starts by looking in the pixel detector after initial tracks called *seeds* which are compatible with the super-cluster. Starting from these seeds, the algorithm constructs outwards all the possible trajectories using a Bethe-Heitler modeling of the electron energy losses up to the end of the tracking volume.

Muon candidates

Two collections of RECO muons are available in CMSSW: the *Standalone muons* where only the muon system is used and the *Global muons* whose reconstruction is performed using information from both the muon system and the silicon tracker. In order to save significant CPU power, the muon reconstruction is based on the concept of regional reconstruction: only the region of the detector where charged particle tracks are compatible with the hits in the muon chambers are used.

The Standalone muon algorithm starts by the reconstruction of muon segments using individual hits in the muon chambers where the DT, the CSC and the RPC tracking detectors participate. These segments are used as seed for the trajectory reconstruction which starts from the innermost muon station and propagates in the outward direction using the Kalman-Filter technique. This propagation from one station to another takes into account the effect of multiple scattering, the non-uniform magnetic field in the muon system as well as the muon energy loss in the material. When the outermost surface of the muons system is reached, a backward Kalman-Filter fit defines the track parameters taking into account the nominal interaction point and the beam-spot size.

The Global muon reconstruction is a more sophisticated algorithm that performs a global fit using hits in the silicon tracker together with hits that were included in the Standalone muon reconstruction track. Taking into account material effects, the Global muon reconstruction algorithm starts by building initial track candidates in the region of interest of the tracker found by the Standalone extrapolation. These are formed by looking for two compatible hits coming from different tracker layers and taking into account all the combinations of compatible pixel and silicon strip layers in order to enhance the final tracking efficiency. Once all the candidates have been found, the track reconstruction proceeds by transforming all the track seeds into a set of trajectories working from inside-out and using the Kalman-Filter technique. Since several tracks can be at this stage reconstructed from a single seed, a cleaning procedure based on the hit multiplicity and the obtained χ^2 normalised to the degrees of freedom of the track is applied to remove ambiguities. Finally, the final track is reconstructed by performing a global fit that uses the hits of the muon chambers and the hits on the silicon tracker.

Jets

The energy that particles deposit in the calorimeters is stored in calorimeter towers referred in CMSSW as the CaloTower constituents. In the CMS detector, a CaloTower is built by combining one or several HCAL cells with the much finer ECAL crystals that cover the same η, ϕ region regarded from the origin of the detector: in the barrel, a CaloTower is formed from the unweighed sum of energy deposits in 5×5 ECAL crystals and in a single HCAL cell whereas in the forward regions the association is more complex.

The reconstruction of jets in CMSSW is performed by using one of the clustering algorithms presented in Section 3.3.2. Even if the input quantities to the algorithm can be either energy deposits in the calorimeters, either their combination with tracks into what is called *particle flow objects*, in this analysis the calorimeter towers are used as an input for the jet reconstruction. The RECO collection of jets is therefore produced, similarly to what has been done in Chapter 3, from the CaloTower constituents. Moreover, the jet algorithm used in the following analysis is the Iterative Cone algorithm with a cone size $R = 0.7$. For the purpose of jet clustering, the CaloTowers are considered as massless particles with an energy given by the sum of the energy of all the contributing cells and a direction defined by the interaction point and the centre of the position of the tower.

Compared to the jet reconstruction in Chapter 3 done considering a perfect detector, in the simulation of the real CMS detector the noise in the calorimeter readout is carefully taken into account. Its impact might be significant in the

Table 5.1: Energy thresholds in GeV for calorimeter noise suppression in the “Scheme B”. Σ_{EB} and Σ_{EE} refer to the sum of ECAL energy deposits associated with the same tower in the barrel and endcap respectively.

Calorimeter cell thresholds [GeV]							
Scheme	HB	HO	HE	Σ_{EB}	Σ_{EE}	HF (S)	HF (L)
B	0.9	1.1	1.4	0.2	0.45	1.8	1.2

reconstruction of jets with low transverse momentum. Hence, a calorimeter tower is used as an input for the jet algorithm if its energy deposit passes the off-line noise rejection energy thresholds summarised in Table 5.1 and referred as the “Scheme-B” thresholds. The various threshold values are given for the different kinds of sub-calorimeter parts and EB and EE stand respectively for the ECAL barrel and endcap. A detailed discussion of the jet reconstruction in CMS as well as the various tower-threshold schemes that can be applied can be found in [102]. Since the calorimeter activity due to underlying events results mainly in low transverse energy deposits in the forward detector region, an additional requirement of a minimal transverse energy of 0.5 GeV of the towers is applied. Finally it should be noticed that in addition to kinematics parameters, the CaloJets RECO collection contains additional information collected from the contributing CaloTowers such as the fractions of electromagnetic and hadronic energies of the jet.

Missing transverse energy

Similarly to the procedure adopted in Chapter 3 for the reconstruction of the missing transverse energy, E_T^{miss} stored in the so-called CaloMET collection is determined from the vectorial sum of all energy deposits in the calorimeter towers passing the “Scheme-B” thresholds:

$$\vec{E}_T^{miss} = - \sum (E_n \sin \theta_n \cos \phi_n \hat{\mathbf{i}} + E_n \sin \theta_n \sin \phi_n \hat{\mathbf{j}}), \quad (5.2)$$

where the index n runs over all the input CaloTowers and $\hat{\mathbf{i}}$ and $\hat{\mathbf{j}}$ are respectively the unit vectors in the direction of the x and y axis of the CMS right-handed coordinate system.

The resolution of this *raw* missing transverse energy is degraded by detector malfunctions, electronic noise and the nonlinearity response of the calorimeters. Therefore there exists corrections [103, 104] that can be applied in order to improve the E_T^{miss} resolution such as the one due to the Jet Energy Scale, also referred as *Type I corrections*. Another straightforward improvement can be obtained by the inclusion of the reconstructed muon

momenta in the calculation of the transverse missing energy since muons only deposit very little energy in the calorimeters. Finally, corrections related to the presence of τ jets can also be applied. Since at the RECO level of this analysis only the Type I corrections are applied, we are only developing further this source of correction.

The jet calibration corrections can be taken into account in the reconstruction of the transverse missing energy by subtracting the shifts in momentum on the reconstructed jets resulting from the Monte-Carlo jet calibration:

$$\vec{E}_{T,corr}^{miss} = \vec{E}_T^{miss} - \sum_{i=1}^{N_{jets}} [\vec{p}_{T,corr}^i - \vec{p}_T^i]. \quad (5.3)$$

In order to take into account the nonlinearity of the calorimeter, in CMSSW the jets are corrected as a function of both the transverse energy (E_T) and the pseudorapidity (η^j) [105]. Based on a study using Minimum Bias events, the corrections are derived by fitting the E_T^{rec}/E_T^{GEN} relative response of the calorimeter with a Gaussian function for each E_T^j and η^j bins. Nevertheless, because the jet corrections are poorly known for jets with low transverse energy, all jets with a $E_T^{rec} < 20$ GeV are excluded from the Type I corrections. Finally, in order to avoid the application of the jet corrections to the electrons identified as jets, all jets with a high fraction of electromagnetic energy (`jetEMfracLimit` > 0.9) are also discarded.

5.2.2 PAT layers

Recently, the CMS collaboration added an additional high-level analysis framework into CMSSW in order to provide common tools to the CMS collaboration and to facilitate the CMS analysis: the reconstructed data samples are further processed using the *Physics Analysis Toolkit* (PAT). Compared to the RECO collection, the PAT delivers all the available high level information related to the electrons, muons, jets and transverse missing energy. The PAT processing is conceptually done in two steps refereed as the *Layer 0* and *Layer 1*. The first layer performs cleaning tasks such as the removal of duplicate reconstructed quantities. Moreover, it computes additional related information needed for selection like the lepton isolation, the jet and missing transverse momentum corrections and the b -tagging. Finally, interestingly, all the quantities are associated to the corresponding generator level and trigger information. The second layer collapses all the previously obtained informations into a compact collection and applies the jet corrections, b -tagging and other high-level tasks: this leads to the final PAT output collections. Even if additional selections may be applied at this stage, in order to conserve the physics content of the PAT very inclusive, only loose cuts are applied on all the selective quantities: it is therefore mandatory to apply further selection

on top of these quantities in the analysis. More specially, for leptons it only serves as the starting point of an additional classification.

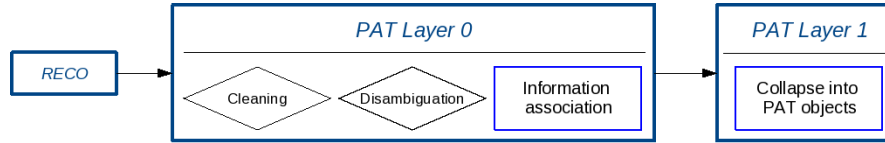


Figure 5.6: Flowchart of the data treatment from the RECO objects to the Layer 1 of the Physics Analysis Toolkit. The role of the two PAT layers is shown.

Electrons

The final PAT electron collection is composed of a list of electron candidates which can arise either from the detection of a real electron or from the misidentification of e.g. pions or photons (named *fake electrons*). In order to improve the purity of the electron collection that will be used in the analysis, a set of quality criteria can be applied to discriminate between fake and real electrons. Amongst others, the following set of characteristic variables is accessible in the PAT collection:

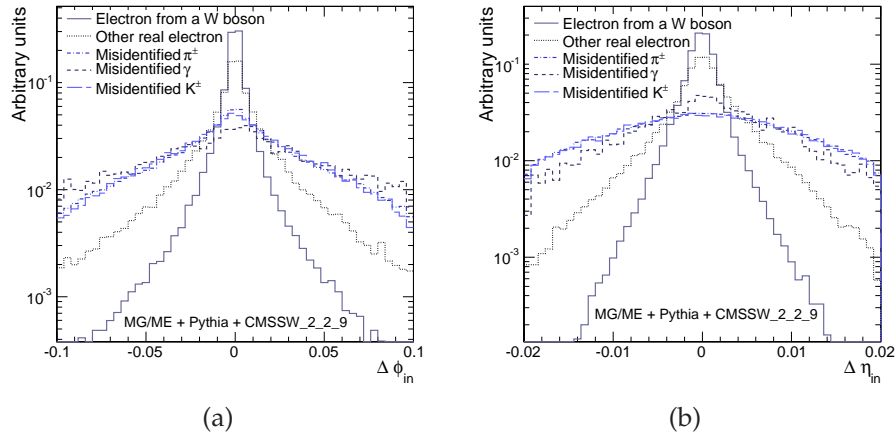


Figure 5.7: Distributions of the $\Delta\phi_{in}$ (left) and $\Delta\eta_{in}$ (right) between the super-cluster and the electron track at vertex. The distributions are normalised to unity in order to compare the shapes of the different contributions. The plots show the behaviour of real electrons compared to fake electron candidates found in the $pp(\gamma b \rightarrow Wt \rightarrow \ell\ell b)pY$ reaction.

- the geometrical matching between the super-cluster and the electron track at vertex applied both on the pseudorapidity position ($\Delta\eta_{in}$) and on the azimuthal angle ($\Delta\phi_{in}$). Figure 5.7 shows these two typical distributions for different electrons: those arising from the decay of a W boson, real electrons coming from the decay of a b -quark and fake electrons due to the misidentification of photons, kaons and pions.
- the pseudorapidity extent of the electron super-cluster ($\sigma_{\eta\eta}$) defined as

$$\sigma_{\eta\eta} = \frac{\sum_i^{5 \times 5} \omega_i (\eta_i - \bar{\eta}_{5 \times 5})^2}{\sum_i^{5 \times 5} \omega_i}, \quad (5.4)$$

where the sum on i runs over all the 5×5 crystals centred on the seed crystal, η_i is the related pseudorapidity position of the crystal, ω_i is its weight and $\bar{\eta}_{5 \times 5}$ is the energy weighted mean pseudorapidity of the 5×5 crystals.

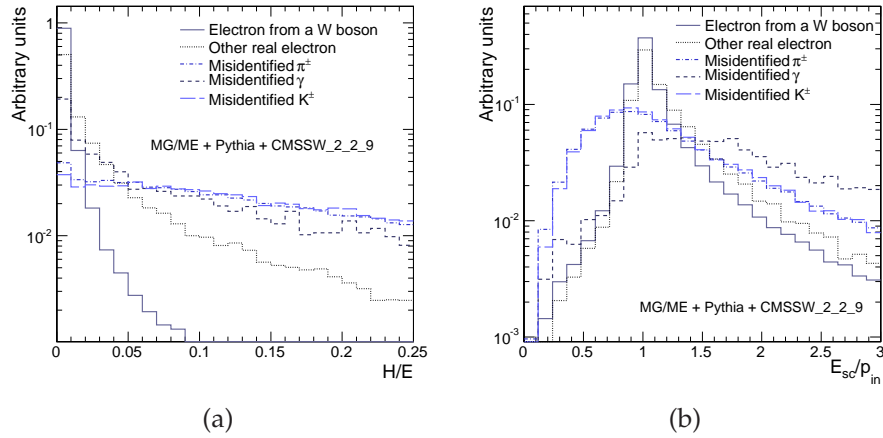


Figure 5.8: Left: ratio of the hadronic energy deposited in the HCAL tower just behind the electromagnetic seed cluster over the energy of the corresponding seed cluster. Right: ratio between the total energy of the super-cluster and the momentum of the associated track measured at the vertex. The plots show the behaviour of real electrons compared to fake electron candidates found in the $pp(\gamma b \rightarrow Wt \rightarrow \ell\ell b)pY$ reaction.

- the ratio of the hadronic energy deposited in the HCAL tower just behind the electromagnetic seed cluster over the energy of the corresponding seed cluster (H/E). For real electrons, the distribution is supposed to be highly peaked around zero. This is clearly visible on Figure 5.8-a for all the electrons of the PAT collection in the $pp(\gamma b \rightarrow Wt \rightarrow \ell\ell b)pY$ events.
- the ratio between the total energy of the super-cluster and the momentum of the associated track measured at the vertex expressed as E_{sc}/p_{in}

that is expected to have a value close to one (see Figure 5.8-b).

- the association of the energy of the seed of the super-cluster to the momentum of the track at the outermost level of the tracker (E_{seed}/p_{out}) and to the momentum of the track at the vertex (E_{seed}/p_{in}). These variables show that the super-cluster is directly related to the associated track.
- the difference between the momentum measured at the outermost state (p_{out}) of the electron track and the momentum measured at the origin (p_{in}). The quantity $f_{brem} = (p_{in} - p_{out})/p_{in}$ may be considered because of its linear dependence with the amount of bremsstrahlung radiated along the trajectory in the tracker.

Table 5.2: List of the thresholds used in the RobustLoose and RobustTight identifications. Two distinct sets of cuts are used in barrel and end-cap regions [106].

	RobustLoose ID		RobustTight ID	
	barrel	end-cap	barrel	end-cap
H/E	0.115	0.150	0.0150	0.0180
$\sigma_{\eta\eta}$	0.0140	0.0275	0.0092	0.0250
$\Delta\eta_{in}$	0.0090	0.0105	0.0025	0.0040
$\Delta\phi_{in}$	0.090	0.092	0.0200	0.0200

In addition to a straightforward access to all these variables, the PAT electron collection allows to directly obtain a quality factor of the electron candidate through an electron identification (electron ID). Four such categories are available in CMSSW namely the *RobustLoose*, the *RobustTight*, *Loose* and *Tight* electron ID's [106]. As an example, the thresholds used in the Robusts identifications are summarised in Table 5.2. The two first electron ID's are suitable to use at the start-up of the LHC since they only rely on the H/E, $\Delta\eta_{in}$, $\Delta\phi_{in}$ and $\sigma_{\eta\eta}$ variables, the last two allow a more efficient electron selection because they use more sophisticated selection methods based on an electron classification depending on the amount of bremsstrahlung radiation along the electron trajectory. The thresholds applied on the four previous quantities are adapted to the electron category. Moreover, an additional selection based on the E_{seed}/p_{out} variable is applied in order to reach a higher purity of the final electron candidates.

Muons

The muon PAT collection allows an easy recovery of the parameters of the global track and the tracker track. Due to the presence of generated kaons

or pions that may result in the PAT muon collection, a refinement of the muon quality requirements is mandatory. In the following analysis a muon-identification algorithm that relies on a set of track-quality requirements has been applied. First, a muon is conserved further for the analysis stage if its global muon normalized- χ^2 is smaller than 10. In Figure 5.9-*a*, the distribution of this normalized- χ^2 for the global fit is shown. Second, the discriminative power of the distribution of valid hits (see Figure 5.9-*b*) can be used. In the following a quite loose requirement of $N_{hits} \geq 11$ is applied.

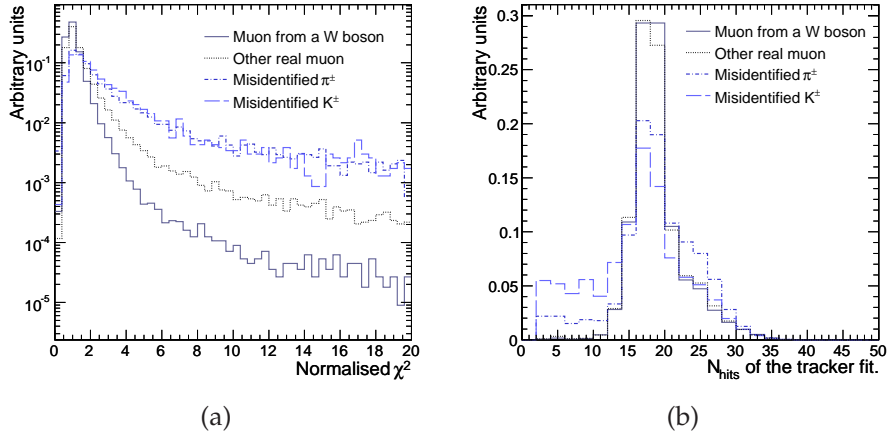


Figure 5.9: Left: normalised- χ^2 of the Global muon fit for real leptons and fake leptons arisen from the misidentification of kaons and pions. Right: number of valid hits in the silicon fit for Global muons. The distributions are normalised to unity and have been obtained using all the muons found in the $pp(\gamma b \rightarrow Wt \rightarrow \ell\ell b)pY$ reaction.

Missing transverse energy

In addition to the jet energy scale correction applied during the RECO procedure, the missing transverse energy used in the analysis is also corrected during the PAT processing for the presence of identified muons. The deposits of the muons in the calorimeter are added to the missing transverse energy and their transverse momentum are subtracted:

$$\vec{E}_{T,corr}^{miss} = \vec{E}_T^{miss} + \sum_{\mu} \vec{E}_{T,calo}^{\mu} - \sum_{\mu} \vec{p}_T^{\mu}, \quad (5.5)$$

where \vec{E}_T^{miss} and $\vec{E}_{T,corr}^{miss}$ are respectively the missing transverse energy before and after the muon correction, $\vec{E}_{T,calo}^{\mu}$ is a two-dimensional vector corresponding to the muon's calorimeter deposit pointing from the IP to the entry

point of the muon to the calorimeter and \vec{p}_T^μ is its transverse momentum. To enter in the correction, a muon must have a $p_T > 10 \text{ GeV}/c$, must possess at least five valid hits in the silicon tracker and the resolution of the track global fit should be better than 50%.

5.3 Signal selection at $L < 10^{32} \text{cm}^{-2} \text{s}^{-1}$

5.3.1 Online selection

Since the study presented in this section assumes a very low instantaneous luminosity of $\mathcal{L} < 10^{32} \text{cm}^{-2} \text{s}^{-1}$, the online selection is based on a candidate trigger table designed for the start-up conditions of the LHC. The study of the trigger efficiency is performed using the $\mathcal{L} = 2 \times 10^{30} \text{cm}^{-2} \text{s}^{-1}$ trigger menu that has been designed for the iCSA08 [107] Monte-Carlo production of CMS since this is the only very low luminosity trigger implemented in the used version of CMSSW. The main trigger paths based on lepton, jet and MET quantities are summarised in Table 5.3.

Table 5.3: Thresholds of the high level triggers considered for the di-leptonic $\gamma p \rightarrow Wt$ analysis at very low luminosity ($2 \times 10^{30} \text{cm}^{-2} \text{s}^{-1}$).

Leptonic triggers		Hadronic triggers	
Name	Thresholds [GeV/c]	Name	Thresholds [GeV/c]
Isol e	15	1 jet	180
Isol ee	10	2 jets	150
e	/	3 jets	85
ee	12	4 jets	60
Isol μ	11	1 jet \wedge MET	180, 60
Isol $\mu\mu$	3	2 jets \wedge MET	125, 60
μ	15	3 jets \wedge MET	60, 60
$\mu\mu$	3	4 jets \wedge MET	35, 60

As already seen in Chapter 4, the selection of the di-leptonic topology employs selection cuts based on the presence of leptons, one jet and missing transverse energy. In order to determine which trigger paths are the most efficient to conserve our signal during the online selection, a comparison of the signal efficiency of all the trigger paths that contain either leptons, either jets, either E_T^{miss} is done. The signal selection efficiency is found to be 75%. Regarding more precisely the different contributions of the sub-triggers (see

Figure 5.10), the selection mainly occurs through the single isolated leptonic paths while the contribution from the hadronic triggers is negligible due to the very high thresholds applied on the transverse momentum of the jets. Finally, for the same reason, the efficiency of the missing transverse energy based trigger paths is also completely insignificant.

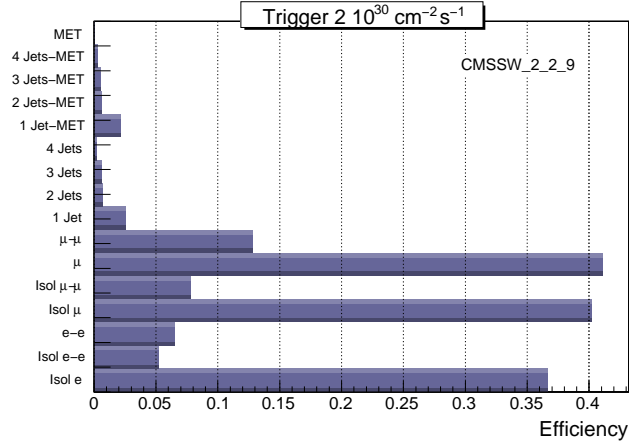


Figure 5.10: Selection efficiencies of the trigger paths containing leptons, jets and missing transverse energy for the di-leptonic $\gamma p \rightarrow Wt$ signal. The trigger paths are shown on the vertical axis while the horizontal axis shows the efficiency defined as the ratio of number of events that are found with the corresponding trigger bit on, divided by the number of all events.

5.3.2 Offline analysis

Because the selection procedure of the $Wt \rightarrow \ell\ell b$ topology has been extensively presented in Chapter 4, emphasis is put on the modifications directly related to the CMSSW simulation. The order of application of the cuts is similar to what has been presented in Section 4.3.3. All the numbers quoted in the Tables of this section are obtained after the application of the previous cuts of the selection chain. The efficiency of the trigger selection is neglected.

Lepton counting

The selection starts by requiring the presence of exactly two isolated leptons. Since muons may leave enough energy in the calorimeters to be identified as electrons, all the electron candidates reconstructed within the $\Delta R < 0.1$ distance of a muon candidate are ignored in the lepton counting. In order

to decide which algorithm gives the best background rejection, the RobustLoose, Loose and Tight identifications have been compared. The obtained visible cross sections after the requirement of the presence of exactly two isolated leptons are summarised in Table 5.4 for the signal and the associated backgrounds. It is clear that no significant impact of the different choices of the electron ID on the respective signal on background ratios is obtained. In the following of the analysis, the Loose identification is therefore chosen since the RobustLoose ID is a category to be used at the early start-up of the LHC and that the Tight ID is rejecting more signal than the other two categories. Nevertheless, when QCD background will be added in the analysis, depending on its remaining contribution, the Tight ID may be used since its tighter identification cuts should allow a greater suppression of the multi-jet background.

Table 5.4: Comparison of signal and background cross sections obtained after requiring the presence of exactly two isolated leptons for three electron identification algorithms: RobustLoose, Loose and Tight ID's. The electron or muon candidates are considered as isolated if no other track with $p_T > 2 \text{ GeV}/c$ within a cone of $\Delta R = \sqrt{\Delta\eta^2 + \Delta\phi^2} < 0.5$ are found around the lepton.

σ [fb]	signal	$t\bar{t}$		WWq'		Zj
		γp	pp	γp	pp	γp
RobustLoose ID	20.3	35.1	14.7×10^3	13.8	822.2	80.2
Loose ID	19.9	34.4	14.3×10^3	13.6	808.1	79.5
Tight ID	19.3	33.4	14.0×10^3	13.1	780.8	77.4

Although results in Table 5.5 have been obtained using an isolation procedure similar than the one implemented in DELPHES³, following the recommendation of the CMS collaboration, an isolation based on the sum of the transverse momentum of the tracks in a cone size $\Delta R < 0.3$ around the lepton direction, excluding the lepton track is preferable ($tk_{Iso} = \sum_i p_T^{i,tk}$). Identically the sum of the transverse energies calculated from the calorimeter deposits ($calo_{Iso} = \sum_i p_T^{i,tower}$) can be defined. Using the hereabove definitions, the *relative isolation* in the tracker I_{tk} and the calorimeter I_{calo} are expressed as

$$I_{tk/cal} = \frac{p_T}{p_T + tk/cal_{Iso}}, \quad (5.6)$$

These distributions are shown in Figure 5.11 for the electron candidates when the presence of at least two leptons in the event is fulfilled. In contrast to

³The electron or muon candidates must be isolated in the tracker from any other tracks with $p_T > 2 \text{ GeV}/c$ within a cone of $\Delta R = \sqrt{\Delta\eta^2 + \Delta\phi^2} < 0.5$ around the lepton.

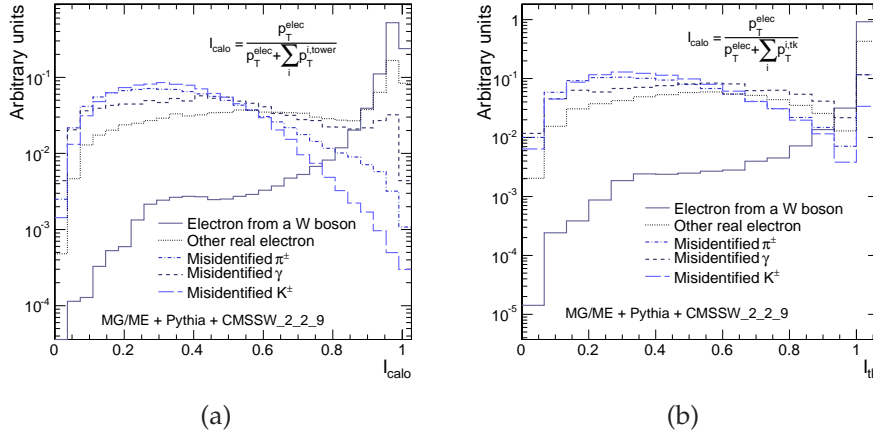


Figure 5.11: Relative isolation in the calorimeters (left) and in the tracker (right) of the selected electrons after the requirement of the presence of at least two leptons. The distributions are normalised to unity and have been obtained using all the electrons found in the $pp(\gamma b \rightarrow Wt \rightarrow \ell\ell b)pY$ reaction.

the real isolated electrons coming from the decay of a W boson, the other contribution does not peak at 1 showing that an effective rejection of fakes and non-isolated leptons can be obtained. The thresholds applied on I_{tk} and I_{calo} have been chosen in order to get similar visible cross section at this stage of the selection procedure than the one obtained using the DELPHES isolation criteria: in this analysis muon candidates are required to have I_{tk} and I_{calo} larger than 0.95 and 0.92, while the request for electrons is done using the respective 0.9 and 0.9 values.

Table 5.5: Comparison between the visible cross sections for the signal and the various backgrounds using the DELPHES-like isolation criteria ($N_{track}^{\Delta R < 0.5} = 0$) and the use of the relative isolation in the tracker and in the calorimeters. The previous requirements for the lepton identification described in the text are applied on both the muon and the electron candidates.

σ [fb]	signal	$t\bar{t}$		WWq'		Zj
		γp	pp	γp	pp	γp
$N_{track}^{\Delta R < 0.5} = 0$	19.9	34.4	14.3×10^3	13.6	808.1	79.5
I_{tk}/I_{calo}	19.6	35.6	15.9×10^3	13.2	854.9	78.3

Table 5.5 summarises the visible cross sections for the signal and dom-

inant backgrounds using the two definitions for the lepton isolation. As it can be seen by comparing these results with the one given in Table 4.7 of Section 4.3.3, a good compatibility with the DELPHES results is seen: at this stage of the selection procedure, the expected yields are roughly identical. At worst, a discrepancy of 10% is found between the CMSSW and the DELPHES results.

Jet counting

Concerning the jet requirements, apart from the jet energy correction applied in the PAT processing, no further CMSSW specific requirements are applied. The jet counting therefore only considers jets whose calibrated transverse momentum is larger than $30 \text{ GeV}/c$, within $|\eta| < 2.5$. The reduction of the $t\bar{t}$ events is again clearly visible since the distribution peaks at 2 jets similarly to what was expected using DELPHES as can be seen on Figure 5.12.

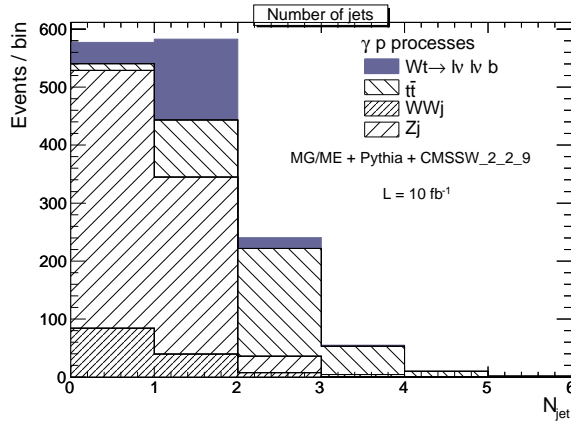


Figure 5.12: Cumulative distribution of the number of reconstructed central ($|\eta| < 2.5$) jets with $p_T > 30 \text{ GeV}/c$ after the cut on the lepton. Jets are reconstructed using the Iterative Cone algorithm with a cone size of 0.7. The normalisation corresponds to 10 fb^{-1} .

γp cuts

The application of the γp cuts is identical to the one used in the DELPHES analysis. Firstly, the energy in the two HF detectors is evaluated by summing

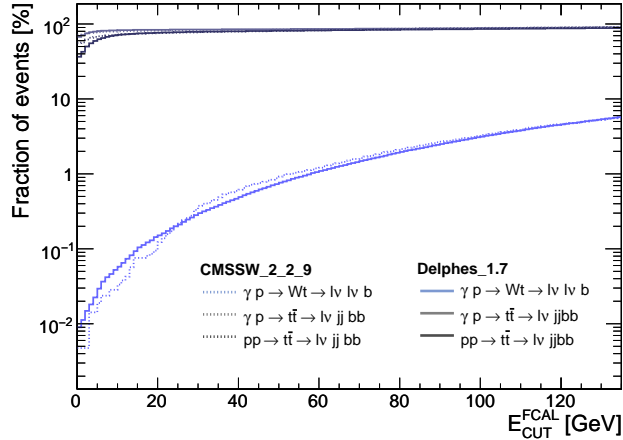


Figure 5.13: Fraction of selected events as a function of the maximum allowed measured energy in the empty hemisphere (E_{CUT}^{FCAL}) for $\gamma b \rightarrow Wt \rightarrow \ell\ell b$ and $\gamma g \rightarrow t\bar{t} \rightarrow \ell j j b b$ photon-induced events and the semi-leptonic $pp \rightarrow t\bar{t}$ process. For comparison, the same distributions obtained using DELPHES are shown.

the energy in the calorimeter towers⁴. Without any noise suppression, the majority of the offline calorimeter cells contain energy. Hopefully, the use of the “Scheme-B” thresholds significantly reduces the number of fired towers in an event. The fraction of events passing the rapidity gap condition is shown on Figure 5.13 as a function of the applied E_{CUT}^{FCAL} value. For comparison, the reduction factor arising from the DELPHES simulation is also depicted for the same samples showing that the two simulations give similar results for both the photon-induced events and the proton-proton interactions. For the signal this simple way to select the “empty hemisphere” gives a probability to chose correctly the gap side of 88%. Finally, the exclusivity condition is applied exactly as what has been done in Chapter 4, by using all tracks from the Global Track collection that possess a number of valid tracker hits greater than 8.

b-tagging

The major difference between the previous study and the actual CMSSW analysis appears in the *b*-tagging requirement of the selected jet candidate

⁴The obtained energy sum is corrected by a factor of 1.7. This factor comes from the combination of a rescale of the HF energy by 0.7 to compensate for a limitation of this specific version of CMSSW and of a correction factor taking into account the $\sim 20\%$ energy loss due to detection inefficiencies at the edges of the HF wedges at $|\eta| \in [3.0; 3.5]$ and $|\eta| \in [4.5; 5.0]$ [108].

in the event. Indeed while in the DELPHES simulation, the b -tagging and mistagging probabilities are applied through the use of efficiency values independent of the transverse momentum of the jets, in CMSSW, several b -tagging algorithms are available that give a response directly related to the p_T of the jet. The two major classes of b -tagging algorithms exploit either the long b -hadrons lifetime [109], or the semi-leptonic decay modes [110].

Table 5.6: Operating points and efficiencies for the Track counting b -tagging algorithm for the LOOSE, MEDIUM and TIGHT operating points defined by CMS. The efficiencies are determined on a dijet QCD sample with $80 < \hat{p}_T < 120 \text{ GeV}/c$ [111].

Algorithm	Point	Discriminator	light mistag	b -efficiency
Track counting	LOOSE	2.03	0.1	0.82
	MEDIUM	4.38	0.01	0.65
	TIGHT	5.36	0.001	0.38

For this analysis, a *Track counting* based algorithm that calculates the signed 3D impact parameter significance (IP/σ_{IP}) of all the tracks associated to the jet that pass tight quality criteria⁵ is chosen. After having sorted the tracks by decreasing transverse momentum, the value of the 3D impact parameter of the second (*high efficiency*) or third (*high purity*) track is used as discriminative variable. The CMS collaboration defined three working points, the LOOSE, MEDIUM and TIGHT points summarised in Table 5.6, which correspond to choose respectively the thresholds of 2.03 and 4.38 on the high-efficiency tagger and the high-purity algorithm with threshold set to 5.36.

The distribution of the high-efficiency algorithm discriminator is represented on Figure 5.14-*a* showing that a cut at 4.38 already significantly reduces the WWj background that does not contain real b -quark in the final state. Interestingly, by looking at Figure 5.14-*b* where the tagging and mistagging efficiencies are shown for a discriminator value of 4.38, it is clear that the mistagging efficiency of light jets was overestimated in the DELPHES analysis, since the efficiency of tagging a light jet falls off rapidly with decreasing transverse momentum of the jet leading to a relative mistagging probability well below 1%. The final signal over background is therefore enhanced compared to the DELPHES analysis.

⁵ $p_T > 1 \text{ GeV}/c$, decay length $< 10 \text{ cm}$, transverse impact parameter $< 2 \text{ mm}$, number of tracker hits ≥ 8 , number of pixel hits ≥ 2 , $\chi^2/dof < 10$ and a track to jet-axis distance $< 0.7 \text{ mm}$ [109].

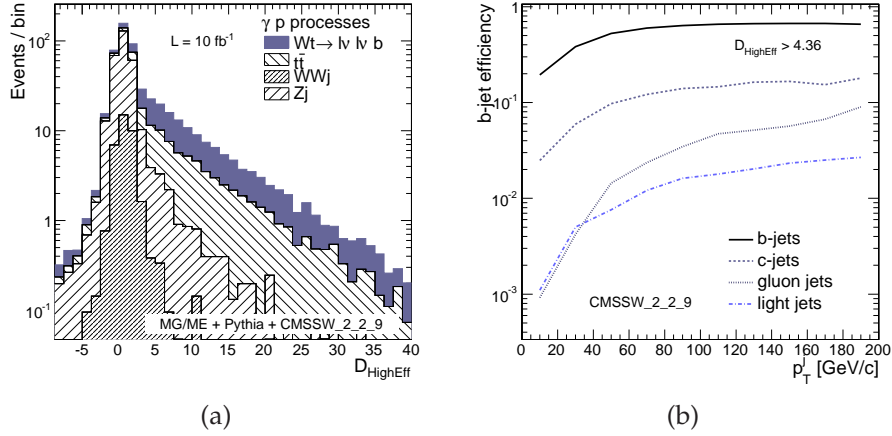


Figure 5.14: Left: cumulative distribution of the high-efficiency algorithm discriminator ($D_{HighEff}$) for the signal and the remaining backgrounds after the application of the cuts on the number of leptons, jets and the use of the γp cuts. The normalisation corresponds to 10 fb^{-1} . Right: b -jet tagging efficiency and non- b jet mistagging efficiencies for a fixed discriminator of 4.38 of the high efficiency algorithm as a function of the jet transverse momentum. All jets found in an event sample of semi-leptonic $pp \rightarrow t\bar{t}$ have been used.

Missing transverse energy

Table 5.7: Comparison between the visible cross sections for the signal and the various backgrounds using the calorimeter and the particle-flow based missing transverse energies after the application of the lepton, jets γp and b -tagging criteria. Selected events must have a missing transverse energy greater than 20 GeV.

σ [fb]	signal	$t\bar{t}$		WWq'		Zj
		γp	pp	γp	pp	γp
CALO E_T^{miss}	5.64	2.20	1.19	0.08	0.02	0.19
PF E_T^{miss}	5.62	2.18	1.18	0.08	0.02	0.07

As seen in the previous Chapter, the requirement of the presence of real missing transverse energy suppresses significantly the Zj background. An accurate determination of the E_T^{miss} value in events without missing energy is therefore a major asset for an efficient signal and background separation. Even using the muon and jet corrections, the resolution of the calorimeter

based missing transverse energy becomes worse with decreasing value [112]. In order to achieve a better precision in events containing only little missing transverse energy, the value reconstructed using the particle-flow event reconstruction should be used. Indeed, this additional information significantly improves the measurement of very low missing transverse energies in comparison with the calorimeter based E_T^{miss} [113]. The improvement is seen in Table 5.7 where the final cross section for the signal and the backgrounds are given. If the impact is quite negligible for processes expected to have true missing transverse energy, the improvement of the rejection for the Zj sample is clear: the final cross section decreases from 0.19 to 0.07 fb when the particle-flow algorithm is used. Figure 5.15 shows the PF missing transverse energy measured in the events that survived the selection procedure on leptons, jets, b-jet and γp cuts.

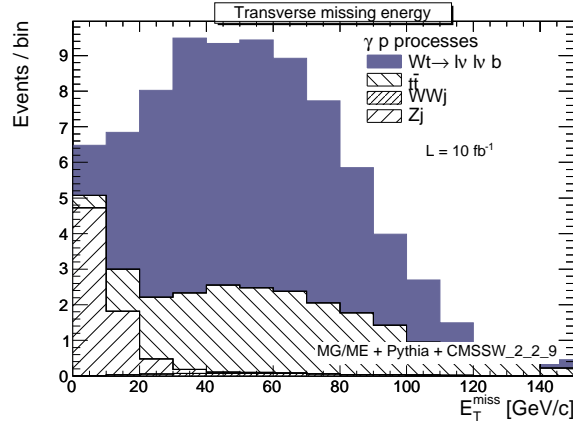


Figure 5.15: Cumulative distribution of the missing transverse energy, after the cut on the lepton, the jet, the rapidity gap selection, the exclusivity condition and the b -tagging requirement. The normalization corresponds to 10 fb^{-1} .

5.3.3 Results after 10 fb^{-1}

Table 5.8 summarises the effect of the offline selection of the $pp(\gamma b \rightarrow Wt)pY$ reaction, and quotes the expected yields for 10 fb^{-1} of accumulated data, at very low luminosity ($\mathcal{L} < 10^{32} \text{ cm}^{-2} \text{ s}^{-1}$). It is remarkable that the signal (56 ± 7) and the sum of the backgrounds (35 ± 6) are roughly of the same magnitude, in spite of the large initial disparity in their production cross sections. In particular the effect of the γp cuts on the pp samples is really important, providing a background reduction factor of several orders of magnitude on these samples, while preserving most of the events from γp processes.

Moreover, the requirement of one and only one b -jet in the event leads to a powerful rejection of WWq' or Zj background samples. Finally, using the full power of particle-flow information allows a very good evaluation of missing transverse energy, which further reduces the contribution of the Zj process to the final sample.

Table 5.8: Effect of various cuts on the cross section of the di-leptonic topology for photon-induced and parton-induced backgrounds for very low luminosity $\mathcal{L} < 10^{32} \text{ cm}^{-2} \text{ s}^{-1}$.

σ [fb]		signal	$t\bar{t}$		WWq'		Zj
			γp	pp	γp	pp	γp
Production		104.3	159.1	77×10^3	62.5	5×10^3	287.3
Topo. cuts	$N_{lept} = 2$	19.6	35.6	15.9×10^3	13.2	854.9	78.3
	$N_{jet} = 1$	13.9	9.9	3.3×10^3	4.0	370.6	30.5
γp cuts		12.5	4.4	2.4	3.7	1.2	23.4
Final cuts	$N_{bjet} = 1$	6.1	2.4	1.3	< 0.1	< 0.1	0.8
	E_T^{miss}	5.6	2.2	1.2	< 0.1	< 0.1	< 0.1
Yields for 10 fb^{-1}		56.2	21.8	11.8	0.8	0.2	0.7

Even if it is difficult to predict the amount of accumulated data during the very low luminosity runs of the LHC, these numbers give an indication of the power of the analysis cuts in a low pile-up environment. Going to higher luminosities implies the necessity to improve the selection cuts to cope with these pile-up events. This is the subject of the next section. Finally, for all the signal events that survived the entire procedure, the application of the trigger selection leads to a selection efficiency of 100%. This was expected since the thresholds applied on the transverse momentum of the leptons during the online selection are smaller than those used for the offline selection procedure.

5.4 Signal selection at $\mathcal{L} = 2 \times 10^{33} \text{ cm}^{-2} \text{ s}^{-1}$

5.4.1 Online selection

Because the CMS collaboration is currently focusing on early data, no recent trigger table for a luminosity of $2 \times 10^{33} \text{ cm}^{-2} \text{ s}^{-1}$ is available in the version of CMSSW used for the analysis. Nevertheless, in order to obtain an expectation of the online selection efficiency for the signal, an approximative estimation of the trigger streams based on leptons, jets and missing transverse energy is given following the hypothesis that the final HLT objects are close to the

one used during the offline analysis. The trigger streams and the associated thresholds summarised in Table 5.9 used are directly taken from the CMS TDR [67].

Table 5.9: Thresholds of the high level triggers considered for the di-leptonic $\gamma p \rightarrow Wt$ analysis at low luminosity ($2 \times 10^{33} \text{ cm}^{-2}\text{s}^{-1}$).

Leptonic triggers		Hadronic triggers	
Name	Thresholds [GeV/c]	Name	Thresholds [GeV/c]
Isol e	26	1 jet	400
Isol ee	12	2 jets	350
e	/	3 jets	195
ee	19	4 jets	80
Isol μ	19	1 jet \wedge MET	180, 80
Isol $\mu\mu$	7	2 jets \wedge MET	155, 80
μ	37	3 jets \wedge MET	85, 80
$\mu\mu$	10	4 jets \wedge MET	35, 80

Considering the entire HLT streams, the global output rate has been estimated to be approximately 120 Hz. Figure 5.16 summarises the selection efficiencies of the individual sub-triggers. Because due to the higher thresholds applied on the hadronic streams, the contributions of the hadronic streams to the online selection are now completely marginal, only the leptonic streams are shown. The total signal efficiency reaches 71% for the signal events. Compared to the very low luminosity case, the thresholds applied during the online selection are greater than those used during the offline analysis procedure, meaning that a loss of events may occur.

5.4.2 γp cuts

HECTOR is not currently implemented into the fast simulation chain of CMSSW for the evaluation of the forward proton tagging rate. Instead, look-up tables for the acceptance of the VFEDs are accessible that allows to derive the acceptance of the RP-220 and FP-420 detectors. Nevertheless, these acceptance tables currently in use are quite old and may not provide a very high precision simulation. A large discrepancy is visible between the results obtained with the look-up tables in CMSSW and those calculated in DELPHES where HECTOR is correctly implemented: while the selection efficiency of the VFED detectors reaches 92% for the signal, it falls down to 77% into CMSSW. Since it is not straightforward that the effect of the initial position

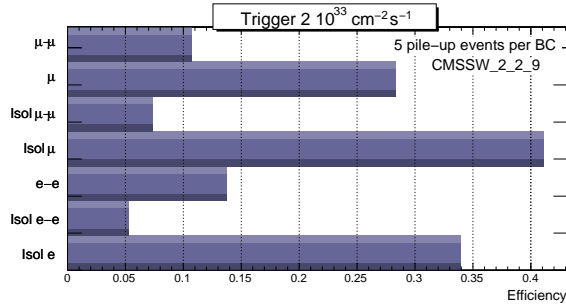


Figure 5.16: Selection efficiencies of the trigger paths containing leptons for the dileptonic $pp(\gamma b \rightarrow Wt)pY$ reaction during the phase of low luminosity. The trigger paths are shown on the vertical axis while the horizontal axis shows the efficiency defined as the ratio of number of events that are found with the corresponding trigger bit on, divided by the number of total events.

and angle of the proton can provide a realistic explanation of this results, a more correct simulation of the HECTOR simulation should be implemented in CMSSW, which would take into account a more realistic smearing of the proton initial conditions at the IP. The rejection factors for photon-induced and proton-induced reactions obtained in Section 4.3.4 are therefore used in this analysis.

During the low luminosity phase of the LHC running, thousands of tracks will be reconstructed at each bunch crossing by the tracking system. In order to realistically apply the exclusivity condition, a method that reconstructs the vertex of the γp interaction is applied. Indeed, thanks to the excellent granularity of the tracker sensors, the reconstruction of primary and secondary vertices is possible, allowing to only take into the exclusivity condition tracks pointing to the vertex created from the interaction of the photon and the incoming parton.

The presence of two leptons in the events allows to easily obtain an estimate of the position of the γp interaction point by reconstructing a vertex using the two associated tracks. This vertex reconstruction is performed by making use of a least-square fit formulated as a Kalman-Filter algorithm. In order to decide if a reconstructed track belongs to the γp interaction or to the pileup events, a matching procedure based on the maximum longitudinal separation Δz between the reconstructed vertex and the position of the considered track at the vertex is applied: only tracks for which the Δz value is smaller than 5 mm are taken into account in the application of the exclusivity condition.

5.4.3 Results after 10 fb^{-1}

Due to the presence of simultaneous interactions, additional tracks with low transverse momentum are present in the final event. The isolation condition based on the number of tracks with $p_T > 2 \text{ GeV}/c$ located around the lepton should therefore be less constraining: during the low luminosity phase, an electron is supposed to be isolated if no track with transverse momentum greater than $2 \text{ GeV}/c$ is present in a distance of $\Delta R = 0.3$ around the lepton direction. Apart from this small modification and the hereabove explained procedure to apply the γp cuts, all the procedure is remaining similar as what introduced in Chapter 4. The obtained visible cross sections at each stage of the selection procedure are given in Table 5.10

Table 5.10: Effect of various cuts on the cross section of the di-leptonic topology for photon-induced and parton-induced backgrounds for low luminosity $\mathcal{L} = 2 \times 10^{33} \text{ cm}^{-2} \text{ s}^{-1}$.

σ [fb]		signal		$t\bar{t}$		WWq'		Zj
			γp	pp	γp	pp	γp	
Production		104.3	159.1	77×10^3	62.5	5×10^3	287.3	
Topo. cuts	$N_{lept} = 2$	19.7	37.3	17×10^3	11.6	925.5	80.2	
	$N_{jet} = 1$	12.6	8.0	2.6×10^3	4.1	356.5	29.6	
γp cuts		8.7	2.5	55.0	2.2	8.6	13.3	
Final cuts	$N_{bjet} = 1$	3.7	1.2	28.5	< 0.1	0.2	0.5	
	E_T^{miss}	3.4	1.1	26.3	< 0.1	< 0.1	< 0.1	
Yields for 30 fb^{-1}		101.6	34.1	787.6	1.1	4.9	2.2	

5.5 Conclusion

Following the results obtained with DELPHES, promising results have been obtained for the Wt di-leptonic topology during the very low and the low luminosity phases. Using the official software of the CMS experiment, a more realistic fast simulation of the experiment has been applied on signal and background events. At very low luminosity ($\mathcal{L} < 10^{32} \text{ cm}^{-2} \text{ s}^{-1}$), it is remarkable that the observed number of events is of the same magnitude as the sum of the remaining background events, in spite of production cross sections differing by several orders of magnitude. Moreover, in this low pile-up conditions, the results from the CMS software are in very good agreement with the estimates obtained with DELPHES. This provides another

important validation of the fast simulation framework.

At low luminosity ($\mathcal{L} = 2 \times 10^{33} \text{ cm}^{-2}\text{s}^{-1}$), the number of pile-up events significantly increases. This imposes the use of relaxed isolation criteria on the selected leptons, as well as modified γp cuts. Even if the reduction of partonic background events is less powerful, the expected signal-to-background ratio is still remarkable after 10 fb^{-1} of accumulated data. It should be mentioned that although in DELPHES, the probability to reconstruct a track was set to 90%, into CMSSW, it falls down to 85% for tracks with a transverse momentum as low as $0.5 \text{ GeV}/c$. The presented analysis would therefore benefit from the possibility to reconstruct tracks with a $p_T > 0.2 \text{ GeV}/c$.

ASSOCIATED WH PRODUCTION

6.1 Higgs production at the LHC

With the start-up of the LHC, the race to hunt for the Standard Model Higgs boson will reach an unprecedented intensity. Indeed, even if during several years, the old facilities such as LEP and the TEVATRON have been operated in an energy range allowing to search for the Higgs boson directly and indirectly, the eluding boson has not yet been observed. Several tantalising hints of a light Higgs boson ($115 - 116 \text{ GeV}/c^2$) were observed at LEP, but its dismantling in 2000 did not allow to claim for the discovery of this particle. Nevertheless, all the collected data are compatible with the existence of a Higgs boson having a mass higher than $114.4 \text{ GeV}/c^2$. At the TEVATRON, the most recent combined results from the TEVATRON experiments have excluded the existence of a SM Higgs boson with a mass ranging from 163 to $166 \text{ GeV}/c^2$ at 95% confidence level.

6.1.1 Higgs boson production processes

Figure 6.1 summarises the production cross section of the Higgs boson at the LHC over the mass range $100 \text{ GeV}/c^2 \lesssim m_H \lesssim 800 \text{ GeV}/c^2$. The main Higgs boson production mode is the *gluon-gluon fusion* $gg \rightarrow H$ with a production cross section that reaches $\sim 40 \text{ pb}$ for $m_H = 120 \text{ GeV}/c^2$. Beside this copious source, the Higgs boson can also be produced by *Vector Boson Fusion* (VBF), $qq \rightarrow Hqq$, with a production cross section approximately one order of magnitude smaller than the dominant one. Finally, *associated production modes*, $q\bar{q}' \rightarrow HW$, $q\bar{q}' \rightarrow HZ$, $gg/q\bar{q} \rightarrow t\bar{t}H$ and $gg/q\bar{q} \rightarrow b\bar{b}H$ are also studied by the LHC collaborations to search for the SM Higgs boson. Compared to the gluon fusion and the Vector Boson Fusion, their cross sections are lower by a factor that ranges from ~ 20 at $m_H \sim 100 \text{ GeV}/c^2$ up to ~ 1000 at larger masses such

as $500 \text{ GeV}/c^2$.

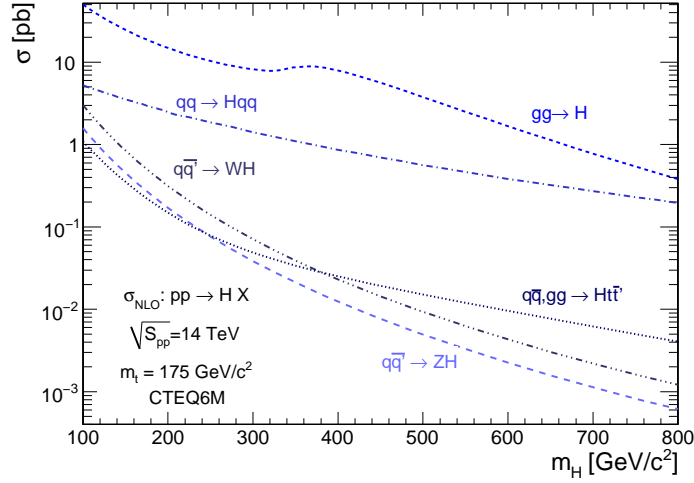


Figure 6.1: Higgs boson production cross section at the LHC in pb [$\sqrt{s} = 14 \text{ TeV}$] for the various relevant production mechanisms as a function of the Higgs mass. The values are taken from [114, 115]. The NNLO-QCD corrected results are employed for the gluon fusion and vector boson fusion mechanisms. Weak boson fusion ($qq \rightarrow Hqq$) and $t\bar{t}$ associated production are at NLO accuracy.

6.1.2 Searches for a SM-like scalar Higgs boson

As seen in Figure 1.3 of Section 1.4.1, the decay branching ratios strongly depend on the Higgs mass. Depending on the assumed mass of the Higgs boson, the most suitable final states to be used for discovery are therefore different. The LHC collaborations performed extensive studies in order to determine the viability of the various possible channels. Figure 6.2 shows the signal significance as a function of the Higgs boson mass for 30 fb^{-1} of the integrated luminosity for the different Higgs boson production and decay channels. The interested reader is referred to the CMS Technical Design Report [62].

Low Mass Higgs Searches

Despite the favourite decay mode of a light Higgs boson ($m_H \lesssim 130 \text{ GeV}/c^2$) is through a $b\bar{b}$ pair, the observation of this channel is challenging at the LHC due to the hadronic final state being hard to separate from the large QCD background. In order to reduce this background, the sensitivity to the $H \rightarrow b\bar{b}$

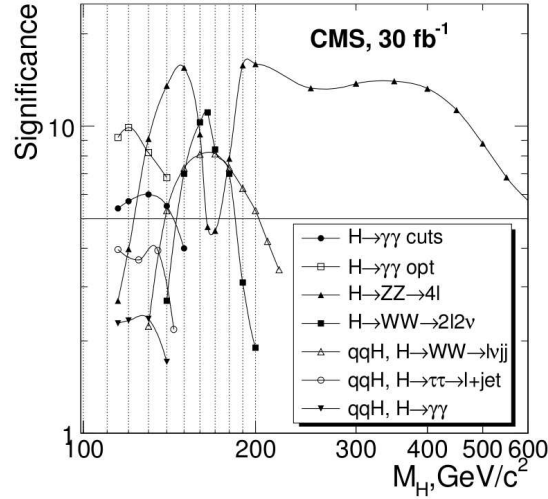


Figure 6.2: SM Higgs discovery potential for CMS as a function of the Higgs boson mass for the different Higgs boson production and decay channels assuming an integrated luminosity of 30 fb^{-1} .

decay using a production via $t\bar{t}$ fusion has also been investigated by the CMS collaboration. Nonetheless, the complicated final state containing four b -jets, the inability to reconstruct the Higgs mass precisely as well as the large theoretical uncertainty on the dominant $t\bar{t}b\bar{b}$ background allow to conclude that the Higgs discovery is unlikely using the $b\bar{b}$ decay mode.

Considering all final states in which at least one τ decays leptonically the $qq \rightarrow Hqq \rightarrow \tau\tau qq$ process provides nowadays one of the best expected sensitivities for the light Higgs boson hypothesis. The major advantages of these topologies are twofold: the hadronically-decayed τ has a distinct experimental signature to jets. Secondly, despite the presence of missing transverse energy due to neutrinos, the $\tau\tau$ invariant mass can be reconstructed within the collinear approximation of the decay products of the τ 's.

In spite of the low branching fraction for $H \rightarrow \gamma\gamma$ ($\sim 1.5 \times 10^{-3}$ for $m_H \lesssim 135 \text{ GeV}/c^2$), this decay mode provides a very clean signature due to the presence of two photons with very high transverse momentum. Even if this process suffers from a large irreducible background coming mainly from $q\bar{q} \rightarrow \gamma\gamma$ and $gg \rightarrow \gamma\gamma$ photon pairs, an excellent electromagnetic calorimeter resolution should allow the signal to appear as a narrow peak over the smoothly falling di-photon invariant mass distribution. Using the $t\bar{t}H$ associated channel as well as optimised analyses such as likelihood and neural network techniques,

the CMS collaboration expects to obtain a significance up to 10σ with an integrated luminosity of 30 fb^{-1} . The $H \rightarrow \gamma\gamma$ decay channel is therefore one of the most promising one for an early discovery of a Higgs boson in the low mass range.

Intermediate mass region, $130\text{ GeV}/c^2 < m_H < 2m_Z$

At $m_H \gtrsim 130\text{ GeV}/c^2$, the decay channel $H \rightarrow ZZ^{(*)} \rightarrow 4\ell$ gains in importance and provides an excellent sensitivity for a wide range except for a gap around twice the W mass. CMS collaboration expects a significance for this channel of more than 5σ for 30 fb^{-1} of integrated luminosity in the whole mass range above $\sim 170\text{ GeV}/c^2$.

High mass region, $m_H > 2m_Z$

As the gap caused by the drop of the ZZ branching fraction is covered by the decay $H \rightarrow WW$ ($\text{BR} \sim 95\%$), the $H \rightarrow WW \rightarrow 2\ell 2\nu$ channel is the most significant channel in the mass range $2m_W < m_H < 2m_Z$. Contrary to the other presented search topologies, the presence of neutrinos with high transverse momentum makes it difficult to reconstruct the Higgs mass peak: the analysis therefore relies on an accurate estimation of the background shape and normalisation. For a Higgs boson mass close to $160\text{ GeV}/c^2$, a sensitivity in excess of 10σ is expected after 30 fb^{-1} of integrated luminosity.

6.2 Higgs photoproduction at the LHC

Even if the possibility of using γp collisions to search for a light Higgs boson was already considered at electron-proton colliders [116], due to the high delivered photon luminosity at the LHC, the $pp(\gamma p \rightarrow HX)pY$ reaction might be used for studying a Higgs boson of $m_H > 115\text{ GeV}/c^2$. For some processes, the Higgs photoproduction processes even represent a non-negligible fraction of the pp events.

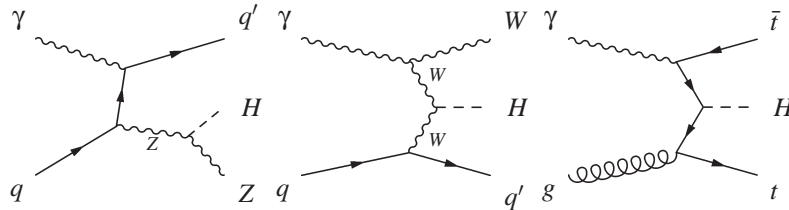


Figure 6.3: Representative leading order Feynman diagrams of the associated Higgs boson photo-production at the LHC. From left to right: ZHq' , WHq' and $Ht\bar{t}$ associated production modes.

Due to the absence of a SM $g_{\gamma H_g}$ coupling, the Higgs boson can not be singly produced and it is therefore mandatory to look at the associated photo-production modes. The more relevant associated modes at the LHC are depicted in Figure 6.3. Since the extraction of the Higgs signal from the background is facilitated by the identification of the accompanying particles, the production modes have been categorised using the particles associated to the Higgs production: ZHq' , WHq' and $Ht\bar{t}$ mechanisms. Although in parton-parton interactions the four associated production channels may provide copious sources of Higgs boson, in photon-induced processes, apart from the W associated mechanism, the other SM Higgs boson production modes are marginal due to their small cross sections as can be seen in Table 6.1 where the production cross sections of the different processes are summarised.

Table 6.1: Production cross sections in fb of the most relevant associated production modes of a Higgs boson at the LHC. All production cross sections have been obtained using MG/ME. No other cut than the regularization cut of $p_T > 1 \text{ GeV}/c$ on q' is applied.

$m_H [\text{GeV}/c^2]$	115	150	170
$\gamma p \rightarrow ZHq'$	149.2×10^{-3}	71.8×10^{-3}	46.3×10^{-3}
$\gamma p \rightarrow WHq'$	23.0	19.0	17.5
$\gamma p \rightarrow Ht\bar{t}$	1.73	0.8038	0.5426

At the LHC the cross section of the $pp(\gamma p \rightarrow WHq')pY$ process reaches 23 fb for a Higgs boson mass of $115 \text{ GeV}/c^2$ and diminishes slowly down to 17.5 fb with increasing Higgs boson masses up to $170 \text{ GeV}/c^2$. Interestingly, this production mechanism is sensitive to the WWH gauge coupling which might be enhanced when considering models where the Higgs boson is fermiophobic. A broad Higgs boson mass window can be investigated using photon-induced processes. It is particularly interesting to look after light ($m_H < 130 \text{ GeV}/c^2$) masses since the preferred decay into $b\bar{b}$ poses a serious challenge at the LHC for parton-parton interactions. Considering that a robust rejection of pp events can be achieved using dedicated selection cuts, backgrounds such as QCD processes may become negligible in the photon-proton production modes: the $pp(\gamma q \rightarrow WH^\pm q')pX$ process might therefore give valuable information on the Hbb coupling. Finally, last but not least, although the cross sections for γp interactions are smaller than the parton-parton ones, the ratio of signal to background cross sections is better in γp processes by more than one order of magnitude as can be seen from Figure 2.5.

6.3 Search for WH associated photoproduction

6.3.1 Signal event signatures

Prospects for the observability of the WH channel are considered for two different mass points of the Higgs boson, $115 \text{ GeV}/c^2$ and $170 \text{ GeV}/c^2$, and for five different final topologies. The WHq' production cross section as well as the cross section times branching ratio for the five topologies are summarised in Figure 6.4.

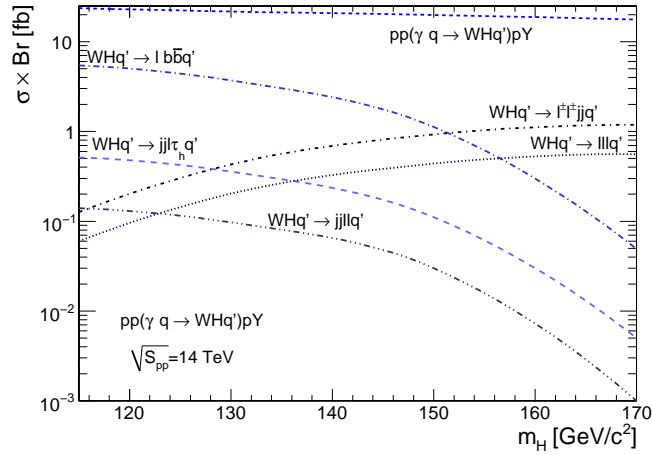


Figure 6.4: The $pp(\gamma q \rightarrow WHq')pY$ production cross sections at the LHC of the five considered topologies: $WHq' \rightarrow lb\bar{b}q'$, $WHq' \rightarrow jjllq'$, $WHq' \rightarrow jjl\tau_h q'$, $WHq' \rightarrow lllq'$ and $WHq' \rightarrow jjl\ell^\pm\ell^\pm q'$. The branching ratios to the considered topologies are included.

For a light Higgs boson ($m_H = 115 \text{ GeV}/c^2$), the first studied final state is provided by the $H \rightarrow b\bar{b}$ decay mode. Since a completely hadronic final state cannot be efficiently selected by a trigger system, the presence of the isolated lepton of the decaying W boson is required to select the signal. The signature of the first studied topology is therefore composed of an isolated lepton accompanying two b -jets whose invariant mass reconstructs the Higgs mass. The key point for the observation of this channel is therefore the capability to reconstruct the invariant mass of the two b -jets with a precise resolution.

When the $H \rightarrow b\bar{b}$ decay is put aside, in the mass range $m_H < 130 \text{ GeV}/c^2$ the Higgs boson is expected to preferentially decay into a τ lepton pair. Because the two τ 's can subsequently decay into leptons or into jets (these jets

are being referred in the rest of this thesis as τ_h), three final states are possible: a fully leptonic one, a semi-leptonic one and a final state containing two τ_h . Again, since a completely hadronic final state is difficult to extract, the following analyses only focus on the $W\tau\tau q' \rightarrow jj\ell\ell q'$ and $W\tau\tau q' \rightarrow jj\ell\tau_h q'$ final states representing respectively 12.4% and 45.6% of the $pp(\gamma q \rightarrow W\tau\tau q')pY$ total cross section.

For a Higgs boson of $m_H = 170 \text{ GeV}/c^2$, the WH associated photoproduction with a subsequent decay of the Higgs boson into a W pair may provide a distinctive signature with three W bosons in the final state. It is worth studying the fully leptonic final state in which all the three W bosons decay into leptons and the topology in which two of them decay leptonically and one hadronically. In the latter case, the choice of the like-sign lepton pairs is very useful to reject many background processes with a two-lepton final state signature such as $t\bar{t}$ events followed by leptonic decay of both W 's from the top quarks. In addition to its discovery potential this channel is interesting for the determination of the coupling to W gauge bosons since this coupling appears both in the production and in the decay chain. Last but not least, if a scenario in which the Higgs boson does not couple to fermions, this channel will remain unaffected whereas all the other decays, except $H \rightarrow \gamma\gamma$ and $H \rightarrow ZZ$, would be suppressed.

6.3.2 Signal and background generation

Similarly to the analysis of the $pp(\gamma b \rightarrow Wt)pY$ reaction, all partonic level processes are generated with MG/ME followed by the fragmentation and hadronisation performed using PYTHIA. In order to study the feasibility of the analyses under realistic experimental conditions, the generated signal and background events are passed through the DELPHES fast simulation of a CMS-like detector. Since in this thesis five analyses will be performed, a large variety of background samples have been generated: the expected cross sections times branching ratios of the various background events, as well as the Higgs boson topology for which they have been used are summarised in Table 6.2.

Because this Chapter focuses on the potential that can be expected from $pp(\gamma q \rightarrow WHq')pY$ events, the ideal case is taken: only the most relevant background processes are considered. Moreover, even if identical final states as those coming from photoproduction may be produced using proton-proton interactions, we do not consider their impact as background events in the following analyses.

Table 6.2: Cross sections times branching ratios, obtained using MG/ME + PYTHIA for the various background samples used in the five WHq' topologies. Moreover, the absolute pseudorapidity of the leptons in the $W\tau\tau q'$ and $W\ell\ell q'$ are restricted to be smaller than 3. The sample size of each process is also given. For the Wtb sample, the following cuts have been applied at generator level: $p_T^b > 10$ GeV/ c and $|\eta^b| < 5$. The symbol ℓ means e, μ, τ .

Process	$\sigma \times Br$ [fb]	Sample size	Used for signal					
			$jj\ell\ell q'$	$jj\ell\tau q'$	$\ell\ell\ell q'$	$jj\ell^\pm\ell^\pm q'$	$\ell b\bar{b}q'$	
$W\tau\tau q' \rightarrow jj\tau\tau q'$								
$m_{\tau\tau} \in [70; 110]$	3.17	18k	×	×				
$m_{\tau\tau} \in [110; \infty[$	0.28	20k	×	×				
$i\bar{i}(2\ell)$	158.4	200k	×	×	×			
$Wt(2\ell)$	103.9	500k	×	×	×			
$WWWq' \rightarrow jj\ell\ell q'$	1.27	9.8k	×	×		×		
$W\tau\tau q' \rightarrow \ell\tau\tau q'$								
$m_{\tau\tau} \in [70; 110]$	1.56	18k			×	×		
$m_{\tau\tau} \in [110; \infty[$	0.13	20k				×		
$W\ell\ell q' \rightarrow \ell\ell\ell q'$								
$m_{\ell\ell} \in [10; 70]$	1.65	30k			×	×		
$m_{\ell\ell} \in [110; \infty[$	0.39	50k			×			
$WWWq' \rightarrow \ell\ell\ell q'$	0.20	4k			×			
$i\bar{i}(1\ell)$	671.8	179k				×	×	
$Wt(1\ell)$	440.6	200k				×		
$Wtb(1\ell)$	265.1	200k					×	
$Wbbq' \rightarrow \ell b\bar{b}q'$								
$m_{bb} \in [80; \infty[$	14.67	10k						×

6.3.3 Topological and γp cuts

The reduction of non-signal events will be performed using a similar reduction procedure as in Section 4.3.2: first, the *topological cuts* which rely mainly on the acceptance of the detector and the identification of final state particles are applied. Hence electron candidates need to fall into the coverage of the tracker, τ_h candidates need to have a transverse momentum higher than 10 GeV/ c and to be located in the pseudorapidity region $|\eta| < 2.5$. Jets are reconstructed using a Midpoint cone algorithm of radius $R = 0.7$ if they lie into the central calorimeters ($|\eta| < 3.0$) and have a $p_T > 20$ GeV/ c . The topological cuts applied for each of the five studied topologies are summarised in Table 6.3. In order to reject in the evaluation of the number of jets those reconstructed around an isolated electron, a minimum angular distance of

$\Delta R = 0.1$ is imposed between the axis of the selected leptons and the jet.

Table 6.3: Topological cuts for five topologies resulting from $pp(\gamma q \rightarrow WHq')pY$ photoproduction. The number of required isolated leptons with transverse momentum greater than p_T^e and p_T^μ are quoted as well as the number of jets lying into the central calorimeters ($|\eta| < 3.0$) with $p_T > 20$ GeV/ c . When two leptons are required in the topology, they might be of same-sign (SS) or opposite-sign (OS).

Topology	m_H [GeV/ c^2]	p_T^e [GeV/ c]	p_T^μ [GeV/ c]	N_ℓ	N_j	N_{τ_h}
$lbbq'$	115	20	20	1	2	-
$jjllq'$	115	10	7	2, OS	≥ 2	-
$jj\ell\tau_hq'$	115	15	10	1	≥ 2	1
$lllq'$	170	15	15	3	≤ 1	-
$jj\ell^\pm\ell^\pm q'$	170	15	15	2, SS	2	-

In order to trigger the event and to identify the presence of the W bosons in the event, the presence of isolated leptons with high transverse momentum is required. Nevertheless, the quite small values applied on the p_T of the leptons summarised in Table 6.3 can be understood by the fact that the interaction is driven by the exchange of a photon and is therefore characterised by a lower energy scale than for pp events. This poses an issue in terms of the trigger chain, as the thresholds applied on the transverse momentum of the reconstructed objects can be considered as high in terms of physical interest for photon physics. Considering that lepton candidates selected by the topological cuts would allow signal events to pass the online trigger selection, the applied thresholds may be realistic during the first month of running of the LHC. When the luminosity will increase, these values will be insufficient to pass the trigger of the experiment. Hopefully, since both the CMS and the ATLAS experiments possess a rich forward physics programme, dedicated triggers [117] may be created in order to retain a fraction of forward events as large as possible. Because the major constraint for a lowering of the trigger threshold is the rates of the passing events, additional requirements specific to low- x physics should be applied in counter-part, such as some exclusivity requirements.

The application of the *topological cuts* is followed by the γp cuts as in Section 4.3.2. Nevertheless, since proton-proton events are neglected as a background source, the E_{CUT}^{FCAL} a rejection based on track multiplicity in the “empty” hemisphere is not applied. Finally, the events will need to fulfil the specific criteria of the *final cuts* that are discussed in the following sections.

6.3.4 Final discrimination of $WHq' \rightarrow \ell b\bar{b}q'$

In order to improve the visibility of the signal, the reconstruction of the invariant mass of the two b -quarks is important: it is therefore mandatory that the two selected jets must be b -tagged. Since the hadronic activity of the $t\bar{t}$ and Wt events is expected to be larger, a good rejection of such backgrounds can be obtained by looking at the number of tracks with $p_T > 0.5$ GeV/ c . As can be seen in Figure 6.5-*a*, while the distribution of the number of reconstructed tracks for the signal reaches its maximum around 16, the distribution of the $t\bar{t}$ background peaks at 26. Requiring that less than 25 low transverse momentum tracks are present in the event allows a strong reduction of the $t\bar{t}$ and Wt backgrounds.

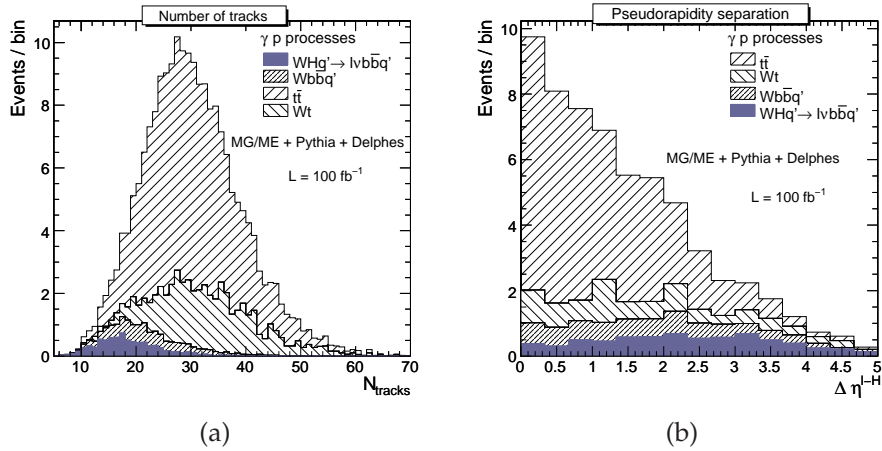


Figure 6.5: Left: cumulative distribution of the number of tracks with transverse momentum greater than 0.5 GeV/ c after the application of the lepton, the jets and the γp cuts, as well as the b -tagging requirement for the signal and the three considered backgrounds. Right: cumulative distribution of the pseudorapidity difference between the reconstructed Higgs boson and the isolated lepton after the application of the lepton, the jets and the γp cuts, as well as the b -tagging and the maximum number of track requirement for the signal and the three backgrounds.

Since in the signal the W and the Higgs bosons are clearly separated, a significant reduction of the $t\bar{t}$ background can be obtained by looking at the pseudorapidity separation ($\Delta\eta^{\ell-H}$) existing between the system reconstructed from the two b -jets and the isolated leptons. Therefore, only events possessing a $\Delta\eta^{\ell-H} > 1.5$ are conserved as signal candidates. While 72% of the Higgs events are passing this cut, the major remaining background is decreased by a factor of roughly three as can be seen on Figure 6.5-*b*.

Summary of selection cuts and results after 100 fb^{-1} Table 6.4: Summary of the selection cuts for the $WHq' \rightarrow \ell b \bar{b} q'$ topology. The effective cross section for the signal and the backgrounds, for each step in the selection is given in fb.

σ [fb]		Signal	$t\bar{t}$	Wt	$Wbbq'$
Production		5.42	671.75	440.57	14.67
Topo cuts	$N_\ell = 1$	2.12	297	112	6.54
	$N_{jet} = 2$	0.76	49.0	19.4	2.16
γp cut		0.75	38.3	15.1	1.73
Final cuts	$N_{bjet} = 2$	0.08	1.46	0.45	0.09
	$N_{tracks} < 25$	0.07	0.40	0.08	0.06
	$\Delta\eta^{\ell-H} > 1.5$	0.05	0.13	0.04	0.04

The effect of the selection cuts presented above is illustrated in Table 6.4 for $m_H = 115 \text{ GeV}/c^2$ and for the three considered backgrounds. The estimated visible cross sections at each stage of the selection procedure is shown. While a b -tagging efficiency of 40% has been assumed, the signal selection efficiency related to the tagging of the two jets is 10%, well below the expected 16%. This small value can easily be explained by remembering that the W and H bosons are produced in association with a primary jet (q') that can be responsible of the selection of the event during the jet counting procedure. Nevertheless it is clear that more efficient b -tagging would be needed to significantly improve the signal selection efficiency.

6.3.5 Final discrimination of $WHq' \rightarrow jj\tau\tau q'$

The lepton-pair invariant mass ($m_{\ell\ell}$) can be viewed on Figure 6.6: samples containing real- τ are preferentially located in the small invariant mass range while the values of $m_{\ell\ell}$ in $t\bar{t}$ and Wt events are larger. Since a cut on this observable is specific to the final state (less neutrinos are produced in the semi-leptonic topology), the maximum allowed invariant mass is different for the two topologies: $70 \text{ GeV}/c^2$ and $110 \text{ GeV}/c^2$ for the fully leptonic and the semi-leptonic topologies respectively. Moreover, this cut would be very effective to reduce the $WZq' \rightarrow W\ell\ell q'$ events that may constitute a very severe background explaining why only the $WZq' \rightarrow W\tau\tau q'$ background is considered in this analysis.

Since no other jet activity apart from the $W \rightarrow qq$ jets is expected in the “empty hemisphere”, the jets used to reconstruct the W boson are the two jets with $p_T > 20 \text{ GeV}/c$ and having the highest positive pseudorapidity. The resulting invariant mass is plotted in Figure 6.7-a. As expected, the signal

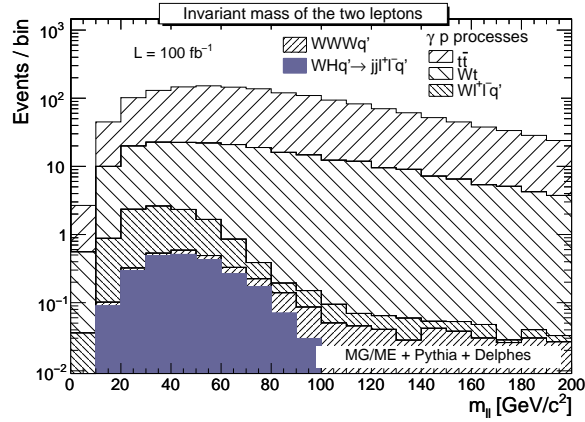


Figure 6.6: Cumulative distribution of the dilepton invariant mass after the topological cuts and the γp selection. Results are normalised for an integrated luminosity of 100 fb^{-1} .

events present a peak around the W boson mass. For the $t\bar{t}$ and Wt events, while the distribution reaches its maximum around $80 \text{ GeV}/c^2$, the other background distributions contain long tails because the two selected jets are not those coming from the W decay. Events with an invariant mass of the two jets $m_{jj} = m_W \pm 20 \text{ GeV}/c^2$ are kept.

Finally, the large remaining $t\bar{t}$ and Wt backgrounds are effectively reduced by requiring a minimum pseudorapidity separation of 1 between the “reconstructed W boson” and the two leading leptons. For the signal this distance is quite large since the two leptons are supposed to come from the Higgs decay while the object reconstructed from the two jets is assimilated to the W boson. Figure 6.7-b shows the minimum pseudorapidity separation existing between the W -boson and the two isolated leptons. The separation power is clearly visible since for the top backgrounds the $\Delta\eta^{\ell-W}$ value is sharply peaked at 0.

Higgs boson mass reconstruction

The reconstruction of the τ -pair invariant mass is mandatory to significantly reduce the various remaining backgrounds and to allow more visibility of the signal. The Higgs mass reconstruction is difficult since part of the energy is lost by the undetectable neutrinos in the final state. Nevertheless, the reconstruction of the $\tau\tau$ invariant mass is possible by making the approximation that the decay products of the τ are collinear with the τ in the laboratory frame. This approximation can be done since $m_H/2 \gg m_\tau$ and hence the two τ

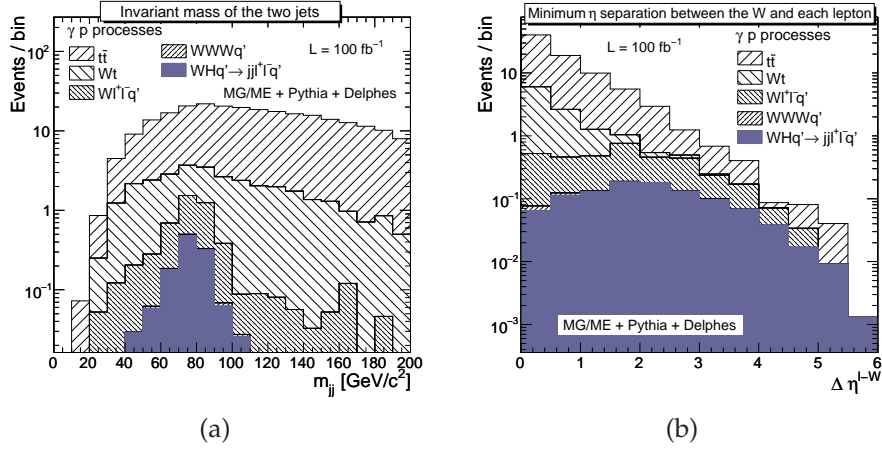


Figure 6.7: Left: Cumulative distribution of the invariant mass of the two jets with $p_T > 20 \text{ GeV}/c$ and having the highest pseudorapidity value in the empty hemisphere for the signal and the four photon-induced backgrounds. Right: cumulative distribution of the minimum pseudorapidity separation between the “reconstructed W boson” and the two leading leptons. The distributions, normalised to 100 fb^{-1} , are obtained after the application of the previous selection cuts.

are highly boosted.

For notational simplicity, in the following the $\tau\tau \rightarrow \ell\tau_h$ channel is considered while the development remains applicable for the fully leptonic topology. By neglecting the τ rest mass and imposing the collinear approximation, the Higgs boson mass can be expressed as

$$m_H = m_{\tau\tau} \approx \sqrt{2E^\ell E^h (1 - \cos\theta_{\ell h}) \frac{E^{\tau\ell} E^{\tau_h}}{E^\ell E^h}}, \quad (6.1)$$

where $E^{\tau\ell}$ and E^{τ_h} are the τ energies, E^ℓ is the energy of the charged lepton, E^h the one of the hadronic decay products and $\theta_{\ell\tau}$ is the angle between the charged lepton and the τ_h .

Defining the fraction of the τ energy which is carried by the τ_h as

$$x_h = \frac{E^h}{E^{\tau_h}} = \frac{E_T^h}{E_T^{\tau_h}} \frac{\sqrt{1 + \left(\frac{E_z^h}{E_T^h}\right)^2}}{\sqrt{1 + \left(\frac{E_z^{\tau_h}}{E_T^{\tau_h}}\right)^2}} \simeq \frac{E_T^h}{E_T^{\tau_h}}, \quad (6.2)$$

where E^{τ_h} is the τ energy given by $E^{\tau_h} = E^h + E^{\nu_h}$ and E^{ν_h} is the neutrino energy reconstructed from the missing transverse energy (and similarly for $E^{\tau\ell}$), the

invariant mass can be rewritten as

$$m_{\tau\tau} \approx \frac{m_{\ell h}}{\sqrt{x_\ell x_h}}, \quad \text{for } x_{\ell,h} \geq 0, \quad (6.3)$$

with x_ℓ defined similarly to Equation 6.2 for the charged lepton and $m_{\ell h}$ is the invariant mass of the two visible decay products. In the collinear approximation, the neutrino energy may be reconstructed from the missing transverse energy because the E_T^{miss} vector can be divided into two components in the basis determined by the transverse directions of the two decay products (the lepton and the τ_h), by projecting the missing energy vector to the visible product momenta. The estimates of the summed neutrino energies in the transverse plane are

$$E_T^{N_h} = \frac{E_T^{miss} \sin \theta_{m\ell}}{\sin \theta_{\ell h}}, \quad E_T^{N_\ell} = \frac{E_T^{miss} \sin \theta_{mh}}{\sin \theta_{\ell h}}, \quad (6.4)$$

where $\theta_{m\ell}$ and θ_{mh} are the polar angles between the missing transverse energy and the visible particles. The mass resolution is therefore sensitive to a mis-measurement of the missing transverse energy both in magnitude and in direction, as well as it depends on the $\theta_{\ell h}$ angle between the visible τ momenta as $1/\sin \theta_{\ell h}$. For a Higgs boson mass of $130 \text{ GeV}/c^2$, the resulting resolution is approximately 25%.

Summary of selection cuts and results after 100 fb^{-1}

The effect of the cuts described in the previous sections is reported in Table 6.5 where the visible cross sections are given in ab after each stage of the selection procedure for signal events at $m_H = 115 \text{ GeV}/c^2$ and for $t\bar{t}$, Wt , $WWWq'$ and $W\ell\ell q'$ photon-induced backgrounds. Except for the $pp(\gamma q \rightarrow W\ell\ell q')pY$ background, in the fully leptonic topology all the backgrounds are strongly rejected by the requirement on the invariant mass of the opposite-sign leptons.

A strong rejection due to the reconstruction of the Higgs boson mass is obtained. Indeed, while in processes that contain two real τ , the missing transverse energy lies between the two visible products of the τ decays, for the $t\bar{t}$, Wt and $WWWq'$ photon-induced backgrounds the collinear approximation is not valid resulting in a significant suppression of these backgrounds. The reduction that appears in the signal events can easily be explained since the division of the missing transverse energy becomes difficult for events topologies where the two leptons are emitted back to back. Moreover, since the measured missing transverse energy is relatively small, its measurement error tends to be large leading to the reconstruction of non-physical negative masses. For the di-leptonic topology, the overall reconstruction efficiency is 91% for the signal, 16% for the top backgrounds, 26% for the $WWWq'$ sample and 87% for the $W\ell\ell q'$. Finally it should be noticed that since the uncertainty

Table 6.5: Summary of the selection cuts for the $WHq' \rightarrow jj\tau\tau q' \rightarrow jj\ell\ell q'$ and the $WHq' \rightarrow jj\tau\tau q' \rightarrow jj\ell\tau_h q'$ topologies. The effective cross sections for the signal and the $t\bar{t}$, Wt , $WWWq'$ and $W\ell\ell q'$ backgrounds, for each step in the selection are given in ab.

σ [ab]		Signal	$t\bar{t}$	Wt	$WWWq'$	$W\ell\ell q'$	
$\gamma\gamma \rightarrow \ell\ell$	Production	140.0	158.4×10^3	103.9×10^3	1.3×10^3	3.45×10^3	
	Topo. cuts	$N_\ell = 2$	52.6	49.3×10^3	30.5×10^3	268	137
		$N_{jets} \geq 2$	35.1	40.7×10^3	5.3×10^3	217	115
	γp cut	25.3	38.0×10^3	5.2×10^3	203	95.3	
	Final cuts	$N_{bjet} = 0$	23.6	15.0×10^3	2.6×10^3	194	89.3
		$m_{\ell\ell} < 70 \text{ GeV}/c^2$	20.8	6.0×10^3	1.1×10^3	50.3	84.0
		$ m_{jj} - m_W < 20 \text{ GeV}/c^2$	10.3	677	89.0	7.5	25.8
		$\Delta\eta^{\ell-W} > 1.0$	8.5	171	12.2	3.4	17.9
		Rec_H	7.7	27.6	2.0	0.9	15.5
	$h\tau\tau \rightarrow \ell\tau\ell$	Production	514.1	158.4×10^3	103.9×10^3	1.3×10^3	4.6×10^3
Topo. cuts		$N_\ell = 1$	271	76.7×10^3	52.0×10^3	619	6.4×10^3
		$N_{\tau_h} = 1$	106	11.0×10^3	8.3×10^3	115	582
		$N_{jets} \geq 2$	70.0	8.8×10^3	1.2×10^3	92.1	437
γp cut		49.5	8.3×10^3	1.2×10^3	85.4	379	
Final cuts		$N_{bjet} = 0$	46.4	3.2×10^3	570	80.9	353
		$m_{\ell\ell} < 110 \text{ GeV}/c^2$	45.8	2.4×10^3	402	39.6	336
		$ m_{jj} - m_W < 20 \text{ GeV}/c^2$	23.8	251	21.1	6.4	79.3
		$\Delta\eta^{\ell-W} > 1.0$	20.1	67.7	3.3	3.2	58.8
		Rec_H	15.3	11.3	0.4	0.7	31.7

on the direction of the τ_h is larger, the reconstruction efficiency is lower in the semi-leptonic topology: 76%.

6.3.6 Final discrimination of $WHq' \rightarrow WWWq'$

Final cuts of events with three leptons

In order to reject the $pp(\gamma q \rightarrow W\ell\ell')pY$ events, a cut can be applied on the invariant mass of opposite-sign same-flavour lepton pairs. Indeed, looking at Figure 6.8 where the invariant mass of the two leptons selected by the topological cuts is visible, it is clear that a Z -resonance peak is visible for this sample while the distributions are roughly flat for other processes. This background is therefore rejected by vetoing events which possess at least one pair of opposite-sign, same flavour leptons with an invariant mass comprised between 70 and 110 GeV/c^2 . This graph has been obtained using a $W\ell\ell'$ sample with $70 < m_{\ell\ell} < 110 \text{ GeV}/c^2$ to evaluate the pertinence of the cut, while in the analysis the $W\tau\tau'$ sample with $70 < m_{\tau\tau} < 110 \text{ GeV}/c^2$ is considered.

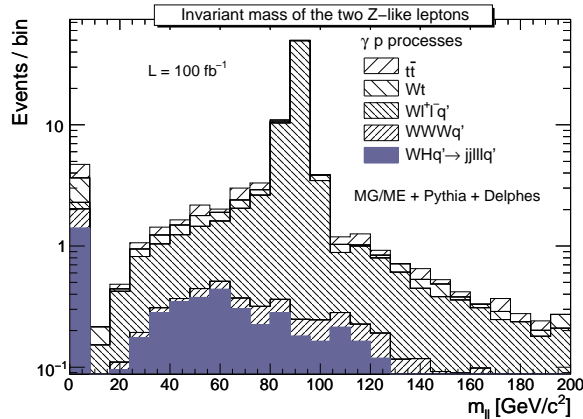


Figure 6.8: Distribution of the invariant mass of the opposite-charge same-flavour leptons for the signal and the photon-induced backgrounds after the application of the lepton and the jet topological cuts and the γp selection. Events in the first bin are those for which no pair is compatible with the Z -hypothesis. The distribution is normalised to 100 fb^{-1} .

A small azimuthal separation is expected for signal events since the decay of a scalar Higgs boson into two vector W -bosons results in two bosons with opposite spin correlation. A reduction of the backgrounds is therefore

obtained by searching in the three selected leptons, at least one pair of opposite sign leptons which fulfils the following kinematic and angular cuts: $\Delta\Phi_{\ell\ell} < \pi/2$, $\Delta\eta_{\ell\ell} < 1$ and an invariant dilepton mass smaller than $80 \text{ GeV}/c^2$. In the following this cut will be denoted as the *HWW tag*.

A selection cut that may be considered to decrease the number of residual $W\ell\ell q'$ background that contains mainly off-shell Z -bosons, $Z \rightarrow \tau\tau \rightarrow \ell\ell$ decays or events with $m_{\ell\ell} < 70 \text{ GeV}/c^2$, is to reject events for which the two leptons compatible with the HWW hypothesis are of same flavour. Additionally this cut strongly suppress $t\bar{t}$ and Wt photon-induced backgrounds. Rejecting SF leptons clearly favours the signal over background ratio since the signal efficiency amounts to $\sim 60\%$ while the fraction of $W\ell\ell q'$ events kept is only 20%. The decrease of the signal comes from the fact that there is a reasonable probability that one of the HWW selected leptons comes from the W which is produced in association with the Higgs boson, and therefore has no charge correlation.

Without losing a huge fraction of signal events, the backgrounds can be further reduced by applying cuts on the jets. Indeed in the signal the only source of jet comes from the presence of the primary jet that is generally located in the forward calorimeter. Hence is this possible to suppress the $t\bar{t}$ background by an additional factor of 2.2 if the only allowed jet is located in the pseudorapidity region $|\eta| < 1$ and if the jet is found to be tagged as a b -jet.

Final cuts of events with two SS leptons

The $pp(\gamma p \rightarrow W\tau\tau q')pY$ events represent a background when one lepton from the fully leptonic decay escapes from the detection or when one of the τ decays hadronically. After applying the previous cuts, an additional reduction of the background is therefore obtained by vetoing events that contains a reconstructed τ -jet. Besides, top backgrounds are decreased by rejecting all events where a jet is identified as originating from a b -quark. Requiring these two conditions on the jets, 92.0% of the signal is kept, while 48.7% and 27.1% of the $t\bar{t}$ and $W\ell\ell q'$ backgrounds are rejected respectively.

Summary of selection cuts and results after 100 fb^{-1}

The visible cross sections at each stage of the selection procedure listed above are summarised in Table 6.6. The upper part of the Table gives results for the fully leptonic topology while the lower part of the Table shows the evolution of the visible cross section in the SS topology. It can be seen that the cumulated efficiencies in the two topologies are respectively 3% and 0.6%.

Table 6.6: Summary of the selection cuts for the $WHq' \rightarrow \ell\ell\ell q'$ and the $WHq' \rightarrow jj\ell^\pm\ell^\pm q'$ topologies. The effective cross sections for the signal and the $t\bar{t}$, Wt , $WWWq'$ and $W\ell\ell q'$ backgrounds, for each step in the selection are given in ab. The mass of the Higgs boson was chosen to be $m_H = 170 \text{ GeV}/c^2$.

σ [ab]		signal	$t\bar{t}$	Wt	$WWWq'$	$W\ell\ell q'$	
$\ell\ell\ell q'$	Production	560	158.4×10^3	103.9×10^3	420	11.8×10^3	
	Topo cuts	$N_{lept} = 3$	69.0	153	66.3	36.0	190
		$N_{jet} \leq 1$	59.1	75.4	60.7	28.1	146
	γp cut	59.0	71.0	60.4	28.0	145	
	Final cuts	Z veto	47.2	50.1	42.6	23.3	125
		HWW tag	32.1	16.1	9.1	4.4	43.3
		SF veto	18.4	9.0	4.1	2.8	8.8
		$ \eta_j > 1$	16.8	4.1	2.5	2.2	6.9
		$N_{bjet} = 0$	16.7	2.7	2.1	2.2	6.8
	$jj\ell^\pm\ell^\pm q'$	Production	16.86×10^3	672.4×10^3	440.8×10^3	1.3×10^3	8.5×10^3
Topo cuts		$N_{lept}^{SS} = 2$	311	561	204	120	288
		$N_{jet} = 2$	107	139	97.6	52.6	69.7
γp cut		105	117	86.5	42.9	69.3	
Final cuts		N_{τ_h}	98.2	117	84.5	42.6	51.8
		$N_{bjet} = 0$	96.7	60.0	71.1	40.5	50.5

It must also be noted that while the $N_{jet} = 2$ cut reduces greatly signal events in the SS topology since only 34% of the signal is passing this selection step, it allows to really improve the signal to background ratio compared to the less restrictive $N_{jet} \geq 2$ requirement. Indeed, using the less constrained selection criteria, the final signal on background ratio yields 0.3 while the requirement of the presence of exactly 2 jets leads to a 0.43 value. Finally, even if additional cuts can be applied in the SS topology, it has been shown that due to the corresponding decrease of the number of surviving signal events, no notable improvement can be obtained.

6.4 Results

6.4.1 Confidence levels

Since the expected numbers of WHq' signals and backgrounds that survive the selection procedure are low, it is required to make use of the Poisson statistics. The quantification of the possible level of observable signal is therefore performed using the modified frequentist confidence level method [118]. Hence, considering n independent counting search channels, the likelihood ratio given by

$$Q = \prod_{i=1}^n Q_i, \quad (6.5)$$

with

$$Q_i = \frac{e^{-(s_i+b_i)}(s_i+b_i)^{d_i}}{d_i!} / \frac{e^{-(b_i)}(b_i)^{d_i}}{d_i!} = e^{-s_i} \left(1 + \frac{s_i}{b_i}\right)^{d_i}, \quad (6.6)$$

may be chosen as the test statistic Q used to distinguish the background-only hypothesis (i.e. the absence of a signal) from the signal-plus-background one. The expected number of signal events in channel i is denoted by s_i , b_i is the associated number of backgrounds and d_i the number of observed number of events collected in data. While in a real experiment the number of observed data is obvious, a predictive analysis would take $s_i + d_i$ as the expectation value of d_i . In both the background-only and the signal-plus-background hypotheses, data counts are predicted in each bin of the discriminant variables. In the following each bin is considered as an independent channel in the sense of Equation 6.5.

For practical reasons the test statistic based on the log-likelihood ratio is used:

$$-2 \ln Q = 2s - 2 \sum_{i=1}^n d_i \ln \left(1 + \frac{s_i}{b_i}\right), \quad (6.7)$$

where s is the total signal ($s = \sum_{i=1}^n s_i$). By performing a large amount of

pseudo-experiments ¹ the values obtained using Equation 6.7 arrange themselves according to a distribution that can be interpreted as a probability density function (PDF) for the background-only and the signal-plus-background hypotheses. Typical distributions are shown in Figure 6.9. Finally, following the method used at LEP [119], the sensitivity of the analysis used to produce the PDF distributions can be extracted.

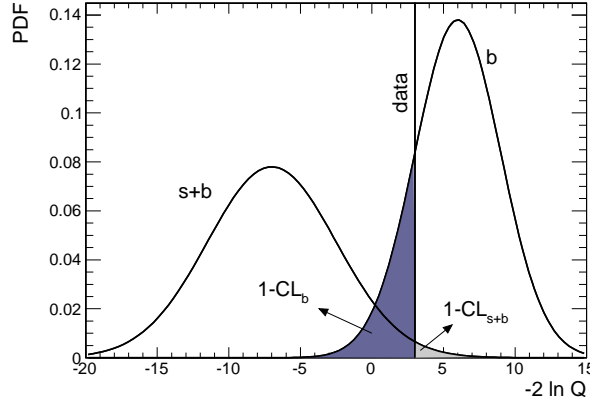


Figure 6.9: Probability density functions for the likelihood ratio in background-only (b) and signal-plus-background ($s+b$) hypotheses. Coloured areas show the corresponding confidence levels (CL_b and CL_{s+b}).

Discovery confidence

To compute the significance of an observed signal, the definition of the so-called *confidence level of the background-only hypothesis* (CL_b) is mandatory. This crucial quantity is defined as the integral over the PDF of the background-only hypothesis from minus infinity to a predefined value Q_{obs} obtained directly from Equation 6.6 using the actual value of d_i . The CL_b value written as

$$CL_b = P_b(Q \leq Q_{obs}), \quad (6.8)$$

represents the probability that an observation is considered as incompatible with the background only hypothesis. Consequently, the $1 - CL_b$ quantity describes the probability that the background mimics a signal with a value Q greater than Q_{obs} . For discovery, a 5σ sensitivity is claimed when the value of $1 - CL_b$ is 2.9×10^{-7} .

¹Using as inputs the distribution used to discriminate between the signal and the background, *pseudo-data distributions* are constructed by generating according to a Poisson statistic in each bin i of the histogram two random numbers, one for the signal and one for the background.

Exclusion confidence

For the exclusion of the SM Higgs boson, the *confidence level of the signal-plus-background hypothesis* (CL_{s+b}) may be defined in the same way:

$$CL_{s+b} = P_{s+b}(Q \leq Q_{obs}). \quad (6.9)$$

It gives therefore the probability, assuming the simultaneous presence of the signal and the background, that the test statistic would be less to that observed in data. A small value of CL_{s+b} therefore favour the background hypothesis. In order to quote exclusion limits the confidence limit $1 - CL_{s+b}$ may be used.

Nevertheless, since the CL_{s+b} has the drawback of being very sensitive to downward fluctuations of the background, the *modified frequentist confidence level* CL_s is defined by normalising the confidence level for the signal-plus-background hypothesis to the confidence level obtained for the background-only hypothesis:

$$CL_s \equiv CL_{s+b}/CL_b. \quad (6.10)$$

Even if by definition CL_s is not a confidence level, a signal hypothesis is considered as excluded at a confidence level CL when $1 - CL_s \leq CL$.

6.4.2 Discriminant distributions

In the $WHq' \rightarrow \ell b\bar{b}q'$ topology, the invariant mass of the two selected b -jets can be used to facilitate the visualisation of the signal above the background continuum even with a low tagging efficiency combined to the poor resolution of the reconstructed jets. Indeed, the efficient background subtraction allows to easily see the signal peak in the final distributions, as can be seen on Figure 6.10. After the jet reconstruction, the peak position of the m_{bb} distribution for the resonant WHq' events is shifted systematically by $\sim 15 \text{ GeV}/c^2$ towards lower values. This effect finds its explanation in the fact that the magnetic field implies a loss of jet energy due to particles ending outside the jet recognition cone, and due to the presence of the neutrinos contained in the b -quark decay.

In the $WHq' \rightarrow jj\tau\tau q'$ topologies, the reconstructed Higgs mass can be used as a clue of the presence of a Higgs signal. The reconstructed τ -pair invariant mass distributions obtained using Equation 6.3 obtained at the end of the related selection procedures are shown in Figure 6.11-*a* and *b* for the $\tau\tau \rightarrow \ell\ell$ and $\tau\tau \rightarrow \ell\tau_h$ topologies. The shown distributions have been normalised for an integrated luminosity of 100 fb^{-1} . While the Wt and $t\bar{t}$ backgrounds are roughly flat, the $W\ell\ell q'$ is almost completely concentrated around the value of the Z boson mass. Concerning the signal, the distribution is strongly peaked at $m_{\tau\tau} = m_H$. It is interesting to notice that for heavier Higgs boson masses,

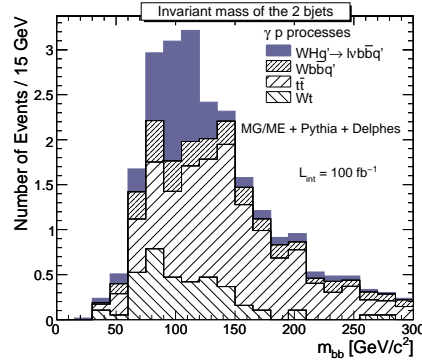


Figure 6.10: Cumulative distribution of the invariant mass of the two selected b -jets used to calculate the confidence level of a discovery or a 95% C.L. rejection of the signal for the $WHq' \rightarrow l\bar{b}bq'$ topology. The invariant mass is used. The distributions are given for a Higgs boson mass of $115 \text{ GeV}/c^2$ after the application of the dedicated selection procedures and are normalised for an integrated luminosity of 100 fb^{-1} .

the signal will appear as an excess of events in the high mass region, beyond the Z mass peak and that therefore backgrounds will greatly be reduced.

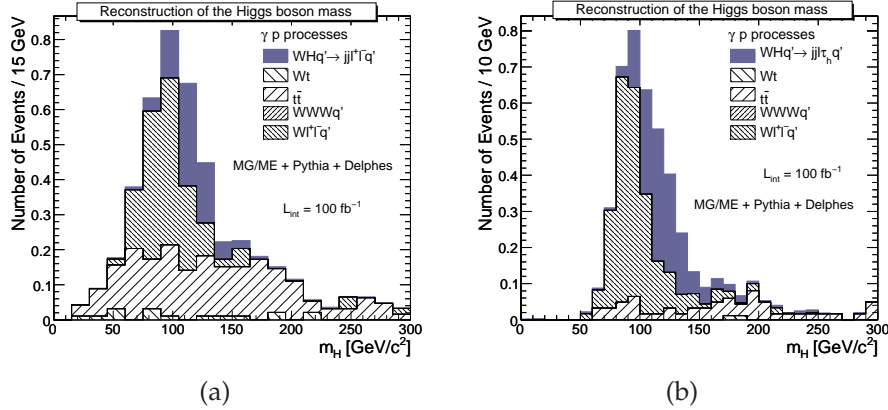


Figure 6.11: Cumulative discriminant distribution used to calculate the confidence level of a discovery or a 95% C.L. rejection of the signal for the two $WHq' \rightarrow jj\tau^+\tau^-q'$ topologies. The invariant mass of the two reconstructed τ is used. The distributions are given for a Higgs boson mass of $115 \text{ GeV}/c^2$ after the application of the dedicated selection procedures and are normalised for an integrated luminosity of 100 fb^{-1} .

For the $WHq' \rightarrow \ell\ell lq'$ topology, the transverse mass of the E_T^{miss} and the two

leptons coming from the Higgs decay can be reconstructed and should contain information on the Higgs boson mass. Nevertheless, due to the presence of the third lepton, an ambiguity is present. In this analysis the choice has been made to use in the transverse mass reconstruction (m_T), and of the dilepton pair ($m_{\ell\ell}$) that fulfils the condition of the $H \rightarrow WW$ tag. Hence the Higgs boson transverse mass is given by

$$m_T = \sqrt{m_T^{\ell\ell^2} + 2E_T^{\ell\ell} E_T^{\text{miss}} - 2p_T^{\ell\ell} E_T^{\text{miss}} \cos \Delta\phi_{\ell\ell E_T^{\text{miss}}}}, \quad (6.11)$$

where $m_T^{\ell\ell}$ is the transverse mass of the lepton pair, $E_T^{\ell\ell}$ its transverse energy and $\Delta\phi_{\ell\ell E_T^{\text{miss}}}$ is the polar angle between the missing transverse energy and the summed momentum of the lepton pair. Although this is only an approximation, since the missing transverse energy is affected by the decay neutrino from the associated W boson. As it can be seen on Figure 6.12-a, the transverse mass distribution is still peaked in the mass range between 115 and 170 GeV/c^2 and can consequently be used as a discriminant variable of the signal.

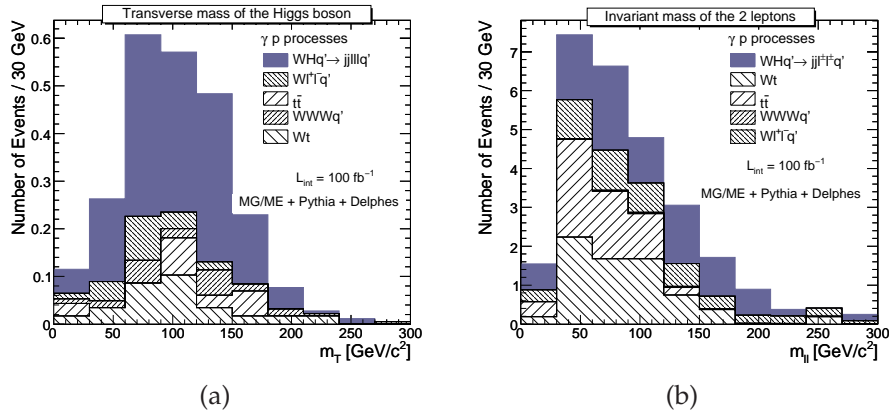


Figure 6.12: Cumulative discriminant distribution used to calculate the confidence level of a discovery or a 95% C.L. rejection of the signal for the two $WHq' \rightarrow WWWq'$ topologies. The transverse mass of the Higgs boson m_T and the invariant mass of the two selected leptons $m_{\ell\ell}$ are used respectively in the fully leptonic and the SS topologies. The distributions are given for a Higgs boson mass of $170 \text{ GeV}/c^2$ after the application of the dedicated selection procedures and are normalised for an integrated luminosity of 100 fb^{-1} .

The reconstruction of the Higgs mass is not easy in the channel $WHq' \rightarrow jj\ell^\pm\ell^\pm q'$ since one has to select the correct charged lepton out of the two present in the final state. As a consequence the variable used to determine the expected significance of this topology is the invariant mass on the two isolated

leptons. The invariant mass distributions of the two leptons are represented in Figure 6.12-b for a Higgs boson of $m_H = 170 \text{ GeV}/c^2$ and the backgrounds.

6.4.3 Expected observability

Using the previously mentioned discriminant distributions and the log-likelihood method, the expected significances for the 5 topologies are calculated. Table 6.7 summarises the obtained significances after an integrated luminosity of 30 and 100 fb^{-1} as well as the required luminosity to exclude the Higgs signal at 95% C.L. or to claim a discovery at 3σ . The values are given for the Higgs boson mass that gives the best sensitivity. These results can be considered as optimistic since no pile-up, proton-proton interactions as well as reducible background are taken into account in these analyses.

After 100 fb^{-1} of integrated luminosity, a significance of 1.5σ is obtained for the $WHq' \rightarrow \ell b \bar{b} q'$ topology for $m_H = 115 \text{ GeV}/c^2$. If a discovery is not expected in this channel, a high integrated luminosity could allow to probe Hbb coupling for a light Higgs boson, which is known to be very challenging to assess in parton-parton processes. Besides this channel, the two topologies arisen from the decays of the two τ 's have a less interesting sensitivity as the significance of the fully leptonic and the semi-leptonic decays of the τ 's are respectively 0.72σ and 1.33σ after an integrated luminosity of 100 fb^{-1} .

The best results are obtained for masses of $150 - 170 \text{ GeV}/c^2$ when the decay into two W boson becomes predominant mainly due to the SS contribution. Indeed, after 100 fb^{-1} , the significance of this topology reaches 2.2σ while the $WWWq' \rightarrow \ell \ell \ell q'$ decays taken apart amounts for 1.4σ . These channels are important to be studied because they belong to the few signatures for fermiophobic Higgs boson model and since in addition, they are doubly dependent on the HWW coupling.

Since the five studied topologies are complementary searches for the W associated single top photoproduction, Table 6.7 gives the significances and the required luminosity to reject a Higgs boson at 95% C.L or to claim a 3σ evidence for the combination of the presented analysis. Five benchmark mass points ranging from 115 to $170 \text{ GeV}/c^2$ have been investigated. Since a very good rejection of the backgrounds has been obtained in the five channels, the rather poor obtained results are certainly due to the very small number of signal events that survived the selection procedure. We can therefore conclude that the Higgs boson may certainly not be discovered at the LHC using photoproduction. For a Higgs boson of $m_H = 170 \text{ GeV}/c^2$, a significance close to 3σ can be reached. At best, after an integrated luminosity of less than 100 fb^{-1} an exclusion of the Higgs boson at 95% confidence level can be obtained in the mass range comprised between 150 and $170 \text{ GeV}/c^2$. Last but not least, larger integrated luminosity, of about hundreds inverse femtobarn, will open com-

Table 6.7: Summary of the obtained significances after an integrated luminosity of 30 and 100 fb⁻¹ as well as the required luminosity to exclude the Higgs signal at 95% C.L. and to claim a discovery at 3 σ . The values are given for the Higgs boson mass that gives the best sensitivity, while the combined results are for five benchmark mass points ranging from 115 to 170 GeV/c².

Topology	m_H [GeV/c ²]	Significance after		L [fb ⁻¹] needed for	
		$L = 30$ fb ⁻¹	$L = 100$ fb ⁻¹	95% C.L. excl.	3 σ
$l\bar{b}\bar{b}q'$	115	0.86	1.45	225	495
$jj\tau^+\tau^-q'$	115	0.62	0.72	1420	5119
$\rightarrow jj\ell^+\ell^-q'$	115	1.01	1.33	370	682
$WWWq'$	170	1.07	1.40	300	541
$\rightarrow jj\ell^\pm\ell^\pm q'$	170	1.27	2.22	97.5	230
Combined 5 channels	115	1.16	1.97	125	250
	130	1.07	1.78	157	333
	150	1.28	2.26	95	212
	170	1.47	2.64	73	153

plementary ways to access important information on the Higgs boson couplings and more specially the coupling of the Higgs boson to b -quarks and W bosons.

CONCLUSION

Photoproduction clearly provides a good complement to the usual physics programme involving proton-proton interactions at the LHC. The high cross section as well as the usually much lower backgrounds offer an ideal framework for studying massive electroweakly interacting particles, more specifically during the first years of running. In particular the observation of single top photoproduction will give a direct access to some crucial information such as the $|V_{tb}|$ element of the CKM matrix.

In experimental terms, the observation of photoproduced events requires several advanced techniques that should be applied to suppress the pp backgrounds by several orders of magnitudes, while preserving most of the signal events. In this thesis, two types of γp tagging techniques are applied: first a selection based on the energy measured in the forward region of the central detector and second a cut based on the number of reconstructed tracks in the $1 < \eta < 2.5$ region of the tracker. Moreover, during the low luminosity phase of the LHC ($\mathcal{L} = 2 \times 10^{33} \text{ cm}^{-2} \text{ s}^{-1}$), efficient photon-induced analyses require the use of the complete set of available detectors, in particular the forward proton taggers located at 220 m and 420 m from the interaction point. A proper estimation of the detection efficiencies with these forward detectors is also a crucial point for analyses.

All these technical considerations led to the development of the DELPHES framework that allows to perform a fast simulation of a general-purpose collider experiment such as CMS and ATLAS. The simulation includes central and forward detectors, and produce realistic observables using standard reconstruction algorithms. DELPHES allows to realistically gauge the feasibility of studies involving topologies with hard jets in the final state such as the ones involved in the $pp(\gamma b \rightarrow Wt)pY$ and $pp(\gamma q \rightarrow WHq')pY$ reactions.

Using DELPHES, the expected uncertainty on the measurement of $|V_{tb}|$ has been estimated using the di-leptonic and semi-leptonic topologies arising

from the decays of the $pp(\gamma b \rightarrow Wt)pY$ reaction. The uncertainty was found to be 14.7% for the semi-leptonic channel and 10.9% for the leptonic one after 10 fb^{-1} of integrated luminosity. This is very competitive with the results obtained at the LHC using the nominal $pp \rightarrow Wt$ reaction. Interestingly, in the di-leptonic topology, the final cross section uncertainty is dominated by the statistical error allowing to perform a complementary measurement to the pp reaction since its obtained value of the $|V_{tb}|$ uncertainty is mainly sensitive to the systematic errors. Since the use of DELPHES allowed to obtain very optimistic results in the di-leptonic final state, this topology was further probed with the dedicated official CMS software. The results at very low luminosity are very promising, with a very efficient background rejection and a good expected signal-to-noise ratio. Even in presence of more numerous pile-up events, the tagging techniques prove to be functional and efficient enough to preserve a significant amount of signal events with respect to the expected backgrounds.

Finally, considering a perfect running environment (no pile-up, proton-proton interactions as well as reducible background are taken into account in the analysis), it as been shown that for a light Higgs boson ($m_H < 130 \text{ GeV}/c^2$), a discovery is not expected using the $pp(\gamma q \rightarrow WHq')pY$ reaction: after 100 fb^{-1} of integrated luminosity, a significance of 1.5σ is obtained for the $WHq' \rightarrow \ell\bar{b}bq'$ topology. Nevertheless, a high integrated luminosity may allow to probe the Hbb coupling for a light Higgs boson, which is known to be very challenging to assess in parton-parton processes. For heavier masses, when the decay into two W boson becomes predominant the observability becomes better: 2.2σ for the $WHq' \rightarrow jj\ell^\pm\ell^\pm q'$ reaction while the $WHq' \rightarrow \ell\ell\ell q'$ topology amounts for 1.4σ . These two channels may therefore be important to study because they belong to the few signatures for fermiophobic Higgs boson model and since in addition, they are doubly dependent on the HWW coupling.

BIBLIOGRAPHY

- [1] S.L. Glashow, *Partial Symmetries of Weak Interactions*, [Nucl. Phys. 22 \(1961\) 579-588](#);
S. Weinberg, *A Model of Leptons*, [Phys. Rev. Lett. 19 \(1967\) 1264-1266](#);
A. Salam, *Elementary particle theory*, ed. N. Svartholm, Stockholm (1968) 367.
- [2] F.J. Hasert et al., *Observation of neutrino-like interactions without muon or electron in the gargamelle neutrino experiment*, [Phys. Lett. B46 \(1973\) 138-140](#).
- [3] UA1 Collaboration, G. Arnison et al., *Experimental observation of isolated large transverse energy electrons with associated missing energy at $\sqrt{s} = 540$ GeV*, [Phys. Lett. B122 \(1983\) 103-116](#);
UA2 Collaboration, M. Banner et al., *Observation of single isolated electrons of high transverse momentum in events with missing transverse energy at the CERN $\bar{p}p$ collider*, [Phys. Lett. B122 \(1983\) 476-485](#).
- [4] Particle Data Group, C. Amsler et al., *Review of Particle Physics*, [Phys. Lett. B 667 \(2008\)](#).
- [5] N. Cabibbo, *Unitary Symmetry and Leptonic Decays*, [Phys. Rev. Lett. 10 \(1963\) 531-532](#);
M. Kobayashi and T. Maskawa, *CP Violation in the Renormalizable Theory of Weak Interaction*, [Prog. Theor. Phys., 49 \(1973\) 652-657](#);
L. Wolfenstein, *Parametrization of the Kobayashi-Maskawa Matrix*, [Phys. Rev. Lett., 51 \(1983\) 1945-1947](#).
- [6] J. Alwall, R. Frederix, J.-M. Gerard, A. Giammanco, M. Herquet, S. Kalinin, E. Kou, V. Lemaitre, F. Maltoni, *Is $V_{tb}=1$?*, [Eur.Phys.J. C49 \(2007\) 791-801](#).
- [7] W.-M. Yao et al., *Review of Particle Physics*, [J. Phys. G: Nucl. Part. Phys. 33, 1\(2006\), p. 142](#).

- [8] CDF Collaboration, F. Abe et al., *Observation of Top Quark Production in $\bar{p}p$ Collisions with the Collider Detector at Fermilab*, *Phys. Rev. Lett.* **74** (1995) 2626-2631;
DØ Collaboration, S. Abachi et al., *Observation of the Top Quark*, *Phys. Rev. Lett.* **74** (1995) 2632-2637.
- [9] The Tevatron Collider, <http://www-bdnew.fnal.gov/tevatron/>.
- [10] The CDF experiment, <http://www-cdf.fnal.gov/>.
- [11] The DØ experiment, <http://www-d0.fnal.gov/>.
- [12] Lyndon Evans et al., *LHC Machine*, *JINST* **3**, S08001 (2008).
- [13] I.I.Y. Bigi et al., *Production and decay properties of ultra-heavy quarks*, *Phys. Lett. B* **181** (1986) 157-161.
- [14] S. Moch and P. Uwer, *Heavy-quark pair production at two loops in QCD*, *Nucl. Phys. B - Proc. Suppl* **183** (2008) 75-80.
- [15] B.W. Harris et al., *Fully differential single-top-quark cross section in next-to-leading order QCD*, *Phys. Rev. D* **66** (2002);
Z. Sullivan, *Understanding single-top-quark production and jets at hadron colliders*, *Phys. Rev. D* **70** (2004) 114012.
- [16] N. Kidonakis, *Single top quark production at the Fermilab Tevatron: Threshold resummation and finite-order soft gluon corrections*, *Phys. Rev. D* **74** (2006) 114012;
N. Kidonakis, *Higher-order soft gluon corrections in single top quark production at the CERN LHC*, *Phys. Rev. D* **75** (2007) 071501.
- [17] M. Schmaltz and D. Tucker-Smith, *Little Higgs theories*, *Ann. Rev. Nucl. Part. Sci.* **55** (2005) 229-270;
C.T. Hill and S.J. Parke, *Top quark production: Sensitivity to new physics*, *Phys. Rev. D* **49** (1994) 4454-4462;
H.P. Nilles, *Supersymmetry, supergravity and particle physics*, *Phys. Rept.* **110** (1984) 1-162.
- [18] T. Aaltonen et al., *Combination of CDF top quark pair production cross section measurements with 2.8 fb^{-1}* , *CDF Conf. Note* **9448**, July 2008.
- [19] DØ Collaboration, V.M. Abazov et al., *Combination and interpretations of $t\bar{t}$ cross section measurements with the D0 detector*, *Phys. Rev. D* **80** (2009) 071102.
- [20] CDF Collaboration, T. Aaltonen et al., *First Observation of Electroweak Single Top Quark Production*, *Phys. Rev. Lett.* **103** (2009) 092002.
- [21] DØ Collaboration, V.M. Abazov et al., *Observation of Single Top Quark Production*, *Phys. Rev. Lett.* **103** (2009) 092002.

- [22] CDF Collaboration, D. Acosta et al., *Measurement of $\mathcal{B}(t \rightarrow Wb)/\mathcal{B}(t \rightarrow Wq)$ at the Collider Detector at Fermilab*, [Phys. Rev. Lett. 95, 102002 \(2005\)](#).
- [23] DØ Collaboration, V. M. Abazov et al., *Simultaneous Measurement of the Ratio $R=\mathcal{B}(t \rightarrow Wb)/\mathcal{B}(t \rightarrow Wq)$ and the Top-Quark Pair Production Cross Section with the DØ Detector at $\sqrt{s} = 1.96$ TeV*, [Phys. Rev. Lett. 100, 192003 \(2008\)](#).
- [24] A. Djouadi, J. Kalinowski and M. Spira. *HDECAY: A program for Higgs boson decays in the Standard Model and its supersymmetric extension*, [Comput. Phys. Commun. 108 \(1998\) 56-74](#).
- [25] ALEPH, DELPHI, L3 and OPAL Collaborations and The LEP Working Group for Higgs Boson Searches, *Search for the Standard Model Higgs boson at LEP*, [Phys. Lett. B565 \(2003\) 61-75](#).
- [26] CDF Collaboration, J. Dittman et al., *Search for Higgs Boson Production in Association with W Boson with 1.7 fb^{-1}* , CDF Conference Note 8957.
DØ Collaboration, *Search for WH Production at $\sqrt{s} = 1.96$ TeV with Neural Networks*, [DØ Conference Note 5472](#).
- [27] CDF Collaboration, *Search for ZH in 1 fb^{-1}* , CDF Conference Note 8742.
DØ Collaboration, *A Search for the Standard Model Higgs boson using the $ZH \rightarrow \nu\bar{\nu}b\bar{b}$ channel in $p\bar{p}$ Collisions at $\sqrt{s} = 1.96$ TeV*, [DØ Conference note 5506](#).
- [28] CDF Collaboration, *Search for $H \rightarrow WW$ Production Using 1.9 fb^{-1}* , CDF Conference Note 8923.
- [29] DØ Collaboration, *Search for the Higgs boson in $H \rightarrow WW^* \rightarrow e\mu$ decays with 0.6 fb^{-1} at DØ in Run IIb*, [DØ Conference Note 5489](#).
DØ Collaboration, *Search for the Higgs boson in $H \rightarrow WW^* \rightarrow ee$ decays with 0.63 fb^{-1} at DØ in Run IIb*, [DØ Conference Note 5502](#).
DØ Collaboration, *Search for the Higgs boson in $H \rightarrow WW^* \rightarrow \ell^+\ell^-$ ($\ell, \ell' = e\mu$) decays with 1.7 fb^{-1} at DØ in Run II*, [DØ Conference Note 5537](#).
- [30] DØ Collaboration, *Search for the standard model Higgs boson in the $t\bar{t}H \rightarrow t\bar{t}b\bar{b}$ channel*, [DØ Conference Note 5739](#).
- [31] Tevatron New Physics, Higgs working group, for the CDF and DØ collaborations, *Combined CDF and DØ Upper Limits on Standard Model Higgs-Boson Production with $2.1 - 5.4 \text{ fb}^{-1}$ of Data*, [arXiv:0911.3930v1 \[hep-ex\]](#).
- [32] DØ Collaboration, I. Bertram et al., *A Recipe for the construction of confidence limits*, [Fermilab-TM-2104 \(2000\)](#), and references therein;
E.T. Jaynes and L. Bretthorst, *Probability Theory: the Logic of Science*, [Cambridge University Press, Cambridge, 2003](#).

- [33] V. M. Budnev et al., *The two-photon particle production mechanism. Physical problems. Applications. Equivalent photon approximation*, *Phys. Rep.* **15**, (1975) 181-282.
- [34] J.R. Dunning et al., *Quasi-Elastic Electron-Deuteron Scattering and Neutron Form Factors*, *Phys. Rev.* **141** (1966) 1286-1297.
- [35] P. Weisenpacher, *Origin of the Nucleon Electromagnetic Form Factors Dipole Formula*, *Czec. Jour. Phys.* **51** (2001) 785-590.
- [36] CMS Collaboration, D. d'Enterria et al., *CMS Physics Technical Design Report: Addendum on High Density QCD with Heavy Ions*, *J. Phys. G: Nucl. Part. Phys.* **34** (2007) 2307-2455.
- [37] F. Maltoni, and T. Stelzer, *MadEvent: automatic event generation with MadGraph*, *JHEP*, **0302** (2003) 027;
T. Stelzer, and W.F. Long, *Automatic Generation of Tree Level Helicity Amplitudes*, *Comp. Phys. Comm.* **81** (1994) 357-371.
- [38] J. Vermaseren, *LPAIR*, *Nucl. Phys. B* **229**, 347 (1983).
- [39] V.M. Budnev et al., *The Process $pp \rightarrow ppe^+e^-$ and the Possibility of Its Calculation by Means of Quantum Electrodynamics Only*, *Nucl. Phys. B* **63** (1973) 519-541.
- [40] X. Rouby and K. Piotrkowski, *Luminosity determination by CMS using exclusive muon pairs with early data*, [CERN CMS AN-2008/061](#).
- [41] M.G. Albrow et al., *The FP420 R&D Project: Higgs and New Physics with forward protons at the LHC*, [JINST 4 T10001](#) (2009).
- [42] X. Rouby, J. de Favereau and K. Piotrkowski, *HECTOR, a fast simulator for the transport of particles in beamlines*, [JINST 2 P09005](#) (2007).
- [43] O. Kepka and C. Royon, *Anomalous $WW\gamma$ coupling in photon-induced processes using forward detectors at the CERN LHC*, *Phys.Rev.D* **78:073005** (2008).
- [44] T. Pierzchala and K. Piotrkowski, *Sensitivity to anomalous quartic gauge couplings in photon-photon interactions at the LHC*, *Nucl. Phys. B, Proc. Suppl.* **179-180** (2008) 257-264.
- [45] J. Ohnemus, T. Walsh and P. Zerwas, *$\gamma\gamma$ production of non strongly-interacting SUSY particles at hadron colliders*, *Phys. Lett.* **B328** (1994) 369.
- [46] N. Schul and K. Piotrkowski, *Detection of two-photon exclusive production of supersymmetric pairs at the LHC*, *Nucl. Phys. Proc. Suppl.* **179-180** (2008) 289-297.
- [47] A. Pukhov, *Nucl. Inst. Meth. A* **502** (2003) 596-598.

- [48] J. de Favereau de Jeneret, S. Ovin, *Single top quark photoproduction at the LHC*, *Nucl. Phys. Proc. Suppl.* 179-180 (2008) 277-284.
- [49] J.D. Bjorken, *A full-acceptance detector for SSC physics at low and intermediate mass scales: an expression of interest to the SSC*, *Int. J. Mod. Phys. A7* (1992) 4189-4257;
J. D. Bjorken, *Rapidity gaps and jets as a new-physics signature in very-high-energy hadron-hadron collisions*, *Phys. Rev. D47* (1993) 101-113.
- [50] B. E. Cox et al., *Outstanding problems in the phenomenology of hard diffractive scattering*, *J. Phys. G26* (2000) 667-671;
R.J.M. Covolan and M.S. Soares, *Analysis of the diffractive production of W's and dijets at the DESY HERA and Fermilab Tevatron colliders*, *Phys. Rev. D 60*, 054005 (1999); Erratum, *Phys. Rev. D 61*, 019901(E) (2000);
CDF Collaboration, A.A. Affolder et al., *Diffractive Dijets with a Leading Antiproton in $\bar{p}p$ Collisions at $\sqrt{s} = 1800$ GeV*, *Phys. Rev. Lett.* 84 (2000) 5043-5048.
- [51] V.A. Khoze, A.D. Martin and M.G. Ryskin, *Insight into double-pomeron-exchange Higgs production and backgrounds*, *Phys. Lett. B 650* (2007) 41-45.
- [52] V.A. Khoze, A.D. Martin and M.G. Ryskin, *Prospects for new physics observations in diffractive processes at the LHC and Tevatron*, *Eur. Phys. J. C 23* (2002) 311-327.
- [53] V.A. Khoze, A.D. Martin and M.G. Ryskin, *Photon exchange processes at hadron colliders as a probe of the dynamics of diffraction*, *Eur. Phys. J. C 24* (2002) 459-468.
- [54] C. Pisano, *Testing the equivalent photon approximation of the proton in the process $ep \rightarrow \nu WX$* , *Eur. Phys. J. C 38* (2004) 79-84;
B.A. Kniehl, *Elastic ep scattering and the Weizsäcker-Williams approximation*, *Phys. Lett. B 254* (1991) 267.
- [55] K. Piotrkowski, *Tagging two-photon production at the CERN Large Hadron Collider*, *Phys. Rev. D63* (2001) 071502.
- [56] V.A. Khoze, A.D. Martin and M.G. Ryskin, *Soft processes at the LHC, II: soft-hard factorisation breaking and gap survival*, *Eur. Phys. J. C 18* (2000) 167.
- [57] F. Abe et al. (CDF Collaboration), *Observation of Diffractive W-Boson Production at the Fermilab Tevatron*, *Phys. Rev. Lett.* 78 (1997) 2698;
V.M. Abazov et al. (D0 Collaboration), *Observation of Diffractively Produced W and Z Bosons in $\bar{p}p$ Collisions at $\sqrt{s} = 1800$ GeV* *Phys. Lett. B 574* (2003) 169.
- [58] L. Bonnet et al., *GASTOF: Ultra-fast ToF forward detector for exclusive processes at the LHC*, *Acta. Phys. Polon. B38* (2007) 477-482.

- [59] The Large Hadron Collider Project, <http://lhc.web.cern.ch/lhc/>.
- [60] *Incident in LHC sector 3-4*, CERN Press Release PR09.08 20.09.2008.
- [61] ATLAS collaboration, *Detector and physics performance technical design report*, CERN/LHCC/99-014, CERN/LHCC/99-015; <http://atlas.web.cern.ch/>.
- [62] CMS collaboration, *The compact muon solenoid technical proposal*, CERN-LHCC-94-38 (1994); <http://cms.cern.ch/>.
- [63] ALICE collaboration, *Technical proposal for A Large Ion Collider Experiment at the CERN LHC*, CERN-LHCC-95-71 (1995); ALICE collaboration, K. Aamodt et al., *The ALICE experiment at the CERN LHC* JINST 3, S08002 (2008); <http://aliceinfo.cern.ch/>.
- [64] LHCb collaboration, *A Large Hadron Collider beauty experiment, Technical Proposal*, CERN-LHCC-98-004 (1998); The LHCb Collaboration, A.A. Alves Jr et al., *The LHCb Detector at the LHC*, JINST 3, S08005 (2008); <http://lhcb.web.cern.ch/lhcb/>.
- [65] Geant 4 collaboration, *Geant 4 - a simulation toolkit*, Nucl. Inst. & Meth. in Phys. Res. A 506 (2003) 250-303.
- [66] S. Ovin, X. Rouby and V. Lemaître, *Delphes, a framework for fast simulation of a generic collider experiment*, arXiv:0903.2225v2 [hep-ph]; <http://www.fynu.ucl.ac.be/delphes.html>, submitted to Comp. Phys. Comm.
- [67] The CMS Collaboration, *CMS Physics Technical Design Report Volume I: Detector Performance and Software*, CERN-LHCC-2006-001 (2006) 521pp.
- [68] The ATLAS Collaboration, *Expected Performance of the ATLAS Experiment - Detector, Trigger and Physics*, CERN-OPEN-2008-020 (2008) 1828pp.
- [69] M. Cacciari, G.P. Salam, *The FastJet package*, Phys. Lett. B 641 (2006) 57.
- [70] F. Abe et al., CDF Collaboration, *CDF Run I legacy algorithm*, Phys. Rev. D 45 (1992) 1448.
- [71] G.C. Blazey et al., *Run II Jet Physics: Proceedings of the Run II QCD and Weak Boson Physics Workshop*, 0005012 [hep-ex] (2000) 32pp.
- [72] G.P. Salam and G. Soyez, *SIScone, A practical Seedless Infrared-Safe Cone jet algorithm*, JHEP 05 (2007) 086.

- [73] S. Catani et al., *Longitudinally-invariant k_{\perp} -clustering algorithms for hadron-hadron collisions*, *Nucl. Phys. B* 406 (1993) 187-224;
S.D. Ellis and D.E. Soper, *Successive combination jet algorithm for hadron collisions*, *Phys. Rev. D* 48 (1993) 3160-3166.
- [74] Y.L. Dokshitzer et al., *On the QCD analysis of jet broadening*, *JHEP* 08 (1997) 001;
M. Wobisch and T. Wengler, *Hadronization Corrections to Jet Cross Sections in Deep-Inelastic Scattering*, 9907280 [hep-ph] (1999) 10pp.
- [75] M. Cacciari, G.P. Salam, G. Soyez, *The anti-kt jet clustering algorithm*, *JHEP* 04 (2008) 063.
- [76] T. Sjöstrand, S. Mrenna and P. Skands, *Pythia 6.4, Physics and Manual*, *JHEP* 05 (2006) 026.
- [77] X. Aslanoglou et al., *Performance of Prototype II for CMS CASTOR forward calorimeter*, *Eur. Phys. J. C* 52 (2007) 495-506;
X. Aslanoglou et al., *First performance studies of a prototype for the CASTOR forward calorimeter at the CMS experiment*, *Acta Phys. Polon. B* 39 (2008) 1429-1454;
X. Aslanoglou et al., *Performance studies of the final prototype for the CASTOR forward calorimeter at the CMS experiment*, CERN-CMS-NOTE-2008-022, (2008), 25pp.
- [78] V. Berardi et al., *Total cross-section, elastic scattering and diffraction dissociation at the Large Hadron Collider at CERN : TOTEM Technical Design Report* CERN-LHCC-2004-002 (2004), 219pp;
TOTEM Collaboration, *The TOTEM Experiment at the CERN Large Hadron Collider*, JINST 3 S08007 (2008);
<http://totem.web.cern.ch/>.
- [79] The CMS and TOTEM diffractive and forward physics working group, *Prospects for Diffractive and Forward Physics at the LHC*, CERN/LHCC 2006-039/G-124 (2006).
- [80] M.G. Albrow et al., *The FP420 R&D Project*, CERN-LHCC-2005-025 (2005) 17pp; <http://www.fp420.com/>.
- [81] R. Kinnunen and A.N. Nikitenko, *Study of τ -jet identification in CMS*, CERN CMS NOTE 1997/002.
- [82] L. Quertenmont and V. Roberfroid, *FROG: The Fast & Realistic OPENGL Displayer*, CERN CMS CR 2009/028, 0901.2718v1 [hep-ex] (2009) 26pp.
- [83] S. Ovin and J. de Favereau de Jeneret, *High energy single top photoproduction at the LHC*, *Nuovo Cimento B* 123:08-09 (2008) 1126-1133.

- [84] J. de Favereau et al., *High energy photon interactions at the LHC*, CP3-09-37, August 2009, 0908.2020v1 [[hep-ph](#)] (2009).
- [85] S. de Visscher et al., *Unconventional phenomenology of a minimal two-Higgs-doublet model*, [JHEP, 08 \(2009\) 042](#).
- [86] R. Bonciani, S. Catani, M.L. Mangano and P. Nason, *NLL resummation of the heavy-quark hadroproduction cross-section*, [Nucl. Phys. B 529 \(1998\) 424-450](#);
R. Bonciani et al., *Erratum-ibid.*, [Nucl. Phys. B 803 \(2008\) 234](#).
- [87] M. Schmaltz and D. Tucker-Smith, *Little Higgs Review* [Ann. Rev. Nucl. Part. Sci. 55 \(2005\) 229-270](#);
H.P. Nilles, *Supersymmetry, supergravity and particle physics*, [Phys. Rept. 110 \(1984\) 1-162](#).
- [88] M. Davids et al., *Measurement of top-pair cross section and top-quark mass in the di-lepton and full-hadronic channels with CMS*, [CMS Note 2006/077 \(2006\)](#).
- [89] T. Stelzer, Z. Sullivan and S. Willenbrock, *Single top quark production via W-gluon fusion at next-to-leading order*, [Phys. Rev. D 56 \(1997\) 5919-5927](#).
- [90] M.C. Smith and S. Willenbrock, *QCD and Yukawa corrections to single top quark production via q anti- $q \rightarrow t$ anti- b* , [Phys. Rev. D 54 \(1996\) 6696-6702](#).
- [91] J. Campbell and F. Tramontano, *Next-to-leading order corrections to Wt production and decay*, [Nucl. Phys. B 726 \(2005\) 109-130](#).
- [92] CMS collaboration, *CMS Physics Technical Design Report, Volume II: Physics Performance*, [J. Phys. G: Nucl. Part. Phys. 34 \(2007\) 995-1579](#).
- [93] F. Sikler, *Reconstruction of low p_T charged particles with the pixel detector*, [CERN CMS AN-2006/100 \(2006\)](#).
- [94] P. Yeh et al., *Search for W-associated Production of Single Top Quarks in CMS*, [CERN CMS NOTE 2006/086 \(2006\)](#).
- [95] *LHC Commissioning with Beam*, <http://lhc-commissioning.web.cern.ch/>.
- [96] M. Beneke et al., *Top Quark Physics*, [hep-ph/0003033 \(2000\) 111pp](#).
- [97] J. Campbell, R.K. Ellis and D.L. Rainwater, *Next-to-leading order QCD predictions for $W+2j$ and $Z+2j$ production at the CERN LHC*, [Phys. Rev. D 68 \(2003\) 094021](#).
- [98] CMS Collaboration, *The CMS experiment at the CERN LHC*, [JINST 3 S08004 \(2008\) 361pp](#).

- [99] V. Kolosov et al., *Test beam results of the CMS forward quartz fibre calorimeter*, 9th ICATPP Conference on Astroparticle, Particle, Space Physics, Detectors and Medical Physics Applications, Como, Italy, 17 - 21 Oct 2005, [Conference proceedings \(2005\) 416-420](#).
- [100] E. Meschi et al., *Electron Reconstruction in the CMS Electromagnetic Calorimeter*, [CERN CMS NOTE 2001/034 \(2001\)](#).
- [101] R. Frühwirth, *Application of Kalman filtering to track and vertex fitting*, [Nucl. Inst. & Meth. in Phys. Res. A 262 \(1987\) 444-450](#).
- [102] R. Demina et al., *Calorimeter Cell Energy Thresholds for Jet Reconstruction in CMS*, [CMS NOTE 2006/020 \(2006\) 8pp](#).
- [103] S. Esen et al., *E_T^{miss} Performance in CMS*, CMS AN-2007/041 (2007).
- [104] J. Alexander et al., *E_T^{miss} Reconstruction, Performance and Validation*, CMS 2008/089.
- [105] M. Vazquez Acosta et al., *Jet and MET Performance in CMSSW 1 2 0*, CMS Note IN-2007/053.
- [106] J. Branson et al., *A cut based method for electron identification in CMS*, CMS AN-2008/082.
- [107] CMS Collaboration, *Trigger Menus for iCSA08: 2E30, 2E31*, https://twiki.cern.ch/twiki/bin/view/CMS/TSG_27_V_08
- [108] Private communication from P. Janot, responsible for the Fast Simulation in CMSSW (19/06/2009).
- [109] A. Rizzi, F. Palla, G. Segneri, *Track impact parameter based b-tagging with CMS*, [CMS NOTE 2006/019 \(2006\) 16pp](#).
- [110] P. Demin et al., *Tagging b-jets with electrons and muons at CMS*, [CMS NOTE 2006/043 \(2006\)](#).
- [111] T. Speer and M. Narain, *Measurement of the b-tagging efficiency with fully-leptonic $t\bar{t}$ decays*
- [112] A. Nikitenko, S. Kunori and R. Kinnunen, *Missing Transverse Energy Measurement with Jet Energy Corrections*, CMS NOTE 2001/040.
- [113] The Particle Flow Physics Object Group, *Particle Flow Reconstruction of Jets, Taus, and MET*, CMS AN-2009/039.
- [114] B. Mellado et al., *Higgs Production Cross-Sections and Branching Ratios for the ATLAS Higgs Working Group*, [Atlas Com. Phys. \(2007\) 024](#).
- [115] T. Hahn et al., *SM and MSSM Higgs Boson Production Cross Sections at the Tevatron and the LHC*, [arXiv 0607308 \[hep-ph\]](#).

- [116] K. Cheung, *Photoproduction of $W H$ signal at electron - proton colliders*, [Phys. Lett. B 319 \(1993\) 244-248](#).
- [117] S. Oryn, X. Rouby, J.J. Hollar, *Forward Physics Triggers*, CMS internal note (CP3-08-07), [CMS IN-2008/028](#).
- [118] T. Junk, *Confidence level computation for combining searches with small statistics*, [Nucl. Inst. & Meth. in Phys. Res. A 434 \(1999\) 435](#).
- [119] A. Read, *Presentation of search results: the $CL(s)$ technique*, [J. Phys. G28 \(2002\) 2693-2704](#).

LIST OF FIGURES

1	Feynman diagrams for photon-induced processes	2
1.1	Scalar Higgs potential	9
1.2	Feynman diagrams for top quark production at the TEVATRON	14
1.3	Branching ratios of the Standard Model Higgs boson	17
1.4	Higgsstrahlung at LEP	17
1.5	Production of the Higgs boson through VBF at LEP	18
1.6	Major Higgs production processes at the TEVATRON	18
1.7	SM Higgs boson production cross sections at the TEVATRON	19
1.8	95% CL upper limits on the Higgs boson production cross section	20
2.1	Schematic view of the photon-induced processes	22
2.2	Sachs form factors and the $F_E(Q^2)$ and $F_M(Q^2)$ functions	24
2.3	Photon luminosity spectrum $\frac{dL_{\gamma\gamma}}{dW_{\gamma\gamma}}$	26
2.4	Cross-section for several $pp(\gamma\gamma \rightarrow X)pp$ processes	28
2.5	Cross sections for photoproduction	30
2.6	Photoproduction without and with rescattering corrections	32
2.7	Diagrams of elastic and inelastic events	33
2.8	Event topologies for elastic and diffractive pp interactions	34
2.9	Differential cross sections for SD and photon-induced events	35
2.10	Representation of the effect of pile-up events on the rapidity gap	36
3.1	Schematic view of the ‘‘CERN accelerator complex’’	38
3.2	Profile of layout of the detector geometry assumed in DELPHES	41
3.3	Propagation of a charged particle in the dipolar magnetic field	42
3.4	Default segmentation of the calorimeters in the (η, ϕ) plane	45
3.5	Distribution of the two variables used to tag a τ -jet	51
3.6	Default location of the very forward detectors at the LHC	54
3.7	Resolution of the E_T of reconstructed jets in a CMS-like detector	57
3.8	Resolution of the E of reconstructed jets in a ATLAS-like detector	58
3.9	$\sigma(E_x^{\text{mis}})$ for a CMS and an ATLAS-like detector	60

3.10	p_T distribution for reconstructed tracks in DELPHES	61
3.11	Layout of the generic detector geometry assumed in DELPHES	62
3.12	$pp(\gamma p \rightarrow Wt)pY$ event display	63
4.1	Feynman diagrams of the LO processes for $t\bar{t}$ production	66
4.2	LO Feynman diagrams for single-top quark production	67
4.3	LO Feynman diagrams of the top quark pair photoproduction	69
4.4	LO Feynman diagrams of the single-top photoproduction	70
4.5	LO diagrams of $pp(\gamma q/g \rightarrow X)pY$ backgrounds	72
4.6	Distribution of the number of central jets with $p_T > 20$ GeV/ c	74
4.7	E_{min}^{FCAL} in the two FCALS and E_{CUT}^{FCAL} distribution	76
4.8	η distribution of tracks with $p_T > 0.5$ GeV/ c in the tracker	77
4.9	Percentage of events that are accepted by the γp cuts	78
4.10	Invariant mass of the two non b -tagged central ($ \eta < 3$) jets	80
4.11	Scalar sum of the p_T of the visible selected objects	81
4.12	Distribution of the reconstructed top mass	83
4.13	Distribution of the invariant mass of the two lepton candidates	86
4.14	Distribution of the number of central jets with $p_T > 30$ GeV/ c	86
4.15	Distribution of the missing transverse energy	87
4.16	Rejection power of pp backgrounds	93
5.1	Overview of the CMS central detector	106
5.2	$r-z$ view of the tracker of CMS	107
5.3	Layout of the electromagnetic calorimeter	108
5.4	Longitudinal view of a quarter of the hadronic calorimeter	109
5.5	Transverse view of the CMS detector	110
5.6	Flowchart of the data treatment into CMSSW	117
5.7	Geometrical matching ($\Delta\phi_{in}$ and $\Delta\eta_{in}$) for electron identification	117
5.8	Quality criteria (H/E and E_{sc}/p_{in}) for electron identification	118
5.9	Quality requirements (χ^2 and N_{hits}) for muon identification	120
5.10	Online selection efficiencies during the very low luminosity	122
5.11	Isolation requirements (I_{calo} and I_{tk}) on selected electrons	124
5.12	Distribution of the number of central jets with $p_T > 30$ GeV/ c	125
5.13	Fraction of selected events as a function of the E_{CUT}^{FCAL} value	126
5.14	b -tagging algorithm characterisation ($D_{HighEff}$ and p_T)	128
5.15	Distribution of the missing transverse energy	129
5.16	Online selection efficiencies during the low luminosity	131
6.1	Higgs boson production cross section at the LHC	136
6.2	SM Higgs discovery potential for CMS	137
6.3	LO Feynman diagrams of the associated Higgs photoproduction	138
6.4	$pp(\gamma q \rightarrow WHq')pY$ production cross sections at the LHC	140
6.5	Final discrimination of $WHq' \rightarrow \ell b\bar{b}q'$ events (N_{tracks} and $\Delta\eta^{\ell-H}$)	144
6.6	Distribution of the dilepton invariant mass	146
6.7	Distributions of m_{jj} and the minimum $\Delta\eta^{\ell-W}$	147

6.8	Invariant mass of the opposite-charge same-flavour leptons . . .	150
6.9	Probability density functions for the likelihood ratio	154
6.10	Distribution of the invariant mass of the two selected b -jets . . .	156
6.11	Discriminant distribution for $WHq' \rightarrow jj\tau^+\tau^-q'$	156
6.12	Discriminant distribution for $WHq' \rightarrow WWWq'$	157